

# REPORT DOCUMENTATION PAGE

*Form Approved  
OMB No. 0704-0188*

Public reporting burden for this collection of information is estimated to average 1 hour per response, including the time for reviewing instructions, searching existing data sources, gathering and maintaining the data needed, and completing and reviewing this collection of information. Send comments regarding this burden estimate or any other aspect of this collection of information, including suggestions for reducing this burden to Department of Defense, Washington Headquarters Services, Directorate for Information Operations and Reports (0704-0188), 1215 Jefferson Davis Highway, Suite 1204, Arlington, VA 22202-4302. Respondents should be aware that notwithstanding any other provision of law, no person shall be subject to any penalty for failing to comply with a collection of information if it does not display a currently valid OMB control number. PLEASE DO NOT RETURN YOUR FORM TO THE ABOVE ADDRESS.

1. REPORT DATE (DD-MM-YYYY) 01-04-2007		2. REPORT TYPE Final Technical		3. DATES COVERED (From - To) 01-01-2004 - 31-12-2006	
4. TITLE AND SUBTITLE (U) Enhancement of Combustion and Flame Stabilization Using Transient Non-Equilibrium Plasma				5a. CONTRACT NUMBER	
				5b. GRANT NUMBER FA9550-04-1-0038	
				5c. PROGRAM ELEMENT NUMBER 61102F	
6. AUTHOR(S) Yiguang Ju, Timothy Ombrello, Alexander Fridman, Alexander Gutsol, Shailesh Gangoli				5d. PROJECT NUMBER 2308	
				5e. TASK NUMBER TA	
				5f. WORK UNIT NUMBER	
7. PERFORMING ORGANIZATION NAME(S) AND ADDRESS(ES)				8. PERFORMING ORGANIZATION REPORT NUMBER	
Princeton University Department of Mechanical and Aerospace Engineering EQUAD on Olden Street Princeton, NJ 08544		Drexel University Drexel Plasma Institute 34 <sup>th</sup> Street and Lancaster Avenue Philadelphia, PA 19104			
9. SPONSORING / MONITORING AGENCY NAME(S) AND ADDRESS(ES) AFOSR/NA 875 North Randolph Street Suite 325, Room 3112 Arlington, VA 22203-1768 <i>Dr Julian Tishkoff</i>				10. SPONSOR/MONITOR'S ACRONYM(S)	
				11. SPONSOR/MONITOR'S REPORT NUMBER(S)	
12. DISTRIBUTION / AVAILABILITY STATEMENT Approved for public release; distribution is unlimited				AFRL-SR-AR-TR-07-0223	
13. SUPPLEMENTARY NOTES					
14. ABSTRACT  The effect of non-equilibrium plasma on both partially premixed and non-premixed flames was investigated through the development of a newly integrated magnetic gliding arc (MGA) system. The lifted jet diffusion flame experiments showed a significant enhancement of the flame stabilization with plasma discharge in the air co-flow. The counterflow experiments also demonstrated that the extinction limits were extended dramatically. Laser diagnostics of flame temperature and OH distribution using planar Rayleigh scattering and planar laser-induced fluorescence revealed that the plasma-flame interaction at low air temperature was dominated by thermal effects due to rapid radical quenching. Counterflow ignition experiments for CH <sub>4</sub> -air and H <sub>2</sub> -air non-premixed flames demonstrated clearly that the MGA significantly decreased the ignition temperatures via kinetic enhancement by the NO <sub>x</sub> catalytic effect. Numerical modeling showed that there were two ignition regimes for plasma enhanced ignition, kinetic at low strain rates and thermal at high strain rates. Comparison between experiment and simulation were in good agreement and also suggested the possibility of enhancement by ions, excited species or other mechanisms. Theoretical analysis of minimum ignition energy in a quiescent mixture showed that the production of small hydrocarbon fuel fragments by plasma discharge also led to a significant decrease of ignition energy due to radiation and transport coupling.					
15. SUBJECT TERMS Non-equilibrium plasma, flame stabilization, ignition enhancement, kinetic enhancement					
16. SECURITY CLASSIFICATION OF:			17. LIMITATION OF ABSTRACT UL	18. NUMBER OF PAGES 138	19a. NAME OF RESPONSIBLE PERSON Julian M. Tishkoff
a. REPORT Unclassified	b. ABSTRACT Unclassified	c. THIS PAGE Unclassified			19b. TELEPHONE NUMBER (include area code) (703) 696-8478

**FINAL REPORT: FA9550-04-1-0038, January 2004 – December 2006**

**ENHANCEMENT OF COMBUSTION AND FLAME STABILIZATION USING  
TRANSIENT NON-EQUILIBRIUM PLASMA**

Principle Investigator: Yiguang Ju

Department of Mechanical and Aerospace Engineering  
Princeton University  
D330, Engineering Quadrangle, Olden Street  
Princeton, NJ 08544  
E-mail: [yju@princeton.edu](mailto:yju@princeton.edu)  
Phone: 609-258-5644, Fax: 609-258-6233

Grant Number: FA9550-04-1-0038

Program Manager: Dr. Julian M. Tishkoff

Research Period: January 2004 – December 2006

Report date: March 31<sup>st</sup>, 2007

## Table of Contents

<u>Section</u>	<u>Page</u>
<b>Nomenclature .....</b>	3
<b>1.0 Introduction .....</b>	4
<b>2.0 Development and Characterization of Non-Equilibrium Gliding Arc System .....</b>	4
2.1 Near-Extinction Magnetic Gliding Arc (MGA) Plasma Discharge Design .....	4
2.2 Plasma Disk.....	5
2.3 Characterization and Modeling of MGA .....	7
2.4 Optical Emission Spectroscopy for Rotational and Vibrational Temperature Measurements	8
2.5 Electron Temperature Measurements of MGA.....	13
2.6 Measurement of Voltage-Current (V-I) Characteristics of MGA.....	14
2.7 Measurements of Current Densities for MGA .....	15
2.8 Plasma Kinetic Modeling.....	16
2.8.1 Dry Air Plasma Mechanism.....	17
2.8.2 MGA Production of O and NO .....	20
2.8.3 Dependence on G-factor and Specific Power Input (SPI) .....	20
2.9 Recombination of Plasma Produced Species in Convection and Diffusion Zone .....	21
<b>3.0 Ignition and Flame Stabilization Enhancement by MGA .....</b>	23
3.1 Stability Enhancement of Jet Diffusion Flames.....	23
3.2 Counterflow Flame Burner Integration .....	24
3.3 Effects on Flame Extinction Limit .....	26
3.4 Rayleigh Scattering and OH Planar Laser Induced Fluorescence Experimental Set-up.....	28
3.5 Temperature Measurements by Using Rayleigh Scattering.....	29
3.5.1 Rayleigh Scattering Intensity Ratio Profiles.....	30
3.5.2 Temperature Distributions .....	30
3.6 OH PLIF Measurements .....	31
3.7 Effects of Radical Addition on Flame Structures.....	32
3.8 Ignition Temperature Measurements by Using the Counterflow Flame .....	33
3.9 Ignition Temperature Measurements.....	35
3.10 Ignition Enhancement by MGA.....	36
3.11 Computational Simulations of Counterflow Non-Premixed Flame Ignition.....	36
3.11.1 Ignition with Pre-heated Air Only .....	37
3.11.2 Kinetic Ignition Enhancement by MGA and Ignition Diagram.....	38
3.12 Sensitivity Analysis and NO <sub>x</sub> Catalytic Path.....	41
3.13 Comparison of Experimental and Computational Results .....	43
3.14 Additional Non-Thermal Enhancing Mechanisms from MGA .....	44
3.14.1 Ignition Enhancement via Ions, Excited Species and Electron-Molecule Collisions	45
3.14.2 Effect of Plasma Produced Hydrocarbon Fragments on the Reduction of Minimum Ignition Energies .....	45
3.14.3 Numerical Modeling of the Electric Field Effect on Premixed Flames .....	48
<b>4.0 Summary .....</b>	50
<b>5.0 References .....</b>	51
<b>6.0 Participating Personnel .....</b>	53
<b>7.0 Publications.....</b>	53

<i>Peer Reviewed Journal Publications</i> .....	53
<i>Presentations at Conferences</i> .....	54
<b>8.0 Interactions and Consultations</b> .....	55
<b>9.0 Honors and Awards</b> .....	55
<b>10.0 Inventions</b> .....	56

## Nomenclature

$a$	=	strain rate
$B$	=	magnetic field strength
$C_d$	=	coefficient of drag
$CS$	=	cathode spot
$D$	=	diameter of MGA device
$D_i$	=	diffusivity of $i^{\text{th}}$ species
$d$	=	diameter of arc
$d_{\text{corrected}}$	=	diametrically corrected diameter of arc
$d_{\text{measured}}$	=	measured diameter of arc
$E$	=	electric field strength
$E_n$	=	energy of state of excitation
$E/n$	=	reduced electric field strength
$e$	=	electron charge
$F_a$	=	Ampere force per unit arc length
$F_d$	=	drag force
$M$	=	flow rate
$F, G$	=	analytic function
$f$	=	frequency of arc rotation
$G_0, G_1, G_{\text{ref}}$	=	identified peaks from OH spectrum
$H$	=	radiation heat loss
$\text{Hz}$	=	Hertz
$h$	=	heat loss constant
$I$	=	intensity
$I_{\text{ref}}$	=	reference intensity
$j$	=	current
$K_p$	=	Planck mean absorption coefficient
$k$	=	current density
$L$	=	distance between two nozzles
$\text{MGA}$	=	Magnetic Gliding Arc
$\text{NG}$	=	negative glow
$n_e$	=	electron energy
$\text{PC}$	=	plasma column
$\text{PW}$	=	input power
$Q$	=	flow rate
$r$	=	radial coordinate
$S_L^0$	=	laminar flame speed
$S_L$	=	adiabatic planar flame speed
$\text{SLPM}$	=	standard liters per minute
$\text{SPI}$	=	specific power input
$S_p$	=	triple flame speed
$T$	=	temperature
$T_e$	=	electron temperature
$T_{\text{ref}}$	=	reference temperature
$t$	=	time
$U$	=	eigenvalue of flame speed
$u$	=	flow velocity
$V_d$	=	electron drift velocity
$Y$	=	fuel mass fraction
$Z(T_{\text{ref}}), Z(T)$	=	partition functions
$\delta_f^0$	=	flame thickness
$\lambda$	=	thermal conductivity
$\omega$	=	reaction rate
$\rho$	=	density
$\sigma$	=	Stefan Boltzmann constant
$\tau$	=	characteristic time of one arc revolution

## **1.0 Introduction**

Research on the enhancement of combustion processes by using non-equilibrium plasma was conducted through a comprehensive experimental and computational study of ignition, extinction and flame speed phenomena. The work was based upon attempting to understand the fundamental mechanisms of plasma-assisted combustion motivated by the concerns of long ignition delay time and incomplete combustion in high speed propulsion systems. The key challenges were to provide simplified experimental platforms to isolate and study the mechanisms of enhancement ranging from elevated temperatures to radicals, excited species production, hydrocarbon fragments, and long lifetime catalytic species.

The focus of the work was first to develop and characterize the properties of a plasma system utilizing the non-equilibrium near-extinction gliding arc plasma discharge and second to integrate the plasma system with a counterflow burner system. Throughout the development and study of plasma-assisted combustion with this novel system, extension of ignition and extinction limits for both premixed and non-premixed flames were investigated. A fundamental understanding of the primary mechanisms of plasma-assisted combustion for ignition and flame stabilization enhancement was achieved.

## **2.0 Development and Characterization of Non-Equilibrium Gliding Arc System**

### **2.1 Near-Extinction Magnetic Gliding Arc (MGA) Plasma Discharge Design**

The near-extinction magnetic gliding arc developed in this study was a special type of electrical discharge that occurred between two diverging high voltage electrodes and had both thermal and non-thermal plasma properties (large electron number density and high electron temperature). The arc first was established when a sufficiently high potential was applied across the electrodes (approximately 3 kV/mm in air) to break down the gas at the gap with the smallest electrode separation distance. Once the equilibrium thermal arc channel was established, the flow velocity moved the arc moved downstream and the arc current decreased rapidly, while the voltage increased simultaneously to maintain constant power. As such, the reduced electric field strength ( $E/n$  ratio) increased rapidly. At a point when the arc elongated such that the power supplied to the source could not balance the amount of heat lost to the surroundings, the arc changed into a near-extinction non-equilibrium arc with a large difference between the neutral gas temperature and the electron temperature. As a result, the primary means of dissociation and ionization then was not dominated by thermal effects but by electron impact dissociation and ionization processes. The part of the gliding arc discharge with both thermal and non-thermal properties had the important benefit of lower energy cost with better chemical selectivity and kinetic efficiency. Without providing a method for arc stabilization, the arc would continue to elongate as it propagated along the diverging electrodes until it finally extinguished. Therefore, in the traditional gliding arc system, the arc regime with non-equilibrium plasma properties exists only for a very short period of time in the entire arc evolution process.

Recently it was found that, by using an appropriate external magnetic field, the arc could be stabilized well past the transition from the thermal equilibrium to the non-equilibrium regime immediately before extinction.<sup>1</sup> The newfound stability is significant because, unlike a

traditional gliding arc, the non-equilibrium process does not have to be cyclic and transient. The non-equilibrium plasma arc can be stabilized near extinction in a regime where there are both thermal and non-thermal properties for an indefinite time, creating a quasi-uniform plasma disk.

The special type of gliding arc plasma discharge device developed with the newfound near-extinction stability was termed the Magnetic Gliding Arc (MGA). The system was comprised of stainless steel inner and outer electrodes, which were the cathode and anode, respectively (Fig. 1). A wire was attached to the cathode, which was separated from the outer anode by 2 mm at the smallest gap (point (1) in Fig. 1). The wire spiraled progressively closer to the cathode, where it was attached at the largest gap between the two electrodes. In addition, there was a magnetic field in the discharge region produced by external donut shaped permanent ceramic magnets. The direction of the magnetic field determined the direction of the rotation of the arc (in this case counterclockwise to follow the wire when looking down upon the system as shown in a) of Fig. 1) and the field strength, as well as the power input, determined the frequency of rotation.

## 2.2 Plasma Disk

When an external magnetic field was applied to the arc, the arc rotated because of the Lorentz force. The length of the arc then increased as the distance between the spiraled wire and the outer electrode increased (Fig. 1 from points (1) to (2) to (3)). The increase of arc length and the decrease of plasma conductivity resulted in an arc transition from the equilibrium regime to a non-equilibrium regime with a significant difference between the arc temperature (2000 K – 3000 K) and the electron temperature (1 eV - 4 eV). Once the arc reached the cylindrical inner electrode (point (4) in Fig. 1), there was a stable, rotating (gliding) near-extinction non-equilibrium arc in the gas flow. A top view of this plasma disk is shown in Fig. 2. The plasma arc rotation frequency ranged from approximately 20 Hz to 50 Hz and only decreased by a few percent when the flow rate was increased (Fig. 3). The increased rotation frequency came from the higher current input (and hence, higher power addition), forcing the arc to rotate faster in the magnetic field. When the arc reached the largest gap, it remained at a fixed axial position with a constant length as it rotated. The stability of the arc at the fixed position

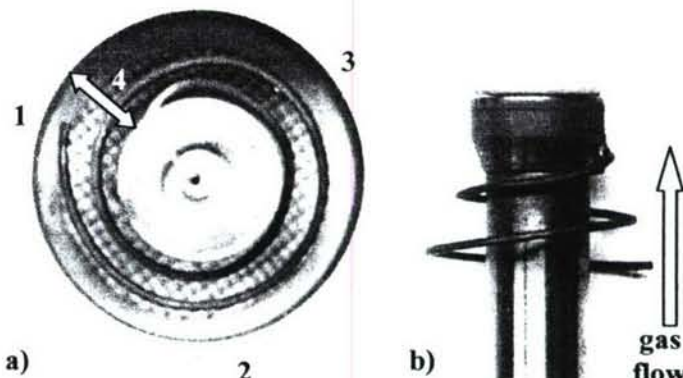


**Fig. 1** MGA plasma system. a) top view of system, b) side view of central electrode. Numbers indicate the path of the gliding arc from initiation (1) to arc rotation/elongation (2) and (3) and finally arc stabilization (4)

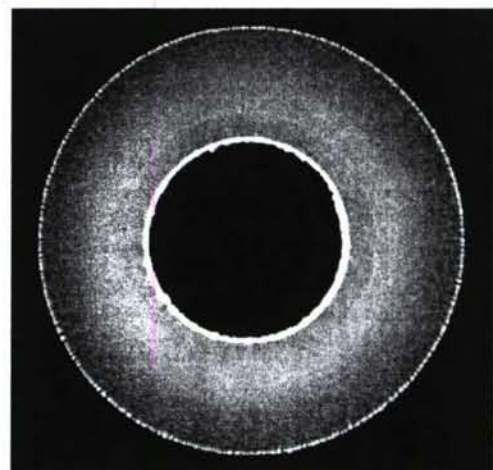


**Fig. 2** Top view of plasma disk

was because the arc was no longer convecting downstream. The arc maintained itself at that position because it was rotating through media that were pre-ionized and not through the initial non-ionized gas. Therefore, the arc required less power to remain at that position, as opposed to quenching and reinitiating at the smallest electrode gap.

Since the frequency of the arc rotation was fast compared to the gas velocity ( $\sim 10$  cm/s), there was quasi-uniform activation of the flow. Calculations were performed to find what flow rate,  $Q$ , of air was quasi-uniformly activated by the gliding arc. The system had a distance of 10 mm at the largest gap where the plasma disk was located and a magnetic field strength,  $B$ , of approximately 0.15 Tesla. The low-current, high-voltage gliding arc operation had an electric field strength,  $E$ , for the case of the gliding arc propagation through non-ionized air of about 0.1 kV/mm. The voltage drop was, therefore, 1 kV for the given length of the gap. The Ampere force per unit arc length that rotated the gliding arc was  $F_a = jB$ , and when in equilibrium conditions, it was equal to the drag force per unit arc length  $F_d$ . The drag force per unit length was estimated from the assumption that all of the gas was flowing around the high temperature cylinder of the arc. The drag force per unit length of the cylinder was calculated as  $F_d = 0.5 C_d \rho v^2 d$ , where  $d$  is the arc diameter, and  $\rho$  and  $v$  are the density and flow velocity, respectively. The limits for the drag coefficient ( $C_d$ ) for a very wide range of Reynolds numbers (from  $10^2$  to  $10^5$ ) were  $1.3 < C_d < 1$ , and thus,<sup>2</sup>

$$\frac{1}{2} C_d \rho u^2 = IB. \quad (1)$$

The arc, which was approximately 2 mm in diameter, moved relative to the gas flow along a spiral trajectory. If  $v < d/\tau$  ( $\tau$  is the characteristic time of one arc rotation), then all the gas flow was discharged uniformly by the arc. For the MGA system, the diameter of the arc and the characteristic time of arc rotation corresponded to  $v < 4 - 10$  cm/s and  $Q < 35 - 88$  cm<sup>3</sup>/s for the range of powers used. In addition to the direct treatment by the rotating gliding arc, all of the gas flow passed through the ionized disk that the gliding arc left behind.

The plasma disk, which allowed a quasi-uniform activation of the flow, was thought of as a piecewise discharge in terms of space or time. For example, as shown in Fig. 4, in a temperature versus time or spatial coordinate plot, if there was a discharge providing a source of heat and/or radicals, the gas temperature would rise due to the combustion process, but then would decrease if the conditions were not satisfactory for sustaining the combustion process. If no more energy was added, the flame would extinguish, but if there was another discharge prior to extinction (within the quenching distance or time), the flame would survive. The continual rotation of the

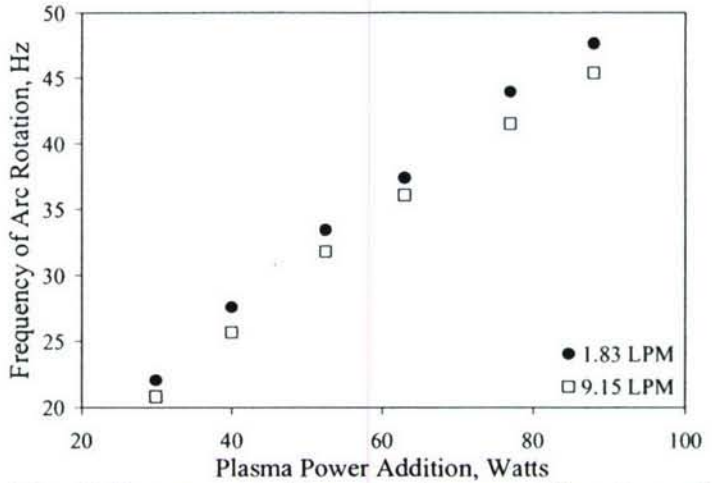


**Fig. 3** Frequency of arc rotation as a function of plasma power and flow rate

arc therefore would sustain the combustion process as long as the arc rotated at a sufficiently high rate compared to the flow rate.

To produce the near-extinction MGA plasma discharge, a power supply was designed specifically to supply the needs of the gliding arc system stabilized by the magnetic field efficiently. The power supply was designed to produce a magnetically stabilized arc with minimum current while maintaining smooth current regulation. The power supply utilized a reactive capacitive resistance that matched the resistive voltage and current characteristics by minimizing the active energy losses. To minimize the output electric capacity and to provide the voltage-current characteristic of the power supply (which was close to the resistive voltage-current characteristics), variation of the virtual resistance was accomplished by changing the frequency of the high voltage converter. After the output rectifier, there was unidirectional voltage and current with a very high frequency of the residual pulsation. The plasma arc behavior was then the same as that of the plasma arc at a constant current and voltage because of the limited response time of the gliding arc. A picture of the power supply is shown in Fig. 5, and a schematic of the electronics is shown in Appendix A.

### 2.3 Characterization and Modeling of MGA

In order to understand the plasma production of species for input to the combustion modeling, the specific characteristics, such as gas and electron temperatures of the MGA, were examined. The procedure to obtain the MGA characteristics is illustrated in Fig. 6. Initially, optical emission spectroscopy was performed to measure the rotational and vibrational temperatures of the MGA. The measured gas and electron temperatures were used to calculate the degree of non-equilibrium of the MGA ( $E/n$  ratio), as well as the gas density in the arc. Measurements were taken of the voltage and current characteristics of the MGA to calculate the strength of the electric field. The reduced

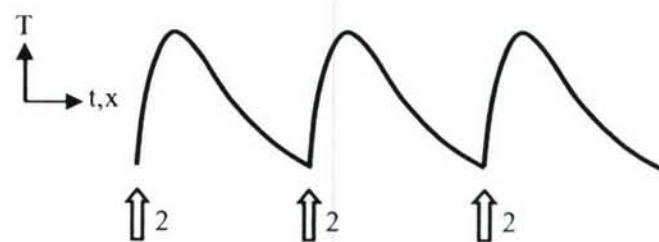


**Fig. 4** Illustration of the piecewise discharge concept. 1. quenching limit of flame, 2. location of plasma discharge

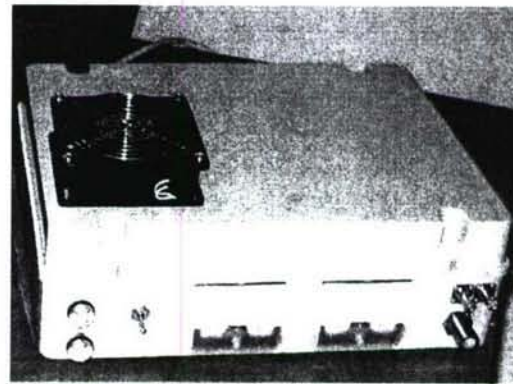


**Fig. 5** MGA power supply

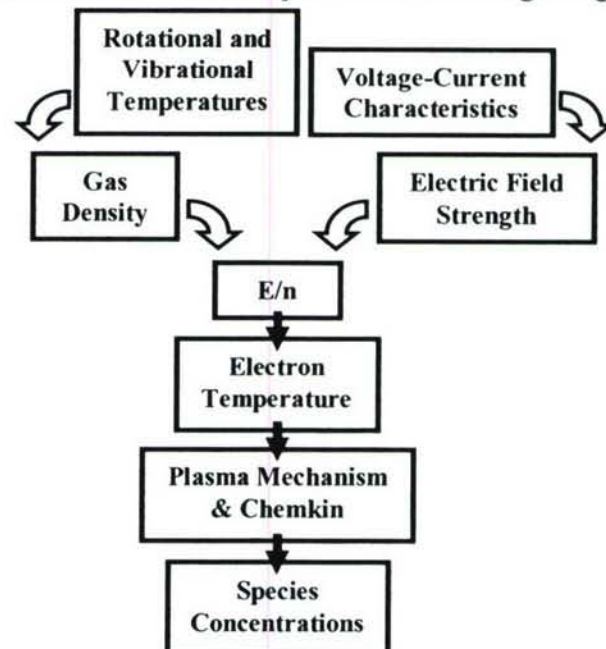


**Fig. 6** Modeling of MGA for production of species

electric field and electron temperature were used together with a dry air plasma mechanism to obtain the correlations between the species concentrations and the plasma power characteristics (current and voltage).

#### 2.4 Optical Emission Spectroscopy for Rotational and Vibrational Temperature Measurements

Since optical emission spectroscopy has been applied successfully to measure rotational and vibrational gas temperatures in the past, it was employed successfully to characterize the MGA plasma discharge. The transitions obtained from the excitation of OH, NO, N<sub>2</sub>, N<sub>2</sub><sup>+</sup> and O<sub>2</sub> can be used as molecular thermometers. Typically, OH spectra were used for low temperature air plasmas, as the OH emission intensity was very strong in non-equilibrium humid air plasmas, while NO spectra were used to analyze plasmas operating in dry air conditions.<sup>3</sup> For this reason, researchers have employed the OH spectra successfully to measure rotational temperatures in non-equilibrium plasmas.<sup>4,5</sup> Pellerin et al. made measurements of the OH spectra of conventional flat gliding arc discharges and obtained rotational temperature results of approximately 3000 K.<sup>4</sup> A similar technique was applied to the MGA to quantify the rotational and vibrational temperatures.

The spatially averaged OH spectrum of the MGA is shown in Fig. 7 and was obtained with the plasma operating at approximately 88 Watts at normal conditions of pressure and temperature in air. An Acton Research SpectraPro 500i scanning monochromator was used to record the OH spectra. The entrance slit to the monochromator was placed a few inches away from the discharge. Spatially averaged emission spectra of the discharge were taken in a wavelength range

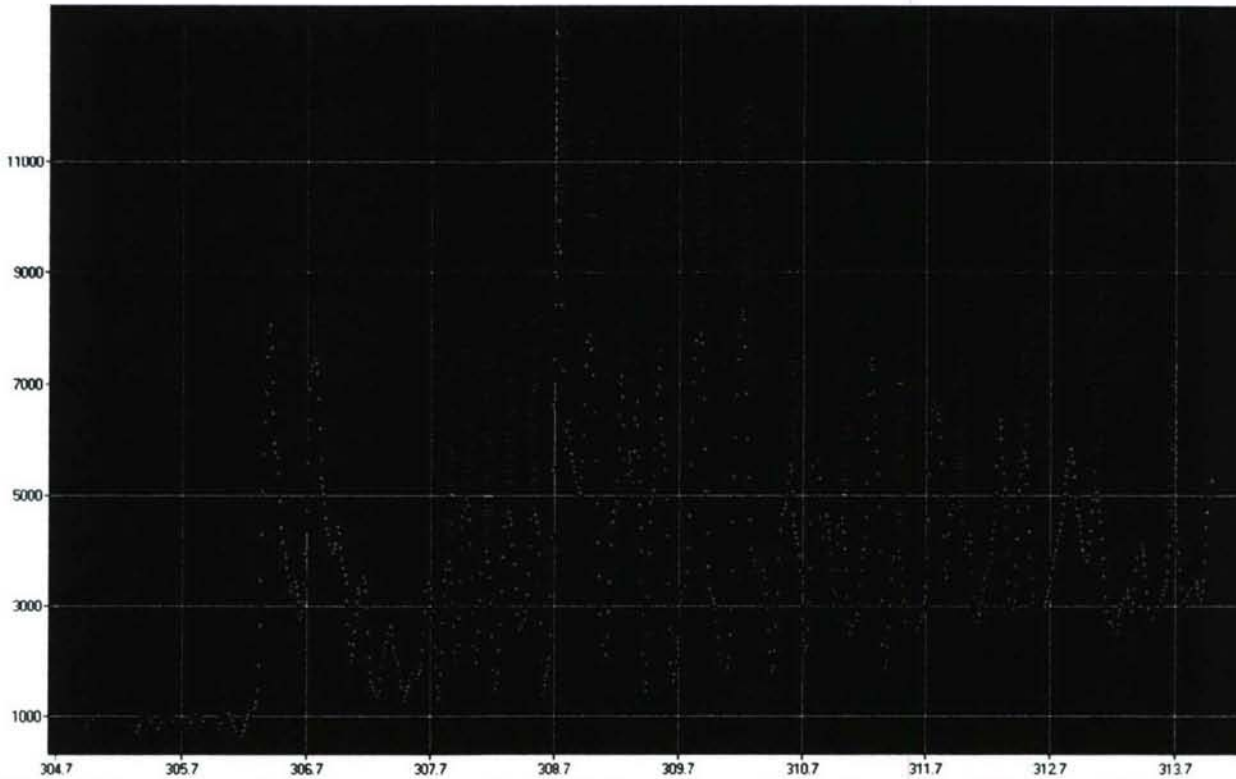


Fig. 7 Experimental OH spectrum obtained from the stabilized non-equilibrium gliding arc plasma discharge

of 200 nm to 450 nm. A Roper Scientific model 7430CCD camera was mounted onto the exit slit to acquire the spectra digitally at approximately 0.6 nm resolution with typical acquisition times for the CCD images between 1 second and 5 seconds.

A theoretical spectrum was generated to compare to the experimental OH spectrum of the gliding arc<sup>4,5</sup> as studied by Charles<sup>5</sup> and Dieke and Crosswhite,<sup>6</sup> wherein weak transitions were eliminated. A set of impulses were generated, as shown in Fig. 8, using the relation

$$I = I_{ref} \cdot \frac{Z(T_{ref})}{Z(T)} \cdot e^{\frac{-E_n \cdot (T_{ref} - T)}{(T_{ref} \cdot T)}} \quad (2)$$

where,  $I_{ref}$ ,  $E_n$  and  $T_{ref}$  were the reference intensity, energy of state of excitation and reference temperature, respectively, and were obtained from the fundamental data as obtained from Dieke and Crosswhite.<sup>6</sup> The ratio of partition function,  $Z(T_{ref})/Z(T)$ , was assumed to be unity. By using different values of temperature  $T$ , the corresponding intensities (normalized) were computed. The impulse responses of the optical device obtained by employing sharp lines emitted by a low pressure mercury lamp were convoluted with an apparatus function.

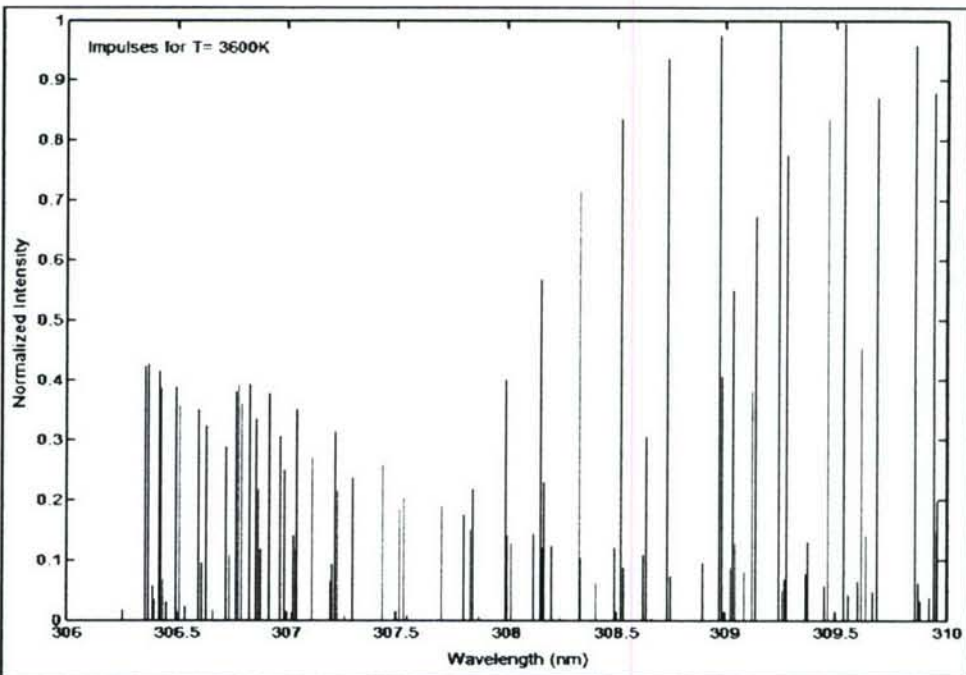


**Fig. 8** Theoretically computed rotational lines of OH shown as impulses for  $T = 3600$  K

Theoretical spectra were generated for different temperatures in the range from 1000 K to 6000 K in 500 K increments. Figure 9 shows the comparison between theoretically generated plots and the experimental results obtained for a MGA current,  $I = 35$  mA. The peaks  $G_0$ ,  $G_1$  and  $G_{ref}$  were considered the most important lines of the OH spectrum in the temperature range of 1000 K to 4000 K. The reference peak,  $G_{ref}$ , was the most stable peak for the range of temperatures and hence provided a basis for comparison. The peaks of  $G_0$  and  $G_1$  were highly sensitive to temperature variation in the same temperature range. For temperatures above 4000 K, their sensitivity was relatively low.<sup>5</sup> Hence, the ratios of  $G_0/G_{ref}$  and  $G_1/G_{ref}$  were considered for diagnostic analysis.

The ratios of  $G_0/G_{\text{ref}}$  and  $G_1/G_{\text{ref}}$  from theoretical spectra were used to compare with those obtained in the experimental results. Figure 10 shows the variation of ratios in the given temperature range.

From the results obtained in Figs. 9 and 10, we found that the MGA rotational temperature was between 2200 K and 2500 K (Fig. 11), which was reasonable in comparison with results reported in literature between 2000 K and 3000 K.<sup>5-8</sup>

A spectrum analyzer<sup>9</sup> was employed to calculate the OH rotational temperature to ensure that there was good agreement with the experimental results. The results obtained conformed reasonably well to those obtained by generation of OH synthetic spectra, with a mean plasma rotational temperature of 2360 K.

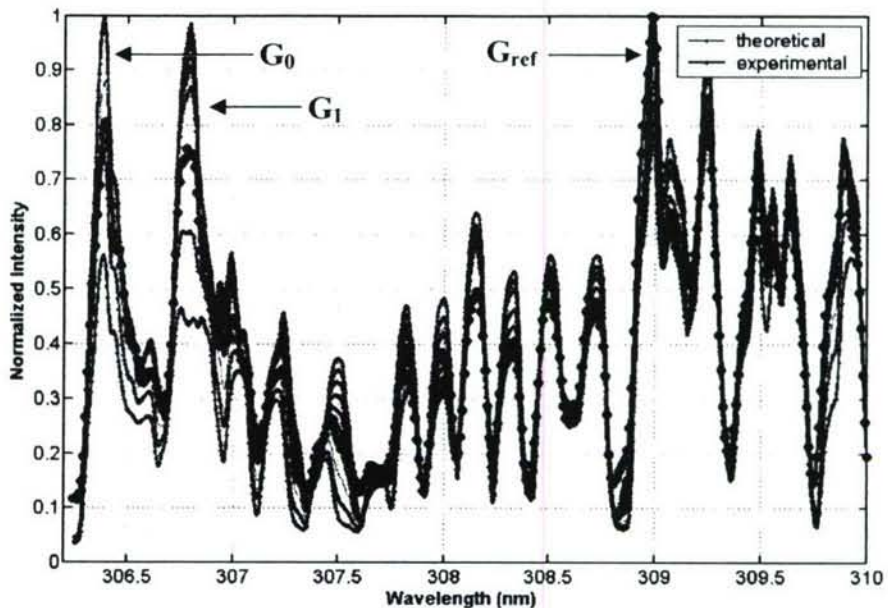


**Fig. 9** Comparison of theoretically generated and experimental spectroscopy curves for OH in the MGA.

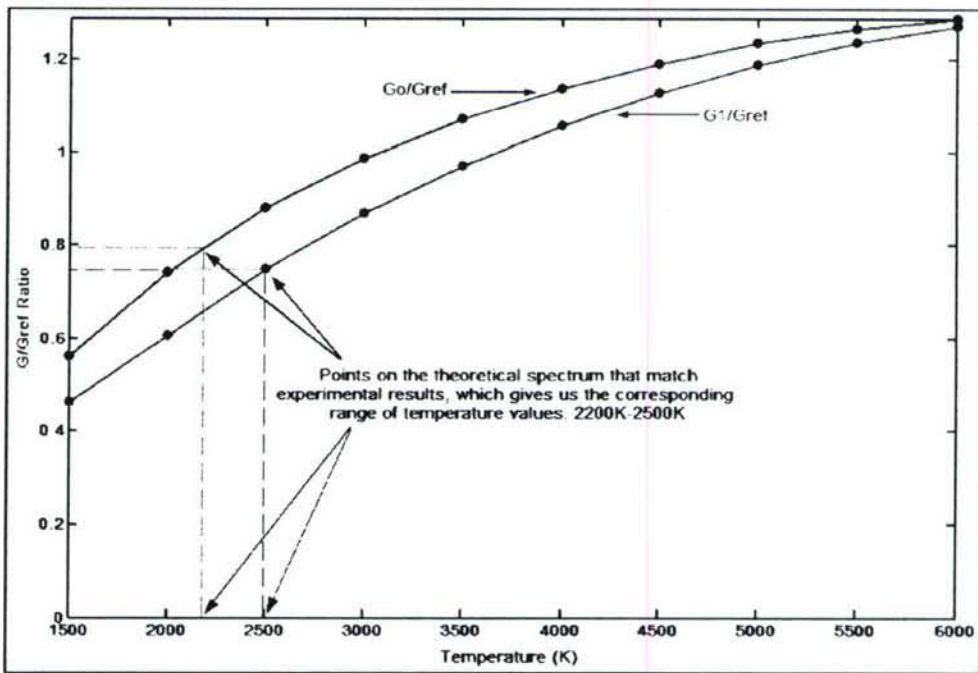


**Fig. 10**  $G_0/G_{\text{ref}}$  and  $G_1/G_{\text{ref}}$  ratios plotted against a range of rotational temperatures that were observed. Accordingly, the ratios were matched up with those from the experimental spectrum, which gave us the range of 2200 K to 2500 K.

Unfortunately, the OH spectrum measurements typically suffered inaccuracy due to factors such as more self-absorption by the  $G_{ref}$  peak in comparison with the  $G_0$  and  $G_1$  peaks and preferential quenching of rotational levels of OH. Moreover, with the increase of the plasma optical thickness, the  $G_0/G_{ref}$  and  $G_1/G_{ref}$  ratios increased, leading to an overestimated temperature (Fig. 11). Hence, the result obtained by the OH spectrum was higher than the actual temperature of the plasma. In order to overcome the

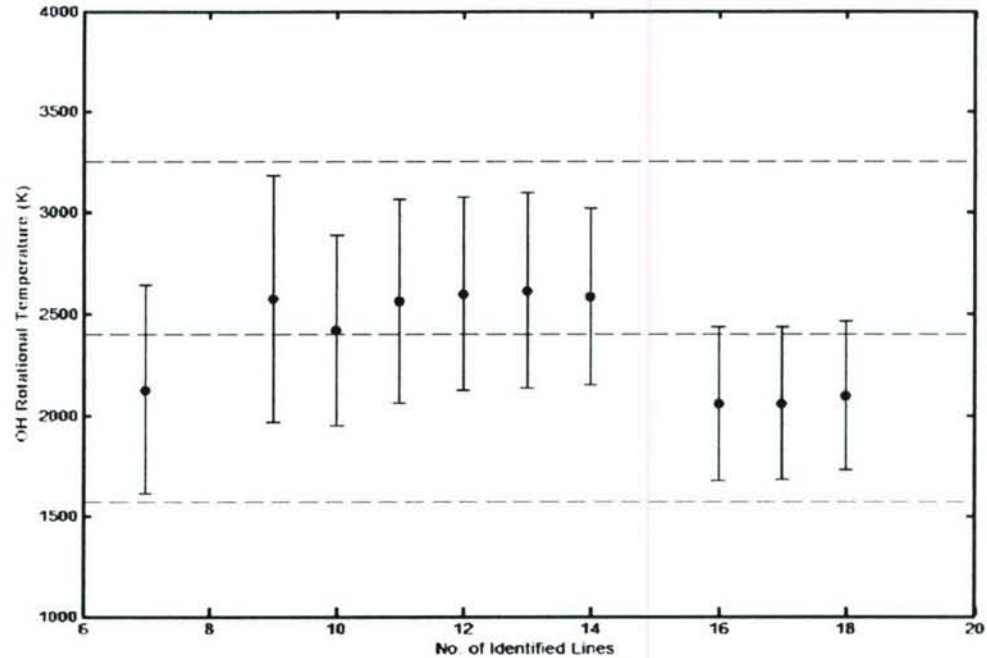


**Fig. 11** Plasma rotational temperature based on OH spectral data, showing the rotational temperature value varying with number of identified lines

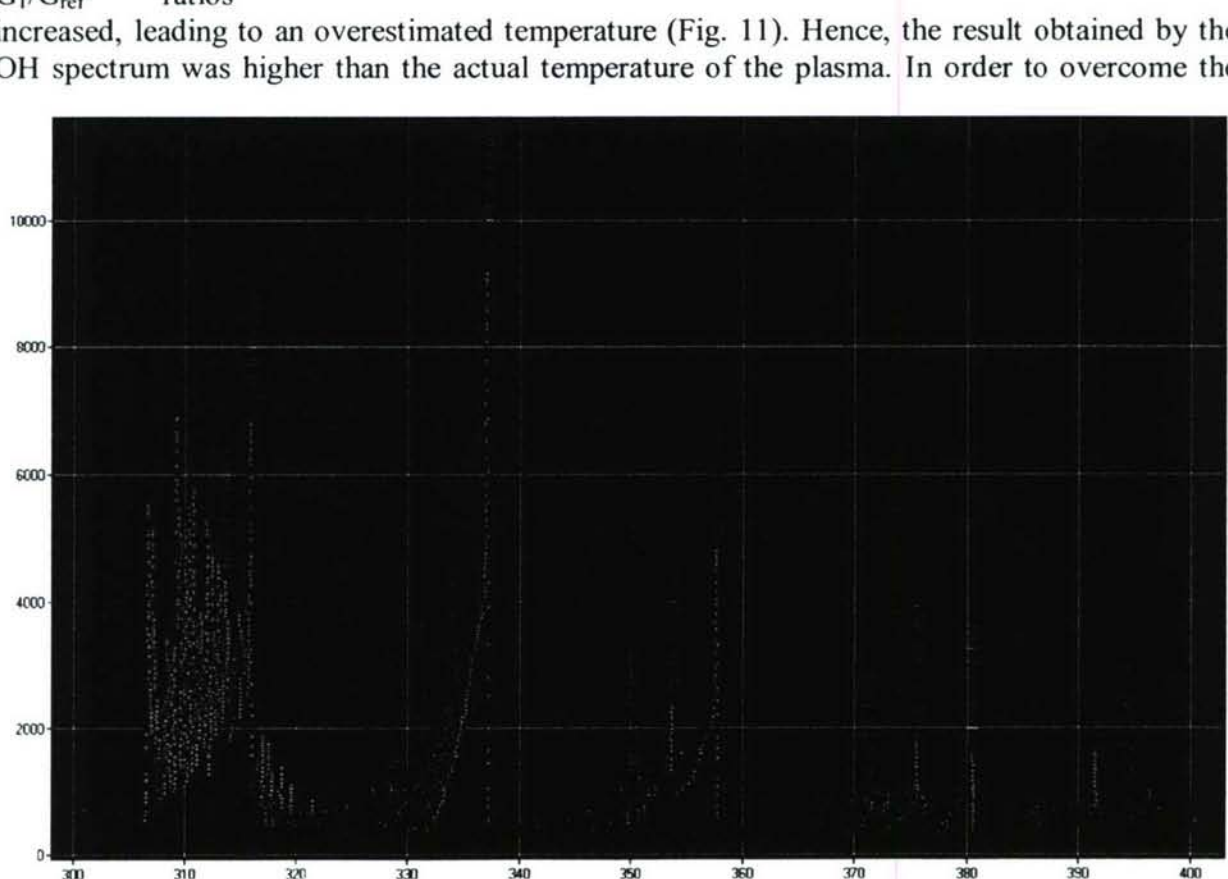


**Fig. 12** Experimental  $N_2$  spectrum obtained from stabilized non-equilibrium MGA plasma discharge

underestimate, spectroscopic diagnostic measurements using N<sub>2</sub> spectra was employed.

The N<sub>2</sub> spectrum for the wavelength range between 370 nm and 390 nm was considered because of the possibility to explore both rotational and vibrational temperatures. Spectra were obtained at various currents of operation with an example shown in Fig. 12, and analyzed using the Specair code.<sup>10</sup> The code generated a theoretical spectrum for a given combination of rotational and vibrational temperatures as input parameters. The combination was varied over a given range of temperatures until a least square fit was obtained between the experimental and theoretical spectra. The dependence rotational temperature on the electric current is shown in Fig. 13. The corresponding vibrational temperature was estimated to be 3400 K ± 200 K. The temperature measurements were also in agreement with past work on gliding arcs.<sup>11</sup>

The N<sub>2</sub> vibrational temperatures were computed using a spectrum analyzer and the results, are shown in Fig. 14. To understand how the MGA properties changed as a function of plasma current and flow rate, the rotational and vibrational temperatures were obtained and plotted in Fig. 15.

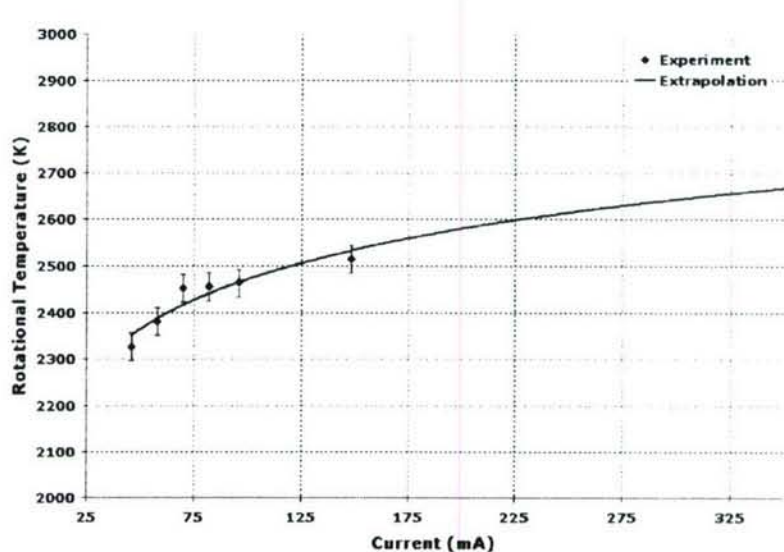


**Fig. 13** Experimental data and logarithmic fit of rotational temperature variation with current. The green line displays the extrapolated results based on this fit

The dependence rotational temperature on the electric current is shown in Fig. 13. The corresponding vibrational temperature was estimated to be 3400 K ± 200 K. The temperature measurements were also in agreement with past work on gliding arcs.<sup>11</sup>

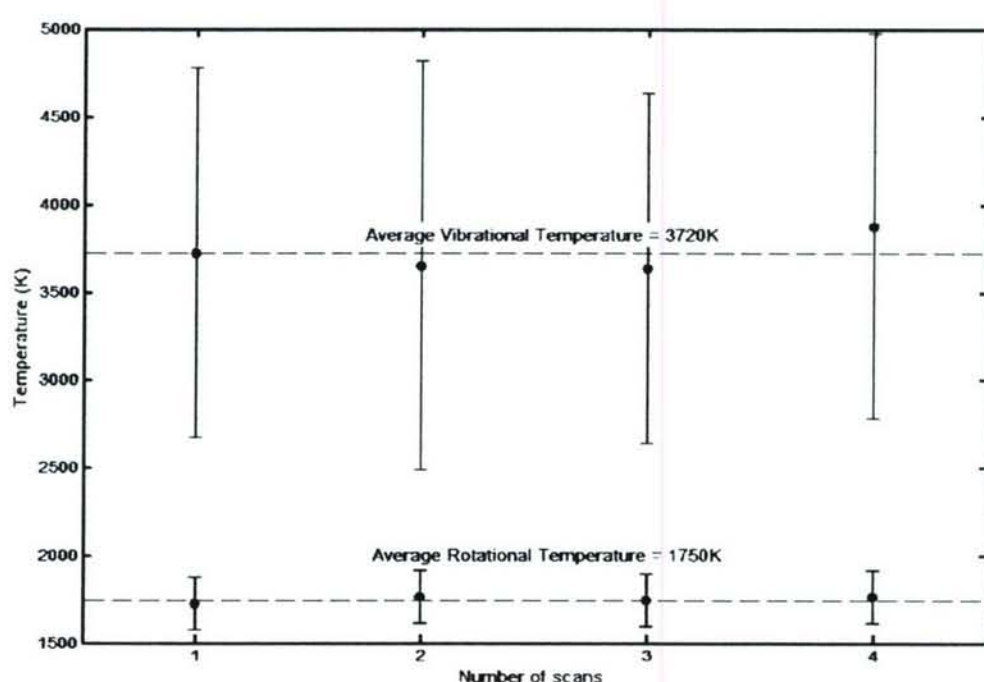


**Fig. 14** Plasma N<sub>2</sub> molecular temperature results obtained by comparison with synthetic spectra (rotational) and a spectrum analyzer (vibrational)

The purpose of the spectroscopic measurements and calculations was to quantitatively measure the rotational and vibrational temperatures by using OH and N<sub>2</sub> spectra, so that the degree of thermodynamic non-equilibrium between the rotation and vibration modes could be verified. The difference between the rotational and vibrational temperatures indicated that the near-extinction MGA is a non-equilibrium plasma.

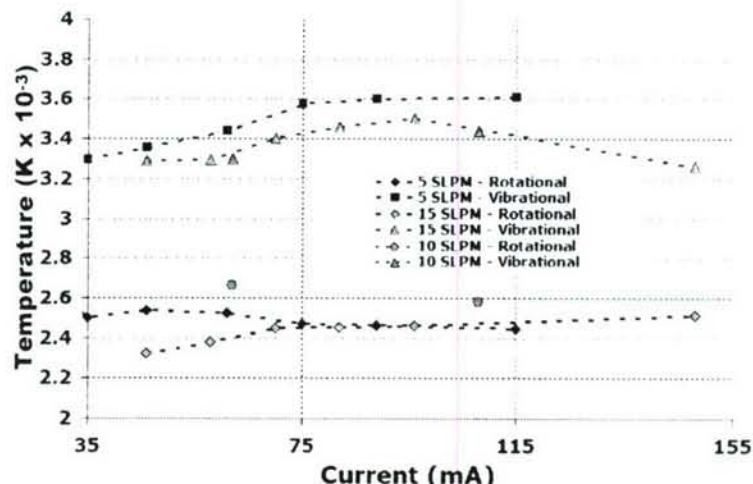


**Fig. 15** N<sub>2</sub> rotational and vibrational temperatures versus current for different air flow rates.

## 2.5 Electron Temperature Measurements of MGA

The electron energy/temperature varied proportionally with the reduced electric field strength (E/n). In order to measure the electron temperature of the MGA, it was assumed that the electric field was uniform throughout the plasma discharge. By solving the Boltzmann equation at a given reduced electric field using BOLSIG, the electron energy distribution could be obtained.<sup>12</sup> For an arc voltage of 2.5 kV and an arc length of 1.5 cm, the electron energy obtained by the above simulation is shown in Fig. 16 and was between 1.28 eV and 1.45 eV. These values were consistent with the data in the literature.<sup>7,8,11</sup>

Typically since thermal plasma has an electron temperature comparable to the gas temperature, the MGA plasma discharge was clearly a non-equilibrium plasma with high power density. The rotational temperature (approximately 1750 K to 2500 K

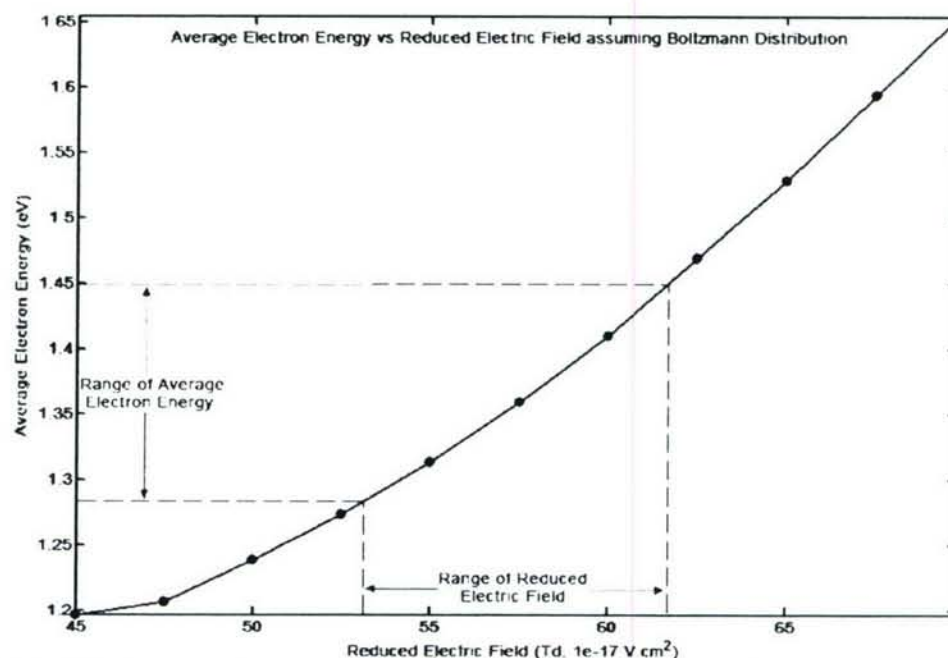


**Fig. 16** Average electron energy versus reduced electric field assuming a Boltzmann distribution

spectroscopy of OH and N<sub>2</sub>) was ten times lower than the electron temperature (approximately 14,700 K to 16,700 K). The difference between the rotational temperature and electron temperature reconfirmed that the MGA was a non-equilibrium plasma.

## 2.6 Measurement of Voltage-Current (V-I) Characteristics of MGA

The voltage-current (V-I) characteristic curves for the operation of the MGA were critical for the development of the plasma model to estimate species production. To obtain the V-I curves, experiments were performed by flowing air through the MGA in a direction normal to the plane of the gliding arc rotation. The correlation between plasma discharge voltage and current was recorded.

Figure 17 shows the V-I characteristic curves for the MGA obtained for 5 SLPM and 13 SLPM (in the range of what was used in the MGA counterflow ignition system). The solid lines represent the fitted experimental data and the dashed lines are the curve extrapolations. An increase in flow rate caused an increase in the discharge voltage. The increase in discharge voltage was attributed to arc elongation from the flow and the reduction of arc conductivity. The MGA, however, was not stabilized at all currents and flow rates of operation. The data on the left hand-side of Fig. 17 (less than 50 mA) represented the extent of stability of the discharge, meaning that the arc began to re-initiate and extinguish beyond these points for a given flow rate cyclically. There was a possibility to achieve lower currents at lower flow rates, maintaining stabilized operation. The instability was associated with rapid cooling and/or out-of-plane curving or lengthening (illustrated in Fig. 18) of the discharge by the increased flow.

Fig.17 also shows that an increase of flow rate led to an increase of plasma voltage due to the transverse elongation of the arc. If the curves were fit using a power variation such

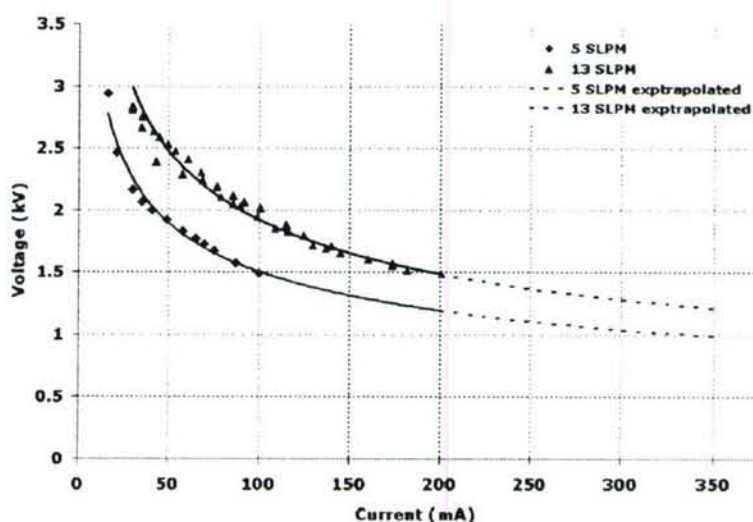


Fig. 17 V-I curves of the MGA at 5 SLPM and 13 SLPM of operation. The dashed lines represent the extrapolated trends

of the MGA, however, was not stabilized at all currents and flow rates of operation. The data on the left hand-side of Fig. 17 (less than 50 mA) represented the extent of stability of the discharge, meaning that the arc began to re-initiate and extinguish beyond these points for a given flow rate cyclically. There was a possibility to achieve lower currents at lower flow rates, maintaining stabilized operation. The instability was associated with rapid cooling and/or out-of-plane curving or lengthening (illustrated in Fig. 18) of the discharge by the increased flow.

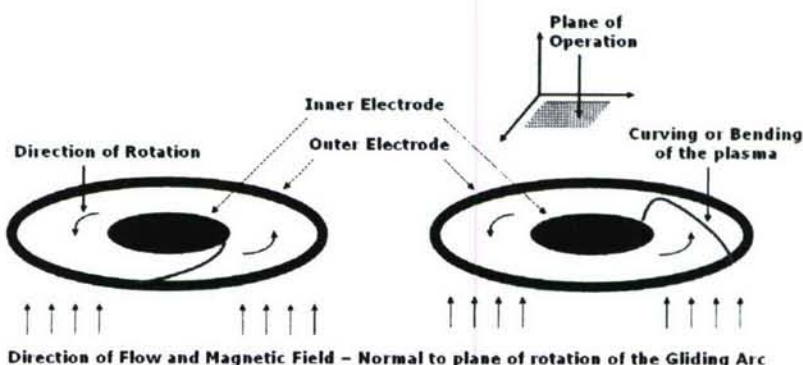


Fig. 18 An illustration of the operation of the MGA with plane of operation in which the MGA was stabilized. An increase in flow rate caused the arc to curve or bend outside the plane of operation

that  $V = a \cdot j^b$ , the values of  $a$  and  $b$  increased with the increase of flow rate. The increasing voltage with flow rate was confirmed further by studying the effect of increasing the air flow rate through the plasma for a given discharge current, as shown in Fig. 19.

Key observations in Fig. 19 were that an increased flow rate through the MGA caused an increase in the discharge voltage and that the slope of the increase in voltage with flow rate was greater at lower currents. In addition, the instability of the arc occurred at low flow rates and/or low current values. These plasma properties will be used to determine the species produced by plasma discharge.

## 2.7 Measurements of Current Densities for MGA

To measure the current densities of the MGA, snapshots were taken of the arc at 44 mA, 140 mA and 220 mA (Fig. 20). The MGA displayed a glow discharge-like behavior with larger coverage of the cathode area and increased current.

The arc was split into two zones for analysis purposes, namely, the cathode spot (CS) (negative glow or NG) and positive column (PC). In traditional non-equilibrium low pressure glow-discharges the typical value of the current density as a function of pressure was approximately  $300\mu\text{A}/\text{cm}^2/\text{Torr}^2$ . Taking values from our discharge parameters in the range of 2300 K to 2500 K yielded approximately  $2.5 \text{ A/cm}^2$  to  $3 \text{ A/cm}^2$  for the current density. The experimentally estimated current densities in the CS, shown in Fig. 21, agreed well with those from the literature. A diametrical correction was applied in order to compensate for the motion of the arc relative to the camera capture speed. Figure 22

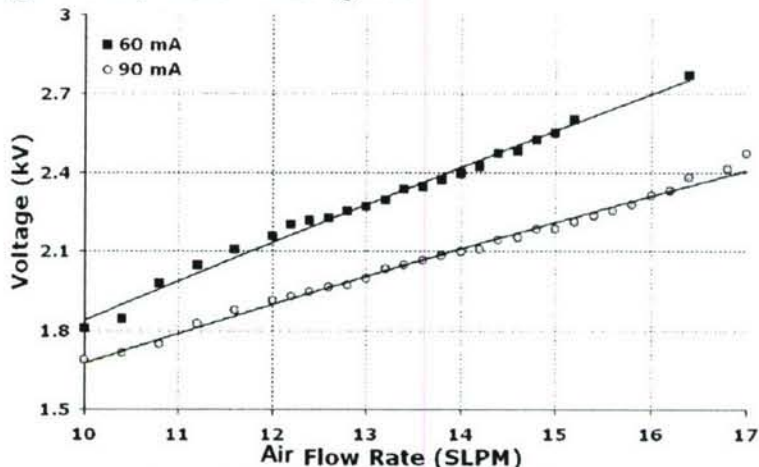


Fig. 19 Voltage on MGA versus air flow rate

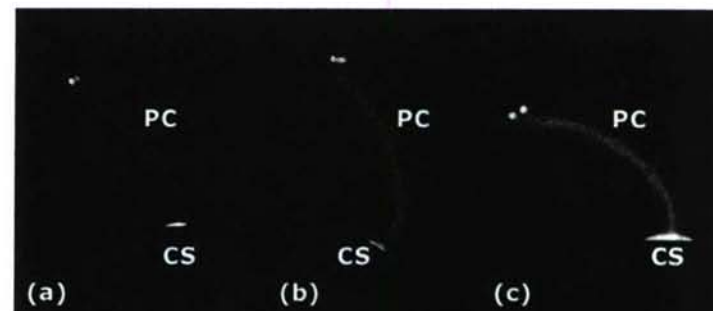


Fig. 20 Snapshots of the Non-Equilibrium MGA for (a) 44 mA, (b) 140 mA and (c) 220 mA.

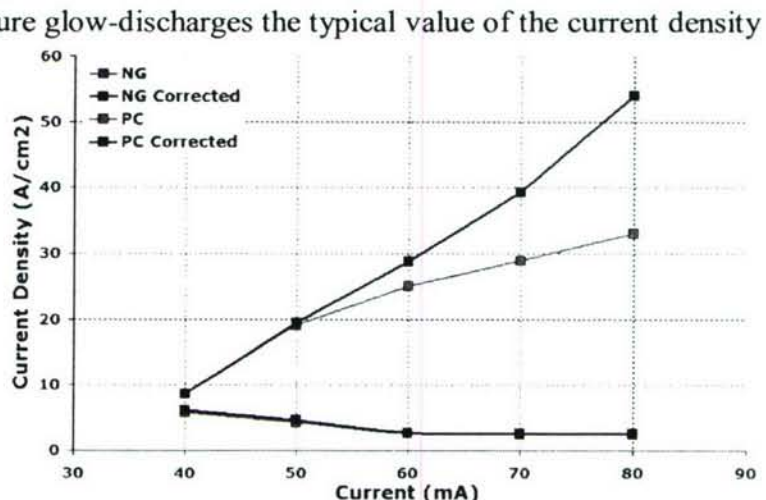


Fig. 21 Current densities versus MGA current for CS and PC

shows the correction for  $d_{corrected} = d_{measured} - \pi D f t$ , where  $D$  is the specific diameter of the reactor,  $f$  the frequency of arc rotation, and  $t$  the time of exposure. The typical drop in voltage in the CS for iron-electrodes is 260 V.<sup>13</sup> The corresponding plasma parameters in the two zones were estimated as:

1. CS:  $E = 8125$  V/cm for  $T_G = 2500$  K, yielding an  $E/n = 276$  Td. The average electron energy was 5 eV.
2. PC: For 35 mA,  $E = 1130$  V/cm for  $T_G = 2500$  K, yielding an  $E/n = 36.5$  Td. Hence, the average electron energy was 1.2 eV. Also, the reduced electric field value (in terms of pressure instead of number density,  $E/p$ ) was 12.4 V/cm/Torr and was higher than was reported in non-thermal zones of the gliding arc of 2.4V/cm/Torr.<sup>8</sup>

The calculation of electron density was based on the current density in the PC using the relation of  $n_e \sim k/(eV_d)$ , where,  $k$  was the current density ( $A/cm^2$ ),  $e$  the electron charge (Coulombs), and  $V_d$  the electron drift velocity ( $cm/s$ ). For the current range of 40 mA to 80 mA, the calculated drift velocities varied from approximately  $7.7 \times 10^7$  cm/s to  $5.1 \times 10^7$  cm/s. These velocities, along with the current density and electron charge, yielded an electron density estimate in the PC of approximately  $5 \times 10^{11}$   $cm^{-3}$  to  $4 \times 10^{12}$   $cm^{-3}$ . Figure 23

shows the estimated average electron density for the PC for the given range of operational currents of the MGA. These results were in agreement with earlier gliding arc diagnostic measurements.<sup>7</sup>

## 2.8 Plasma Kinetic Modeling

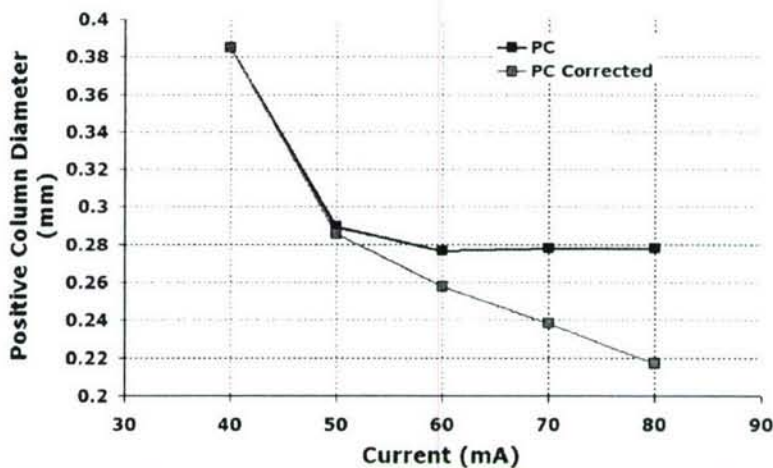


Fig. 22 Diametric correction of PC for various MGA currents

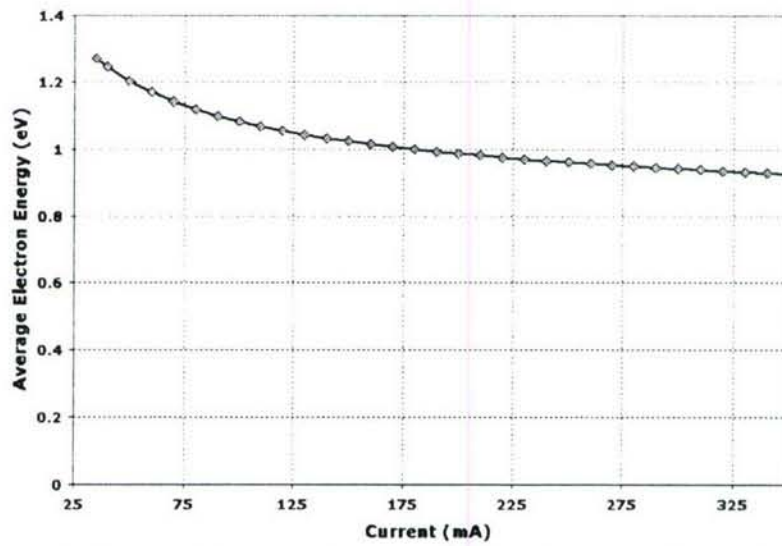


Fig. 23 Dependence of the average electron energies on the plasma current in the PC of the MGA

### 2.8.1 Dry Air Plasma Mechanism

Plasmas are complex systems in which a number of species interact simultaneously via various production and recombination pathways that consume or release energy in the process. From the point of view of gas-phase chemical kinetics, the key parameter that governs the evolution of species is usually temperature. The Arrhenius expression is used to describe the exponential dependence of rate constants on temperature. To obtain species concentrations of a given system, input variables such as temperature, time, and kinetic chemistry need to be given in the computation.

In the case of non-equilibrium plasma systems such as the MGA, the situation is more complicated due to the characteristic deviation of the electron temperature from the surrounding gas temperature, thereby making them two-temperature systems. Therefore, the rates of electron impact processes and neutral species interactions must be considered as functions of electron temperature and gas (rotational) temperature, respectively. Hence, it is necessary to obtain and fix the electron and gas temperatures in order to obtain concentrations of species corresponding to given experimental conditions.

For air, we used a dry air plasma mechanism to predict the species and their concentrations produced via the MGA. The reaction mechanism, given below, was taken from Becker et al.<sup>14</sup> and was valid for temperatures greater than 1500 K. The mechanism consisted of O<sub>2</sub>, N<sub>2</sub>, and NO dissociation and recombination reactions, the high-temperature Zeldovich NO<sub>x</sub> mechanism, and charge exchange/transfer reactions. Chemkin 4.0 was chosen as the computational package due to its robustness and ability to incorporate two-temperature kinetics (i.e. appropriate usage of gas temperature and electron temperature,  $T_e$ , as input parameters in the calculation of reaction rate constants).

Reaction	A (cm-mole-sec)	b	E <sub>a</sub> (K)
<b>O<sub>2</sub> Dissociation / Recombination</b>			
O <sub>2</sub> +O <sub>2</sub> ⇌ O+O+O <sub>2</sub>	2e21	-1.5	59500
O <sub>2</sub> +NO ⇌ O+O+NO	2e21	-1.5	59500
O <sub>2</sub> +N <sub>2</sub> ⇌ O+O+N <sub>2</sub>	2e21	-1.5	59500
O <sub>2</sub> +O ⇌ O+O+O	1e22	-1.5	59500
O <sub>2</sub> +N ⇌ O+O+N	1e22	-1.5	59500
O <sub>2</sub> +E → O+O+E	2.85e17	-0.6	59500
TDEP /E/			
O+O+E → O <sub>2</sub> +E	4.03e18	-0.4	0
TDEP /E/			
<b>NO Dissociation / Recombination</b>			
NO+O <sub>2</sub> ⇌ N+O+O <sub>2</sub>	5e15	0.0	75500
NO+NO ⇌ N+O+NO	1.1e17	0.0	75500
NO+N <sub>2</sub> ⇌ N+O+N <sub>2</sub>	5e15	0.0	75500
NO+O ⇌ N+O+O	1.1e17	0.0	75500
NO+N ⇌ N+N+O	1.1e17	0.0	75500

$\text{NO+E} \rightarrow \text{N+O+E}$	3.54e16	-0.2	75500
TDEP /E/			
$\text{N+O+E} \rightarrow \text{NO+E}$	8.42e21	-1.1	0
TDEP /E/			

#### N<sub>2</sub> Dissociation / Recombination

$\text{N}_2+\text{O}_2 \leftrightarrow \text{N+N+O}_2$	7e21	-1.6	113200
$\text{N}_2+\text{NO} \leftrightarrow \text{N+N+NO}$	7e21	-1.6	113200
$\text{N}_2+\text{N}_2 \leftrightarrow \text{N+N+N}_2$	7e21	-1.6	113200
$\text{N}_2+\text{O} \leftrightarrow \text{N+N+O}$	3e22	-1.6	113200
$\text{N}_2+\text{N} \leftrightarrow \text{N+N+N}$	3e22	-1.6	113200
$\text{N}_2+\text{E} \rightarrow \text{N+N+E}$	1.18e18	-0.7	113200
TDEP /E/			
$\text{N+N+E} \rightarrow \text{N}_2+\text{E}$	1.36e23	-1.3	0
TDEP /E/			

#### Zeldovich Reactions

$\text{N}_2+\text{O} \leftrightarrow \text{NO+N}$	6.4e17	-1.0	38400
$\text{NO+O} \leftrightarrow \text{O}_2+\text{N}$	8.4e12	0.0	19400

#### Associative Ionization / Dissociation

$\text{N+O} \rightarrow \text{NO}^++\text{E}$	8.8e8	1.0	31900
$\text{NO}^++\text{E} \rightarrow \text{N+O}$	9e18	-0.7	0
TDEP /E/			
$\text{N+N} \rightarrow \text{N}_2^++\text{E}$	6e7	1.5	67500
$\text{N}_2^++\text{E} \rightarrow \text{N+N}$	1.53e18	-0.5	0
TDEP /E/			
$\text{O+O} \rightarrow \text{O}_2^++\text{E}$	7.1e2	2.7	80600
$\text{O}_2^++\text{E} \rightarrow \text{O+O}$	1.5e18	-0.5	0
TDEP /E/			

#### Electron Impact Ionization / Three-Body Recombination

$\text{O+E} \rightarrow \text{O}^++\text{E+E}$	7.74e12	0.7	157760
TDEP /E/			
$\text{O}^++\text{E+E} \rightarrow \text{O+E}$	2.19e21	-0.8	0
TDEP /E/			
$\text{N+E} \rightarrow \text{N}^++\text{E+E}$	5.06e19	0.0	168200
TDEP /E/			
$\text{N}^++\text{E+E} \rightarrow \text{N+E}$	5.75e26	-1.3	0
TDEP /E/			
$\text{O}_2+\text{E} \rightarrow \text{O}_2^++\text{E+E}$	5.03e12	0.5	146160
TDEP /E/			
$\text{O}_2^++\text{E+E} \rightarrow \text{O}_2+\text{E}$	8.49e23	-1.9	0
TDEP /E/			
$\text{N}_2+\text{E} \rightarrow \text{N}_2^++\text{E+E}$	2.7e17	-0.3	181000
TDEP /E/			

$N_2^+ + E \rightarrow N_2 + E$	2.05e21	-0.8	0
TDEP /E/			
$NO + E \rightarrow NO^+ + E + E$	2.2e16	-0.3	107400
TDEP /E/			
$NO^+ + E + E \rightarrow NO + E$	2.06e25	-2.0	0
TDEP /E/			

### Charge Exchange / Charge Transfer

$N^+ + N_2 \rightarrow N_2^+ + N$	4.6e11	0.5	12200
$N + N_2^+ \rightarrow N_2 + N^+$	1.93e13	0.0	0
$NO^+ + O \leftrightarrow N^+ + O_2$	1e12	0.5	77200
$NO + O^+ \leftrightarrow N^+ + O_2$	1.4e5	1.9	15300
$O^+ + N_2 \leftrightarrow NO^+ + N$	4.4e13	0.0	5664
$O^+ + N_2 \leftrightarrow N_2^+ + O$	9e11	0.4	22800
$NO^+ + N \leftrightarrow N_2^+ + O$	7.2e13	0.0	35500
$O_2^+ + N \leftrightarrow N^+ + O_2$	8.7e13	0.1	28600
$O_2^+ + N_2 \leftrightarrow N_2^+ + O_2$	9.9e12	0.0	40700
$NO^+ + O_2 \leftrightarrow O_2^+ + NO$	2.4e13	0.4	32600
$NO^+ + O \leftrightarrow O_2^+ + N$	7.2e12	0.3	48600
$O^+ + O_2 \leftrightarrow O_2^+ + O$	3.26e13	0.0	2064
$O^+ + NO \leftrightarrow NO^+ + O$	2.42e13	0.0	902

All reaction rate constants were described by the Arrhenius expression. The abbreviation TDEP /E/ from the reaction mechanism given above indicated that the reaction rate constant was dependent on the average electron temperature and all other reactions were dependent on gas temperature.

The production and interaction of electronically excited species were not included in the model, but they were used to predict the evolution of active radicals, namely O and NO, in the MGA plasma discharge. The effects of radical-induced ignition were sought to provide an explanation for the ignition enhancement observed by the experimentally measured ignition temperatures shown and discussed in Section 3.

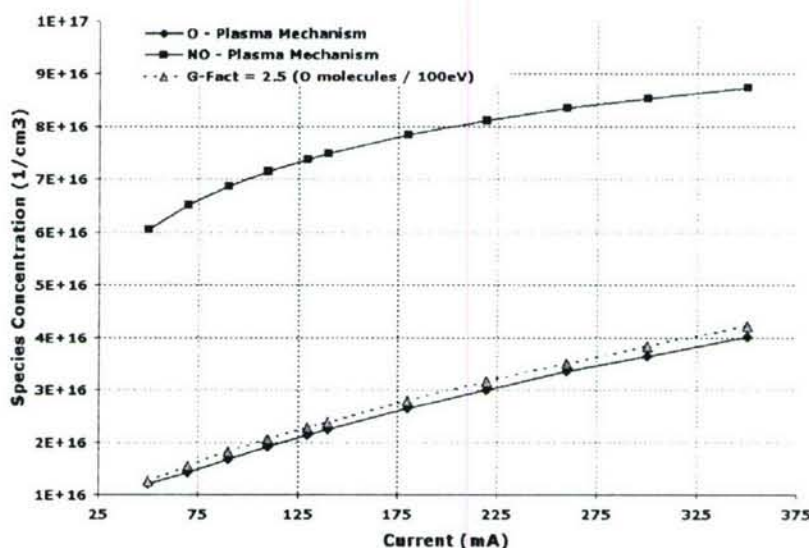


**Fig. 24** Steady state concentration of O and NO radicals as a function of plasma current. Using a G-factor of 2.5, the predicted results were in good agreement with the air plasma mechanism results

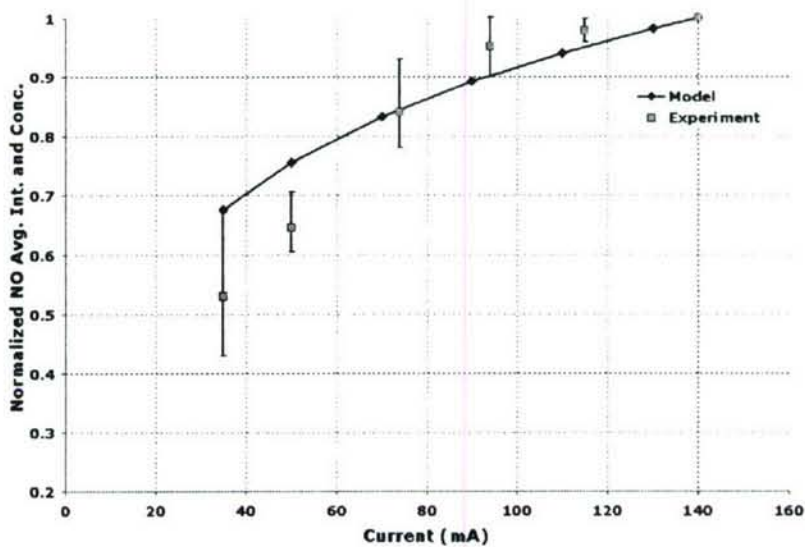
### 2.8.2 MGA Production of O and NO

Figure 24 shows the steady state concentrations of O and NO radicals as functions of current. The results obtained from the kinetic mechanism were compared to average intensities of experimentally obtained NO spectra from five lines at various locations for the wavelength range of 200 nm to 300 nm. It was assumed that relative intensities were indicative of relative concentrations of NO at various currents of operation. The intensity value at 140 mA was used as the normalization maximum (unity) for comparison purposes. The error bars in the figure represented the deviation of the minimum and maximum values of relative intensities from the average. The increasing trend of NO concentration with current is shown in Fig. 25.

### 2.8.3 Dependence on G-factor and Specific Power Input (SPI)

The G-factor was another important parameter that indicated the production of a species in the system. It usually was defined as the number of molecules of a species produced for 100

eV of energy input. The SPI was the ratio of the input power,  $PW$ , to the flow rate,  $Q$ , (SLPM). The SPI was also indicative of the input energy ( $\text{eV} \cdot \text{molecule}^{-1}$ ) to the system. By the comparison shown in Fig. 24, it was deduced that a G-factor of 2.5 gave a good estimate of the amount of O radical produced by the MGA. A logarithmic fit described the prediction of NO species concentration,  $2 \cdot 10^{16} \cdot \ln(\text{SPI}) + 10^{16}$ , where the SPI was expressed in Watt·min/liter. The logarithmic fit allowed for the possibility to explore the production of species over the experimental range of flow rates and electric current conditions. Figures 26 and 27 show the



**Fig. 25** Comparison of experimental and modeling results of concentrations of NO produced by the MGA

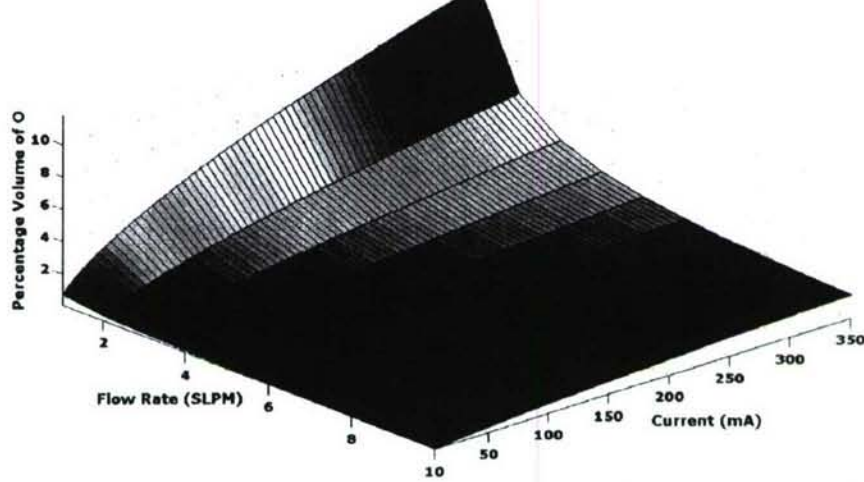


**Fig. 26** Predicted steady-state percentage by volume concentration of O radical as a function of plasma current and flow rate

estimated steady state concentrations of O and NO for currents up to 350 mA and flow rates up to 10 SLPM based on the G-factor for O radicals and a logarithmic fit for NO production.

## 2.9 Recombination of Plasma Produced Species in Convection and Diffusion Zone

The MGA was a good source for the production of O and NO radicals, but in order to characterize the system, the recombination losses in the convection-diffusion zone between plasma discharge and reaction zone needed to be calculated. Due to the rapid recombination of the O radicals at low temperatures, their lifetimes in the convection-diffusion zone was short. The typical residence times of the plasma-discharge flow in the convection-diffusion zone (e.g. flow rates of 3 SLPM to 10 SLPM) were between 37 msec and 100 msec in the experimental system. Hence, there was considerable post-plasma recombination of O. Using the rate of production analysis, the reaction  $O + O + M \rightarrow O_2 + M$ , where M was the participating third body (e.g. N<sub>2</sub> and O<sub>2</sub>), is dominant. In comparison, the NO concentration did not change appreciably, with only a negligible increase owing to the reaction  $O + N + M \rightarrow NO + M$ .

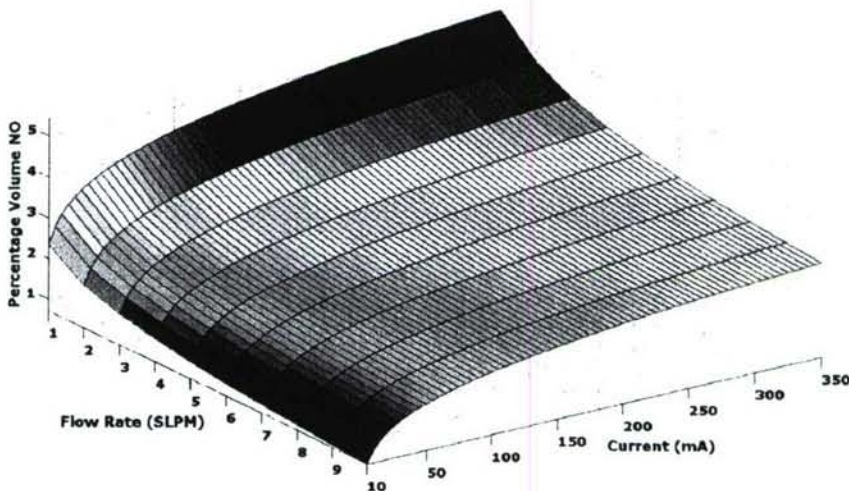


**Fig. 27** Predicted steady-state percentage by volume concentration of NO radical as a function of plasma current and flow rate

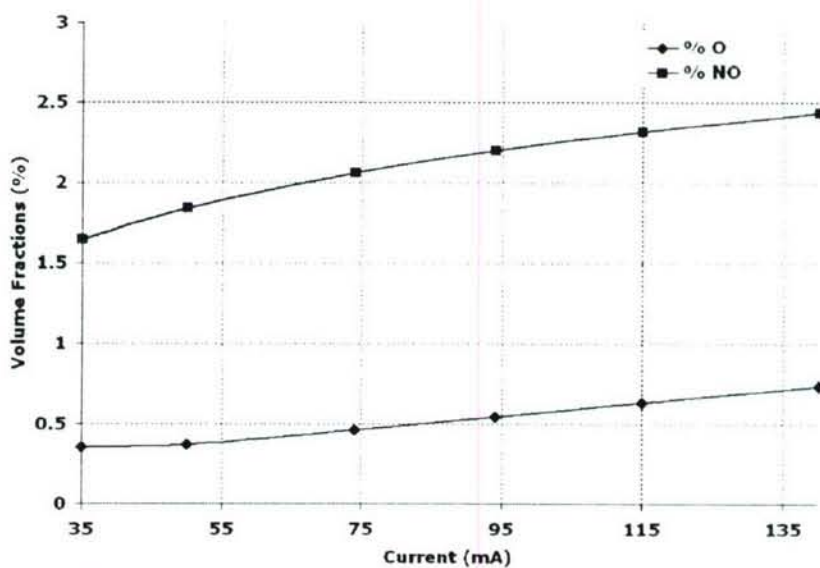


**Fig. 28** Oxygen radical and NO percent concentration by volume versus current for MGA activation of the air stream

The steady-state simulations from the chemical kinetic mechanism described above revealed that both the O and NO percent volume concentrations increased with an increase of the current of the MGA (Fig. 28); however, the absolute concentration and the slope of the increase of NO with current were higher than that of O. Furthermore, the plots show that the maximum concentrations

of O and NO were at low flow rates and high plasma current. This trend can be explained by taking into account residence times of the flow through the arc. When the flow rates are low, the MGA activated more volume of air per unit time.

### 3.0 Ignition and Flame Stabilization Enhancement by MGA

The results of the plasma-assisted combustion studies were divided into two categories: (1) the enhancement of flame stabilization and extinction limit of partially premixed flames and non-premixed flames, and (2) the enhancement of ignition limits. The partially premixed flames were studied on a lifted flame burner integrated with the MGA plasma discharge device to observe the effects on flame stability of a lifted flame. The non-premixed flames were studied on a counterflow burner integrated with the MGA plasma discharge device to observe quantitatively the thermal and non-thermal effects by plasma discharge on the extinction limit. The effects of the MGA on extinction and ignition phenomena of the non-premixed flames were studied in detail both experimentally and computationally.

#### 3.1 Stability Enhancement of Jet Diffusion Flames

Due to short flow residence time, the turbulent combustion in a supersonic flow and in engines is diffusion controlled and mainly in the partially premixed flame regime. Therefore, the enhancement of plasma discharge on the partially premixed flame propagation speed is vital to flame stabilization in high-speed turbulent flow. Since the triple flame speed can be scaled as

$$S_p = S_L \cdot (\rho_u / \rho_b)^{1/2} \quad (3)$$

and the fraction of the unburned,  $\rho_u$ , to the burned,  $\rho_b$ , gas density would remain constant, the principal means of an increase in the triple flame speed,  $S_p$ , would be the laminar flame speed,  $S_L$ . Therefore, measurements of the increase of the triple flame speed would provide a good indication of the increase of the premixed laminar flame speed.

To study the effects of the MGA on the lifted jet diffusion flame stability, the plasma system was integrated with a co-flow burner shown in Fig. 29. The co-flow burner utilized the plasma system with a coaxial fuel jet. The fuel jet introduced propane to be diffused into the plasma activated air stream. Propane was chosen because of its highly stabilizing characteristics as a lifted flame. A lifted triple flame structure was formed downstream, and the system was tested using three propane flow rates and eight levels of power addition.

Initially, the partially premixed triple flame was established without plasma activation at a given lifted height. Without plasma activation of the air, the flame was in the lean premixed

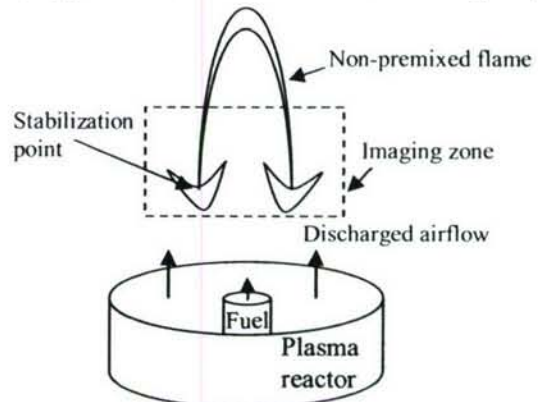


**Fig. 29** Plasma enhanced partially premixed co-flow flame burner

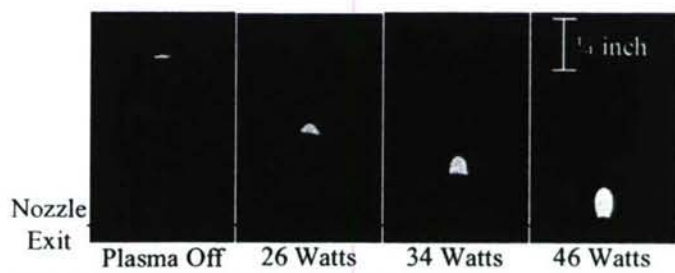


**Fig. 30** Flame Heights at Different Power Additions

flame regime with a low flame speed, as indicated by its lifted height in Fig. 30. As the plasma was turned on, the triple flame propagated faster and moved upstream to a smaller lifted height. Finally, at 46 Watts, the flame propagated to the origin of the fuel jet, which indicated a significant enhancement of the stability of the partially premixed combustion and hence the triple flame speed (Fig. 30).

To quantify the plasma enhancement of the triple flame speed further, two approaches were taken. For the first approach, the lifted triple flame was established at the limit of quenching. As the plasma was turned on and the power increased, the extinction was suppressed, and the flame became stable at much higher air co-flow rates. With a MGA plasma power addition of 100 Watts, the air co-flow rate was capable of being increased by almost 70% before extinction (Fig. 31). For the second approach, the flame was established at the exit of the propane jet. The air co-flow then was increased until the flame lifted off. The procedure was repeated for eight levels of plasma power. With a MGA plasma power of only 100 Watts, the air co-flow rate was increased by over 100% before the flame lifted (Fig. 32).

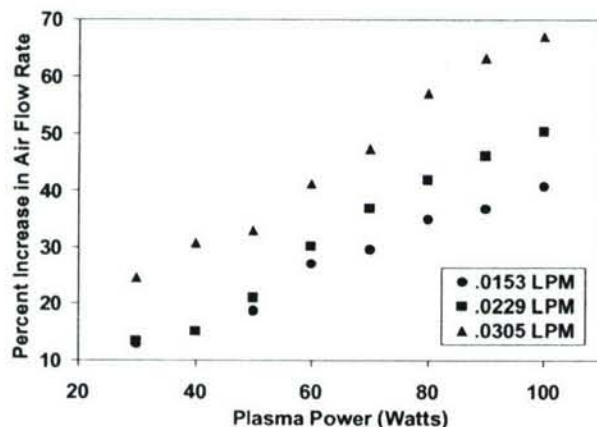


Fig. 31 Lifted Flame Quenching Limits

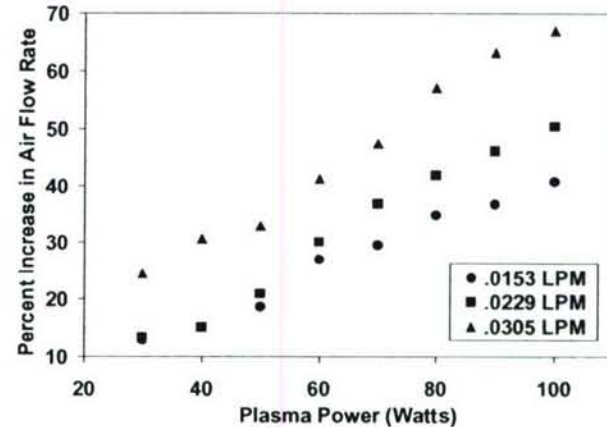


Fig. 32 Limit of Liftoff

There was a clear enhancement of the triple flame speed and stabilization properties with MGA plasma activation of the air co-flow for the lifted flames. A comprehensive analysis of the enhancement required a complex model of the interaction of the hydrodynamics and the mixing layers of the triple flame with the plasma production of species and combustion chemistry. As such, in order to understand the fundamental mechanism for the enhancement quantitatively, a simpler platform to study the plasma-flame interaction was desired.

### 3.2 Counterflow Flame Burner Integration

To establish a simplified platform for the study of plasma-flame kinetic coupling, the MGA plasma discharge was integrated with the counterflow flame burner. The counterflow system provided four key benefits: minimal buoyancy effects, simplified flame geometry, ability to define a flow velocity gradient (strain rate or inverse of residence time) on the centerline near the stagnation plane of the two impinging jets, defined as,<sup>15-19</sup>

$$a_i = \frac{2v_i}{L} \left( 1 + \frac{v_j}{v_i} \sqrt{\frac{\rho_j}{\rho_i}} \right), \quad (4)$$

where  $v$  is the velocity,  $L$  the length between the two nozzle,  $\rho$  the density, and subscript designations  $i$  and  $j$  the fuel and oxidizer stream, respectively, and lastly, excellent optical access for advanced laser diagnostics for species and temperature measurements.

A schematic of the system is shown in Fig. 33. The counterflow burner system consisted of two converging nozzles of 15 mm in diameter, separated by 13 mm. The upper nozzle was water-cooled. The feedstock for the plasma device upstream of the lower nozzle was air, while nitrogen-diluted methane flowed through the upper nozzle. To isolate the flame from the ambient air and disturbances, a nitrogen co-flow was used. The nitrogen co-flow passed through an annular slit of 0.75 mm in radial direction around the circumference of each nozzle exit. The velocity of the co-flow was maintained at or below the nozzle exit speed to minimize diffusion into the stream. The flame was established on the upstream air side of the stagnation plane. The designed system allowed for the examination of the quenching limits of the flame as a function of the flow velocity gradient for different levels of plasma power addition.

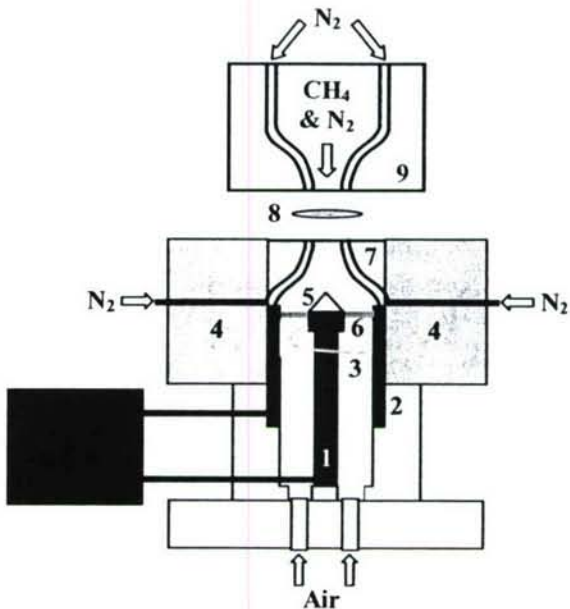


**Fig. 33** Schematic of counterflow diffusion flame extinction apparatus. 1. Cathode, 2. Anode, 3. Gliding Arc Initiation Wire, 4. Permanent Ceramic Magnets, 5. Ceramic Insulator, 6. MGA, 7. Nozzle w/  $N_2$  Co-Flow, 8. Counterflow non-premixed flame, 9. Water Cooled Nozzle w/  $N_2$  Co-Flow

The flow rates of the individual gases were controlled with sonic nozzles that were calibrated with a DryCal dry piston flow meter (1% error). The methane and nitrogen were mixed in a hollow mixing cylinder (for minimal back pressure). To ensure that the mixture input to the flame was held constant while the velocity was increased through the nozzles, a bypass system was used. The methane/nitrogen mixture, as well as the air, was bled off before it reached the respective nozzles. The flow rate then was increased or decreased through the nozzles by closing or opening the valves of the bypass, respectively. By measuring the flow through the bypass using the DryCal flow meter, the nozzle exit velocities were calculated.

To measure the extinction limits, the flame first was established with the bypass fully open, producing the lowest flow rate through the nozzles (and strain on the flame). Then each bypass was slowly closed, while maintaining the stagnation plane at a fixed position. During this process the flame moved closer to the stagnation plane between the two nozzles, which decreased the residence mixing time, as well as increasing the strain rate until flame extinction.

Two pictures of the nitrogen-diluted methane-air counterflow flames are shown in Fig. 34 with and without plasma power addition. The side view of the one-dimensional structure of the flame is shown. In all cases the flame was very steady and had minimal curvature, providing an

excellent platform to perform experimental measurements via laser diagnostics and geometry that was easy to reproduce computationally. There was also a significant difference in luminosity between the flame with and without plasma activation of the air stream.

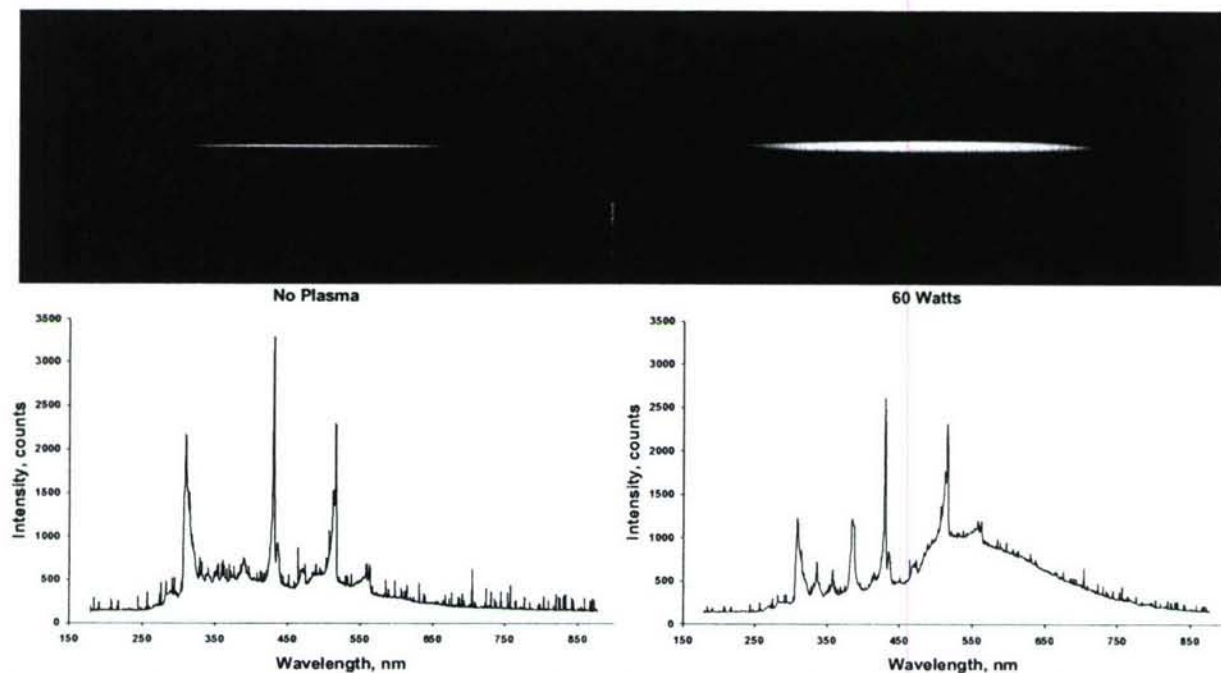


**Fig. 34** Pictures of counterflow non-premixed flames with and without plasma activation of the air and the corresponding luminescent spectrum

Luminescent spectrum measurements were taken of the nitrogen diluted methane/air non-premixed flame because of the noticeable difference observed in the visible spectrum when the plasma was on. The strain rate was fixed at  $83\text{ s}^{-1}$ , and measurements were taken with no plasma power addition and with approximately 60 Watts of plasma power addition. The two flames and their respective spectra are shown in Fig. 34. The integration time was different for each measurement, 5 seconds for no plasma and 2.5 seconds for 60 Watts. The spectra were not compared quantitatively, but rather their general shape and peaks were compared for qualitative analysis. For both spectra there were three common peaks around 309 nm, 431 nm, and 517 nm. These peaks were associated primarily with OH and some HCO around 309 nm, with CH around 431 nm, and with C<sub>2</sub> around 517 nm. These peaks are typical for a methane/air flame. The flame with plasma power addition had additional peaks around 336 nm, 359 nm, and 388 nm, and broadband emission between approximately 477 nm and 850 nm. The 336 nm peak was associated with NH, HCO and O<sub>2</sub> band emission, the 359 nm mostly with HCO and some O<sub>2</sub>, and the 388 nm mostly with CN and some CH band emission.<sup>20</sup>

### 3.3 Effects on Flame Extinction Limit

The extinction limits for the counterflow flames were found with and without plasma power addition. When the bypass valves were closed, the nozzle exit velocities increased, pushing the flame closer to the stagnation plane. As the flame approached the stagnation plane, the strain rate increased. As such, the flame lost more thermal energy and had less residence time for reaction completion until finally, it extinguished. The effect of the MGA plasma discharge on the

extinction limits of the flame was investigated by using three nitrogen diluted methane mixtures, and the results are shown in Fig. 35. The extinction limits with no plasma power addition agreed well with the data reported by both Puri and Seshadri<sup>15</sup> and Bundy et al.<sup>19</sup> With only 78 Watts of plasma power input, there was a 220% increase in the extinction strain rate. The power input was less than six percent of the flame power, defined as the maximum power that could be obtained from the given amount of fuel in the mixture. The results showed that there was a significant extinction limit enhancement when using the MGA plasma discharge, but the reasons for this effect were not yet apparent.

Initially, the results for the extinction strain rates were compared to those of the numerical computation. The computations were performed using a modified version of PREMIX code<sup>21</sup> with both potential and plug flow boundary conditions using the detailed chemical mechanism of GRI-3.0.<sup>22</sup> The temperature input to the numerical computation came from the measured temperatures found just downstream of the exit of the nozzles via planar Rayleigh scattering thermometry for each of the various flow, concentration, and plasma power conditions.

Since strain rate was proportional to velocity, the comparison was done in relation to velocities at extinction. The results are shown in Fig. 36. Since the input to the computation was only elevated temperatures to mimic the plasma and since both the experiment and computation extinction results were in good agreement, this result indicated that the effect of the MGA on the flame was predominately thermal.

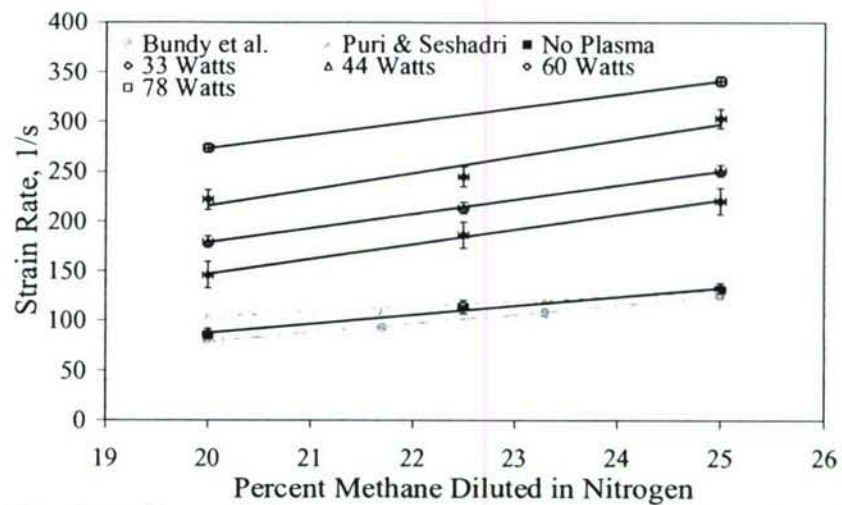


**Fig. 35** Effects of plasma power addition on the strain rates at extinction for different levels of nitrogen dilution

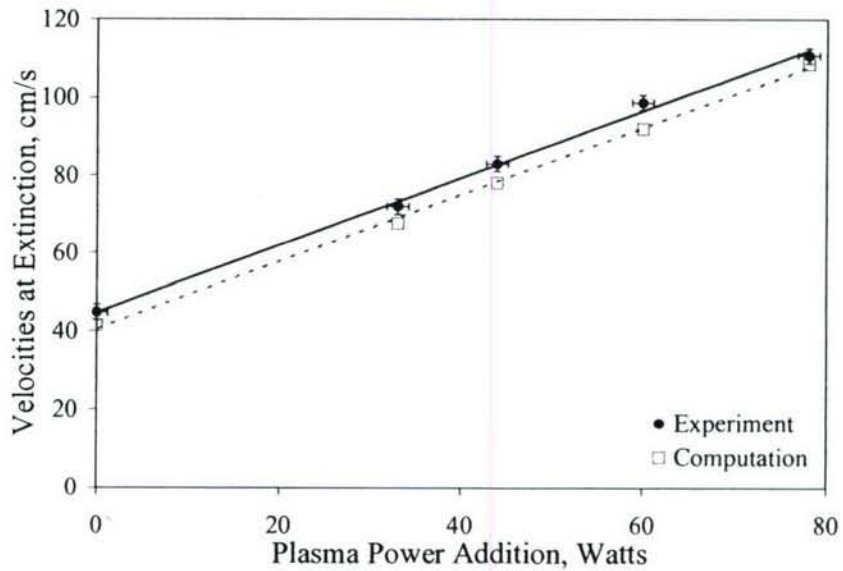


**Fig. 36** Comparison of nozzle exit velocities at extinction

### 3.4 Rayleigh Scattering and OH Planar Laser Induced Fluorescence (PLIF) Experimental Set-up

To measure the temperature profiles of the non-premixed flame between the two nozzles, a Rayleigh scattering system was utilized (see Fig. 37). A frequency-doubled, injection-seeded Nd:YAG laser (Quanta-Ray GCR-4) with an output of approximately 450 mJ per pulse was used. For OH measurements, the OH was excited via a Lumonics HD-300 dye laser pumped with the Nd:YAG laser (Fig. 37). The wavelength was tuned to 567.106 nm so that the frequency-doubled radiation matched the wavelength for the  $Q_1(8)$  transition of the  $A^2\Sigma^+ - X^2\Pi$  (1,0) band. The Boltzmann population fraction of the ground state ( $N = 8$ ) reached a maximum near 1600 K and varied

little over the temperature range of 1200 K to 2200 K, for example  $f_B(2200 \text{ K})/f_B(1600 \text{ K}) = 0.934$ . The resulting pump linewidth was approximately  $0.1 \text{ cm}^{-1}$ , while the 283 nm beam energy was 12 mJ/pulse. The beam energy was measured and recorded for each image taken by directing a small portion of the beam (either 532 nm or 283 nm) to a photodiode or Molelectron Joulemeter. For both temperature and OH measurements, a laser sheet was formed using two lenses. The optics consisted of a plano-concave cylindrical lens (-300 mm focal length) to spread the beam in the vertical direction and a plano-convex spherical lens (1 m focal length) to focus the beam in the horizontal direction and to collimate the beam in the vertical direction. The laser sheet then was directed between the two nozzles of the counterflow flame burner. To minimize any stray scattering of the laser sheet in the vertical direction, band-pass absorption filters were used to “clip” the sheet. The scattering and fluorescence were imaged with Princeton Instruments PIMAX intensified CCD cameras (one camera with a photocathode optimized for the visible spectrum for Rayleigh scattering and one camera with a photocathode optimized for the UV spectrum for OH fluorescence). For Rayleigh scattering, a Nikon 105 mm, f/2.8 macro lens was used while for OH PLIF, a Nikon UV Nikkor 105 mm f/4.5 lens was used along with UG-11 and WG-295 Schott glass filters to isolate fluorescence from the  $A-X(0,0)$  and  $A-X(1,1)$  bands and block background scattering. Both cameras employed a 512 by 512 pixel array that was binned to improve the framing rate.

To calibrate the Rayleigh scattering signal, images of scattering intensity were taken of clean, particle-free air (at a known temperature) that was directed through the lower nozzle. Even though great care was taken to minimize the background scattering, some still existed. To account for the background scattering, high purity helium was passed through the nozzles of the

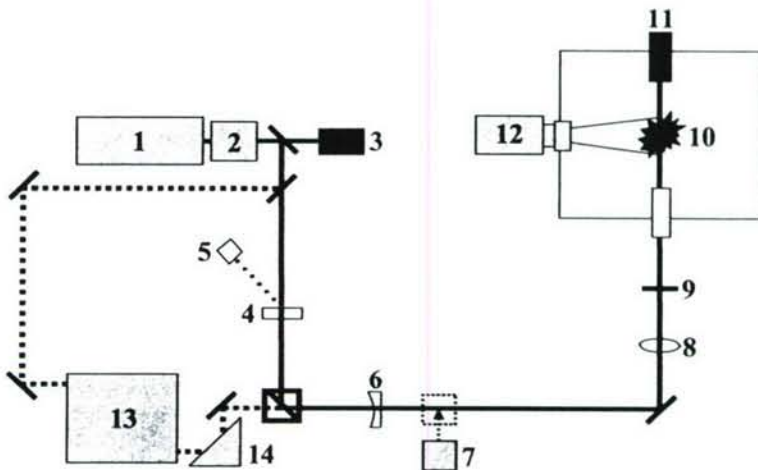


**Fig. 37** Planar Rayleigh scattering and OH PLIF set-up. 1. injection seeded Nd:YAG laser, 2. frequency doubler, 3. beam dump, 4. half-wave plate, 5. diode energy meter, 6. lens, 7. power meter, 8. lens, 9. clipper, 10. flame, 11. beam dump, 12. ICCD camera, 13. dye laser with frequency doubler, 14. Pellin-Broca prism.

burner system, allowing the background to be measured. Helium was used for this purpose because its scattering cross section was very small compared to that of air (less than 1.5%). Also, to account for any variations in the system (and minimize error) as the experiments were conducted, such as shifts in the laser sheet, the air reference and background scattering were checked periodically.

To calibrate the intensity from the OH PLIF to an absolute number density of OH, measurements first were taken of a known system with the equivalent experimental arrangement. A 25.4-mm-square Hencken burner<sup>23</sup> using a pre-mixture of methane and air (equivalence ratio of 0.95) was used as the calibration flame. Though there was a small difference in electronic quenching rate between this flame and that expected in the counterflow non-premixed flames (due to the nitrogen in the fuel), the difference was mitigated due to transition saturation. The number density in the Hencken burner flame (in the burnt gas region) was determined with an absorption measurement—using the Q<sub>1</sub>(6) transition of the A-X(0,0) band—along with a laser-induced fluorescence measurement of the absorption pathlength. The measurement gave an OH number density of  $0.94 \pm 0.07 \times 10^{16} \text{ cm}^{-3}$ , a value consistent with a burnt-gas temperature of 2170 K (versus the adiabatic equilibrium value of 2194 K). The ratio of fluorescence signals between the counterflow flames and the Hencken burner flame, along with the number density in the Hencken burner flame, allowed calculation of the counterflow flame number densities. A 10% correction factor also was applied to the Hencken burner flame fluorescence signals to account for the greater degree of fluorescence trapping and sheet absorption compared to the counterflow flames. Measured temperatures were used to correct the slight change in Boltzmann population fraction from Hencken burner to counterflow flames. The total fractional uncertainty for the counterflow OH number densities is estimated to be  $\pm 15\%$ . The uncertainty represented a combination of absorption measurement uncertainty and uncertainty of application of the calibration to the counterflow flames.

### 3.5 Temperature Measurements by Using Rayleigh Scattering

To measure the temperature distribution quantitatively and compare it with numerical simulations, Rayleigh scattering measurements were made on the counterflow flame for various strain rates. The laser sheet was passed through the diameter of the disk shaped counterflow flame between the nozzles of the burner. Two sample images are shown in Fig. 38, where (a) is with no plasma power addition and (b) is with approximately 33 Watts of plasma power addition. The background was subtracted and the air-reference divided into each image. The intensity seen was both a function of scattering cross section and number density distributions between the nozzles. A scale is shown below the images with the darkest extreme for the

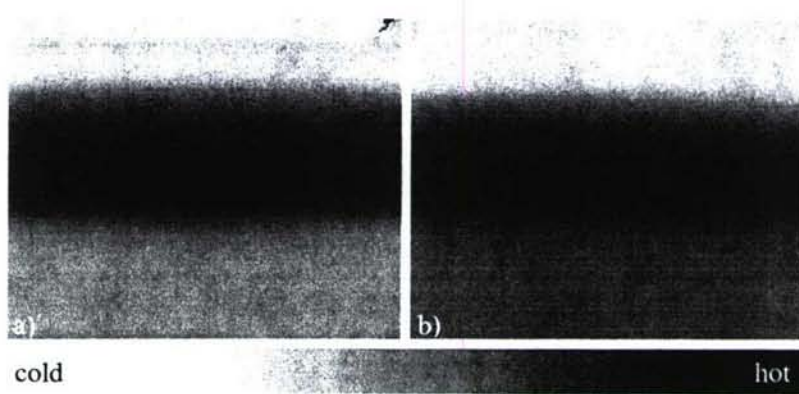


**Fig. 38** Rayleigh scattering images at a strain rate of  $98.6 \text{ s}^{-1}$ .  
a) no plasma power addition, b) 33 Watts of plasma power addition

lowest scattering and the highest temperature, and the lighter extreme for the highest scattering and the lowest temperature. The flame was located in the darkest region of these images just above the middle of the picture, spanning the width. The nitrogen-diluted methane mixture entered the field of view from the top of the images and the air (plasma side) from the bottom of the images. Even with the non-equilibrium MGA plasma discharge, the present burner design yielded a very good one-dimensional flame structure along the flow direction. The result greatly simplified the coupling between the flow field and the plasma-flame interaction. A comparison of the two images shows that the region below the flame in (b) (plasma on) was darker than (a) (plasma off) below the flame. The difference indicated less scattering and hence a higher temperature. In each case, a ten-pixel-wide “stripe” was taken from each image and averaged to yield the best distribution between the nozzles. The temperatures measured at the boundaries (just downstream of the nozzles) were used as boundary conditions in the numerical computation.

### 3.5.1 Rayleigh Scattering Intensity Ratio Profiles

To gain more insight into how the flame was being enhanced by the non-equilibrium plasma, Rayleigh scattering thermometry was performed to obtain the distribution of temperature between the two nozzles. The intensity observed by the ICCD camera was a function of both the scattering cross section, because of the distribution of different species, and number density change between the two nozzles. By simply referencing those intensities to the intensity of air at room temperature, ratios were found. The ratio measurements then were compared to numerical

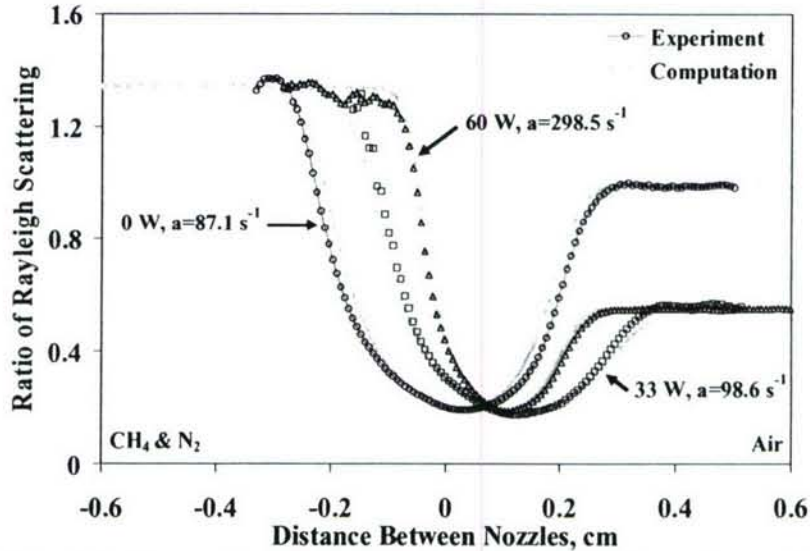


**Fig. 39** Comparison of Rayleigh scattering intensity ratio profiles with and without plasma power addition at different strain rates

computations and the results are shown in Fig. 39 for both the plasma power off and on. Oscillations were evident in the scattering profiles, especially near the upper (fuel) nozzle. The oscillations resulted from diffraction from the edge of the absorption filters used to “clip” the beam (and prevent scattering from the burner surfaces) and slight movement of the sheet between the measurements in the flame and in the air reference. Nonetheless, there was reasonably good agreement between the experiment and computation. The good agreement once again showed that the effect of the non-equilibrium MGA plasma discharge on the flame was predominately thermal.

### 3.5.2 Temperature Distributions

Even though the measurements directly from the Rayleigh scattering were in good agreement with the computation and were also completely independent quantities, the actual temperatures were not realized. To get a better estimate of the temperatures, the ratio profiles, as described above, were used. Since the species concentrations and temperature changed between the nozzles due to the presence of the flame, the scattering cross sections and number densities changed. Number density could be accounted for simply by the temperature, but the scattering cross sections could not. The scattering cross sections needed to be known at each point along the profile as a reference to calculate the temperature. Therefore, the species concentrations associated with specific temperatures and axial positions from the numerical computation were used to convert scattering signal to temperature. The scattering cross sections for species in molar concentrations of a tenth of a percent and larger were calculated using refractory data from Gardiner et al.<sup>24</sup> These calculations accounted for the variation in scattering cross section and gave accurate temperature profiles from the Rayleigh scattering images. The temperature profiles found from the Rayleigh scattering images then were compared to the results of the numerical computation at the same input temperatures and flow conditions. Figure 40 shows temperature profile comparisons between the experimental results via Rayleigh scattering and the numerical computation using the GRI-3.0 chemical mechanism. The profiles were in good agreement. A similar comparison between the experimental results and the numerical computation also were made with the addition of plasma power (Fig. 40). Once again, the temperature profiles were all in good agreement. On the air side (the right side of the plots), the temperature was elevated, mimicking the thermal effect of the plasma. The air temperature was determined experimentally from the Rayleigh scattering. The air temperature was the only experimentally measured value that was input to the numerical computation. Overall, the temperature profiles agreed, once again showing that the effect of the non-equilibrium MGA plasma discharge was predominately thermal for the cases investigated.

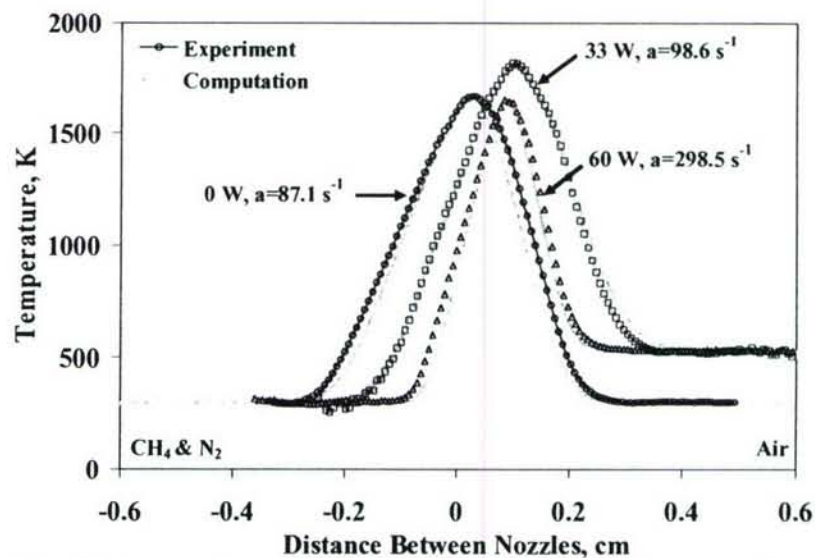


**Fig. 40** Comparison of temperature profiles with and without plasma power addition at different strain rates

### 3.6 OH PLIF Measurements

To reinforce further that the enhancement of the flame via the non-equilibrium plasma was dominated by thermal effects, OH PLIF measurements were performed. ICCD images of the relative intensities of the OH in the flame as a function of plasma power are shown in Fig. 41. From the images, the OH number density was obtained for different plasma powers and strain rates and referenced to a Hencken burner flame, as described previously, to find the absolute OH number density. Figure 42 shows the results from the OH PLIF measurements when compared to the computation with and without plasma power addition. The experimental profiles were

consistently taller and broader than the computational profiles, but overall, the agreement was within the uncertainty of the measurement,  $\pm 15\%$ , as described above. Also, since the 283 nm laser sheet was approximately 250  $\mu\text{m}$  in width in the probe region (and transition saturation gave an effective probe thickness

somewhat greater than this), it was expected that there would be a slight broadening of the experimental profiles. Nonetheless, the plots showed reasonably good agreement between the experiment and the computation, once again showing that the effect of the non-equilibrium MGA plasma discharge on the flame was predominately thermal.

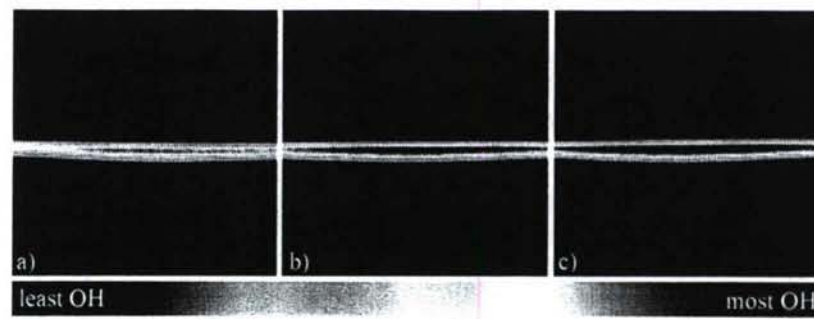


**Fig. 41** OH PLIF images. a) no plasma power addition, b) 33 Watts, c) 48 Watts

### 3.7 Effects of Radical Addition on Flame Structures

What would be the lifetime of radicals produced by the plasma discharge in the air stream and would they reach the flame? This question was reasonable to ask because, as observed, the effect appeared to be predominately thermal, rather than non-thermal. Since the plasma was activating only dry air in the experiment, it was assumed that the radicals produced in the flame consisted of oxygen and nitrogen only. The effect of atomic oxygen addition at the air side boundary on the flame structure was shown (once again mimicking the plasma) because atomic nitrogen addition played a similar role. Atomic oxygen concentrations from 0.01 percent to 1 percent were added at the air (plasma) side boundary. The temperature was fixed at 400 K at this boundary to ensure that low temperature chemistry did not come into play. Also, the velocities at the boundaries were similar to those used in the experiment for a flame that was highly strained and near extinction, where radical addition was important. A plot of the temperature profiles and oxygen atom concentration distributions between the nozzles is shown in Fig. 43. There was no significant effect until almost 1 percent addition of atomic oxygen. Considering that the plasma disk was located almost 4 cm upstream of the boundary, where the

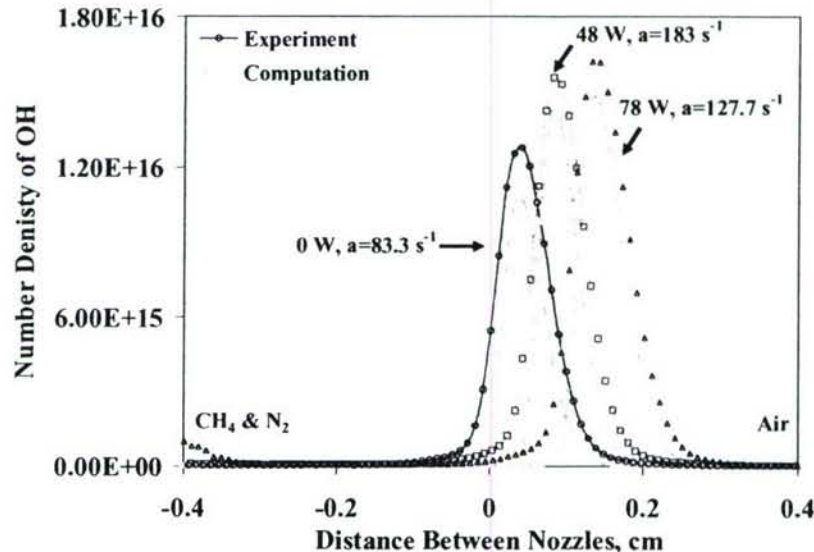


**Fig. 42** Comparison of OH number density distributions with and without plasma power addition at different strain rates

atomic oxygen was added, it appeared that the atoms would recombine well before the flame, therefore having no non-thermal effect on the flame.

From the above discussion, conclusions were made that the radical induced non-thermal effects on the burning rate of non-premixed flames were very limited at low air temperatures because the radical lifetime was too short to affect the chain branching reaction path. The oxygen radicals recombined and increased the air temperature before reaching the flame. In addition, the low temperature of air excluded the occurrence of low temperature chemistry.

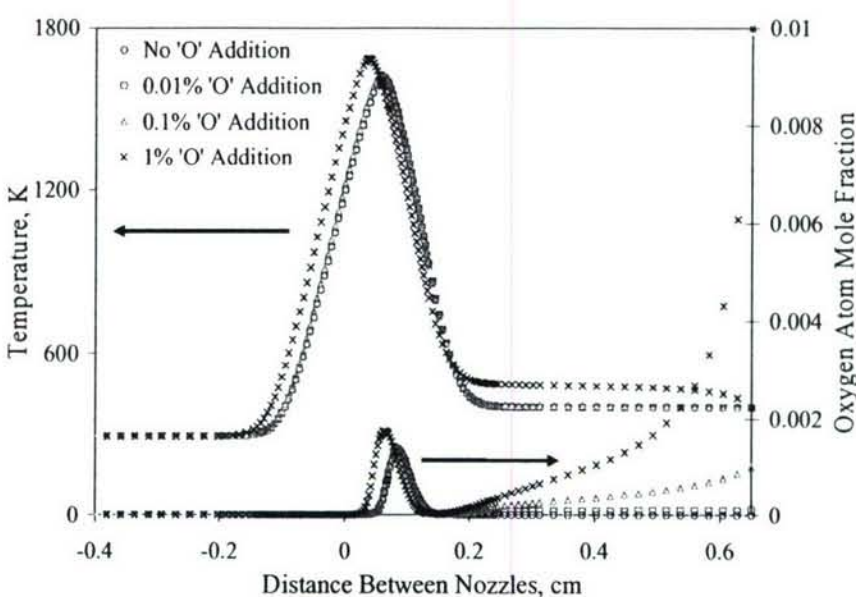


**Fig. 43** Computed temperature and oxygen atom distributions between the nozzles of the counterflow system with atomic oxygen addition

### 3.8 Ignition Temperature Measurements by Using the Counterflow Flame

Since the effect of the MGA on the counterflow flames was predominately thermal, other experimental methods were sought to produce non-thermal enhancement. The only ways to accomplish the task were to go to higher temperatures or lower pressures to extend the lifetimes of the plasma-produced species. Furthermore, since the experiments for extinction had the pre-existing condition of a flame that already produced significant amounts of radicals to sustain itself, the addition of small concentrations of radicals would not have as much of an observable non-thermal effect. The solution was counterflow ignition experiments where the air would be pre-heated and then passed through the MGA device with the plasma on and off. Therefore, the lifetimes of the plasma-produced species were extended, and there was no flame to produce radicals, so any radical addition would lead to non-thermal ignition enhancement. The same basic design again was chosen for the ignition work because of its simple flame geometry; however, for ignition, the system was redesigned for pre-heating of the air to high temperatures. The system was capable of igniting the non-premixed flames with and without the MGA while only producing non-thermal effects of the MGA on the ignition process, eliminating any localized thermal effects. The counterflow burner was redesigned to have two attachments to accommodate both a heated nozzle and the MGA device.

The upper nozzle of the counterflow system consisted of a water-cooled 15 millimeter inner diameter nozzle with a nitrogen co-flow to isolate the jet from any ambient effects. The upper nozzle also was fixed to a vertical translation table to adjust the distance between the upper and lower nozzles. Methane was used as the fuel to pass through the upper nozzle and was diluted in

eighty percent nitrogen to weaken the strength of the flame. The lower nozzle of the counterflow system consisted of both a pre-heating system and either a heated nozzle or the MGA device. The pre-heating system was housed in high-temperature silica ceramic and contained a silicon carbide heater that was capable of raising the temperature of the air in excess of 1600 K. A thermocouple was placed approximately one millimeter from the surface of the heater and was used as a feedback sensor to the heater's power supply to maintain the desired temperatures. The entire pre-heating system was fixed to a planar two axis translation table to allow for fine adjustment of the axial alignment of the upper and lower nozzles.

The two attachments to the pre-heating system were the heated nozzle for only heated air experiments to provide the baseline of ignition temperatures without plasma activation and the MGA device for the

plasma ignition experiments. The heated nozzle attachment consisted of a 15 millimeter inner diameter quartz tube and a schematic of the system is shown in Fig. 44 with a picture of an ignited flame. To minimize heat loss, Kanthal heater wire was wrapped around the outside of the quartz tube, with a variable AC power supply providing the power. The MGA device attachment to the pre-heating assembly consisted of high-temperature silica ceramic to hold the stainless steel electrodes in place. Since high temperatures required in the ignition system, the permanent magnets used on the extinction apparatus could not be used for the ignition experiments because of their low

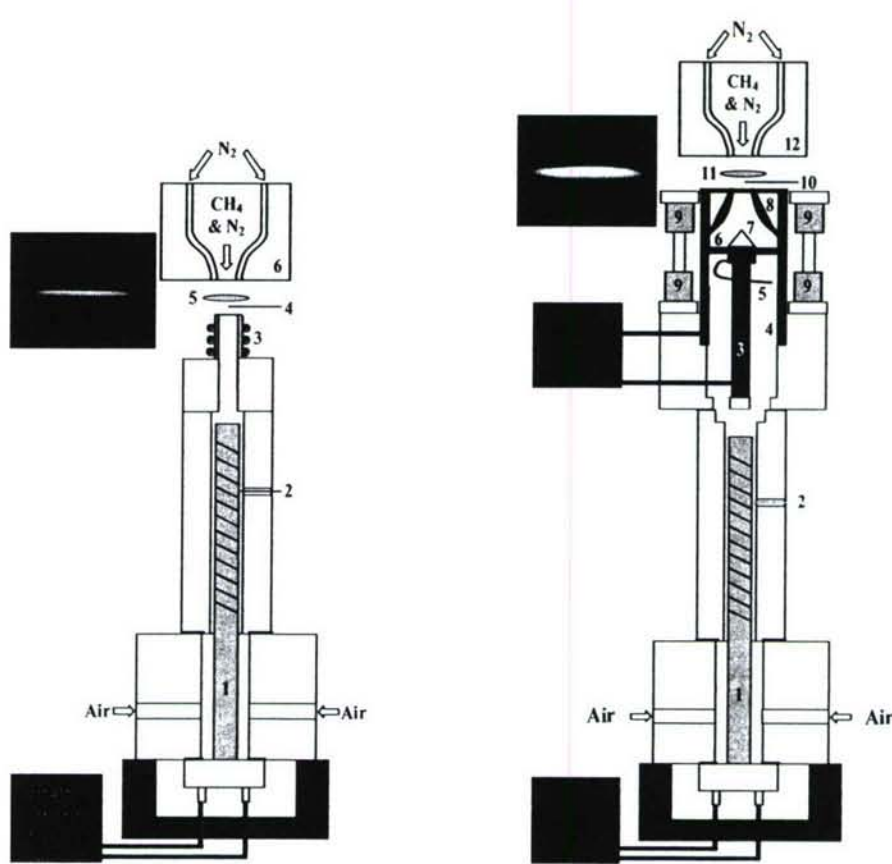


**Fig. 44 (left)** Heated Air Counterflow Ignition Apparatus 1. SiC heater, 2. R-type Thermocouple, 3. Kanthal wire heated quartz nozzle, 4. K-type thermocouple, 5. Diffusion flame, 6. Water-cooled nozzle with  $N_2$  co-flow

**Fig. 45 (right)** MGA Counterflow Ignition Apparatus 1. SiC heater, 2. R-type Thermocouple, 3. Cathode, 4. Anode 5. Gliding arc initiation wire, 6. MGA, 7. Insulator, 8. Nozzle with  $N_2$  co-flow, 9. Magnets, 10. K-type thermocouple, 11. Diffusion flame, 12. Water-cooled nozzle with  $N_2$  co-flow

demagnetizing temperature. Instead, permanent neodymium magnets were located radially, but not adjacent to the outer electrodes to minimize heat loss and keep the magnets well below their demagnetizing temperature. The new set-up correctly produced the magnetic field that was present with the old donut shaped permanent magnet system. A 15 millimeter inner diameter nozzle was placed downstream of the MGA device as the lower nozzle of the counterflow burner. A schematic of the system is shown in Fig. 45 with a picture of an ignited flame.

### 3.9 Ignition Temperature Measurements

Measurements were taken of the ignition temperatures on both the heated nozzle and MGA device counterflow apparatus. The counterflow system allowed for a comparison of the ignition temperatures with and without plasma activation of the air for the same flow conditions. For the heated nozzle system, the flow initially was fixed through the system (20% CH<sub>4</sub> in 80% N<sub>2</sub> versus air), and the power was supplied to the silicon carbide heater and Kanthal wire heater to raise the temperature of the air close to the ignition temperature of the combustible flow. The system was allowed to sit for about an hour to ensure that it was in steady state. The flow then was ignited with an external source to allow for visualization and adjustments to optimize alignment and flow in the system. Temperature profile measurements across the exit of the lower nozzle and between the lower nozzle and the stagnation plane were obtained to ensure that the temperature peaked along the axis of the nozzle and was highest at the exit of the lower nozzle. A K-type thermocouple was used to measure the ignition temperature because it would not suffer from any catalytic surface effects. Care had to be taken to ensure that the same location in the flow always was measured. Temperature measurements were made consistently at the exit of the lower nozzle along the centerline axis. Since the thermocouple could not remain in the flow during ignition because it would disrupt the flow locally, allowing for premature ignition, it was placed on a translation apparatus that could move it repeatedly and consistently from a location outside of the flow to the same axial location at the exit of the lower nozzle.

To achieve ignition, the temperature of the air was raised slowly in small increments (by approximately 2 K to 3 K close to the ignition temperature) until ignition was achieved by increasing the power supplied to the silicon carbide heater. The heater power at which ignition occurred was recorded, and the flame was extinguished by closing off the supply of methane. The heater power then was lowered, the methane turned on, and the flow field correctly adjusted and optimized again. The heater power was then raised, ignition achieved, and power recorded. Once the power at ignition was found to be consistently the same, the methane supply was closed off and the heater turned to that power. The thermocouple was placed in the flow on the center axis at the exit of the lower nozzle and the temperature measured. The measured temperature was defined as the ignition temperature for that flow condition. The procedure to find the temperature at ignition was completed several times to establish repeatability. For radiation corrections to be made, temperature measurements of the parts of the apparatus in the line-of-sight and in close proximity to the thermocouple for ignition were made.

A similar procedure was followed for obtaining the ignition temperatures when using the MGA device. In addition to the silicon carbide heater being brought up to a temperature close to ignition, the plasma power supply was turned on to a fixed power and the system allowed to sit for about an hour to achieve steady state. The same procedure as that of the heated nozzle was

followed to obtain the ignition temperatures for plasma activation of the air. Special care was taken to ensure that the MGA did not become unstable and produce any hot spots that would lead to localized ignition and hence false underestimates of the actual ignition temperatures.

Due to the design of the experiment, any difference in ignition temperature was predominately non-thermal because of the minimization of any thermal effects. The experiment, therefore, offered a well-defined system to study non-thermal ignition enhancement by a non-equilibrium plasma.

### 3.10 Ignition Enhancement by MGA

The ignition temperature was measured by using both the electrically heated nozzle and MGA attachment to the counterflow non-premixed flame burner for a strain rate range from  $200 \text{ s}^{-1}$  to  $350 \text{ s}^{-1}$ . For the MGA, the current was fixed at 350 mA, yielding a power around 250 Watts. The results for the ignition temperatures are shown in Fig. 46. There was a clear and significant decrease in the ignition temperature when using the MGA; as much as 200 K at a strain rate of  $200 \text{ s}^{-1}$ . To confirm the ignition enhancing effects of the MGA on the system with simple fuel chemistry, hydrogen was also chosen as a fuel. The same procedure as with methane was followed and the results are shown in Fig. 47. Once again, for hydrogen ignition, there was also a significant non-thermal enhancement with the MGA, with ignition temperatures more than 180 K lower than pre-heated air alone.

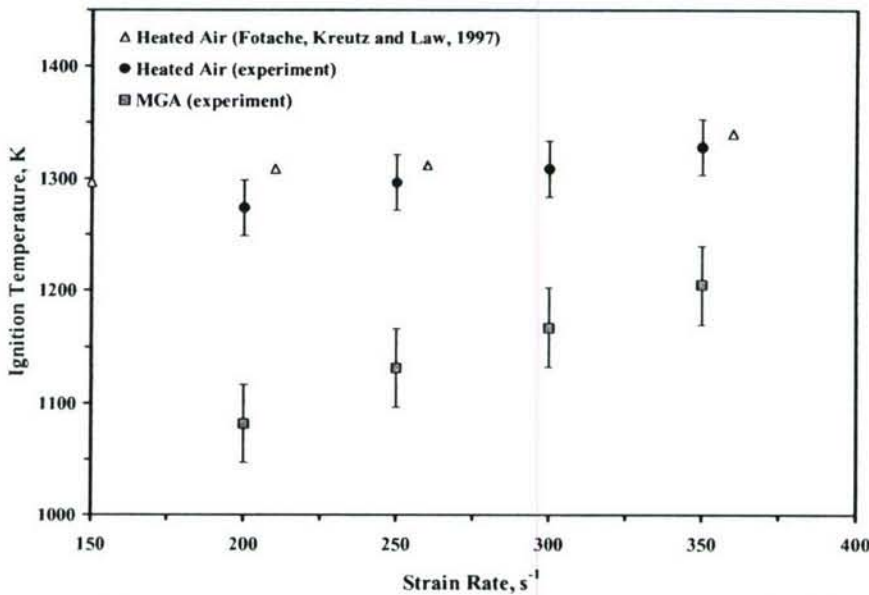


**Fig. 46** Comparison of experimental measurements of ignition temperatures with 20%  $\text{CH}_4$  in  $\text{N}_2$  versus air for pre-heated air and MGA (at 350 mA) from  $a = 200 - 350 \text{ s}^{-1}$

The results shown here were the first experiments designed to isolate completely and observe non-thermal enhancement by a non-equilibrium plasma. The MGA was capable of non-thermally enhancing the ignition of the methane counterflow non-premixed flame system, but what were the mechanisms of enhancement? To answer this question, systematic computational examination of the kinetic mechanisms of enhancement was completed. These mechanisms focused on radical enhancement and also enhancement through intermediate stable species such as  $\text{NO}_x$ .

### 3.11 Computational Simulations of Counterflow Non-Premixed Flame Ignition

Computational simulations were performed to validate and explain qualitatively the interaction of the MGA with the ignition of the counterflow non-premixed flames. The code was an adaption of a previously-generated code for counterflow flame simulations by Ju's group.<sup>21</sup> With the geometry of the counterflow burner, a simulation using detailed chemistry (GRI-3.0) was performed to find the ignition temperatures as a function of strain rate. The S-curve responses for the counterflow system were found using a temperature and radical continuation method.

### 3.11.1 Ignition with Pre-heated Air Only

The ignition S-curves were computed for the pre-heated air only case as functions of air temperature. The curves are shown in Fig. 48. As expected, the curves exhibited two ignition and two extinction turning points, which also was observed and explained in a recent paper by Liu and Law.<sup>25</sup> The lower temperature/strain rate ignition limits (the first ignition limit) had a maximum temperature in the flow field that was equal to the pre-heated air temperature, indicating that thermal feedback was negligible for ignition. Therefore, the lower ignition limit was the

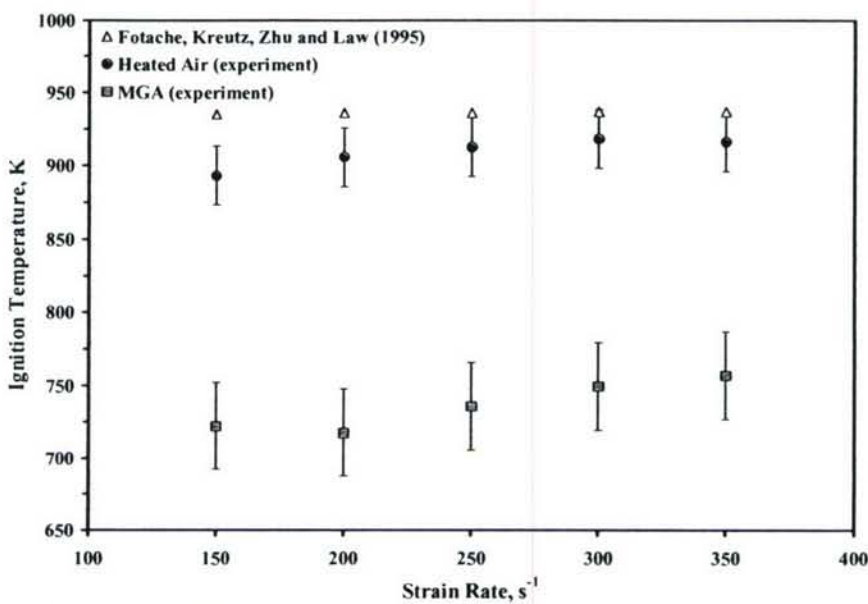


**Fig. 47** Comparison of experimental measurements of ignition temperatures with 20% H<sub>2</sub> in N<sub>2</sub> versus air for pre-heated air and MGA (at 140 mA) from  $\alpha = 150 - 350 \text{ s}^{-1}$

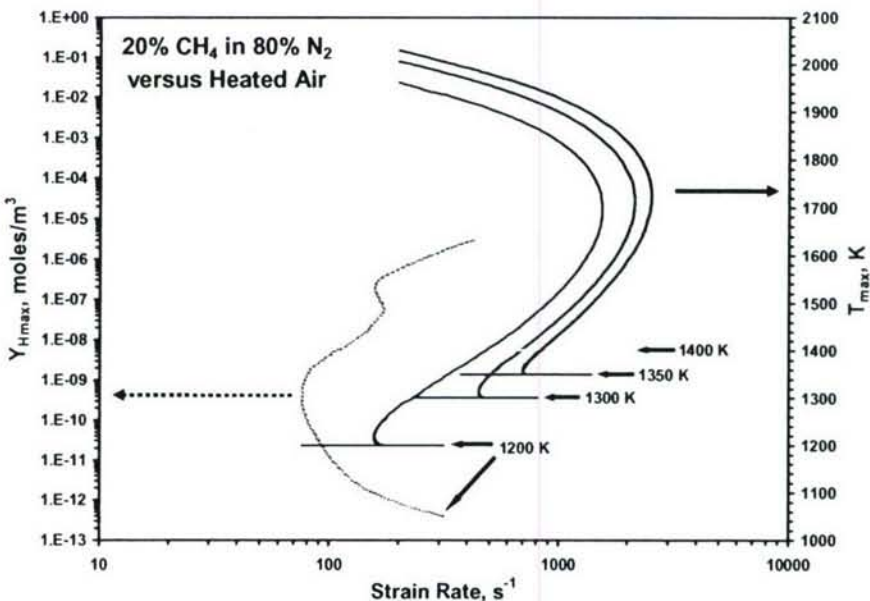


**Fig. 48** S-curve response for 20% CH<sub>4</sub> in N<sub>2</sub> versus pre-heated air as a function of maximum temperature and hydrogen concentration for various strain rates

kinetic ignition limit since thermal feedback from fuel oxidation was not required for ignition.<sup>25,28,29</sup> On the other hand, the high temperature ignition limit, with maximum temperatures well above the pre-heated air temperature, was the thermal ignition limit.

Due to the difficulty in observing the kinetic ignition limit in the temperature coordinate, the maximum hydrogen radical concentration curve is shown as an analogous curve for the 1200 K case in Fig. 48. At the ignition limit, the concentration of hydrogen radicals and maximum temperature have local extrema at the same strain rate.

### 3.11.2 Kinetic Ignition Enhancement by MGA and Ignition Diagram

The MGA produced radicals, ions, electrons and excited species. Since the plasma was located more than four centimeters upstream of the reaction zone, no electrons would be present in the reaction zone. Furthermore, for a first order approximation, it was assumed that the ions and excited species were negligible. The MGA activated dry air, so the species present only contained nitrogen and oxygen. The species included O as well as NO<sub>x</sub>. Therefore only O and NO<sub>x</sub> were used as boundary inputs to the air side of the counterflow code and the S-curve responses were computed. Up to a 1,000 parts per million (ppm) of O input at the air side boundary yielded negligible enhancement, even when combined with NO<sub>x</sub> addition, because of the rapid recombination during transport between the nozzle exit and reaction zone. Since 1000 ppm of O was well above what was expected at the exit of the nozzle, the effect of O was negligible.

NO<sub>x</sub> produced by plasma is stable and has catalytic effects on radical production.<sup>26,27,30</sup> In the past work by Tan, Fotache, and Law,<sup>26</sup> NO addition on the order of 10,000 ppm would yield the greatest enhancement, with little additional enhancement at higher NO concentrations. The S-curve responses were calculated for 100, 1000, 10,000, 50,000 and 100,000 ppm. The curves for 10,000 ppm of NO addition are shown in Fig. 49.

For lower strain rates at low air temperatures, there were two ignition and two extinction limits on the S-curves; however, for temperatures higher than 1025 K, the curves only had a single ignition and extinction limit. The transition to only one ignition limit could be explained by the

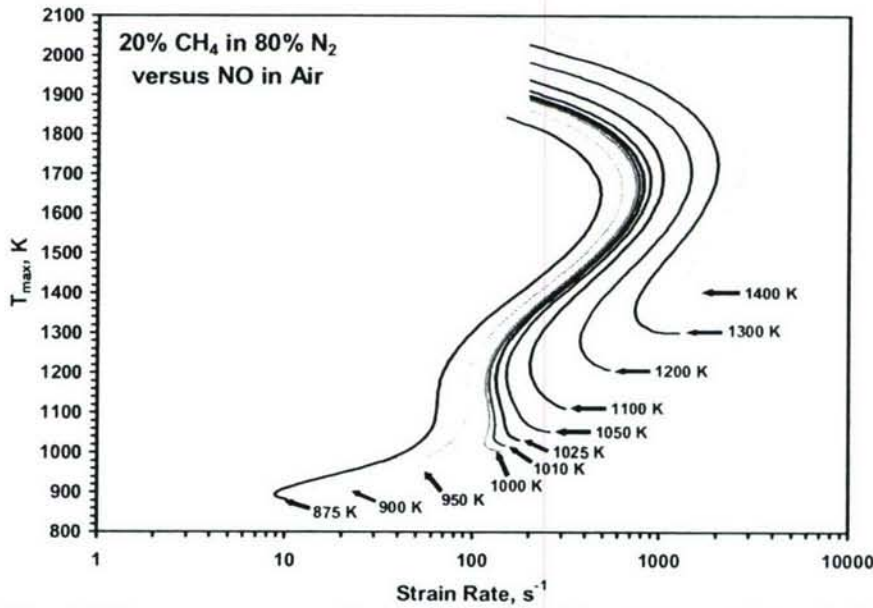


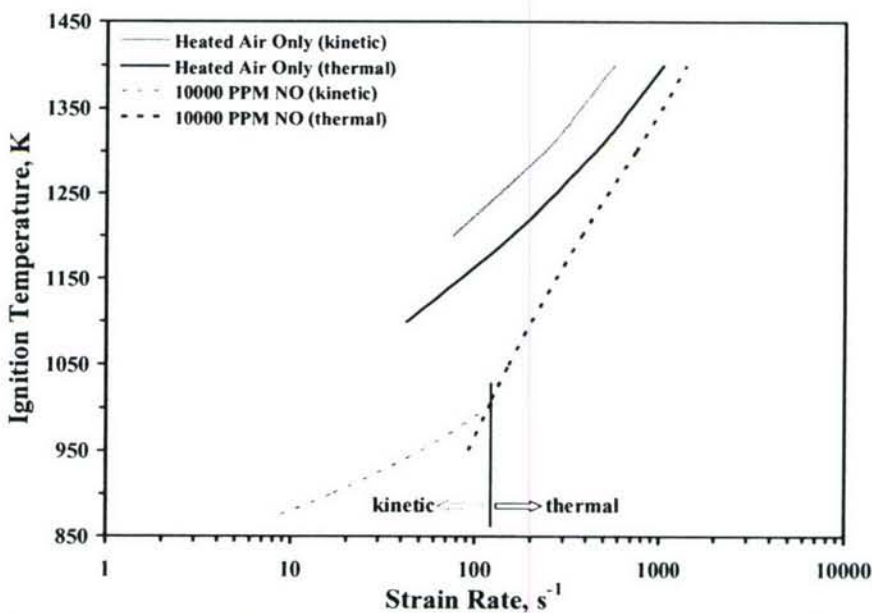
**Fig. 49** S-curve response for 20% CH<sub>4</sub> in N<sub>2</sub> versus pre-heated air with 10,000 ppm NO as a function of maximum temperature for various strain rates

competition between the catalytic  $\text{NO}_x$  effect and thermal feedback. At lower strain rates the ignition temperatures (air temperatures) were low. At low temperatures, the catalytic effects of NO contributed significantly to the build-up of radicals to allow for ignition before significant heat release. On the S-curves of Fig. 49 below 1025 K, the lower strain rate ignition occurred at the same temperature of the pre-heated air. This result demonstrated that heat release from fuel oxidation was not important and that the ignition was enhanced kinetically by the  $\text{NO}_x$  catalytic effect.

The S-curves in Fig. 49 that were at higher strain rates and temperatures above 1025 K only had one ignition limit at a maximum temperature much higher than the air temperature. This result was explained by realizing that higher ignition temperatures were needed at higher strain rates (due to heat and radical losses). The NO continued to enhance ignition but was not the dominant pathway. The NO catalytic effect allowed for the production of radicals and provided some heat release, but overall it was not enough

to allow for complete reaction and ignition. Moreover, at high temperatures, the  $\text{NO}_x$  catalytic effect decreased. Therefore, there needed to be heat release and thermal feedback for ignition to occur. Figure 50 provides an ignition diagram for the two different regimes of ignition enhancement by NO. For the 10000 ppm NO ignition curves there was a clear difference in the dependence of ignition temperature on the strain rate. For lower strain rates, the NO addition provided a sufficient amount radical production to ignite the flame. This ignition regime was the kinetic ignition enhancement regime. At higher strain rates, ignition required the aid of heat release and thermal feedback to occur. This was the thermal ignition regime. Figure 50 is a diagram showing these two ignition regimes.

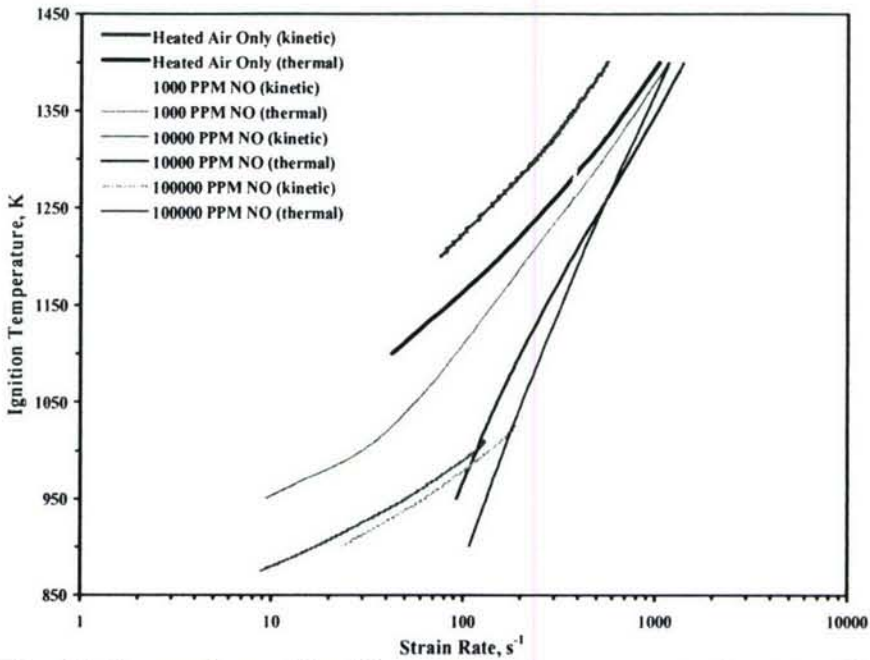
To provide a better comparison between ignition with and without the MGA plasma discharge, a plot of the ignition temperatures versus strain rate for different levels NO addition is shown in Fig. 51. The figure shows that there was significant ignition enhancement at up to 10,000 ppm of NO addition but decreased enhancement for larger amounts of NO addition. The decreased enhancement with larger NO addition qualitatively matched the trends of past work on NO enhancement with an optimal amount of NO addition.<sup>26,27</sup>



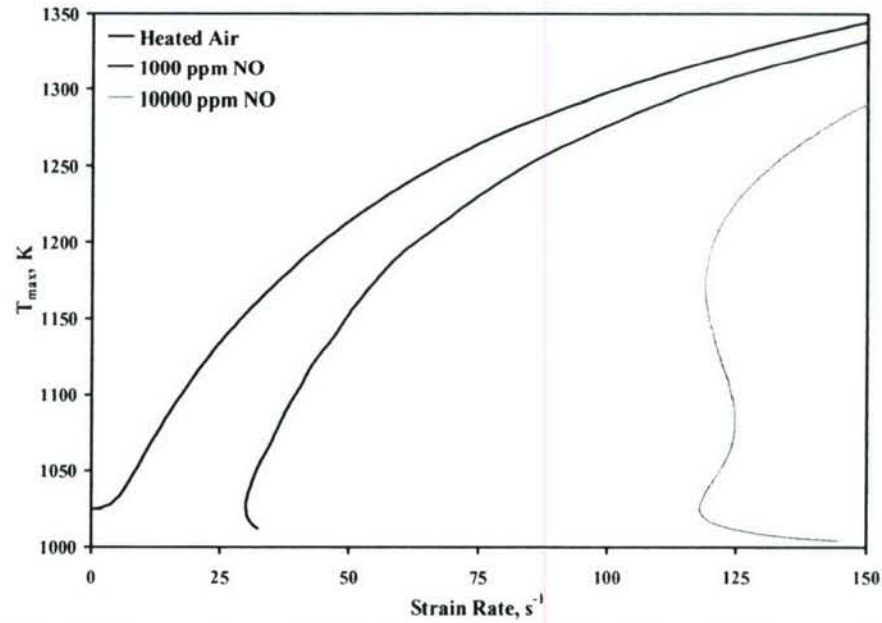
**Fig. 50** Kinetic versus thermal regimes of ignition extracted from S-curve responses for 20%  $\text{CH}_4$  in  $\text{N}_2$  versus pre-heated air with and without 10,000 ppm NO

Figure 51 shows the interesting phenomenon where the curves for 10,000 ppm NO and 100,000 ppm NO addition crossed. The crossover of the two curves implied that the addition of more NO beyond 10,000 ppm yielded little additional ignition enhancement and led to less enhancement at strain rates above 5000 s<sup>-1</sup>. There was an optimal amount of NO addition to enhance ignition depending upon the strain rate. Therefore either cold non-equilibrium plasma or pure thermal plasma alone may not be the best choice to enhance ignition. Furthermore, NO addition allowed for ignition at much lower air temperatures and even ignition where it was not possible with ignition by pre-heated air alone. The ignition at lower air temperatures with the plasma indicated clearly that plasma produces non-thermal ignition.

The ability of NO production to ignite the mixture at even higher strain rates is apparent in Fig. 52 which shows the ignition limits for the same boundary temperature of 1000 K. The pre-heated air was not capable of igniting the flame, but NO addition allowed for ignition at strain rates over 120 s<sup>-1</sup>.



**Fig. 51** Comparison of ignition temperature versus strain rate with and without NO addition showing multiple ignition points at the same temperature



**Fig. 52** Comparison of NO enhancement of ignition at higher strain rates than pre-heated air ignition for the same boundary temperature of 1000 K.

### 3.12 Sensitivity Analysis and NO<sub>x</sub> Catalytic Path

Sensitivity analysis was performed to examine the differences observed in the response curves and identify the key reactions of the kinetic-versus-thermal regimes of ignition, as well as the high temperature/high strain rate crossing point of the 100,000 ppm NO addition curve of Fig. 51. The sensitivity coefficient was defined as

$$\text{sensitivity coefficient} = \frac{\partial \ln(a_{ignition})}{\partial \ln(\omega_i)} \quad (5)$$

where  $a_{ignition}$  was the strain rate at ignition and  $\omega_i$  was the reaction rate of the  $i^{\text{th}}$  reaction. A positive sensitivity coefficient meant that increasing the reaction rate accelerated ignition.

The results of the sensitivity analysis for the heated air only and for 10,000 ppm of NO addition both at an air temperature of 1200 K, are shown in Fig. 53. For the pre-heated air only case, the most important reactions were identified correctly as those previously reported by Liu and Law.<sup>25</sup> The reactions are related to the oxidation of CH<sub>3</sub> radicals; however, NO<sub>x</sub> addition significantly changed the reaction paths. There were two reactions that became very important when NO was added

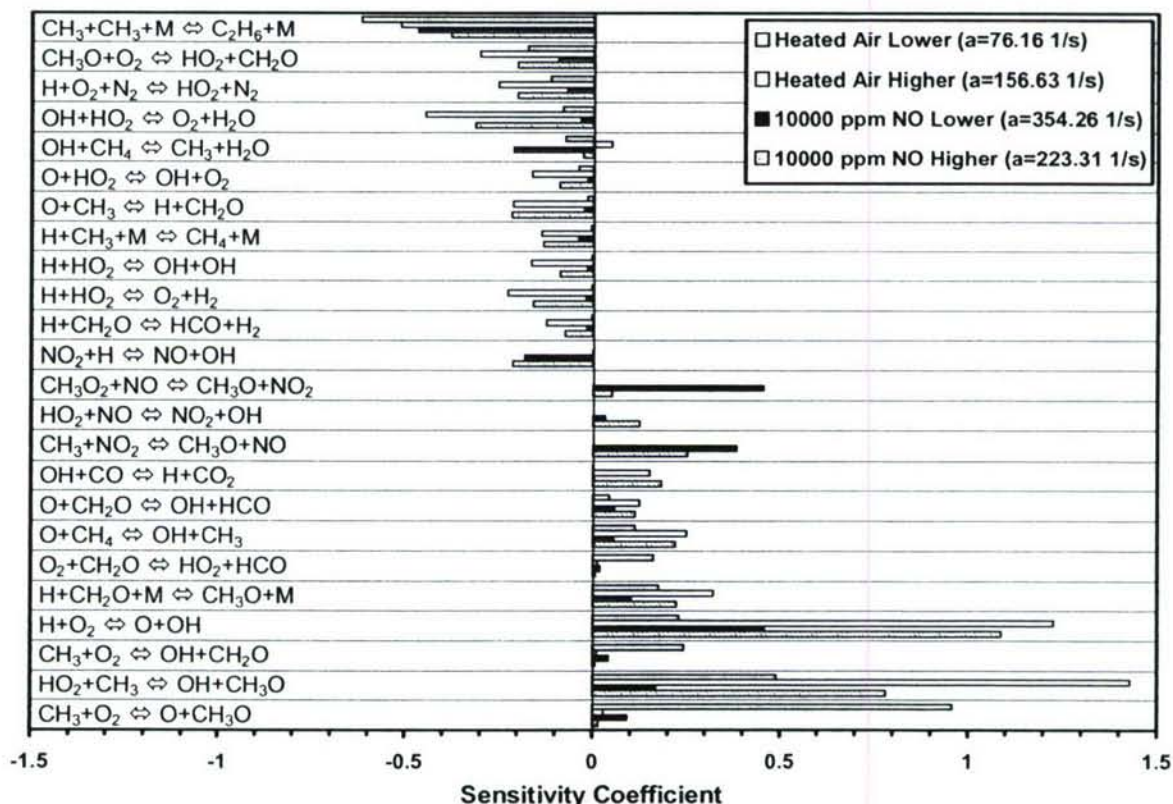


**Fig. 53** Comparison of S-curve sensitivity results at ignition for 20% CH<sub>4</sub> in N<sub>2</sub> versus air for pre-heated air and 10000 ppm NO at 1200 K



These reactions competed with, but dominated over, the two methyl radical reactions that were important for the pre-heated air case:



The present results followed what was expected, since (R1) and (R2) were the two key reactions that led to NO catalytic enhancement for methane ignition. Comparison of the lower and higher ignition limits for pre-heated air and 10,000 ppm of NO addition, (R1) and (R2) did not play as critical of a role at higher temperatures, where heat release and thermal feedback was needed. The results also followed the trends discussed previously in this report. At higher temperatures for both heated air and 10,000 ppm of NO addition, the active radicals O, H, and OH reacted more readily with CH<sub>3</sub> and HO<sub>2</sub>. The reactions negatively affected ignition because they were removing very active radicals from the system; therefore, an ideal plasma would need to produce both a kinetic effect and a thermal effect in order to enhance ignition at both low and high strain rates.

To understand why too much NO addition began to inhibit ignition, sensitivity analysis was performed at the ignition limits at 1400 K for 10,000 ppm of NO and 100,000 ppm of NO addition. The strain rate for ignition at 100,000 ppm of NO was lower than that for 10,000 ppm of NO addition. Sensitivity analysis showed that three reactions gained significant importance for ignition when increasing from 10,000 to 100,000 ppm of NO. They were



and reaction (R2). Reaction (R5) consumed NO<sub>2</sub>, which was needed for the conversion of CH<sub>3</sub> to CH<sub>3</sub>O via reaction (R2) and H for the chain branching reaction with O<sub>2</sub>. Reaction (R6) was a three-body chain termination reaction, effectively consuming the active O radical and somewhat active NO. Overall, these reactions combined to give the reaction of H + O  $\rightleftharpoons$  OH; therefore, even though there was an order-of-magnitude increase in NO addition, there was less ignition enhancement because two active radicals reacted to form one.

Lastly, sensitivity analysis was performed to confirm the differences between ignition at low and high temperatures with NO addition and to understand the important reactions. The results are shown in Fig. 54. The addition of NO (10,000 ppm) at 1400 K first was compared with pre-heated air only. Pre-heated air ignition at 1400 K was heavily reliant upon the reaction



with other reactions being of much less importance. With 10,000 ppm of NO addition at 1400 K, the emergence of many more reactions with significant importance arose. The dominant pathway

of heated air only, reaction (R7), became negligible because CH<sub>3</sub> had other oxidation pathways to produce CH<sub>3</sub>O.

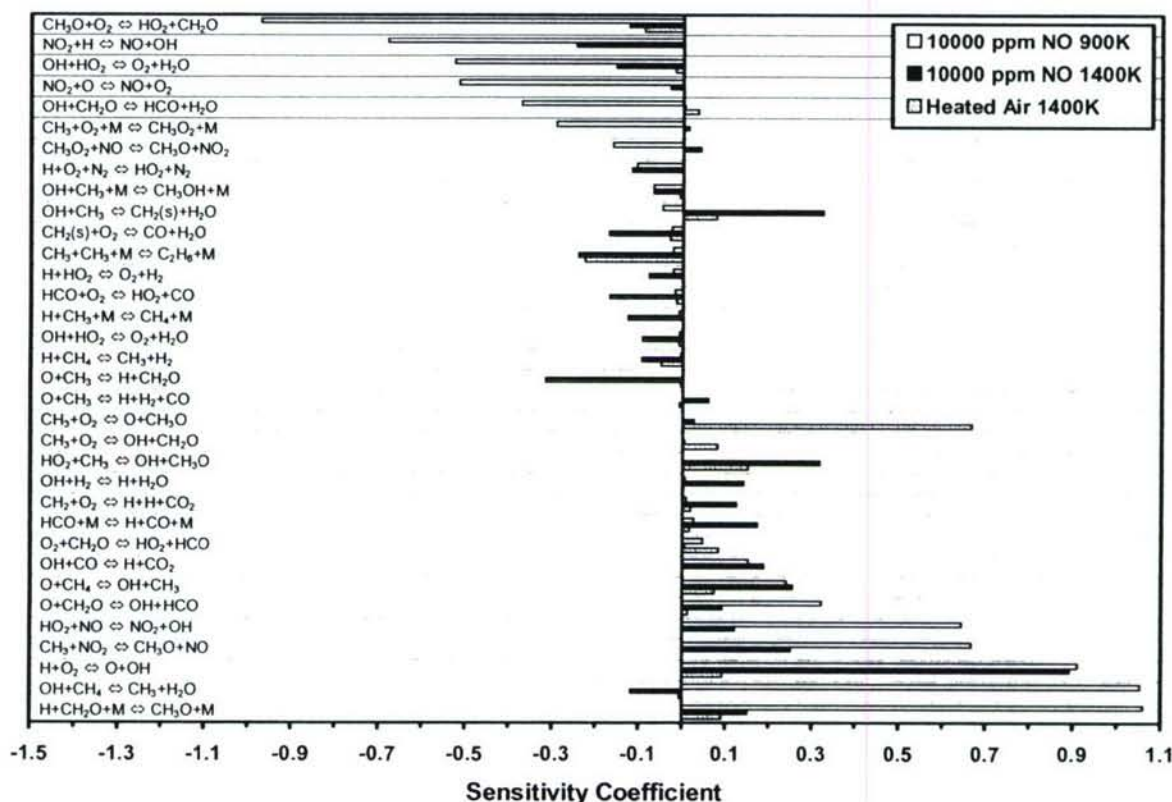


**Fig. 54** Comparison of S-curve sensitivity results at ignition for 20% CH<sub>4</sub> in N<sub>2</sub> versus air for pre-heated air and 10000 ppm NO at 900 K and 1400 K

One of the most important comparisons made in Fig. 54 was between 10,000 ppm of NO addition at 900 K and 1400 K. At low ignition temperatures (900 K) the reactions with NO were some of the most important reactions. At higher ignition temperatures (1400 K) with the same amount of NO addition, the NO reactions became significantly less important, while reactions with species such as CH<sub>3</sub> and HO<sub>2</sub>, which were far less important at lower temperatures, now were equally, if not more, important to the ignition process than the NO reactions. The different reaction pathways for ignition clearly showed that NO did not play as critical of a role in the ignition process at higher temperatures; therefore, NO continued to have an enhancing effect on the ignition process for a wide range of temperatures but became far less important with increasing temperature. These results confirmed what was discussed previously for the analysis of the S-curve responses by showing clearly the distinction between the kinetic feedback/domination for lower strain/temperature ignition versus the thermal feedback/domination for higher strain/temperature ignition.

### 3.13 Comparison of Experimental and Computational Results

Lastly, since the computations followed expected trends, an explanation of the non-thermal ignition enhancement that was observed clearly in the experiments was sought. The computational ignition results with pre-heated air were shown in Fig. 48. The computational

results were used as a direct comparison to the pre-heated air only experiments. The pre-heated air curves of ignition temperature versus strain rate were obtained and are superimposed on the experimental results (Fig. 55). There was good agreement between the experiment and computational simulations for the pre-heated air. The agreement confirmed that the computations were valid and could be used to explain the MGA enhancement.

To mimic the MGA, a concentration of NO from preliminary calculations was used. Since the MGA was rotating at a frequency much higher than the characteristic time of flow through the thickness of the arc, a quasi-steady assumption allowed the MGA to be simplified as a uniform plasma disk, as shown in Fig. 2. Measurements were taken of the MGA as a basis to compute the reduced electric field,  $E/n$ , and electron temperature (Section 2). Recombination in the nozzle between the MGA and the exit of the nozzle was taken into account to give the concentration of NO at the nozzle exit, as previously described in sections 2.8 and 2.9. The average calculated concentration of NO was approximately 4000 ppm of  $\text{NO}_x$  and was used as an input to the counterflow non-premixed flame ignition code to find the ignition temperatures and strain rates.

To confirm the concentrations of NO experimentally, measurements were taken at the exit of the lower nozzle at the same conditions that the ignition results were obtained. A chemiluminescent  $\text{NO}_x$  analyzer (California Analytical Instruments, Model 300-CLD) was calibrated and used to measure the concentrations of  $\text{NO}_x$  at the nozzle exit. The measured concentrations averaged around 6000 ppm of  $\text{NO}_x$ . The measured results were higher than those obtained by the simulations but of the same order of magnitude. The highest concentration of  $\text{NO}_x$  was chosen as the input to the computational simulations and is shown superimposed on Fig. 55.

The curve from the numerical computations with NO addition under-predicted the experimental data. The under-prediction suggested that there were additional mechanisms from plasma produced species to enhance ignition.

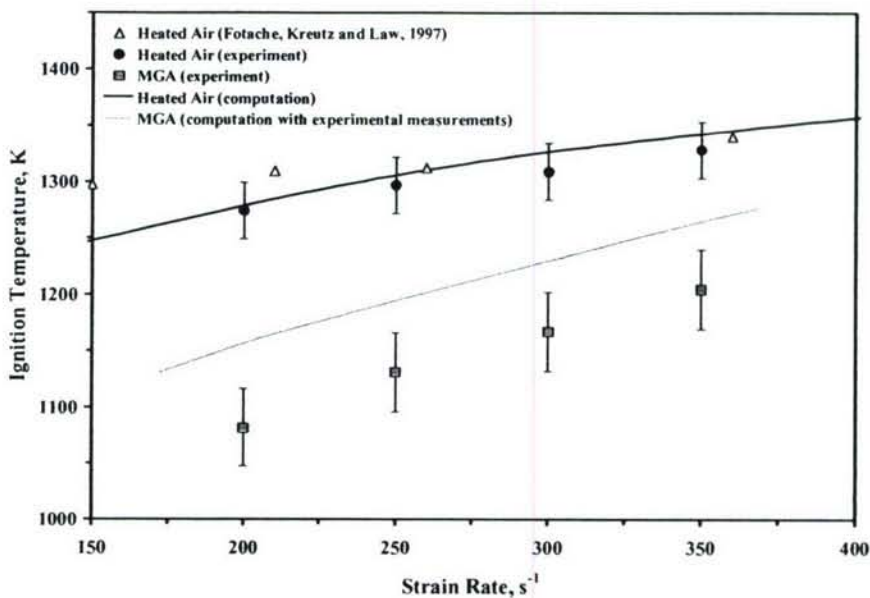
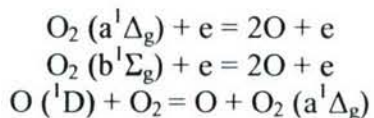


**Fig. 55** Comparison of experimental and computational results of ignition temperatures with 20%  $\text{CH}_4$  in  $\text{N}_2$  versus air for heated air and MGA (at 350 mA for experiment and preliminary NO calculations for computation) from  $a = 200 - 350 \text{ s}^{-1}$

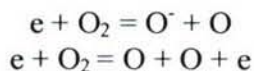
### 3.14 Additional Non-Thermal Enhancing Mechanisms from MGA

### 3.14.1 Ignition Enhancement via Ions, Excited Species and Electron-Molecule Collisions

A possible non-thermal enhancing effect comes in the form of ions and excited species that were produced in the non-equilibrium MGA plasma discharge. It has been shown that high energy electrons produced via a plasma discharge have the ability to make electronically and vibrationally excited molecules.<sup>31</sup> For plasma activation of air, as in the MGA, electronically excited species, such as singlet oxygen,  $O_2(a^1\Delta_g)$ ,  $O_2(b^1\Sigma_g)$ , and  $O(^1D)$ , can be produced. These excited species can play important roles in producing chemically active radicals,



and are expected to affect the ignition time of hydrocarbon fuels. In particular, the excited species of major interest was  $O_2(a^1\Delta_g)$  because of its low energy potential of 0.98 eV, large population and long lifetime (3000 s). Furthermore, vibrationally excited molecules, such as  $O_2(v)$  and  $N_2(v)$ , and the electron impact dissociation reactions such as



can be important in the plasma ignition process. These avenues currently are being sought to obtain a better understanding of non-equilibrium MGA plasma discharge ignition enhancement that cannot be explained fully by radical addition only.

### 3.14.2 Effect of Plasma Produced Hydrocarbon Fragments on the Reduction of Minimum Ignition Energies

In addition to the ignition enhancement from the excited species, the transport property change via the formation of hydrocarbon fragments by a plasma discharge also may affect the ignition energy. When external energy (whether by elevated temperatures, radicals, or other species) was deposited locally into a combustible mixture, there were several possible outcomes: a.) successful ignition kernel evolution to a large flame; b.) extinction of the ignition kernel; and c.) a self-extinguishing outward propagating flame. The successful transition from an ignition kernel to a propagating flame was strongly dependent on the transport properties of the fuel-air mixture (Lewis number) and the radiation heat loss from the hot ignition kernel (by the plasma discharge). The question was how did the fuel properties affect the minimum ignition energy? In other words, did the fragment formation via the plasma discharge help in reducing minimum ignition energy? If it did, how large was the magnitude? The following analysis answered these questions.

To understand the effect of hydrocarbon fragments on the ignition of a combustible mixture, unsteady ignition kernel formation by external energy deposition in a homogeneous mixture was

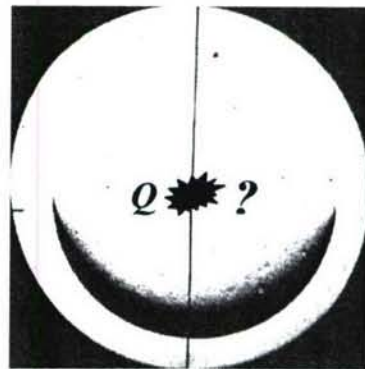


**Fig. 56** Ignition kernel formation in a homogeneous premixture

considered (see Fig. 56). To understand the dynamic flame kernel evolution process, we used the conventional constant density and constant transport property model.<sup>32</sup> By further assuming a spherically symmetric quasi-steady flame structure and using the radial coordinate,  $r$ , moving with the flame front, the governing equations for temperature,  $T$ , and fuel mass fraction,  $Y$ , the governing conservation equations of energy and species were simplified to

$$-U \frac{dT}{dr} = \frac{1}{r^2} \frac{d}{dr} (r^2 \frac{dT}{dr}) - h \cdot T + \omega \quad (6a)$$

$$-U \frac{dY}{dr} = \frac{Le^{-1}}{r^2} \frac{d}{dr} (r^2 \frac{dY}{dr}) - \omega \quad (6b)$$

in which  $U$  was the eigenvalue of flame speed and  $\omega$  the reaction rate. In addition, the radiation heat loss term,  $H$ , was approximated by a linear function of normalized temperature as  $H = h \cdot T$  where  $h$  was the heat loss constant, which took the following form

$$h = \frac{4\tilde{\sigma}\tilde{K}_p\tilde{\delta}_f^0(\tilde{T}^4 - \tilde{T}_\infty^4)}{\tilde{\rho}\tilde{C}_P\tilde{S}_L^0(\tilde{T} - \tilde{T}_\infty)} \approx \frac{4\tilde{\sigma}\tilde{K}_p\tilde{\lambda}}{(\tilde{\rho}\tilde{C}_P\tilde{S}_L^0)^2} \tilde{T}_{ad}^3 \quad (7)$$

$\tilde{\sigma}$  was the Stefan-Boltzmann constant,  $\tilde{K}_p$  the Planck mean absorption coefficient of the combustible mixture,  $\tilde{\delta}_f^0 = \tilde{\lambda} / \tilde{\rho}\tilde{C}_P\tilde{S}_L^0$  the flame thickness,  $\tilde{T}$  the temperature,  $\tilde{\rho}$  the density,  $\tilde{C}_P$  the specific heat capacity at constant pressure,  $\tilde{S}_L^0$  the adiabatic planar flame speed, and  $\tilde{\lambda}$  the thermal conductivity. Each specific mixture would have constant transport properties and therefore a constant Lewis number. The radiation heat loss constant involved the radiation intensity and the fuel concentrations in the system. For example, as the fuel concentration decreased (i.e. lean), the flame speed decreased, hence,  $h$  increased. The fuel concentration, flame speed, and  $h$  relationship was also true for rich mixtures, yielding a local minimum of the radiative heat loss constant at an equivalence ratio of 1. Furthermore,  $h$  was calculated for methane-air flames and yielded a range from 0.001 to 0.1.

The external energy addition,  $M$ , was modeled by continuous energy addition in the center of the ignition kernel, which was written as a boundary condition,

$$r = 0, \quad r^2 \partial T / \partial r = -M, \quad Y = 0 \quad (8)$$

The Lewis number was defined as the ratio of the thermal diffusivity to the fuel diffusion coefficient estimated from the binary diffusion model of the mixture as in the equation

$$Le = \frac{\lambda / \rho C_p}{D_i} \quad (9)$$

where  $D_i$  defined as the diffusivity of the  $i^{\text{th}}$  constituent. For example, for a lean methane-air mixture ( $\phi < 1$ ), the Lewis number was less than one. The equivalence ratio and Lewis number relationship was based on the observation that the thermal diffusivity was relatively constant, whereas the diffusion coefficient changed depending upon the minor combustion constituent in the system. For lean methane, the diffusion coefficient was less than that of the major combustion constituent,  $O_2$ . The method also applied to all systems such as larger hydrocarbon fuel molecules, with  $D_i$ 's that were larger than the other combustion constituent,  $O_2$ .

By using asymptotic analysis, the flame speed equation for an ignition kernel growth was obtained as

$$\Omega \cdot T_f + \Omega_Q \cdot M = \frac{1}{Le} R^{-2} e^{-ULeR} / \int_R^\infty \tau^{-2} e^{-ULe\tau} d\tau = \exp \left[ \frac{Z}{2} \frac{T_f - 1}{\sigma + (1-\sigma)T_f} \right] \quad (10)$$

where  $\Omega$  was given by

$$\Omega_M = \begin{cases} -R^{-2} e^{-UR} & \text{if } h_1 = 0 \\ k_1 e^{-0.5(U+k_1)R} \left[ -C_1 \cdot G(-k_1 R, 1 + \frac{U}{k_1}, -\frac{U}{k_1}) + C_2 \cdot F(k_1 R, 1 + \frac{U}{k_1}, -\frac{U}{k_1}) \right] & \text{if } h_1 \neq 0 \end{cases} \quad (11)$$

where  $F$  and  $G$  were two analytic functions.<sup>32</sup> The effects of ignition power and Lewis number on flame transition were studied by solving the analytical equation (10) numerically.

The dependence of minimum ignition energy on the Lewis number is shown in Fig. 57.<sup>32</sup> For both the adiabatic ( $h = 0$ ) and non-adiabatic ( $h = 0.01$ ) cases, the critical ignition power increased with increasing Lewis number, but the change was much more drastic for the non-adiabatic, more realistic case. Three regimes of the non-adiabatic curve were defined in the following manner. There was a linear region for small Lewis numbers ( $Le < 1$ ), a nonlinear region for intermediate Lewis numbers ( $1 < Le < 1.6$ ) and a linear region for large Lewis numbers ( $Le > 1.6$ ). The appearance of the nonlinear region was due to the coupling of the radiation heat loss from the unburned region and the Lewis number effect, showing that the radiation heat loss from the unburned gas region affected the ignition energy significantly. If larger hydrocarbon fuel

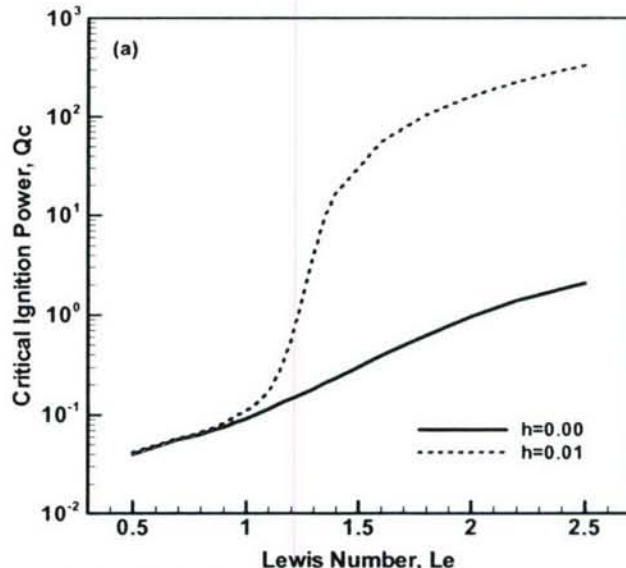


**Fig. 57** Critical ignition power with respect to Lewis number for adiabatic and non-adiabatic cases<sup>32</sup>

molecules were broken down into smaller hydrocarbon fragments, the Lewis number was decreased and a lower ignition power was required. The same methodology was applied to plasma ignition in Fig. 58 and was a possible explanation to why the ignition temperatures using the MGA activation of the air stream yielded temperatures that were lower than those from the plasma radicals.

The Lewis number effect became a major factor affecting the minimum ignition energies of a combustible mixture. Consider a system with a large hydrocarbon fuel species, such as n-heptane or iso-octane. The fuels have diffusion coefficients that are much larger than  $O_2$ . The differences in the diffusion coefficients would, in a lean system, yield a Lewis number that was much larger than one. When energy is added to the system, the large fuel species break up into hydrocarbon fragments with much lower Lewis numbers.

### 3.14.3 Numerical Modeling of the Electric Field Effect on Premixed Flames

The understanding of the electric field/premixed flame interaction was crucial for studying the effects of non-equilibrium plasma enhancement. Numerical simulations were performed to study the effect of a microwave discharge on a premixed methane-air flame. The work was done by the PI and collaborators<sup>33</sup> using modified detailed oxidization and chemionization mechanisms. A simplified numerical algorithm was developed for the microwave-flame interaction to simulate the impact of electric fields on freely propagating one-dimensional premixed flames. The microwave discharge was used in this case to produce an electric field because of its simplicity

Figure 59 shows the comparison of the predicted electron number density with the experimental data of ion number density measured by MacLatchy et al.<sup>34</sup> using a Langmuir probe for a stoichiometric premixed methane-air Bunsen flame. The measured peak ion number density was between  $3.5 \times 10^{11}$  and  $3.75 \times 10^{11}$  per  $cm^3$ . The half peak width was between 0.6 and 0.7 mm. The predicted maximum electron number density was  $3.85 \times 10^{11} cm^{-3}$  and the half peak value was 0.53 mm,

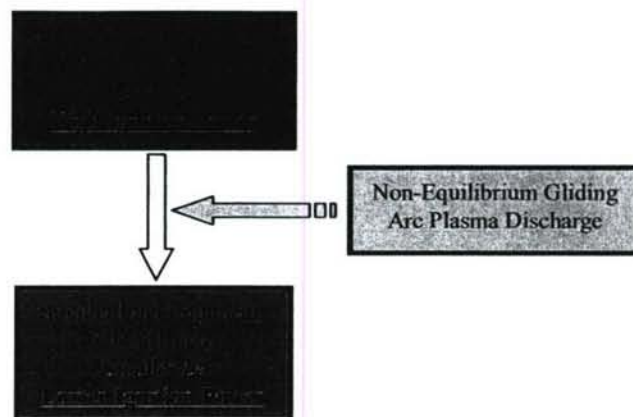


**Fig. 58** Flow chart of Lewis number effects on plasma assisted ignition systems

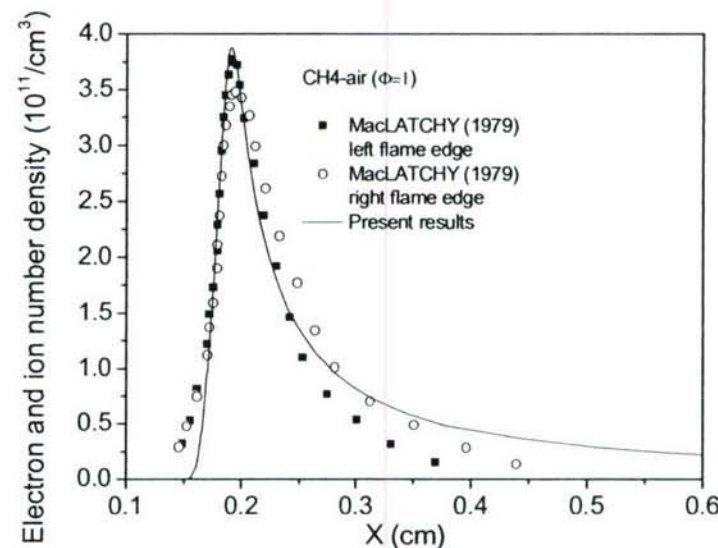


**Fig. 59** Comparison of predicted electron number density with experimental data of MacLatchy (1979) for a stoichiometric CH<sub>4</sub>-air flame

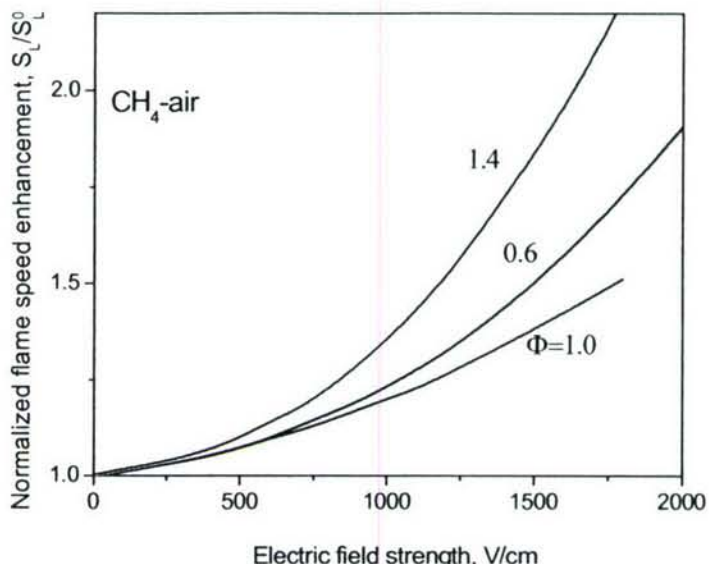
which agreed well with the experimental data.

Figure 60 shows the non-dimensional enhancement of the flame speed at equivalence ratios of 0.6, 1.0, and 1.4, respectively. The breakdown field strength was about 2,000 V/cm. The flame speed was increased significantly with increasing electric field strength. In particular, near the breakdown field strength, the flame speed could be increased by 50% to 100%; however, with a field strength below the plasma sustaining limit (900 V/cm), the maximum increase in the flame speed was less than 25%. Figure 60 shows that the combustion enhancement for lean flames was more significant than for the stoichiometric flame. For example, at an equivalence ratio of 0.6, the flame speed increase at 900 V/cm was about 19%. The result was consistent with the results reported by Clements et al.<sup>35</sup> in which the flame speed enhancement for very lean ethylene flames before breakdown was 20%. In their experiments the flame speed enhancement decreased with an increase in equivalence ratio. The present results also supported this conclusion. Moreover, the results also demonstrated that the flame speed was enhanced significantly in rich conditions because of the existence of the high electron number density.

To examine the effect of flame structure on flame speed enhancement, the distribution of the accumulated fraction of the electron heating compared to the total chemical heat release

$$\frac{q_{0-x}}{q_{rt}} = \frac{\int_0^x \dot{q}_e dx}{\int_0^\infty \dot{q}_r dx} \quad (12)$$

is shown in Fig. 61 for an equivalence ratio of 1.0 and electric field strength  $E = 900$  V/cm. At the flame downstream location  $x = 0.8$  cm, the accumulated fraction of electron heating was 16% of the



**Fig. 60** Enhancement of flame speed at the equivalence ratios of 0.6, 1.0, and 1.4

For example, at an equivalence ratio of 0.6, the flame speed increase at 900 V/cm was about 19%. The result was consistent with the results reported by Clements et al.<sup>35</sup> in which the flame speed enhancement for very lean ethylene flames before breakdown was 20%. In their experiments the flame speed enhancement decreased with an increase in equivalence ratio. The present results also supported this conclusion. Moreover, the results also demonstrated that the flame speed was enhanced significantly in rich conditions because of the existence of the high electron number density.

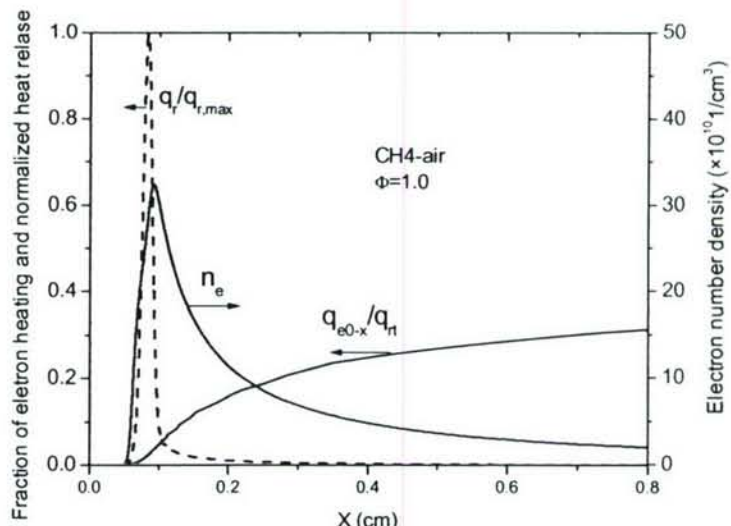


**Fig. 61** Distribution of the accumulated fraction of electron heating and electron number density at  $E=900$  V/cm

total chemical heat release. However, the energy absorbed before the end of the reaction zone at  $x = 0.15$  cm was less than 5% of the total chemical heat release, which meant that less than 30% of the microwave energy was added directly to raise the flame temperature and speed. The rest of the microwave energy only heated the burned gas. Although the temperature increase in the burned gas also indirectly increased the flame speed through conductive heat transfer, it was much less efficient than the direct heating effect.

Numerical simulations for lean mixtures indicated that due to flame thickening, the total energy absorbed in the flame pre-heating zone increased. This result explained why the microwave enhancement was better in lean and rich conditions.

Although the predicted results qualitatively agreed with the experiments, the measured velocity increase was much larger than the predicted results. In order to understand the mechanism, detailed measurements of the flow fields, including chemionization via CH reaction, temperature, and species concentrations, in laminar flames were necessary.

#### 4.0 Summary

The effects of non-equilibrium plasma on both partially premixed and non-premixed flames were investigated through the development of a new lifted flame burner and counterflow flame burner integrated with the MGA system.

The characteristics of the near-extinction gliding arc were investigated. The results showed that the MGA was non-equilibrium, with a rotational temperature of approximately 2000 K and an electron temperature of several electron volts in the cathode spot and more than one electron volt in the plasma column. A two-temperature numerical model with a detailed air plasma kinetic mechanism was developed for predicting the production of radicals and NO<sub>x</sub>. A correlation between plasma characteristics and the production of atomic oxygen and NO was obtained.

The MGA plasma system was integrated with three different combustion systems: a lifted jet diffusion flame burner, a counterflow extinction burner, and a counterflow ignition burner with pre-heated air. The experiments of the lifted jet diffusion flames with the MGA plasma discharge in the air co-flow showed a significant enhancement of flame stabilization. The counterflow system provided an excellent platform for the study of plasma-flame interactions and for the validation of kinetic models. The results showed that the MGA discharge in air led to dramatic extensions of the extinction limits. Laser diagnostic measurements of flame temperature and OH distribution by using planar Rayleigh scattering and planar laser induced fluorescence respectively, were made, and the results were compared with numerical simulations. The results showed that the plasma-flame interaction at low air temperature was predominately thermal due to rapid radical quenching.

The counterflow ignition experiments for methane, hydrogen, and air mixtures demonstrated that the MGA significantly decreased the ignition temperatures via kinetic enhancement. Measurements and modeling of the plasma-produced species, such as O and NO<sub>x</sub> were conducted systematically.

It was demonstrated clearly that the NO<sub>x</sub> catalytic path to convert HO<sub>2</sub> to OH and CH<sub>3</sub> to CH<sub>3</sub>O at low temperature played a dominant role to enhance ignition. Numerical modeling showed that

there were two ignition regimes, kinetic ignition and thermal ignition, for plasma-enhanced ignition at low and high strain rates, respectively. The results showed that, for the kinetic ignition limit at low strain rates, the NO catalytic effect enhanced ignition without the need of heat release from fuel oxidation; however, for the thermal ignition limit, even with the NO catalytic effect, heat release from fuel oxidation was required for ignition to occur. Depending upon the characteristic strain rates in the combustible system, the temperature, hence thermal feedback, was of critical importance to the development of the plasma enhanced combustion system. In addition, the comparison between experiment and simulation showed that radicals and  $\text{NO}_x$  production from the plasma could not explain completely the large decrease in ignition temperature. These results opened up the possibility of enhancement by ions and excited species or other mechanisms, such as plasma produced hydrocarbon fragments and electric field effects.

Theoretical analysis of minimum ignition energy in a quiescent mixture showed that the production of small hydrocarbon molecules by plasma discharge could lead to a significant decrease of ignition energy from radiation and transport coupling.

## 5.0 References

- <sup>1</sup>Kuznetsova, I.V., Kalashnikov, A.F., Gutsol, A.F., Fridman, A.A., and Kennedy, L.A., "Effect of 'Overshooting' in the Transitional Regimes of the Low-Current Gliding Arc Discharge," *Journal of Applied Physics*, Vol. 92, No. 8, 15 October 2002, pp. 4231-4237.
- <sup>2</sup>White, F., *Viscous Fluid Flow*, McGraw-Hill Book Company, New York, 1974, pp. 207.
- <sup>3</sup>Laux, C.O., Spence, T.G., Kruger, C.H. and Zare, R.N., "Optical Diagnostics of Atmospheric Pressure Air Plasmas," *Plasma Sources Science & Technology*, Vol. 12, No. 2, May 2003, pp. 125-138.
- <sup>4</sup>Pellerin, S., Cormier, J.M., Richard, F., Musiol, K. and Chapelle, J., "A Spectroscopic Diagnostics Technique Using UV OH Band Spectrum," *Journal of Physics D: Applied Physics*, Vol. 29, No. 3, 14 March 1996, pp. 726-739.
- <sup>5</sup>Charles de, I., "UV OH Spectrum Used as a Molecular Pyrometer," *Journal of Physics D: Applied Physics*, Vol. 33, No. 14, 21 July 2000, pp. 1697-1704.
- <sup>6</sup>Dieke, G.H. and Crosswhite, H.M., "The Ultraviolet Bands of OH, Fundamental Data," *Journal of Quantum Spectroscopy and Radiation Transfer*, Vol. 2, 1961, pp. 97-199.
- <sup>7</sup>Kossitsyn, M., Gutsol, A., Fridman, A., "Generation and Diagnostics of Non-Equilibrium Plasma in Gliding Arc Discharge," *Electronic Proceedings of 16<sup>th</sup> International Symposium on Plasma Chemistry*, Taormina, Italy, ISPC-564, 22-27 June 2003.
- <sup>8</sup>Ozlem, M.Y., Saveliev A.V., Porshnev, P.I., Fridman, A., Kennedy, L.A., "Non-Equilibrium Effects in Gilding Arc discharge," *2<sup>nd</sup> International Symposium on Heat and Mass Transfer*, 1999.
- <sup>9</sup>Spectrum Analyzer, Department of Physical Electronics, Faculty of Science, Masaryk University in Brno, <http://www.physics.muni.cz/~zdenek/span/>.
- <sup>10</sup>Laux, C.O., Spence, T.G., Kruger, C.H. and Zare, R.N., "Optical Diagnostics of Atmospheric Pressure Air Plasmas," *Plasma Sources Science and Technology*, Vol. 12, 2003, pp. 125.
- <sup>11</sup>Fridman, A., Nester, S., Kennedy, L.A., Saveliev, A. and Yardimci, O.M., "Gliding Arc Gas Discharge," *Progress in Energy and Combustion Science*, Vol. 25, 1999, pp. 211-231.
- <sup>12</sup>BOLSIG, Boltzmann Equation Solver, [www.kinema.com](http://www.kinema.com).

- <sup>13</sup>Fridman, A. and Kennedy, L.A., "Plasma Physics and Engineering," Taylor & Francis Books, 2004.
- <sup>14</sup>Becker K.H., Kogelschatz, U., Schoenbach, K.H. and Barker, R.J., "Non-Equilibrium Air Plasmas at Atmospheric Pressure," *IOP publishing*, 2005.
- <sup>15</sup>Puri, I.K. and Seshadri, K., "Extinction of Diffusion Flames Burning Diluted Methane and Diluted Propane in Diluted Air," *Combustion and Flame*, Vol. 65, No. 2, August 1986, pp. 137-150.
- <sup>16</sup>Maruta, K., Yoshida, M., Guo, H., Ju, Y., and Niioka, T., "Extinction of Low-Stretched Diffusion Flame in Microgravity," *Combustion and Flame*, Vol. 112, No. 1-2, January 1998, pp. 181-187.
- <sup>17</sup>Seiser, R., Seshadri, K., Piskernik, E., and Linan, A., "Ignition in the Viscous Layer Between Counterflowing Streams: Asymptotic Theory with Comparison to Experiments," *Combustion and Flame*, Vol. 122, No. 3, August 2000, pp. 339-349.
- <sup>18</sup>Humer, S., Seiser, R., and Seshadri, K., "Non-Premixed and Premixed Extinction and Autoignition of C<sub>2</sub>H<sub>4</sub>, C<sub>2</sub>H<sub>6</sub>, C<sub>3</sub>H<sub>6</sub>, C<sub>3</sub>H<sub>8</sub>," *Proceedings of the Combustion Institute*, Vol. 29, 2002, pp. 1597-1604.
- <sup>19</sup>Bundy, M., Hammins, A., and Lee, K.Y., "Suppression Limits of Low Strain Rate Non-Premixed Methane Flames," *Combustion and Flame*, Vol. 133, No. 3, May 2003, pp. 299-310.
- <sup>20</sup>Gaydon, A.G., *The Spectroscopy of Flames*, John Wiley & Sons Inc., New York, 1957.
- <sup>21</sup>Ju, Y., Guo, H., Maruta, K., and Liu, F., "On the Extinction Limit and Flammability Limit of Non-Adiabatic Stretched Methane-Air Premixed Flames," *Journal of Fluid Mechanics*, Vol. 342, 1997, pp. 315-334.
- <sup>22</sup>Bowman et al., GRI-Mech Homepage, Gas Research Institute, Chicago, 1994, URL: [http://www.me.berkeley.edu/gri\\_mech/](http://www.me.berkeley.edu/gri_mech/).
- <sup>23</sup>Barlow, R. S., Karpetis, A.N., Frank, J. H., and Chen, J. -Y., "Scalar Profiles and NO Formation in Laminar Opposed-Flow Partially Premixed Methane/Air Flames," *Combustion and Flame*, Vol. 127, No. 3, November 2001, pp. 2102-2118.
- <sup>24</sup>Gardiner, W.C., Jr., Hidaka, Y., and Tanzawa, T., "Refractivity of Combustion Gases," *Combustion and Flame*, Vol. 40, 1981, pp. 213-219.
- <sup>25</sup>Liu, Wei and Law, C.K., "On Multiple Criticality in Hydrocarbon Ignition," *45<sup>th</sup> AIAA Aerospace Sciences Meeting and Exhibit*, AIAA-2007-1425, Reno, Nevada, 8-11 January 2007.
- <sup>26</sup>Tan, Y., Fotache, C., and Law, C. K., "Effects of NO on the Ignition of Hydrogen and Hydrocarbons by Heated Counterflowing Air," *Combustion and Flame*, v 119, 1999, pp. 346-355.
- <sup>27</sup>Amano, T. and Dryer, F.L., "Effect of Dimethyl Ether , NOx, and Ethane on CH4 Oxidation: High Pressure, Intermediate-Temperature Experiments and Modeling," *27<sup>th</sup> International Symposium on Combustion*, Proceedings of the Combustion Institute, 1998, pp. 397-404.
- <sup>28</sup>Kreutz, T.G., Nishioka, M. and Law, C.K., "The Role of Kinetic versus Thermal Feedback in Nonpremixed Ignition of Hydrogen versus Heated Air," *Combustion and Flame*, Vol. 99, 1994, pp. 758-766.
- <sup>29</sup>Fotache, C.G., Sung, C.J., Sun, C.J. and Law, C.K., "Mild Oxidation Regimes and Multiple Criticality in Nonpremixed Hydrogen-Air Counterflow," *Combustion and Flame*, Vol. 112, 1998, pp. 457-471.

<sup>30</sup>Bromly, J.H., Barnes, F.J., Muris, S., You, X., and Haynes, B.S., "Kinetic and Thermodynamic Sensitivity Analysis of the NO-Sensitized Oxidation of Methane," *Combustion Science and Technology*, Vol. 115, 1996, pp. 259-296.

<sup>31</sup>Starikovskii, A. Yu., "Plasma supported combustion," *Proceedings of the Combustion Institute*, Vol. 30, 2005, pp. 2405-2417.

<sup>32</sup>Chen, Z. and Ju, Y., "Theoretical Analysis of the Evolution From Ignition Kernel to Flame Ball and Planar Flame," *Combustion Theory and Modeling*, Vol. 11, No. 3, June 2007, 427-453.

<sup>33</sup>Y. Ju, S. O. Macheret, M. N. Schneider and R. B. Miles, D. J. Sullivan, "Numerical study of the effect of microwave discharge on the premixed methane-air flame," 40<sup>th</sup> AIAA/ASME/SAE ASEE Joint Propulsion Conference and Exhibit. *AIAA 2004-3707*, Fort Lauderdale, Florida. 11-14 July 2004.

<sup>34</sup>MacLatchy, C. S., "Langmuir Probe Measurements of Ion Density in an Atmospheric-Pressure Air-Propane Flame," *Combustion and Flame*, Vol. 36, 1979, pp. 171-178.

<sup>35</sup>Clements, R.M., Smith, R.D., and Smy, P.R., *Combustion Science and Technology*, Vol. 26, 1981, pp. 77-81.

## 6.0 Participating Personnel

*Princeton University:*

Fully or Partially Supported by the Project: Professor Yiguang Ju, PI  
Timothy Ombrello, graduate student  
Zheng Chen, graduate student  
Xiao Qin, Research staff

*Drexel University:*

Fully or Partially Supported by the Project: Professor Alexander Fridman, co-PI  
Professor Alexander Gutsol  
Shailesh Gangoli, graduate student

## 7.0 Publications

*Peer Reviewed Journal Publications*

1. Ombrello, T., Qin, X., Ju, Y., Gutsol, A., Fridman, A. and Carter, C., "Combustion Enhancement via Stabilized Piecewise Non-Equilibrium Gliding Arc Plasma Discharge," *AIAA Journal*, Vol. 44, No. 1, 2006, pp 142-150.
2. Takita, K., Abe, N., Masuya, G. and Ju, Y., "Ignition Enhancement by Addition of NO and NO<sub>2</sub> from N<sub>2</sub>/O<sub>2</sub> Plasma Torch in Supersonic Flow," *Proceedings of the Combustion Institute*, 31<sup>st</sup> International Symposium on Combustion, Heidelberg, 2007, pp. 2489 – 2496.
3. Ju, Y., "Non-Equilibrium Plasma Assisted Combustion Enhancement for Hypersonic Propulsion," *Aerospace America*, 2005 Year in Review, 2005.

4. Fridman, A., Gutsol, A., Gangoli, S., Ju, Y. and Ombrello, T., "Characteristics of Gliding Arc and its Application in Combustion Enhancement," *Journal of Propulsion and Power*, Special Plasma Assisted Combustion Issue, in press, 2007.
5. Chen, Z. and Ju, Y., "Theoretical Analysis of the Evolution From Ignition Kernel to Flame Ball and Planar Flame," *Combustion Theory and Modeling*, Vol. 11, No. 3, June 2007, 427–453.

*Presentations at Conferences*

1. Gangoli S., Gutsol, A., Fridman, A., Ombrello, T., Qin, X., and Ju, Y., "Characterization of Magnetically Stabilized Gliding Arc for Study of Flame Ignition and Stabilization," *International Conference on Plasma Science*, Poster Presentation, June 4 – 8, 2006, Traverse City, Michigan.
2. Yiguang Ju, "Plasma Assisted Ignition and Combustion Control in Scramjet Engines," Keynote Lecture at the Annual Meeting of North Branch of Japan Society for Aeronautical and Space Sciences, March 9-11, 2006, Sendai, Japan.
3. Ombrello, T., Qin, X., Ju, Y., Gangoli, S., Gutsol, A. and Fridman, A., "Non-Equilibrium Plasma Discharge Characterization and Effect on Ignition," *44<sup>th</sup> AIAA Aerospace Sciences Meeting and Exhibit*, Reno, Nevada, 9-12 January, 2006.
4. Takita, K. and Ju, Y., "Effect of Radical Addition on Flame Extinction Limits of H<sub>2</sub>/Air and CH<sub>4</sub>/Air Mixtures," *44<sup>th</sup> AIAA Aerospace Sciences Meeting and Exhibit*, Reno, Nevada, 9-12 January, 2006.
5. Gangoli S., Gutsol A., Fridman A., "Rotating Non-Equilibrium Gliding Arc (MGA) Plasma Disc for Enhancement in Ignition and Combustion of Hydrocarbon Fuels," *17<sup>th</sup> International Symposium of Plasma Chemistry*, Toronto, Canada, 7-12 August, 2005.
6. Ombrello, T., Qin, X., Ju, Y., Carter, C., "Flammability Limit Extension of Non-Premixed Counterflow Flames Via Stabilized Non-Equilibrium Plasma Gliding Arc," *5<sup>th</sup> Asia-Pacific Conference on Combustion*, University of Adelaide, Australia, 17-20 July, 2005.
7. Gangoli S., Gutsol A., Fridman A., "Applications of Gliding Arc as a Source of Atmospheric Pressure Transitional Plasma," *32<sup>nd</sup> IEEE International Conference on Plasma Science*, Monterey, California, 20-23 June, 2005.
8. Ombrello, T., Qin, X., Ju, Y., Gutsol, A., Fridman, A., Carter, C., Extension of the Flammability Limits of Non-Premixed Counterflow Flames Via Stabilized Non-Equilibrium Plasma Gliding Arc," *4<sup>th</sup> Joint Meeting of The U.S. Sections of The Combustion Institute*, Drexel University, Philadelphia, Pennsylvania, 21-24 March, 2005.

9. Ombrello, T., Qin, X., Ju, Y., Gutsol, A., Fridman, A., Carter, C., Enhancement of Combustion and Flame Stabilization Using Stabilized Non-Equilibrium Plasma," *43<sup>rd</sup> AIAA Aerospace Sciences Meeting and Exhibit*, Reno, Nevada, 10-13 January, 2005.
10. Ju, Y., Macheret, S., Shneider, M., Miles, R., Sullivan, D., "Numerical Study of the Effect of Microwave Discharge on the Premixed Methane-Air Flame," *40<sup>th</sup> AIAA/ASME/SAE/ASEE Joint Propulsion Conference*, July 2004.

## **8.0 Interactions and Consultations**

Professor Ju and Timothy Ombrello have been in collaboration with Professor Fridman and his associates Professor Gutsol and Shailesh Gangoli at the Drexel Plasma Institute of Drexel University on a regular basis. This interaction has allowed for a discussion and work forum to take the knowledge obtained via the analysis of the MGA plasma discharge and apply it to the knowledge of combustion to develop a model of the plasma/flame interaction.

Professor Ju, Dr. Xiao Qin and Timothy Ombrello have also worked with Dr. Skip Williams of the Air Force Research Laboratory at Wright-Patterson Air Force Base to design and develop a low pressure chamber to be used for combustion experiments to examine the effects of radical and excited species addition via the non-equilibrium MGA plasma discharge on the ignition and extinction aspects of hydrocarbon fueled counterflow flames.

Professor Ju and Timothy Ombrello have also worked closely with Dr. Campbell Carter of the Air Force Research Laboratory at Wright-Patterson Air Force Base. Timothy Ombrello has traveled to Wright-Patterson Air Force Base twice (November and December of 2004) to perform laser diagnostic measurements of planar Rayleigh scattering and OH planar laser induced fluorescence under the guidance and expertise of Dr. Carter.

In addition to this, for the above paper of electric field and premixed flame interaction, Professor Ju collaborated with Professor Miles and associates, as well as Dr. Daniel Sullivan of Research Support Instruments. The study was done over a three-month period from May of 2004 to July of 2004.

In order to validate the kinetic enhancement model via NO<sub>x</sub> production by the plasma discharge, Professor Ju collaborated with Prof. Kenichi Takita at Tohoku University and conducted ignition experiments in a supersonic flow with NO<sub>x</sub> production by a plasma torch.

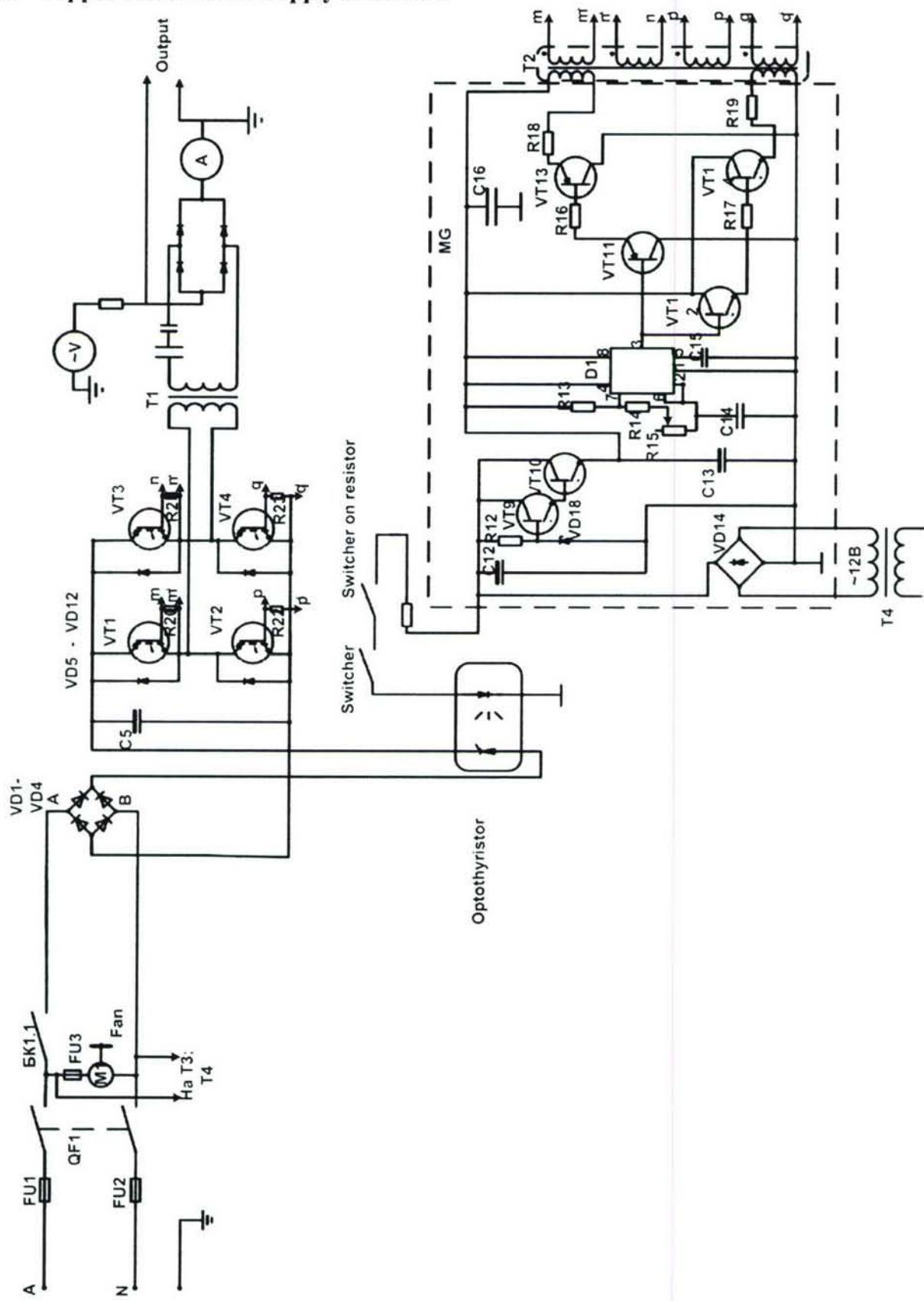
## **9.0 Honors and Awards**

Timothy Ombrello received the ASPACC (Asia-Pacific Conference on Combustion) 2005 Young Investigators Award, which is given for the most outstanding paper by a young researcher where the principal author and presenter are less than 35 years of age. The paper presented was titled "Flammability Limit Extension of Non-Premixed Counterflow Flames Via Stabilized Non-Equilibrium Plasma Gliding Arc" and was co-authored by Professor Yiguang Ju, Dr. Xiao Qin and Dr. Campbell Carter.

## **10.0 Inventions**

A special type of gliding arc found to be quasi-stable just prior to the limit of quenching in the non-equilibrium regime. The newly developed magnetic gliding arc was the foundation for the work on plasma assisted flame stabilization and ignition.

## 6.0 Appendix A: Power Supply Schematic



# Combustion Enhancement via Stabilized Piecewise Nonequilibrium Gliding Arc Plasma Discharge

Timothy Ombrello,\* Xiao Qin,† and Yiguang Ju‡

Princeton University, Princeton, New Jersey 08544

Alexander Gutsoi§ and Alexander Fridman¶

Drexel University, Philadelphia, Pennsylvania 19104

and

Campbell Carter\*\*

U.S. Air Force Research Laboratory, Wright-Patterson Air Force Base, Ohio 45433

A new piecewise nonequilibrium gliding arc plasma discharge integrated with a counterflow flame burner was developed and validated to study the effect of a plasma discharge on the combustion enhancement of methane-air diffusion flames. The results showed that the new system provided a well-defined flame geometry for the understanding of the basic mechanism of the plasma-flame interaction. It was shown that with a plasma discharge of the airstream, up to a 220% increase in the extinction strain rate was possible at low-power inputs. The impacts of thermal and nonthermal mechanisms on the combustion enhancement was examined by direct comparison of measured temperature profiles via Rayleigh scattering thermometry and OH number density profiles via planar laser-induced fluorescence (calibrated with absorption) with detailed numerical simulations at elevated air temperatures and radical addition. It was shown that the predicted extinction limits and temperature and OH distributions of the diffusion flames, with only an increase in air temperature, agreed well with the experimental results. These results suggested that the effect of a stabilized piecewise nonequilibrium gliding arc plasma discharge of air at low air temperatures on a diffusion flame was dominated by thermal effects.

## Nomenclature

$a$	= strain rate of the counterflow flame
$B$	= magnetic field
$C_d$	= drag coefficient
$d$	= arc surface area
$F_a$	= ampere force per unit arc length
$F_d$	= drag force
$I$	= current
$i, j$	= indices representing the two nozzles streams
$L$	= distance between counterflow nozzles
$Q$	= volumetric flow rate
$u$	= gas velocity
$\rho$	= gas density

## I. Introduction

THE quest for practical high-speed airbreathing propulsion systems has been a subject of much attention for almost a half of a century in the world of aerospace and aeronautics. From the

Presented as Paper 2005-1194 at the AIAA 43rd Aerospace Sciences Meeting, Reno, NV, 10–13 January 2005; received 7 April 2005; revision received 19 August 2005; accepted for publication 22 August 2005. Copyright © 2005 by the American Institute of Aeronautics and Astronautics, Inc. All rights reserved. Copies of this paper may be made for personal or internal use, on condition that the copier pay the \$10.00 per-copy fee to the Copyright Clearance Center, Inc., 222 Rosewood Drive, Danvers, MA 01923; include the code 0001-1452/06 \$10.00 in correspondence with the CCC.

\*Graduate Student, Department of Mechanical and Aerospace Engineering, Engineering Quadrangle on Olden Street. Student Member AIAA.

†Research Staff, Department of Mechanical and Aerospace Engineering, Engineering Quadrangle on Olden Street. Member AIAA.

‡Assistant Professor, Department of Mechanical and Aerospace Engineering, Engineering Quadrangle on Olden Street. Associate Fellow AIAA.

§Research Professor, Drexel Plasma Institute, 34th and Lancaster Avenue. Member AIAA.

¶Professor, Drexel Plasma Institute, 34th and Lancaster Avenue. Member AIAA.

\*\*Senior Aerospace Engineer, Aerospace Propulsion Division. Associate Fellow AIAA.

initial designs of ramjets and supersonic combustion ramjets, there have been significant advancements over this period of time, bringing us closer to a reliable system. Two of the most critical issues in developing these systems have come in the form of ignition and stabilization of the flame in the propulsion device. This is because of the flow speed being so high, leaving only a very short residence time from initiation to completion for combustion reactions.

Many different approaches have been put forth to combat these problems, from changing the geometry of the combustor to adding additional energy to the system. From the standpoint of geometric changes, cavities or struts can be added to the wall of the combustor to provide better mixing, longer residence time, and subsonic regions necessary for anchoring and stabilization of the flame.<sup>1–5</sup> These passive methods primarily provide enhancement by increasing mixing or creating a low-speed region of the flow to allow for flameholding and stabilization. To go hand-in-hand with cavities, the method of precombustion can be used in these isolated parts of the flow in a cavity or in a separate combustion chamber.<sup>6–8</sup> Here, the heat and products of the combustion have proven to be an effective means of decreasing the ignition time and increasing the flame stabilization. However, one practical problem with this approach is the requirement of the additional combustion chamber (and perhaps additional fuel and air for that chamber). Furthermore, there is also the constraint of the flammability limits of the fuel in the precombustor, especially for hydrocarbon fuels.

An attractive means to resolve these problems comes in the form of plasma-enhanced combustion. Many forms of plasma have been developed for this duty and have shown significant enhancement.<sup>9–15</sup> When looking at all of these different types of plasma systems, two questions may arise. First, what is the optimal type of plasma system? Second, how does it work to enhance the combustion? The types of plasma and their benefits first need to be discussed. Plasmas can be categorized as either thermal or nonthermal, that is, nonequilibrium. Thermal plasmas include arc discharges, plasma torches, and radio frequency inductively coupled plasmas. They mainly ionize and dissociate the reactants thermally, leading to large amounts of joule heating. Because of this heat addition, the gas temperatures are very high (5000–50,000 K), with electron temperatures of the same order and energy input in all degrees

of freedom. This results in poor chemical reaction selectivity, just increasing all of the reaction rates due to the elevated temperatures. Furthermore, there would be either large power requirements or localized activation such as with a plasma jet, for example, only penetrating into a small portion of a transverse supersonic flow. Nonequilibrium plasmas, which include low-pressure glow, radio frequency, corona, microwave, and nanosecond high-voltage discharges, have the benefit of high chemical selectivity and homogeneous activation. The primary means of dissociation and ionization is direct electron impact from high-temperature ( $\sim$ speed) electrons accelerated by a high electric field. The homogeneous activation leads to power requirements that can become extremely high, sometimes in excess of several kilowatts. Therefore, an ideal plasma discharge should have intermediate temperatures between that of a thermal and nonthermal discharge, which is high enough for the ignition of the mixture, and the activation benefits of a homogeneous discharge, providing high levels of chemical reaction selectivity, high electron temperatures, and high electron densities with low-power requirements.<sup>16</sup>

Once the criteria for an ideal discharge have been established, the next step is to understand at what conditions and to what extent there will be thermal and nonthermal effects. For ignition, it is very clear that radical addition will shorten the ignition time. However, for flame stabilization and burning rates, it has long been debated whether there is a nonthermal effect in plasma-assisted combustion.<sup>9,10</sup> The main factor that complicates the answer to this question is the complexity of a plasma discharge and the flowfield. Therefore, to understand the nonthermal and thermal effects at specific conditions, the plasma system has to be simplified and integrated with a flow system so that the interaction between the flow and flame can be isolated and that the detailed mechanism of the interaction between the flame and the plasma can be well understood. Therefore, it is particularly important to design a simplified combustion device for nonequilibrium plasma-assisted combustion enhancement so that the effects of nonequilibrium plasma on a flame can be observed and to what extent those effects are thermal and/or nonthermal can be understood.

The present research is motivated by the preceding discussion. The goal of this research was to develop an ideal and simplified plasma discharge using piecewise activation for minimal power consumption and the integration with a counterflow burner to understand the fundamental interaction between nonequilibrium plasma and diffusion flames. This was accomplished by first designing a stabilized nonequilibrium gliding arc plasma discharge system to provide piecewise activation. Then by the integration of this plasma system with a counterflow burner, a simple platform was established to study the plasma flame interaction. This included experimental studies of the extinction behavior, laser diagnostics for flame temperatures via planar Rayleigh scattering and OH number densities via OH planar laser-induced fluorescence (PLIF). These results were then compared to numerical computations using detailed chemistry to validate the measurements and clarify the roles of thermal and nonthermal effects in nonequilibrium plasma-assisted combustion.

## II. Apparatus

### A. Piecewise Discharge Plasma System

#### 1. Gliding Arc

The stabilized gliding arc is a special type of electrical discharge that occurs between two diverging high-voltage electrodes and has both thermal and nonthermal plasma merits. The arc is first established when a sufficiently high enough potential is applied across the electrodes (approximately 3 kV/mm in air) to break down the gas at the smallest gap. Once a conductive channel is established (arc), the current very rapidly increases while the voltage decreases simultaneously to maintain the discharge. This is a thermal plasma, with thermal dissociation and ionization being the primary means of maintaining the arc discharge with a low voltage and high current. The arc then moves downstream due to the buoyancy and/or flow, elongating as the gap between the electrodes increases. During this process, the arc continually loses heat to the surroundings because of the increased arc surface area. The voltage is also continually

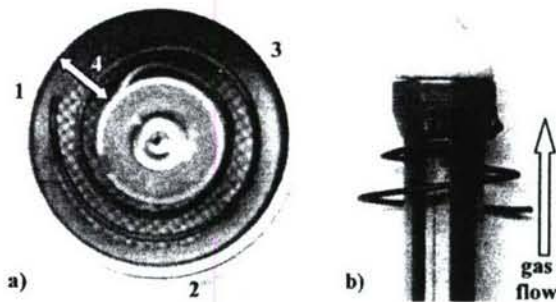


**Fig. 1** Gliding arc plasma system: path of the gliding arc from initiation, point 1, to arc rotation/elongation, points 2 and 3, and finally arc stabilization, point 4: a) top view of system and b) side view of central electrode.

increasing while the current is simultaneously decreasing to maintain a constant power. At a point when the arc elongates such that the power supplied to the source cannot balance the amount of heat lost to the surroundings, the arc makes a transition to a nonequilibrium regime. The primary means of dissociation and ionization is then due to direct electron impact from high-temperature electrons accelerated by the higher electric field. This part of the gliding arc discharge, in the nonequilibrium regime, has the important benefit of lower gas temperature to provide better chemical selectivity. The arc then continues to elongate as it propagates along the diverging electrodes until it finally extinguishes. Once there is a sufficiently high potential built up between the electrodes, the process starts again, being cyclic in nature.

Unfortunately in a gliding arc system, the nonequilibrium regime exists only for a short period of time in the arc evolution process. Recently, however, it was found that during the gliding arc process, the arc can be stabilized well past the transition from the thermal equilibrium to the nonequilibrium regime before extinction.<sup>17</sup> This is significant because the process would not have to be cyclic, like a traditional gliding arc, to observe the benefits for a small nonequilibrium portion of the process of each cycle. Because of this newfound stability, the plasma arc can be stabilized near extinction in the nonequilibrium regime for an indefinite amount of time, creating a plasma disk. This study utilizes this special type of gliding arc discharge. As seen in Fig. 1, it comprises a stainless-steel inner and outer electrode, which is the cathode and the anode (as well as the ground), respectively. There is a wire attached to the cathode that is separated from the outer anode by 2 mm at the smallest gap (point 1, Fig. 1). The wire spirals progressively closer to the cathode to where it is attached, which is at the largest gap between the two electrodes. In addition, there is a magnetic field in the discharge region produced by an external donut-shaped permanent ceramic magnet. The direction of the magnetic field determines the direction of the rotation of the arc (in this case counterclockwise to follow the wire when looking down upon the system as in Fig. 1), and the field strength, as well as the power input, determines the frequency of rotation.

#### 2. Plasma Disk

When a high voltage is applied to the plasma device, there is an initial breakdown of the feedstock at the smallest gap and a thermal plasma is established. The arc then rotates in the magnetic field and increases in length as the distance between the spiraled wire and the outer electrode increases (Fig. 1, from point 1 to point 2 to point 3). The increased length of the arc results in a transition to a nonequilibrium plasma leading to more rapid cooling and intermediate temperatures (2000–3000 K), as well as an increased electric field and electron temperature (>1 eV). Once the arc reaches the cylindrical inner electrode (point 4, Fig. 1), there is a stable rotating intermediate temperature arc in the gas flow. A top view of this plasma disk can be seen in Fig. 2. The plasma arc rotation frequency ranges from approximately 20 to 50 Hz and only decreases by a few percent when the flow rate is increased (Fig. 3). The increased

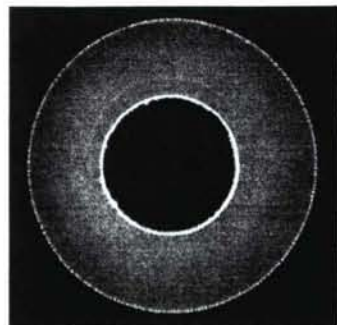


Fig. 2 Top view of plasma disk.

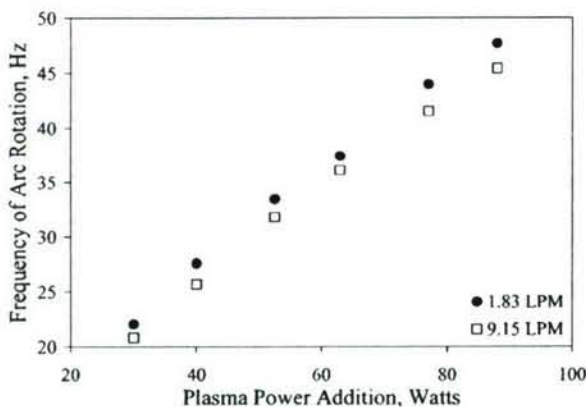


Fig. 3 Frequency of arc rotation for two airflow rates.

rotation frequency comes from the higher current input (and, hence, higher power addition), forcing the arc to rotate faster in the magnetic field. When the arc reaches the largest gap, it remains at a fixed axial position with a constant length as it rotates. This is because the arc is no longer convecting downstream. It maintains itself there because it is rotating through media that was previously ionized, not through the initial nonionized gas. Therefore, it requires less power for the arc to remain at that position as opposed to quenching and reinitiating at the smallest electrode gap.

Because the frequency of rotation of the arc is fast when compared to the gas velocity, there is quasi-uniform activation of the flow. To show this, calculations were performed to find what flow rate  $Q$  of air could be quasi uniformly activated by the gliding arc. The system had a distance of 10 mm at the largest gap where the plasma disk was located and a magnetic field  $B$  of 0.15 T (a typical value that is possible to obtain with permanent ceramic magnets). The low-current, high-voltage gliding arc operation would have an electric field strength  $E$  for the case of the gliding arc propagation through nonionized air of about 0.1 kV/mm. This would lead to a gliding arc voltage drop of 1 kV for the given length of the gap. The ampere force per unit of arc length that would rotate the gliding arc would be  $F_a = IB$ , and when in equilibrium conditions, it would be equal to the drag force  $F_d$ . It was possible to estimate the drag force per unit length from the assumption that all of the gas was flowing around the high-temperature cylinder of the arc. The drag force on the cylinder can be calculated as  $F_d = 0.5 C_d \rho u^2$ . The limits for the drag coefficient for a very wide range of Reynolds numbers (from  $10^2$  to  $10^5$ ) are  $1.3 < C_d < 1$ , and thus,<sup>18</sup>

$$\frac{1}{2} C_d \rho u^2 = IB \quad (1)$$

Therefore, the arc, which was approximately 2 mm in diameter, moved relative to the gas flow along a spiral trajectory, and if the gas velocity  $u < d/\tau$ , then all of the gas flow would be uniformly treated by the arc. For the plasma system, this corresponded to  $u < 4-10$  cm/s and  $Q < 35-88$  cm<sup>3</sup>/s for the range of powers used. In addition to the direct treatment by the rotating gliding arc, all of the gas flow would pass through the ionized disk that the gliding arc left behind.

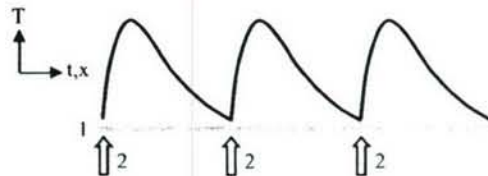


Fig. 4 Piecewise discharge concept: 1) quenching limit of a flame and 2) points of plasma discharge.

This plasma disk, which would allow a quasi-uniform activation of the flow, can be thought of as a piecewise discharge in terms of space or time. For example, in Fig. 4, it can be seen in a temperature vs time or spatial coordinate plot, if there is a discharge, providing a source of some heat and/or radicals, the gas temperature will rise due to the combustion process, but then will decrease if the conditions are not satisfactory for the survival of the combustion process. If no more energy is added, the flame will extinguish, but if there is another discharge before that (within the quenching distance or time), the flame will survive. This can be continually done, sustaining the burning of the flame.

To produce this gliding arc discharge, a power supply was specifically created to supply efficiently the needs of the gliding arc system stabilized by the magnetic field. It was designed to produce a magnetically stabilized arc with minimum current while maintaining smooth current regulation. This was accomplished by minimizing the active energy losses by using a reactive capacitive resistance that imitated the resistive voltage and current characteristics. To minimize the output electric capacity and to provide the voltage-current characteristic of the power supply (which is close to the resistive voltage-current characteristics), changing the frequency of the high-voltage converter allowed variation of the virtual resistance. After the output rectifier, there was unidirectional voltage and current with a very high frequency of the residual pulsation. The plasma arc behavior was then the same as that for the plasma arc at a constant current and voltage because of the limited time response of the gliding arc.

#### B. Counterflow Flame Burner Integration

To provide an ideal platform to integrate the stabilized gliding arc plasma discharge with a combustion system, the counterflow flame burner was chosen. The counterflow system provides four key benefits of minimal buoyancy effects, simplified flame geometry, ability to define a flow velocity gradient (strain rate or inverse of residence time) on the centerline near the stagnation plane of the two impinging jets, defined as<sup>19-23</sup>

$$a_i = (2v_i/L) [1 + (v_j/v_i) \sqrt{\rho_j/\rho_i}] \quad (2)$$

and, last, excellent optical access for advanced laser diagnostics for species and temperature measurements.

A schematic of the system is shown in Fig. 5. The system consists of two converging nozzles 15 mm in diameter, separated by 13 mm. The upper nozzle was water cooled. The feedstock for the plasma device, upstream of the lower nozzle, was air, whereas nitrogen-diluted methane flowed through the upper nozzle. To isolate the flame from the ambient air and disturbances, a nitrogen "curtain" was used. The nitrogen curtain passed through a 0.75-mm annular slit around the circumference of each nozzle exit. The velocity of the curtain was maintained at or below the exit speed of the nozzle to minimize diffusion into the stream. The flame was established on the upstream air side of the stagnation plane. This system allowed for the examination of the effects of stretch on the quenching limit of the flame as a function of the flow velocity gradient for different levels of plasma power addition.

The flow rates of the individual gases were controlled with sonic nozzles that were calibrated with a DryCal dry piston flow meter (1% error). The methane and nitrogen were then mixed in a hollow mixing cylinder (for minimal backpressure). To ensure that the mixture input to the flame was held constant while the velocity was increased through the nozzles, a bypass system was used. Here, the

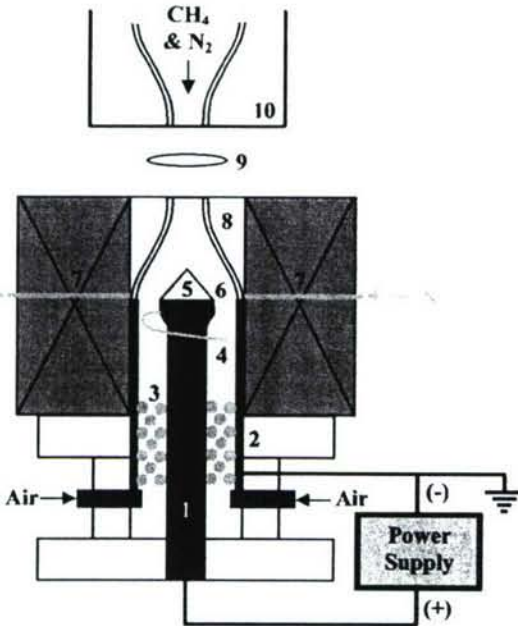


Fig. 5 Counterflow burner with integrated plasma system: 1) cathode, 2) anode, 3) diffuser, 4) gliding arc initiation wire, 5) insulator, 6) plasma disk, 7) magnet, 8) converging nozzle with  $N_2$  curtain, 9) flat diffusion flame, and 10) water-cooled converging nozzle with  $N_2$  curtain.

methane–nitrogen mixture, as well as the air, was teed off before the respective nozzles. The flow rate could then be increased or decreased through the nozzles by closing or opening the valves of the bypasses, respectively. By then measuring the flow through the bypass using the DryCal flow meter, the nozzle exit velocities could be calculated.

To find the extinction limits, the flame was first established with the bypass fully open and, hence, the lowest flow rate through the nozzles (and strain exerted on the flame). Then each bypass was slowly closed, while maintaining the stagnation plane at a fixed position. During this process, the flame moved closer to the stagnation plane between the two nozzles, which decreased the residence mixing time as well as increased the strain rate until flame extinction.

Two photographs of the nitrogen-diluted methane–air counterflow flames with and without plasma power addition can be seen in Fig. 6. Note the one-dimensional structure of the flame. In all cases, the flame was very steady and had minimal curvature, providing an excellent platform to perform experimental measurements via laser diagnostics and geometry that was easy to reproduce computationally. There was also a difference in luminosity between the flame with (Fig. 6a) and without (Fig. 6b) plasma activation of the airstream. The flame with plasma activation of the air has a larger luminous zone with a distinct white and orange coloring as compared to the typical bright blue of the nonactivated flame. This indicates that there is an effect of the stabilized piecewise gliding arc plasma discharge on the diffusion flame.

### C. Rayleigh Scattering and OH PLIF

To measure the temperature profiles of the diffusion flame between the two nozzles, a Rayleigh scattering system was utilized (Fig. 7). A frequency-doubled, injection-seeded Nd:YAG laser (Quanta-Ray GCR-4) with an output of approximately 450 mJ/pulse was used. For OH measurements, the OH was excited via a Lumonics HD-300 dye laser pumped with the Nd:YAG laser already described (Fig. 7). The wavelength was tuned to 567.106 nm so that the frequency-doubled radiation matched the wavelength for the  $Q_1(8)$  transition of the  $A^2\Sigma^+ - X^2\Pi(1,0)$  band; the Boltzmann population fraction of the ground state ( $N = 8$ ) reaches a maximum near 1600 K and varies little over the temperature range of 1200–2200 K;

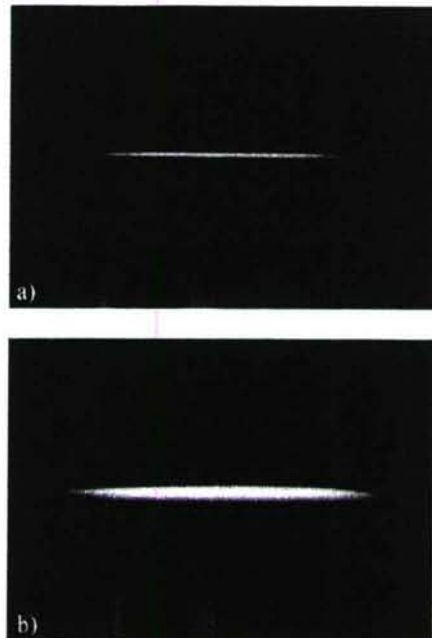


Fig. 6 Methane–air counterflow diffusion flames at strain rate of  $298.5 \text{ s}^{-1}$ : a) no plasma power addition and b) 60 W of plasma power addition.

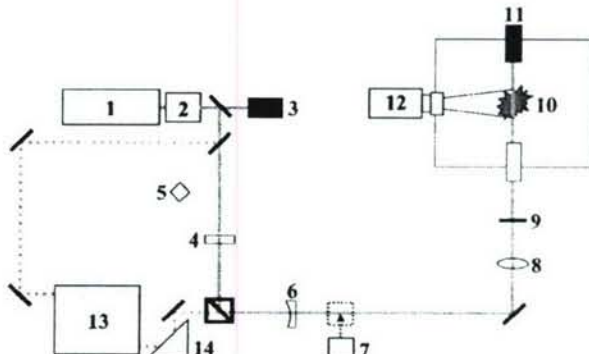


Fig. 7 Planar Rayleigh scattering and OH PLIF setup: 1) injection seeded Nd:YAG laser, 2) frequency doubler, 3) beam dump, 4) half-wave plate, 5) diode energy meter, 6) lens, 7) power meter, 8) lens, 9) clipper, 10) flame, 11) beam dump, 12) ICCD camera, 13) dye laser with frequency doubler, and 14) Pellin–Broca prism.

for example,  $f_B(2200 \text{ K})/f_B(1600 \text{ K}) = 0.934$ . The resulting pump linewidth was approximately  $0.1 \text{ cm}^{-1}$ , whereas the 283-nm beam energy was 12 mJ/pulse. The beam energy was measured and recorded for each image taken by directing a small portion of the beam (either 532 or 283 nm) to a photodiode (or Molelectron Joulemeter). For both temperature and OH measurements, a laser sheet was formed using two lenses. These consisted of a plano-concave cylindrical lens ( $-300\text{-mm focal length}$ ) to spread the beam in the vertical direction and a plano-convex spherical lens ( $1\text{-m focal length}$ ) to focus the beam in the horizontal direction and also collimate the beam in the vertical direction. The laser sheet was then directed between the two nozzles of the counterflow flame burner. To define clearly the laser sheet and minimize any stray scattering in the vertical direction, absorptive filters were used to “clip” the sheet. The scattering was imaged with a Princeton Instruments PIMAX intensified charge-coupled device (ICCD) camera (one with a photocathode optimized for the visible spectrum for Rayleigh scattering and one for the UV spectrum for OH fluorescence). For Rayleigh scattering, a Nikon 105-mm, f/2.8 macrolens was used, whereas for OH PLIF, a Nikon UV Nikkor 105 mm f/4.5 lens was used along with UG-11 and WG-295 Schott glass filters to isolate fluorescence from the  $A-X(0,0)$  and  $A-X(1,1)$  bands and

block background scattering. Both cameras employed a  $512 \times 512$  pixel array that was binned to improve the framing rate.

To calibrate the Rayleigh scattering signal, images of the scattering intensity were taken of clean, particle-free air (at a known temperature) that was directed through the lower nozzle. Even though great care was taken to minimize the background scattering, some still existed. To account for this, high-purity helium was passed through the nozzles of the burner system, allowing the background to be measured. Helium was used for this purpose because its scattering cross section is very small compared to that of air (less than 1.5%). Also to account for any variations in the system (and minimize error) as the experiments were conducted, such as shifts in the laser sheet, the air-reference and background scattering were checked periodically.

To calibrate the intensity seen from the OH PLIF to an absolute number density of OH, measurements were first taken of a known system with the equivalent experimental arrangement. A 25.4-mm-square Hencken burner (see Ref. 24) using a premixture of methane and air (equivalence ratio of 0.95) was used as the calibration flame. Though there is a small difference in electronic quenching rate between this flame and that expected in the counterflow diffusion flames (due to the nitrogen in the fuel), the difference was mitigated due to transition saturation. The number density in the Hencken burner flame (in the burnt gas region) was determined with an absorption measurement, using the  $Q_1(6)$  transition of the  $A-X(0,0)$  band, along with a LIF measurement of the absorption pathlength. This measurement gave an OH number density of  $(0.94 \pm 0.07) \times 10^{16} \text{ cm}^{-3}$ , a value consistent with a burnt gas temperature of 2170 K (vs the adiabatic equilibrium value of 2194 K). The ratio of fluorescence signals between the counterflow flames and the Hencken burner flame, along with the number density in the Hencken burner flame, allowed for calculation of the counterflow flame number densities. A 10% correction factor was also applied to the Hencken burner flame fluorescence signals to account for the greater degree of fluorescence trapping and sheet absorption (compared to the counterflow flames); measured temperatures were used to correct the slight change in Boltzmann population fraction from Hencken burner to counterflow flames. The total fractional uncertainty for the counterflow OH number densities is estimated to be  $\pm 15\%$ ; this represents a combination of absorption measurement uncertainty and uncertainty of application of the calibration to the opposed flow flames.

### III. Results and Discussion

This section is divided into four subsections describing experimental measurements of extinction limits, Rayleigh scattering for temperature profiles, OH PLIF for absolute OH number density, and numerical computations with radical addition. Numerical computations were performed using a modified version of PREMIX code<sup>25</sup> with both potential and plug flow boundary conditions and using the detailed chemical mechanism of GRI-3.0 (Ref. 26). The temperature input to the numerical computation came from the measured temperatures found just downstream of the exit of the nozzles via Rayleigh scattering thermometry for each of the various flow, concentration, and plasma power conditions.

#### A. Extinction Measurements

The extinction limits for the counterflow flames were found with and without plasma power addition. When the bypass valves were closed, the nozzle exit velocities increased, pushing the flame closer to the stagnation plane. As the flame approached the stagnation plane, the strain rate increased. The flame lost more heat and had less residence time for reaction completion until, finally, it extinguished. The effect of the stabilized piecewise nonequilibrium gliding arc plasma discharge on the extinction limits of the flame was observed. This was accomplished by using three different nitrogen-diluted methane mixtures, and the results can be seen in Fig. 8. The extinction limits with no plasma power addition agreed well with values reported by both Puri and Seshadri<sup>19</sup> and Bundy et al.<sup>23</sup> With only 78 W of plasma power input, there was a 220% increase in the extinction strain rate. This power input was less than 6% of the flame

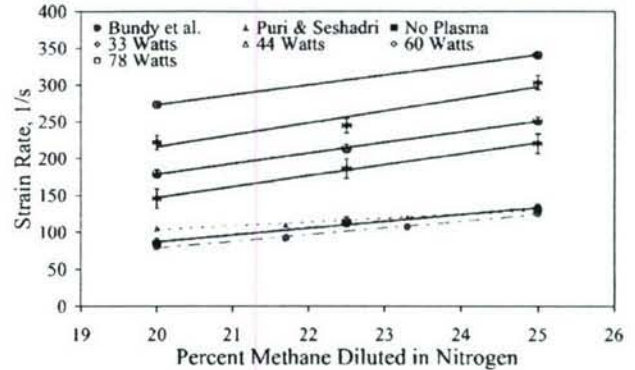


Fig. 8 Effects of plasma power addition on strain rates at extinction for different levels of nitrogen dilution.

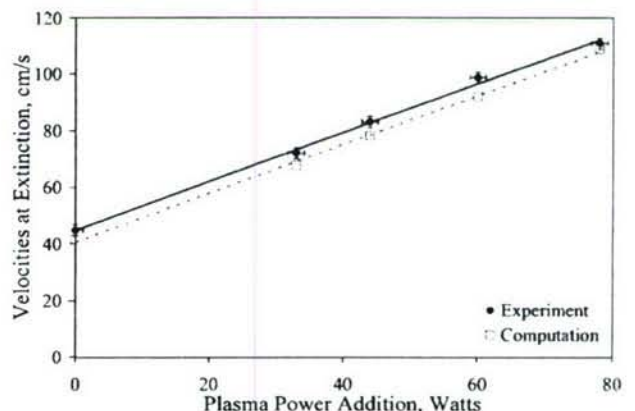


Fig. 9 Comparison of nozzle exit velocities at extinction.

power, defined as the maximum power that could be obtained from the given amount of fuel in the mixture. These results showed that by using a stabilized piecewise nonequilibrium gliding arc plasma discharge there was a significant extinction limit enhancement, but the reasons for this effect were not yet apparent.

To get an initial idea, the results for the extinction strain rates were then compared to that of the numerical computation. Because strain rate is proportional to velocity, the comparison was done in relation to velocities at extinction. The results can be seen in Fig. 9. Because the input to the computation was only elevated temperatures (obtained from the Rayleigh scattering, to be described in the next section) to mimic the plasma, and because both the experiment and computation extinction results are in good agreement, this gives an indication that the effect of the nonequilibrium plasma on the flame is predominately thermal.

#### B. Rayleigh Scattering

To measure quantitatively the temperature distribution and compare it with numerical simulations, Rayleigh scattering was performed on the counterflow flame for various strain rates. The laser sheet was passed through the diameter of the disk-shaped counterflow flame between the nozzles of the burner. Two sample images are shown with no plasma power addition (Fig. 10a) and with approximately 33 W of plasma power addition (Fig. 10b). The background has been subtracted and the air reference divided into each image. The intensity seen was both a function of scattering cross section and number density distributions between the nozzles. The scale below Fig. 10 shows the darkest for the least scattering and the highest temperature and the lighter for the most scattering and the lowest temperature. Therefore, the flame is located in the darkest region of these images just above the middle of the photograph, spanning the width. The nitrogen-diluted methane mixture is entering the field of view from the top of Fig. 10 and the air (plasma side) from the bottom. It is seen that even with the nonequilibrium plasma discharge,

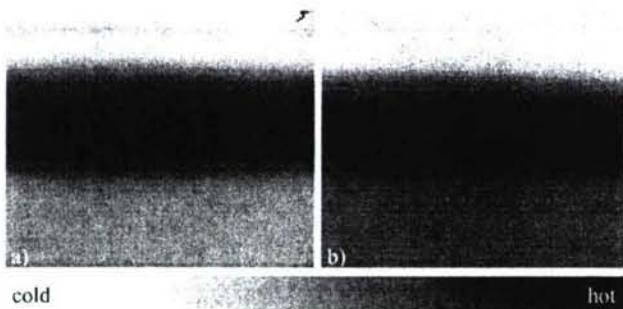


Fig. 10 Rayleigh scattering images at a strain rate of  $98.6 \text{ s}^{-1}$ : a) no plasma power addition and b) 33-W plasma power addition.

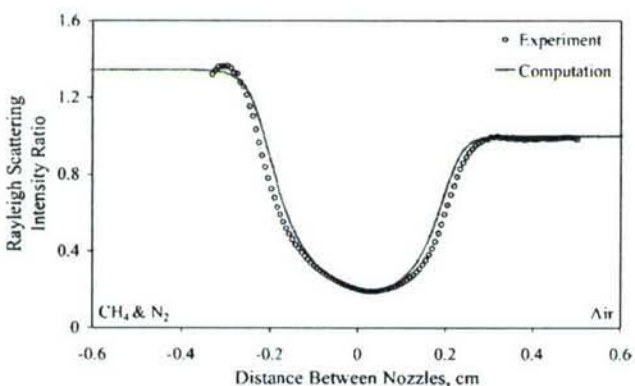


Fig. 11 Comparison of Rayleigh scattering intensity ratio profiles with 0 W of plasma power addition at a strain rate of  $87.1 \text{ s}^{-1}$ .

the present burner design yields a very good one-dimensional flame structure along the flow direction. This result greatly simplifies the coupling between the flowfield and the plasma–flame interaction. When comparing the two images, notice that the region below the flame in Fig. 10b (plasma on) is darker than Fig. 10a (plasma off) below the flame. This indicates less scattering and, hence, a higher temperature. In each case, a 10-pixel-wide “stripe” was taken from each image and averaged to yield the best distribution between the nozzles. The temperatures measured at the boundaries (just downstream of the nozzles) were then used as boundary conditions in the numerical computation.

### 1. Rayleigh Scattering Intensity Ratio Profiles

To get a better idea of how the flame was being enhanced by the nonequilibrium plasma, Rayleigh scattering thermometry was performed to obtain the distribution of temperature between the two nozzles. The intensity observed by the ICCD camera was a function of both the scattering cross section, because of the distribution of different species, and number density change between the two nozzles. By the simple referencing of those intensities to the intensity of air at room temperature, ratios were found. These measurements were then compared to that of numerical computation, and the results can be seen in Figs. 11–13 for both the plasma power off and on. Note that oscillations are evident in the scattering profiles, especially near the upper (fuel) nozzle; these resulted from diffraction from the edge of the absorptive filters used to clip the beam (and prevent scattering from the burner surfaces) and slight movement of the sheet between the measurements in the flame and of the air reference. Nonetheless, it can be seen that there is reasonably good agreement between the experiment and computation. This once again showed that the effect of the nonequilibrium plasma on the flame was predominately thermal.

### 2. Temperature Profiles

Even though the measurements directly from the Rayleigh scattering were in good agreement with the computation, and were also

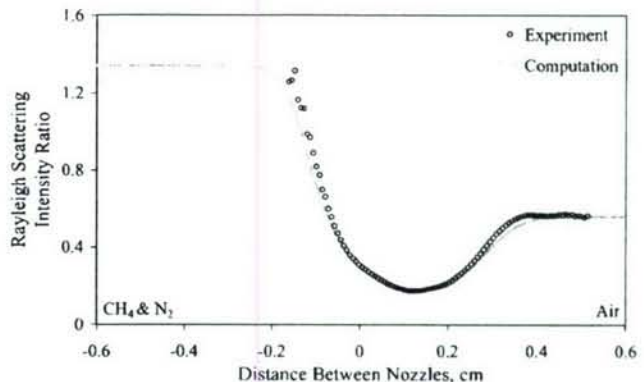


Fig. 12 Comparison of Rayleigh scattering intensity ratio profiles with 33 W of plasma power addition at a strain rate of  $98.6 \text{ s}^{-1}$ .

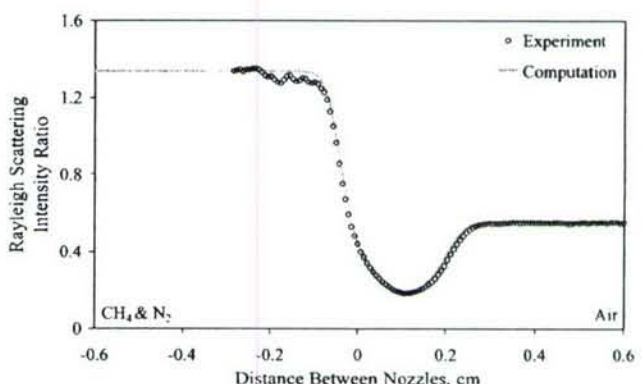


Fig. 13 Comparison of Rayleigh scattering intensity ratio profiles with 60 W of plasma power addition at a strain rate of  $298.5 \text{ s}^{-1}$ .

completely independent quantities, the actual temperatures were not realized. To then get a better idea of the temperatures, the ratio profiles as described earlier were used. Because the species concentrations and temperature changed between the nozzles due to the presence of the flame, the scattering cross sections and number densities changed. Number density could simply be accounted for by the temperature, but the scattering cross sections could not. Therefore, the scattering cross sections needed to be known at each point along the profile as a reference to derive the temperature. Therefore, the species concentrations associated with specific temperatures and axial positions from the numerical computation were used to convert scattering signal to temperature. The scattering cross sections for species in molar concentrations of 10ths of a percent and larger were calculated using refractory data from Gardiner et al.<sup>27</sup> This accounted for the variation in scattering cross section and gave accurate temperature profiles from the Rayleigh scattering. The temperature profiles found from the Rayleigh scattering were then compared to the results of the numerical computation at the same input temperatures and flow conditions. Figure 14 shows temperature profile comparisons between the experimental results via Rayleigh scattering and the numerical computation using the GRI-3.0 mechanism. The profiles are in good agreement. Figures 15 and 16 show similar comparisons between the experimental results and the numerical computation, except with the addition of plasma power. Once again, the temperature profiles are all in good agreement. Note that on the air side (the right-hand sides) is where the elevated temperature inputs were, mimicking the plasma. The air temperature was found experimentally from the Rayleigh scattering and given as the only input to the numerical computation. Overall, the temperature profiles agreed, therefore, once again showing that the effect of the nonequilibrium plasma can be seen as predominately thermal for the cases investigated.

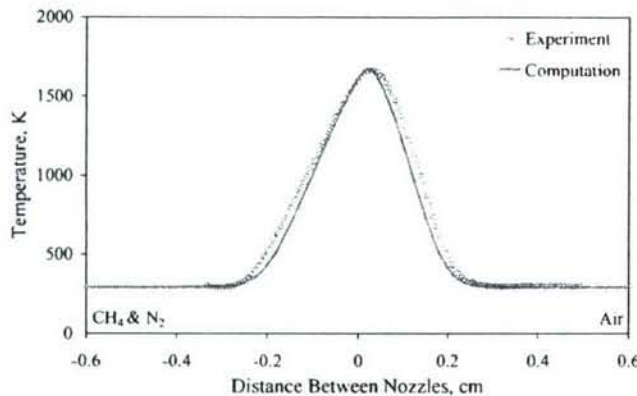


Fig. 14 Comparison of temperature profiles with 0 W of plasma power addition at a strain rate of  $87.1 \text{ s}^{-1}$ .

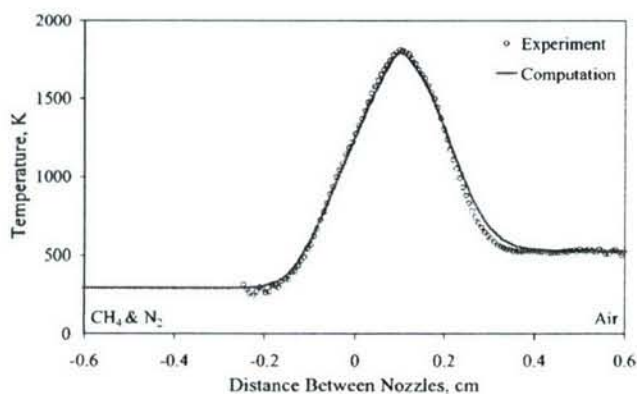


Fig. 15 Comparison of temperature profiles with 33 W of plasma power addition at a strain rate of  $98.6 \text{ s}^{-1}$ .

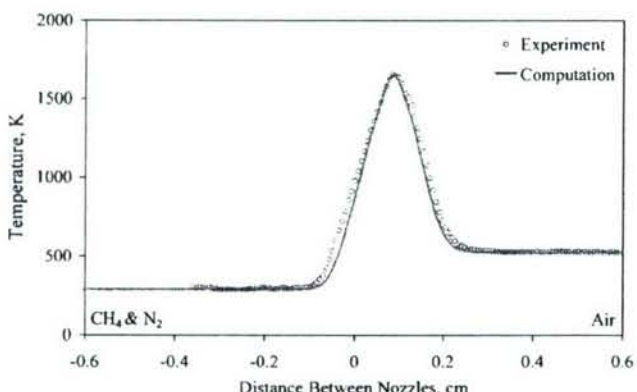


Fig. 16 Comparison of temperature profiles with 60 W of plasma power addition at a strain rate of  $298.5 \text{ s}^{-1}$ .

### C. OH PLIF

To further reinforce that the enhancement of the flame via the nonequilibrium plasma was dominated by thermal effects, OH PLIF measurements were performed. The OH number density was measured for different plasma powers and strain rates and referenced to a Hencken burner flame, as described earlier, to find the absolute OH number density. Figure 17 shows the results from the OH PLIF measurements when compared to the computation with no plasma power addition and Figs. 18 and 19 with plasma power addition. Note that the experimental profiles are consistently taller and broader than the computational profiles, but overall the agreement is within the uncertainty of the measurement,  $\pm 15\%$ , as described earlier. Note also that because the 283-nm laser sheet was approximately 250  $\mu\text{m}$  in width in the probe region (and transition sat-

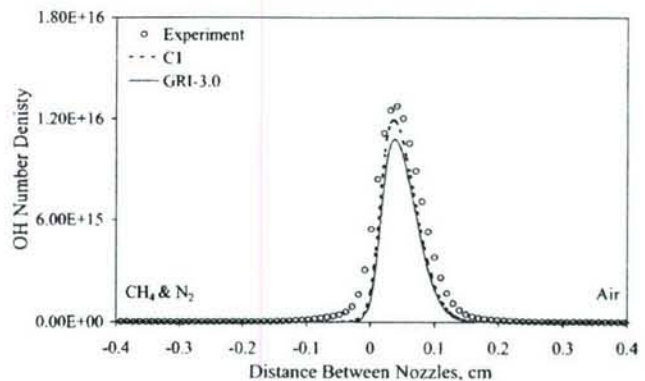


Fig. 17 Comparison of OH number density distributions with 0 W of plasma power addition at a strain rate of  $83.3 \text{ s}^{-1}$ .

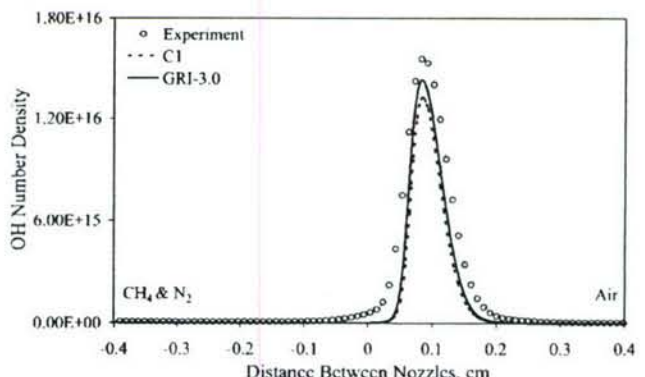


Fig. 18 Comparison of OH number density distributions with 48 W of plasma power addition at a strain rate of  $183.0 \text{ s}^{-1}$ .

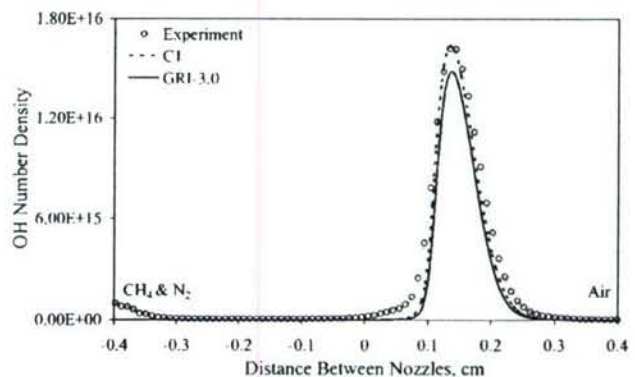


Fig. 19 Comparison of OH number density distributions with 78 W of plasma power addition at a strain rate of  $127.7 \text{ s}^{-1}$ .

uration gives an effective probe thickness somewhat greater than this), one would expect a slight broadening of the experimental profiles. Nonetheless, Figs. 17–19 show reasonably good agreement between the experiment and the computation, therefore, once again showing that the effect of the nonequilibrium plasma on the flame is predominately thermal.

### D. Radical Addition

What would be the lifetime of radicals produced by the plasma discharge in the airstream and would they reach the flame? This is reasonable to ask because, as observed, the effect appears to be predominately thermal, rather than nonthermal. Because the plasma is only activating dry air, it can be assumed that the radicals produced in the flame will only consist of oxygen and nitrogen. Here, only the effect of oxygen atom addition at the air side boundary on the flame structure will be shown (once again mimicking the plasma)

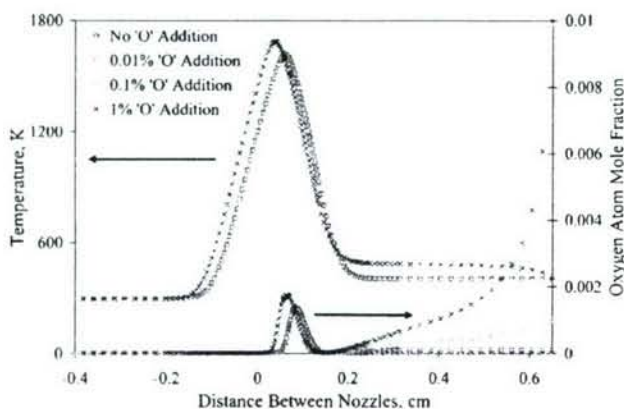


Fig. 20 Computed temperature and oxygen atom distributions between nozzles of counterflow system with oxygen atom addition.

because the nitrogen atom addition plays a similar role. Oxygen atom concentrations from 0.01 to 1% were added at the air (plasma) side boundary. The temperature was fixed at 400 K at this boundary to ensure that low-temperature chemistry did not come into play. Also, the velocities at the boundaries were similar to those used in the experiment for a flame that is highly strained and near extinction, where radical addition may be important. The temperature profiles and oxygen atom concentration distributions between the nozzles can be seen in Fig. 20. It is shown that there is no significant effect until almost 1% oxygen atom addition. When it is considered that the plasma disk is located almost 4 cm upstream of this boundary where the oxygen atoms were added, it appears that these atoms will recombine well before the flame, therefore, having no nonthermal effect on the flame.

From the preceding discussion, we can conclude that the radical-induced nonthermal effects on the burning rate of diffusion flames are very limited at low air temperatures because the radical lifetime is too short to affect the chain branching reaction path. The oxygen radicals simply recombine and increase the air temperature before reaching the flame. In addition, the low temperature of air excludes the occurrence of the low-temperature chemistry. Future experiments to observe the nonthermal plasma–flame interaction should be conducted at reduced pressures and elevated air temperatures so that the radical lifetime can be extended and low-temperature fuel oxidation chemistry can be involved.

#### IV. Conclusions

A new stabilized piecewise nonequilibrium gliding arc plasma discharge system was developed and validated for the study of nonequilibrium plasma–flame interaction by integrating it with a counterflow burner. Experiments showed that the present system yields a well-defined one-dimensional flame structure. The excellent agreement between laser diagnostics of temperature and OH radical distributions with numerical simulations confirmed that the present plasma discharge system provides an ideal platform to study the mechanism of the nonequilibrium plasma–flame interaction. Experimental results of a low-power plasma discharge in the airstream showed that a plasma discharge could significantly increase the extinction limits of the diffusion flame at low-power input. Direct comparisons of the extinction limits and temperature and OH distributions between the experiment and numerical simulations demonstrated that the combustion enhancement at a low-power discharge in the airstream was dominated by thermal effects, that is, heating of the airstream. Numerical computations with oxygen radical addition in the airstream confirmed this conclusion. The results also showed that the lack of the nonthermal effect on the flame burning limit at low-power discharge was caused by the fast recombination of active radicals. Future experiments to observe nonthermal enhancement of combustion via the plasma–flame interaction needs to be conducted at elevated air temperatures or reduced pressures.

#### Acknowledgments

This work was graciously supported by the Air Force Office of Scientific Research under Contract F49620-04-1-0038. Also, Yiguang Ju thanks the Air Force Research Laboratory and the National Science Foundation under Grant CTS-0418403 for support for the laser diagnostic equipment.

#### References

- <sup>1</sup>Gruber, M. R., Baurle, R. A., Mathur, T., and Hsu, K.-Y., "Fundamental Studies of Cavity-Based Flameholder Concepts for Supersonic Combustors," *Journal of Propulsion and Power*, Vol. 17, No. 1, 2001, pp. 146–153.
- <sup>2</sup>Gruber, M. R., Donbar, J. M., Carter, C. D., and Hsu, K.-Y., "Mixing and Combustion Studies Using Cavity-Based Flameholders in Supersonic Flow," *Journal of Propulsion and Power*, Vol. 20, No. 5, 2004, pp. 769–778.
- <sup>3</sup>Yu, K. H., Wilson, K. J., and Schadow, K. C., "Effect of Flame-Holding Cavities on Supersonic-Combustion Performance," *Journal of Propulsion and Power*, Vol. 17, No. 6, 2001, pp. 1287–1295.
- <sup>4</sup>Yu, G., Li, J. G., Chang, X. Y., Chen, L. H., and Sung, C. J., "Fuel Injection and Flame Stabilization in Liquid-Kerosene-Fueled Supersonic Combustor," *Journal of Propulsion and Power*, Vol. 19, No. 5, 2003, pp. 885–893.
- <sup>5</sup>Yu, G., Li, J. G., Zhang, X. Y., Chen, L. H., Han, B., and Sung, C. J., "Experimental Investigation on Flameholding Mechanism and Combustion Performance in Hydrogen-Fueled Supersonic Combustors," *Combustion Science and Technology*, Vol. 174, No. 3, 2002, pp. 1–27.
- <sup>6</sup>Guerra, R., Waidmann, W., and Laible, C., "An Experimental Investigation of the Combustion of a Hydrogen Jet Injected Parallel in a Supersonic Air Stream," AIAA Paper 91-5102, Dec. 1991.
- <sup>7</sup>Ju, Y., and Niioka, T., "Ignition Simulation of Methane/Hydrogen Mixtures in a Supersonic Mixing Layer," *Combustion and Flame*, Vol. 102, No. 4, 1995, pp. 462–470.
- <sup>8</sup>Tabejamaat, S., Ju, Y., and Niioka, T., "Numerical Simulation of Secondary Combustion of Hydrogen Injected from Preburner into Supersonic Airflow," *AIAA Journal*, Vol. 35, No. 9, 1997, pp. 1441–1447.
- <sup>9</sup>Takita, K., "Ignition and Flame-Holding by Oxygen, Nitrogen and Argon Plasma Torches in Supersonic Airflow," *Combustion and Flame*, Vol. 128, No. 3, 2002, pp. 301–313.
- <sup>10</sup>Takita, K., Moriwaki, A., Kitagawa, T., and Masuya, G., "Ignition of H<sub>2</sub> and CH<sub>4</sub> in High Temperature Airflow by Plasma Torch," *Combustion and Flame*, Vol. 132, No. 4, 2003, pp. 679–689.
- <sup>11</sup>Bozhenkov, S. M., Starikovskaya, S. M., and Starikovskii, A. Yu., "Nanosecond Gas Discharge Ignition of H<sub>2</sub>- and CH<sub>4</sub> Containing Mixtures," *Combustion and Flame*, Vol. 133, No. 1–2, 2003, pp. 133–146.
- <sup>12</sup>Starikovskaya, S. M., Kukav, E. N., Kuksin, A. Y., Nudnova, M. M., and Starikovskii, A. Yu., "Analysis of the Spatial Uniformity of the Combustion of Gaseous Mixture Initiated by Nanosecond Discharge," *Combustion and Flame*, Vol. 139, No. 3, 2004, pp. 177–187.
- <sup>13</sup>Chintala, N., Meyer, R., Hicks, A., Bystricky, B., Rich, J. W., Lempert, W. R., and Adamovich, I. V., "Non-Thermal Ignition of Premixed Hydrocarbon-Air and CO-Air Flows by Non-Equilibrium RF Plasma," AIAA Paper 2004-0835, Jan. 2004.
- <sup>14</sup>Sullivan, D., Zaidi, S. H., Macheret, S. O., Ju, Y., and Miles, R. B., "Microwave Techniques for the Combustion Enhancement of Laminar Flames," AIAA Paper 2004-3713, July 2004.
- <sup>15</sup>Zaidi, S., Macheret, S., Vasilyak, L., Miles, R., and Ju, Y., "Increased Speed of Premixed Laminar Flames in a Microwave Resonator," AIAA Paper 2004-2721, June–July 2004.
- <sup>16</sup>Kalra, C., Gutsol, A., and Fridman, A., "Gliding Arc Discharges as a Source of Intermediate Plasma for Methane Partial Oxidation," *IEEE Transactions on Plasma Science*, Vol. 33, No. 1, 2005, pp. 32–41.
- <sup>17</sup>Kuznetsova, I. V., Kalashnikov, A. F., Gutsol, A. F., Fridman, A. A., and Kennedy, L. A., "Effect of 'Overshooting' in the Transitional Regimes of the Low-Current Gliding Arc Discharge," *Journal of Applied Physics*, Vol. 92, No. 8, 2002, pp. 4231–4237.
- <sup>18</sup>White, F., *Viscous Fluid Flow*, McGraw-Hill, New York, 1974, pp. 204–208.
- <sup>19</sup>Puri, I. K., and Seshadri, K., "Extinction of Diffusion Flames Burning Diluted Methane and Diluted Propane in Diluted Air," *Combustion and Flame*, Vol. 65, No. 2, 1986, pp. 137–150.
- <sup>20</sup>Maruta, K., Yoshida, M., Guo, H., Ju, Y., and Niioka, T., "Extinction of Low-Stretched Diffusion Flame in Microgravity," *Combustion and Flame*, Vol. 112, No. 1–2, 1998, pp. 181–187.
- <sup>21</sup>Seiser, R., Seshadri, K., Piskernik, E., and Linan, A., "Ignition in the Viscous Layer Between Counterflowing Streams: Asymptotic Theory with Comparison to Experiments," *Combustion and Flame*, Vol. 122, No. 3, 2000, pp. 339–349.

<sup>22</sup>Humer, S., Seiser, R., and Seshadri, K., "Non-Premixed and Premixed Extinction and Autoignition of C<sub>2</sub>H<sub>4</sub>, C<sub>2</sub>H<sub>6</sub>, C<sub>3</sub>H<sub>6</sub>, C<sub>3</sub>H<sub>8</sub>," *Proceedings of the Combustion Institute*, Vol. 29, 2002, pp. 1597–1604.

<sup>23</sup>Bundy, M., Hammins, A., and Lee, K. Y., "Suppression Limits of Low Strain Rate Non-Premixed Methane Flames," *Combustion and Flame*, Vol. 133, No. 3, 2003, pp. 299–310.

<sup>24</sup>Barlow, R. S., Karpetis, A. N., Frank, J. H., and Chen, J.-Y., "Scalar Profiles and NO Formation in Laminar Opposed-Flow Partially Premixed Methane/Air Flames," *Combustion and Flame*, Vol. 127, No. 3, 2001, pp. 2102–2118.

<sup>25</sup>Ju, Y., Guo, H., Maruta, K., and Liu, F., "On the Extinction Limit and Flammability Limit of Non-Adiabatic Stretched Methane-

Air Premixed Flames," *Journal of Fluid Mechanics*, Vol. 342, 1997, pp. 315–334.

<sup>26</sup>Smith, G. P., Golden, D. M., Frenklach, M., Moriarty, N. W., Eiteneer, B., Goldenberg, M., Bowman, C. T., Hanson, R. K., Song, S., Gardiner, W. C., Jr., Lissianski, V. V., and Qin, Z., GRI-Mech Homepage, Gas Research Inst., Chicago, URL: [http://www.me.berkeley.edu/gri\\_mech/](http://www.me.berkeley.edu/gri_mech/) [cited 20 December 2004].

<sup>27</sup>Gardiner, W. C., Jr., Hidaka, Y., and Tanzawa, T., "Refractivity of Combustion Gases," *Combustion and Flame*, Vol. 40, 1981, pp. 213–219.

R. Lucht  
Associate Editor

Color reproductions courtesy of the U.S. Air Force Research Laboratory.

## Theoretical analysis of the evolution from ignition kernel to flame ball and planar flame

Z. CHEN and Y. JU<sup>\*</sup>

Q1

Department of Mechanical and Aerospace Engineering, Princeton University,  
Princeton, NJ 08544, USA

Dynamics of flame kernel evolution with and without external energy addition has been investigated analytically and numerically. Emphasis is placed on the effects of radiation heat loss, ignition power and Lewis number on the correlation and transition between the initial flame kernel, the self-extinguishing flame, the flame ball, the outwardly propagating spherical flame and the propagating planar flame. The present study extends previous results by bridging the theories of the non-adiabatic stationary flame balls and travelling flames and allowing rigorous consideration of radiation heat losses. The results show that the effects of radiation heat loss play an important role in flame regimes and flame transition and result in a new isolated self-extinguishing flame. Furthermore, it is found that radiation heat losses significantly increase the critical ignition radius and result in three different dependences of the minimum ignition power on the Lewis number. Comparisons between the results from the transient numerical simulation and those from the quasi-steady state analysis show a good agreement. The results suggest that prediction of flame initiation without appropriate consideration of radiation is not acceptable.

**Keywords:** Radiation heat loss; Flame extinction; Flame initiation; Minimum ignition energy

### 1. Introduction

Understanding of flame initiation is important not only for fundamental combustion research but also for fire safety control and the development of low-emission gasoline and homogeneous charge compression ignition (HCCI) engines. When an external energy is locally deposited into a combustible mixture, there are four possible outcomes: an evolution from outwardly propagating spherical flame to planar flame; a stationary flame ball; a propagating self-extinguishing flame; or a decaying ignition kernel (partially burning hot pocket) [1–3]. The evolution of the flame kernel and the final outcome depends on the magnitude of energy addition, fuel concentration, radiation heat loss and transport and kinetic properties. Efficient flame initiation with minimum energy deposition and successful control of fire spreading highly depend on the understanding of the correlations between ignition kernels, flame balls, self-extinguishing flames and propagating spherical and planar flames, as well as the impacts of radiation intensity and the transport properties on the flame regime transitions.

It is well known that for an unstretched planar flame, radiation heat loss defines the lean and rich flammability limits of a fuel [4, 5]. If the planar flame is stretched, sub-limit flames

\*Corresponding author. E-mail: yju@princeton.edu

may exist when the Lewis number is below a critical value [6–8]. For the same reason, sub-limit flames also exist for curved flames such as spherical flames. It has been known since the work of Zel'dovich *et al.* [9] that a diffusion controlled stationary flame ball with a characteristic equilibrium radius (flame ball radius) can exist at a mixture concentration lower than the flammability limit. A stability analysis showed that the adiabatic flame balls are inherently unstable [10]. A small perturbation will cause the flame either to propagate inward and eventually extinguish or to propagate outward and evolve into a planar flame. The flame ball size is considered to be a critical parameter in controlling flame initiation [9–11]. It was in Ronney's microgravity experiments [1, 12–15] that stable flame balls and self-extinguishing flames were first observed. Theoretical and numerical studies of flame balls [16–18] demonstrated that radiation heat loss plays an important role in affecting the flame ball size and stability. A flame ball with large equilibrium radius can be stabilized by radiation heat loss. Recently, the self-extinguishing flames and self-wrinkling flames were studied by Bechtold *et al.* [19], and the effects of radiation heat loss were investigated. However, since these theoretical studies were only focused on the dynamics of separated phenomena such as flame balls and self-extinguishing flames, the travelling flames were isolated from flame balls and self-extinguishing flames. As a result, the relation between self-extinguishing flames and flame balls and the relation between flame ball size and successful flame initiation of outwardly propagating flames were not well understood.

Recognizing the importance of the missing relationship between flame balls and travelling flames, a theoretical analysis by He and Law [3] was conducted to examine the transition of a propagating spherical flame to a flame ball. Although it was concluded that radiation heat loss has a significant effect on flame transition, the impact of radiation heat loss in the unburned region was not considered. In order further to examine the effect of detailed chemistry and transport properties on the flame transition between travelling flames and flame balls, numerical simulations were conducted for hydrogen-air mixtures at normal and elevated pressures [20, 21]. The results confirmed the existence of flame transition predicted by theory and provided quantitative comparison with experimental data. Because of the tremendous computation cost of travelling flames, the numerical simulations were unfortunately only limited to hydrogen mixtures. The effects of Lewis number on the flame transition and the different contributions of radiation heat losses from burned and unburned zones on the flame transitions remain unclear. A recent study by He [22] was motivated to study the flame initiation at large Lewis numbers, but it did not consider radiation heat loss. This makes the results less realistic because near limit flame initiation is dominantly affected by radiation heat loss. Therefore, the role of the heat loss on flame transition and the correlation between the flame regimes from ignition kernels to flame balls and propagating flames remain unknown.

The present study is aimed at: (a) providing a general theoretical description of the flame transition between the initial flame kernel, the self-extinguishing flame, the flame ball and the outwardly propagating flame; and (b) bridging both the flame ball theory and the travelling flame theory with specific emphasis on the effects of Lewis number and the individual contribution of radiation heat losses from burned and unburned zones on the flame regimes, flame transition and minimum flame initiation energy and initiation kernel size. First, the mathematical model is given. Then, based on the quasi-steady assumption, an analytical expression describing the flame propagating speed is obtained and validation in limiting cases is demonstrated. The effects of radiation heat losses on flame regimes and flame transition, and ignition energy effects on flame initiation are studied. Finally, numerical simulation of the time-dependent flame initiation problem is conducted to verify the theoretical results.

## 2. Mathematical model

We consider an unsteady spherical flame kernel evolution with and without an external ignition source at the centre. By assuming constant thermal properties, the conservation equations for energy and fuel mass are given as

$$\tilde{\rho} \tilde{C}_P \frac{\partial \tilde{T}}{\partial \tilde{t}} = \frac{1}{\tilde{r}^2} \frac{\partial}{\partial \tilde{r}} \left( \tilde{r}^2 \tilde{\lambda} \frac{\partial \tilde{T}}{\partial \tilde{r}} \right) - \tilde{H} + \tilde{q} \tilde{\omega} \quad (1a)$$

$$\tilde{\rho} \frac{\partial \tilde{Y}}{\partial \tilde{t}} = \frac{1}{\tilde{r}^2} \frac{\partial}{\partial \tilde{r}} \left( \tilde{r}^2 \tilde{\rho} \tilde{D} \frac{\partial \tilde{Y}}{\partial \tilde{r}} \right) - \tilde{\omega} \quad (1b)$$

where  $\tilde{t}$ ,  $\tilde{r}$ ,  $\tilde{\rho}$ ,  $\tilde{T}$  and  $\tilde{Y}$  are time, radial coordinate, density, temperature and fuel mass fraction, respectively.  $\tilde{q}$  is the reaction heat-release per unit mass of fuel.  $\tilde{C}_P$  is the specific heat capacity at constant pressure,  $\tilde{\lambda}$  is the thermal conductivity and  $\tilde{D}$  is the mass diffusivity of fuel. To simplify further the problem in the theoretical analysis, we also adopt the commonly used constant density model [23] so that the convection flux is absent. The validation of this assumption will be made later by transient numerical simulation.  $\tilde{\omega}$  is the reaction rate for one-step irreversible reaction,  $\tilde{\rho} \tilde{A} \tilde{Y} \exp(-\tilde{E}/\tilde{R}^0 \tilde{T})$ , in which  $\tilde{A}$  is the pre-factor of Arrhenius law,  $\tilde{E}$  the activation energy, and  $\tilde{R}^0$  the universal gas constant. The volumetric radiation heat loss  $\tilde{H}$  is estimated by using the optically thin model,  $\tilde{H} = 4\tilde{\sigma} \tilde{K}_p (\tilde{T}^4 - \tilde{T}_{\infty}^4)$ , where  $\tilde{\sigma}$  is the Stefan-Boltzmann constant and  $\tilde{K}_p$  denotes the Planck mean absorption coefficient of the mixture.

By using the adiabatic planar flame speed  $\tilde{S}_L^0$  and the flame thickness  $\tilde{\delta}_f^0 = \tilde{\lambda}/\tilde{\rho} \tilde{C}_P \tilde{S}_L^0$ , the velocity, length, time, temperature and fuel mass fraction can be normalized as

$$u = \frac{\tilde{u}}{\tilde{S}_L^0} \quad r = \frac{\tilde{r}}{\tilde{\delta}_f^0} \quad t = \frac{\tilde{t}}{\tilde{\delta}_f^0/\tilde{S}_L^0} \quad T = \frac{\tilde{T} - \tilde{T}_{\infty}}{\tilde{T}_{ad} - \tilde{T}_{\infty}} \quad Y = \frac{\tilde{Y}}{\tilde{Y}_{\infty}} \quad (2)$$

where  $\tilde{T}_{\infty}$  and  $\tilde{Y}_{\infty}$  denote the temperature and fuel mass fraction in the fresh mixture, and  $\tilde{T}_{ad} = \tilde{T}_{\infty} + \tilde{Y}_{\infty} \tilde{q}/\tilde{C}_P$  is the adiabatic flame temperature of planar flame. By further attaching the coordinate to the moving flame front,  $R = R(t)$ , the non-dimensional equations take the following form

$$\frac{\partial T}{\partial t} - U \frac{\partial T}{\partial r} = \frac{1}{r^2} \frac{\partial}{\partial r} \left( r^2 \frac{\partial T}{\partial r} \right) - H + \omega \quad (3a)$$

$$\frac{\partial Y}{\partial t} - U \frac{\partial Y}{\partial r} = \frac{Le^{-1}}{r^2} \frac{\partial}{\partial r} \left( r^2 \frac{\partial Y}{\partial r} \right) - \omega \quad (3b)$$

where  $Le = \tilde{\lambda}/\tilde{\rho} \tilde{C}_P \tilde{D}$  is the Lewis number and  $U$  the flame front propagating speed,  $U(t) = dR(t)/dt$ . The radiation heat loss and chemical reaction rate are normalized, respectively, as

$$H = \frac{\tilde{H} \tilde{\delta}_f^0}{\tilde{\rho} \tilde{C}_P \tilde{S}_L^0 (\tilde{T}_{ad} - \tilde{T}_{\infty})} \quad \omega = \frac{\tilde{\omega} \tilde{\delta}_f^0}{\tilde{\rho} \tilde{S}_L^0 \tilde{Y}_{\infty}} \quad (4)$$

It can be seen the present model extends the previous theoretical flame ball models [9, 16, 17] by including travelling flames and radiation heat loss on both the burned and unburned sides, so that the correlation between flame ball and travelling flames and the impact of radiation on the flame transition between different flame regimes can be qualitatively examined and understood.

In the limit of large activation energy, chemical reaction occurs only within a very thin zone of high temperature and the reaction rate can be replaced by a Delta function with jump

conditions used at the flame front [23]

$$\omega = \exp \left[ \frac{Z}{2} \frac{T_f - 1}{\sigma + (1 - \sigma)T_f} \right] \cdot \delta(r - R) \quad (5)$$

where  $Z = \tilde{E}(1 - \sigma)/\tilde{R}^0\tilde{T}_{ad}$  is the Zel'dovich number and  $\sigma = \tilde{T}_\infty/\tilde{T}_{ad}$  the expansion ratio. The jump relations at the flame interface becomes

$$\frac{dT}{dr} \Big|_R^- = \frac{dT}{dr} \Big|_{R^+} = \frac{1}{Le} \left( \frac{dY}{dr} \Big|_{R^+} - \frac{dY}{dr} \Big|_{R^-} \right) = \exp \left[ \frac{Z}{2} \frac{T_f - 1}{\sigma + (1 - \sigma)T_f} \right] \quad (6)$$

In the present study, we also examine the impact of external energy deposition on successful flame initiation and flame transition. A constant energy flux is locally deposited in an initially homogeneous mixture. For an initial flame kernel with a radius of  $R$ , the centre of the flame kernel is located at  $r = 0$ , and  $0 \leq r \leq R$  and  $R \leq r < \infty$  are respectively the burned and unburned regions. By defining the flame as the location where fuel concentration goes to zero, the boundary conditions for temperature and fuel mass fraction can be given as

$$r = 0, \quad r^2 \partial T / \partial r = -Q, \quad Y = 0 \quad (7a)$$

$$r = R, \quad T = T_f, \quad Y = 0 \quad (7b)$$

$$r = \infty, \quad T = 0, \quad Y = 1 \quad (7c)$$

where  $Q$  is the normalized ignition power given by

$$Q = \frac{\tilde{Q}}{4\pi\tilde{\lambda}\tilde{\delta}_f^0(\tilde{T}_{ad} - \tilde{T}_\infty)} \quad (8)$$

### 3. Theoretical analysis

The unsteady problem given by equations (3a) and (3b) cannot be solved analytically. In fact, as will be demonstrated later by unsteady numerical simulations, it is reasonable to assume that in the attached coordinate moving with flame front, the flame can be considered as in quasi-steady state ( $\partial/\partial t = 0$ ). This assumption has been widely used in previous studies [10, 22, 24]. Therefore, the governing equations can be simplified to

$$-U \frac{dT}{dr} = \frac{1}{r^2} \frac{d}{dr} \left( r^2 \frac{dT}{dr} \right) - h \cdot T + \omega \quad (9a)$$

$$-U \frac{dY}{dr} = \frac{Le^{-1}}{r^2} \frac{d}{dr} \left( r^2 \frac{dY}{dr} \right) - \omega \quad (9b)$$

In addition, for the convenience of the algebraic manipulation the heat loss term  $H$  is approximated by a linear function of normalized temperature as  $H = h \cdot T$  and  $h$  is the heat loss constant which takes the following form

$$h = \frac{4\tilde{\sigma}\tilde{K}_P\tilde{\delta}_f^0(\tilde{T}^4 - \tilde{T}_\infty^4)}{\tilde{\rho}\tilde{C}_P\tilde{S}_L^0(\tilde{T} - \tilde{T}_\infty)} \approx \frac{4\tilde{\sigma}\tilde{K}_P\tilde{\lambda}}{(\tilde{\rho}\tilde{C}_P\tilde{S}_L^0)^2} \tilde{T}_{ad}^3 \quad (10)$$

Note that the radiation heat loss constant involves the radiation intensity and the fuel concentration. For any given mixture composition, an increase of  $h$  means a decrease of fuel concentration (decrease of flame speed). For methane-air flames, the heat loss constant  $h$  calculated according to equation (10) is in the range of 0.001 to 0.1.

### 3.1 Analytical solution without external energy addition

Equation (9) with boundary conditions given by equation (7) can be solved analytically for  $Q = 0$ . An exact solution of temperature and fuel mass fraction distribution can be found. For fuel lean cases, the fuel mass fraction in burned gas region ( $0 \leq r \leq R$ ) is zero and that in unburned gas region ( $R \leq r < \infty$ ) is obtained by solving equation (9b) with boundary conditions given by equations (7b) and (7c).

$$Y(r) = 1 - \int_r^\infty \frac{e^{-UL\sigma}}{\tau^2} d\tau \Big/ \int_R^\infty \frac{e^{-UL\sigma}}{\tau^2} d\tau \quad \text{for } r \geq R \quad (11)$$

As to the temperature distribution, for adiabatic flames ( $h = 0$ ), the analytical solution is

$$T(r) = \begin{cases} T_f & \text{for } 0 \leq r \leq R \\ T_f \int_r^\infty \frac{e^{-U\tau}}{\tau^2} d\tau \Big/ \int_R^\infty \frac{e^{-U\tau}}{\tau^2} d\tau & \text{for } r \geq R \end{cases} \quad (12)$$

For non-adiabatic flames, since the radiation properties in burned and unburned gases may be different, we use  $h_1$  and  $h_2$  to represent the heat loss constants in the burned and unburned regions, respectively, in order to examine the individual contribution of the radiation heat losses from these two regions. By defining  $k_i = \sqrt{U^2 + 4h_i}$  ( $i = 1, 2$ ), an analytical solution of temperature distribution is obtained

$$T(r) = \begin{cases} T_f \cdot e^{[0.5(U+k_1)(R-r)]} \frac{F(k_1r, U/k_1, -U/k_1)}{F(k_1R, U/k_1, -U/k_1)} & \text{for } 0 \leq r \leq R \\ T_f \cdot e^{[0.5(U+k_2)(R-r)]} \frac{G(-k_2r, U/k_2, -U/k_2)}{G(-k_2R, U/k_2, -U/k_2)} & \text{for } r \geq R \end{cases} \quad (13)$$

where

$$F(a, b, c) = \int_0^1 e^{at} t^b (1-t)^c dt$$

and

$$G(a, b, c) = \int_0^\infty e^{at} t^b (1+t)^c dt.$$

Note that this exact solution removes the requirement of small heat loss assumption ( $h \sim 1/Z \leq 1$ ) which is commonly used in the previous studies [16, 17, 23]. Therefore, the present study provides a more rigorous consideration of radiation modelling to understand the relation between the spherical flames and the far field propagating planar flames in the limit of  $R \rightarrow \infty$ .

By using jump relations given by equation (6), one obtains an algebraic system of equations for flame propagating speed  $U$ , flame radius  $R$  and flame temperature  $T_f$

$$\Omega \cdot T_f = \frac{1}{Le} R^{-2} e^{-UL\sigma} \Big/ \int_R^\infty \tau^{-2} e^{-UL\sigma} d\tau = \exp \left[ \frac{Z}{2} \frac{T_f - 1}{\sigma + (1-\sigma)T_f} \right] \quad (14a)$$

where

$$\Omega = \begin{cases} R^{-2} e^{-UR} \int_R^\infty \tau^{-2} e^{-U\tau} d\tau & \text{if } h_1 = 0, h_2 = 0 \\ -\frac{U+k_1}{2} + k_1 \frac{F(k_1 R, 1+U/k_1, -U/k_1)}{F(k_1 R, U/k_1, -U/k_1)} & \text{if } h_1 \neq 0, h_2 = 0 \\ +R^{-2} e^{-UR} \int_R^\infty \tau^{-2} e^{-U\tau} d\tau \\ T_f \frac{U+k_2}{2} + T_f k_2 \frac{G(-k_2 R, 1+U/k_2, -U/k_2)}{G(-k_2 R, U/k_2, -U/k_2)} & \text{if } h_1 = 0, h_2 \neq 0 \\ \frac{k_2-k_1}{2} + k_1 \frac{F(k_1 R, 1+U/k_1, -U/k_1)}{F(k_1 R, U/k_1, -U/k_1)} \\ + k_2 \frac{G(-k_2 R, 1+U/k_2, -U/k_2)}{G(-k_2 R, U/k_2, -U/k_2)} & \text{if } h_1 h_2 \neq 0 \end{cases} \quad (14b)$$

Therefore, the present study extends the study of He [22] by considering the coupling of radiation heat loss with the flame kernel evolution, which is the key mechanism for near limit flames, and allows bridging between the spherical flame limits and the flammability limit of planar flames. By numerically solving equation (14), the relation between flame propagating speed, flame radius and flame temperature and the existence of different flame regimes at different radiation heat loss constants (or different fuel concentrations) and Lewis numbers can be obtained.

### 3.2 Validation in limiting cases

In the following it will be shown that, in different limiting cases, the current model recovers the previous results of stationary flame balls [16, 17], outwardly propagating spherical flames [24] and planar flames [4, 23].

**3.2.1 Stationary flame ball.** In previous studies [16, 17], the non-adiabatic stationary flame ball was investigated via asymptotic analysis assuming small heat loss ( $h_1 = h_{in}/Z, h_2 = h_{out}/Z^2$ ) and the relation between heat loss and flame radius was obtained

$$Ln\left(\frac{R}{R_Z}\right) = L_{in}\left(\frac{R}{R_Z}\right)^2 + L_{out}\left(\frac{R}{R_Z}\right) \quad (15)$$

where

$$L_{in} = \frac{h_{in}}{6} \frac{R_Z^2 T_{fZ}}{\{\sigma + (1-\sigma)T_{fZ}\}^2}$$

and

$$L_{out} = \frac{\sqrt{h_{out}}}{2} \frac{R_Z T_{fZ}}{\{\sigma + (1-\sigma)T_{fZ}\}^2},$$

Q2  $T_{fZ}$  and  $R_Z$  are flame temperature and radius of adiabatic stationary flame ball [29].

$$T_{fZ} = \frac{1}{Le} \quad R_Z = \frac{1}{Le} \cdot \exp\left[-\frac{Z}{2} \frac{1-Le}{1-\sigma(1-Le)}\right] \quad (16)$$

In the present study, the exact solution for fuel mass fraction and temperature distribution is obtained without using small heat loss assumption. In the limit of  $U = 0$ , equation (14)

reduces to the following form for non-adiabatic stationary flame ball

$$T_f \sqrt{h_2} + T_f \frac{\sqrt{h_1}}{\tanh(\sqrt{h_1}R)} = \frac{1}{R \cdot Le} = \exp \left[ \frac{Z}{2} \frac{T_f - 1}{\sigma + (1 - \sigma)T_f} \right] \quad (17)$$

If small heat loss assumption ( $h_1 = h_{in}/Z$ ,  $h_2 = h_{out}/Z^2$ ) is used and high-order terms of  $1/Z$  are neglected, the above relation can be reduced to the same form as equation (15). Therefore, the flame ball solution [16, 17] is a limiting case of the present result.

**3.2.2 Outwardly propagating spherical flames.** A flame speed relation for propagating spherical flames was obtained by Frankel and Sivashinsky [24]. It is readily seen that the present result given by equation (14) recovers the same result in the limit of zero heat loss and large flame radius ( $h_1 = h_2 = 0$  and  $R \gg 1$ ). Specifically, for  $R \gg 1$ , the exponential integral can be represented by an asymptotic series

$$R^{-2} e^{-ULeR} \int_R^\infty \tau^{-2} e^{-ULe\tau} d\tau \approx ULe + \frac{2}{R} \quad (18)$$

By using the above expansion and defining  $V = U + 2/R$ , equation (14) reduces to the following form

$$T_f V = V + \frac{2}{R} \left( \frac{1}{Le} - 1 \right) = \exp \left[ \frac{Z}{2} \frac{T_f - 1}{\sigma + (1 - \sigma)T_f} \right] \quad (19)$$

The following relation can be immediately derived from equation (19), which is exactly the same equation given by Frankel and Sivashinsky [24]

$$VLnV = \frac{Z}{R} \left( \frac{1}{Le} - 1 \right) \quad (20)$$

As such, the present models are valid in both limits of flame ball and travelling flames and can provide the relationship and transition mechanism between these two flames during flame kernel growth.

**3.2.3 Planar flame speed and flammability limit.** In the limit of  $R \rightarrow \infty$ , the functions  $F$  and  $G$  become

$$\frac{F(k_1 R, 1 + U/k_1, -U/k_1)}{F(k_1 R, U/k_1, -U/k_1)} \rightarrow 1 \quad \frac{G(-k_2 R, 1 + U/k_2, -U/k_2)}{G(-k_2 R, U/k_2, -U/k_2)} \rightarrow 0$$

Therefore, equation (14) reduces to

$$T_f \frac{k_1 + k_2}{2} = U = \exp \left[ \frac{Z}{2} \frac{T_f - 1}{\sigma + (1 - \sigma)T_f} \right] \quad (21)$$

Asymptotically, when the heat loss is in the order of  $1/Z$  in the limit of large Zeldovich number ( $h_1 = h_{in}/Z$ ,  $h_2 = h_{out}/Z$ , and  $Z \gg 1$ ), equation (21) recovers the classical theory of flammability limit for planar flames [4, 23]

$$L = -U^2 \ln(U^2) \quad \text{with} \quad L = h_{in} + h_{out} = Z(h_1 + h_2) \quad (22)$$

The flammability limit is defined by  $L = 1/e$  and  $U = e^{-1/2}$ . Therefore, equation (14) is a general solution to describe the dynamics of flame kernel growth and depicts a clear correlation between the ignition kernel, flame ball, propagating curved flames and planar flames. In the following section, we will demonstrate the role of radiation heat loss, Lewis number and external energy addition in flame regimes and flame initiation.

### 3.3 Effects of radiation heat losses from the burned and unburned regions

Radiation heat losses from the burned and unburned zones affect the flame temperature in different ways. Heat loss from the unburned zone will directly reduce the flame temperature. However, heat loss from the burned region only affects the flame temperature via the heat conduction loss from the flame. In addition, the radiation heat loss depends on the ratio of high temperature volume and the flame front surface area. As the flame kernel grows, the ratio changes significantly. For example, the normalized radiation heat losses from burned and unburned zones can be given as

$$H_{in} = h_1 \int_0^R T(r) \cdot r^2 dr \left/ \left( R^2 \frac{dT}{dr} \Big|_{R^-} - R^2 \frac{dT}{dr} \Big|_{R^+} \right) \right. \quad (23a)$$

$$H_{out} = h_2 \int_R^\infty T(r) \cdot r^2 dr \left/ \left( R^2 \frac{dT}{dr} \Big|_{R^-} - R^2 \frac{dT}{dr} \Big|_{R^+} \right) \right. \quad (23b)$$

where  $(R^2 \frac{dT}{dr} \Big|_{R^-} - R^2 \frac{dT}{dr} \Big|_{R^+})$  is the total heat generation from chemical reaction. By using the temperature distribution obtained in equation (13), the ratio of these heat losses in the limit of small and large flame radius becomes

$$\frac{H_{in}}{H_{out}} = \begin{cases} 0 & \text{if } R \rightarrow 0 \\ \frac{h_1}{h_2} \cdot \frac{\sqrt{1 + 4h_2/U^2} + 1}{\sqrt{1 + 4h_1/U^2} - 1} & \text{if } R \rightarrow \infty \end{cases} \quad (24)$$

The above qualitative result shows that the radiation heat losses from burned and unburned zones will have different impact on flame temperature and flame transition. Unfortunately, in previous theoretical studies [3, 22], the radiation heat loss in the unburned region was simply neglected and the competing role of radiation heat losses from the unburned and burned zones as the flame kernel grows were not well understood.

In the following we will take an example of CH<sub>4</sub>-air flames and use equation (14) to demonstrate how differently the radiation heat losses from the burned and unburned regions affect the flame temperature and speed. For flames around stoichiometric equivalence ratio, we choose  $Z = 10$  and  $\sigma = 0.15$ . Equation (23) is used to evaluate the radiation heat losses from different zones and the total normalized radiation heat loss is the summation of them  $H_{all} = H_{in} + H_{out}$ .

Figure 1 shows the dependence of normalized heat loss and flame propagating speed on the flame radius for  $Le = 1$  and  $h = 0.015$ . It is seen that there are two branches in the  $U - R$  diagram: the fast stable branch *abc* and the slow unstable branch *cde*. At point *c*, the flame is extinguished at a finite propagating speed because the normalized heat loss reaches its maximum on the fast flame branch *abc*. It is also observed that the normalized total heat loss changes non-monotonically as the flame radius increases. There exists a minimum value as the flame reaches point *b* for fast branch and point *d* for slow branch. This phenomenon can only be explained by considering the individual contributions of heat losses in the burned and unburned zones.

The dependences of the normalized radiation heat losses in the burned and unburned zones,  $H_{in}$  and  $H_{out}$ , are shown in figure 1(b). It is seen that  $H_{in}$  increases monotonically with flame radius while  $H_{out}$  decreases monotonically with flame radius. It is shown that the radiation heat loss from the unburned zone  $H_{out}$  remains nearly constant when flame radius is larger than 20 and it is one order smaller than  $H_{in}$  ( $H_{out}/H_{in} < 0.1$  when  $R > 20$ ). This means that the effect of heat loss in the unburned zone becomes weaker as the flame grows, but it does not mean that the heat loss from the unburned zone can be neglected because heat losses from these zones affect flame temperature in different ways. The rapid increase of flame speed and

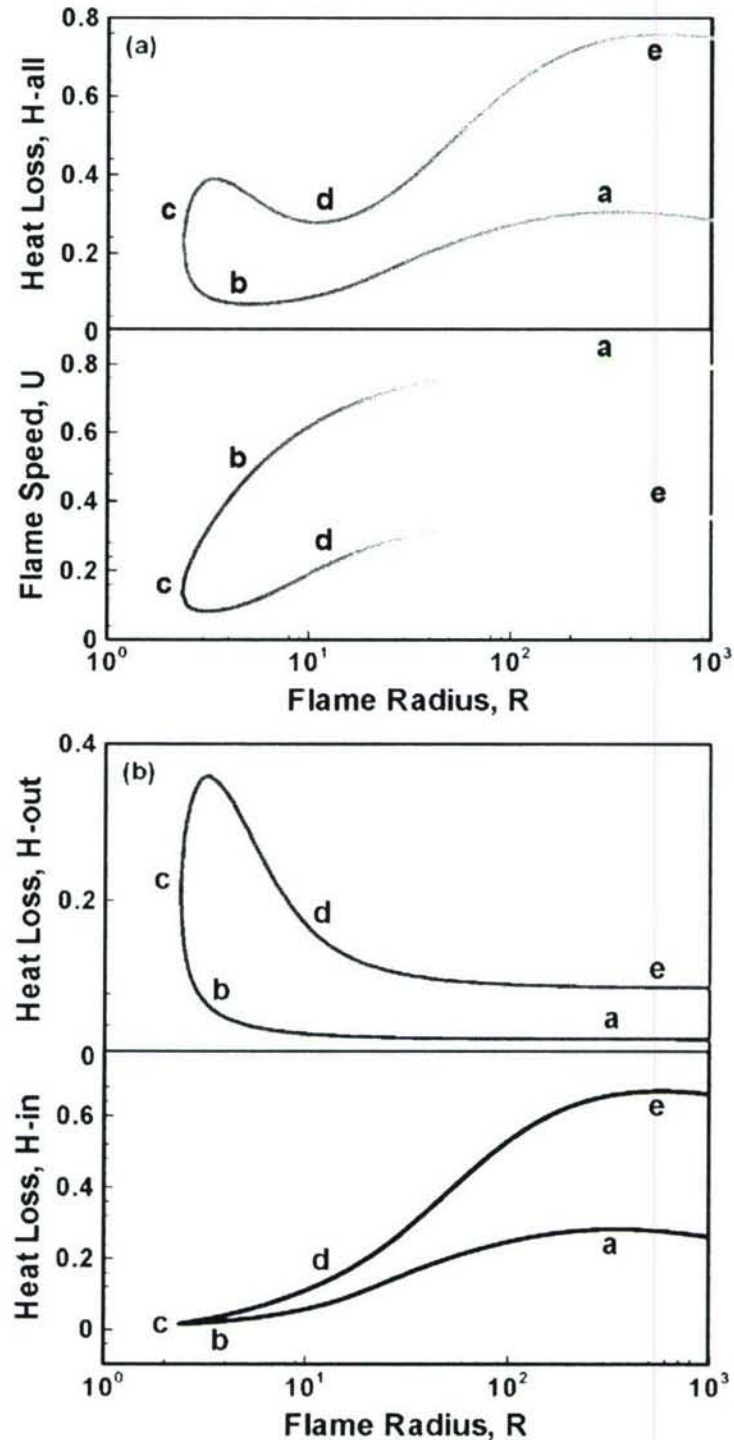


Figure 1. The dependence of normalized radiation heat loss and flame propagating speed on flame radius for  $Lc = 1$  and  $h = 0.015$ ; (a),  $H_{all} = R$  and  $U = R$ ; (b),  $H_{in} = R$  and  $H_{out} = R$ .

the peak of the radiation heat loss in the region of  $R < 20$  are caused by the competition of radiation heat losses from the burned and unburned zones.

For the radiation heat loss larger than the critical heat loss ( $L = 1/e$  and  $h_c = 0.0184$ ) of the flammability of the planar flame, a flame will not exist at large flame radius. Figure 2 shows the dependences of normalized heat loss and flame propagating speed on the flame radius for  $Le = 1$  and  $h = 0.0197$ . It is interesting to note that propagating spherical flame still exists at intermediate flame radii and there are two extinction limits, respectively, at small and large radii. The normalized total heat loss also changes non-monotonically and peaks at both extinction limits. This indicates that the extinction at small radius is caused by the heat loss in the unburned zone and the extinction at large radius by that from the burned zone [figure 2(b)]. The appearance of the extinction limit at small flame radius has not been reported in previous studies and the existence of this extinction limit will significantly affect the ignition kernel size for successful flame initiation. Therefore, in order to understand the flame kernel evolution adequate inclusion of the effect of radiation heat loss in the unburned gas is particularly important.

### 3.4 Correlation between different flame regimes at different Lewis numbers

Figure 3(a) shows the flame propagating speed as a function of flame radius for various radiation heat loss constants (or different fuel concentrations) with  $Le = 1$ . To demonstrate further the importance of heat loss in the unburned zone, the results with radiation heat loss only from the burned gas is shown in figure 3(b). In figure 3, solutions on the horizontal axis of  $U = 0$  denote the stationary flame balls [equation (17)] and those on the vertical axis at large flame radius denote the planar flame [equation (21)]. The solution curves between the flame ball solutions and the planar flame solutions represent the travelling spherical flames. It is seen from figure 3(a) that for adiabatic flame ( $h = 0$ ), the quasi-steady state flame ball exists at small radius. As the flame size grows the flame speed increases rapidly because of the increase of diffusion flux and eventually reaches the planar flame speed ( $U = 1$ ) at a large flame radius. When there is a small radiation heat loss ( $h = 0.005$ ), the quasi-steady state flame ball solution does not exist, and at a small flame radius, flame extinguishes at a finite flame speed. As the flame radius increases, flame speed increases and ultimately reaches the corresponding non-adiabatic planar flame speed. As the radiation heat loss further increases and becomes larger than the critical heat loss associated with the flammability limit, as explained in figure 2(a), sub-limit flames only exist at intermediate sizes and the radiation heat losses from the unburned and burned zones yield two extinction limits at small and large flame radii, respectively. To distinguish this flame regime from the self-extinguishing flame observed in the microgravity experiments [1, 13], we will refer to it as an isolated self-extinguishing flame because this flame cannot be initiated by a small localized ignition source. When only the radiation heat loss in the burned zone is considered [figure 3(b)], it is seen that the quasi-steady state solution of stationary flame ball exists for all heat losses. This obviously contradicts to the experimental observation [14]. Therefore, it can be concluded that the present model can successfully predict the existence of multiple flame regimes and the transition between the flame ball and travelling flame. Radiation from the unburned zone yields a new flame island at intermediate flame radii. The exclusion of radiation heat loss from unburned zone prevents correct prediction of the flame regimes and their transitions.

The flame speed dependences on flame radius for  $Le = 0.8$  and  $1.2$  are shown in figures 4(a) and 5(a), respectively. For comparison, the results without radiation heat loss in the unburned zone are shown in figures 4(b) and 5(b). The effects of Lewis number on the flame regime and the flame transition can be found by comparing the results with figure 3. It can be seen

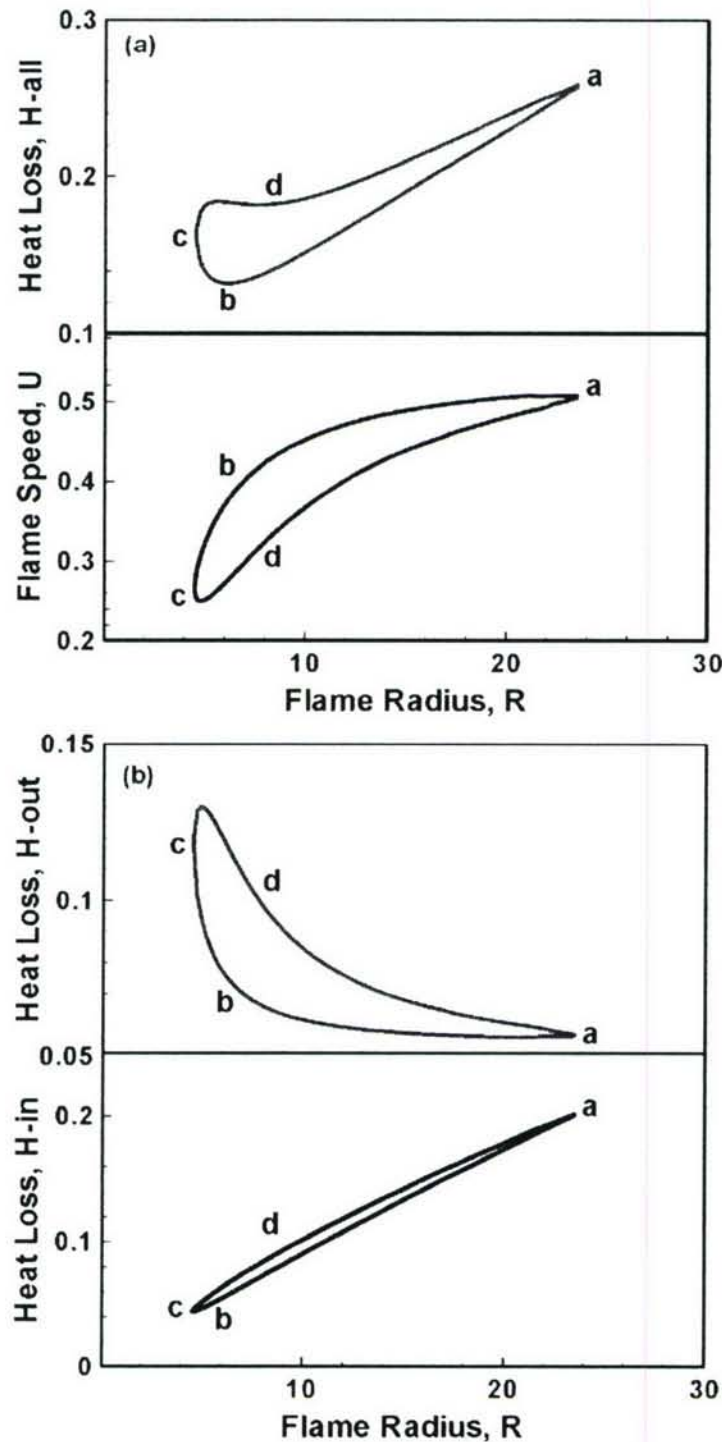


Figure 2. The dependence of normalized radiation heat loss and flame propagating speed on flame radius for  $Lc = 1$  and  $h = 0.0197$ : (a),  $H_{in} = R$  and  $U = R$ ; (b),  $H_{in} = R$  and  $H_{out} = R$ .

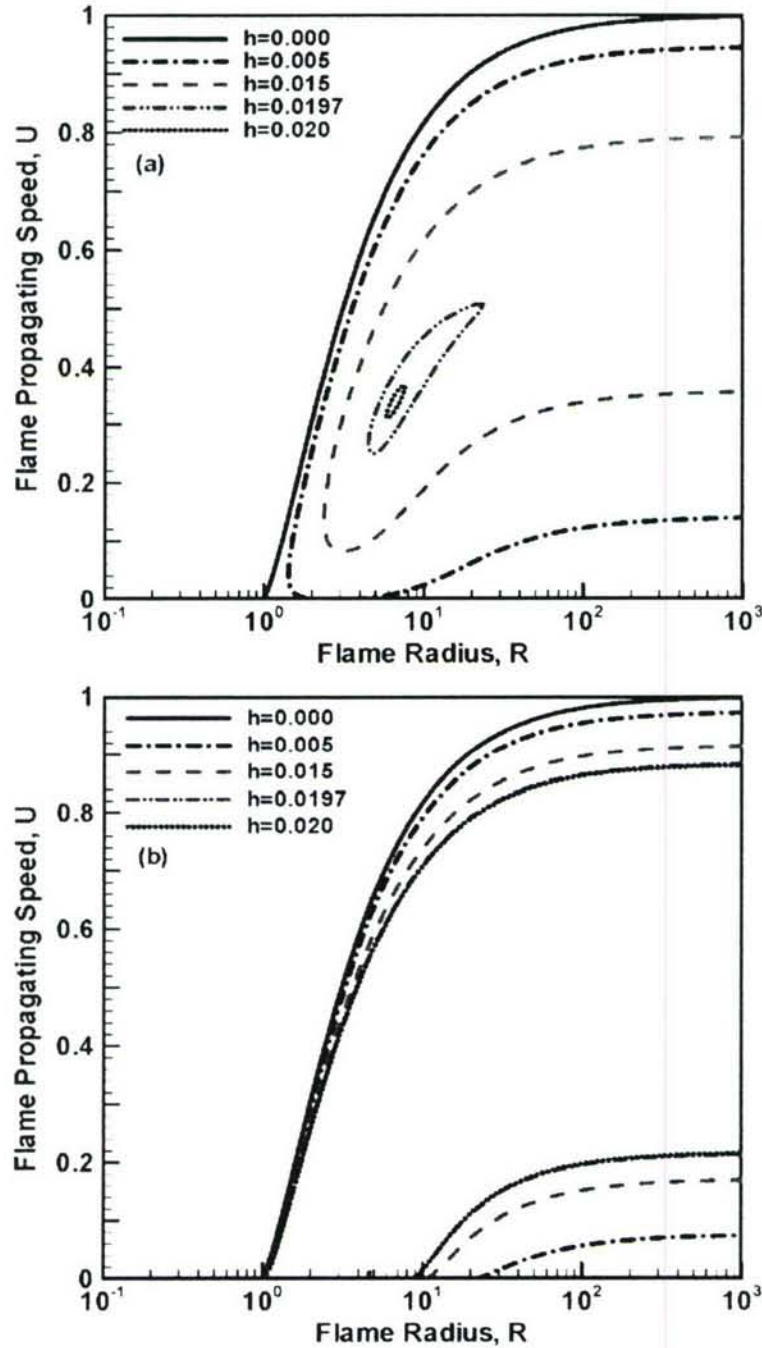


Figure 3. Flame propagating speed as a function of flame radius for  $Le = 1.0$  with different values of radiation heat loss constants: (a), with heat losses in both the burned and unburned zones; (b), with heat loss only in the burned zone.

that in a mixture at  $Le = 0.8$ , depending on the fuel concentration, there exists five different flames: the flame ball, the outwardly propagating spherical flame, the planar flame, the self-extinguishing flame (SEF) and the isolated self-extinguishing flame (ISEF). Because of the Lewis number effect, the sub-limit SEF and ISEF can exist at much lower concentrations than

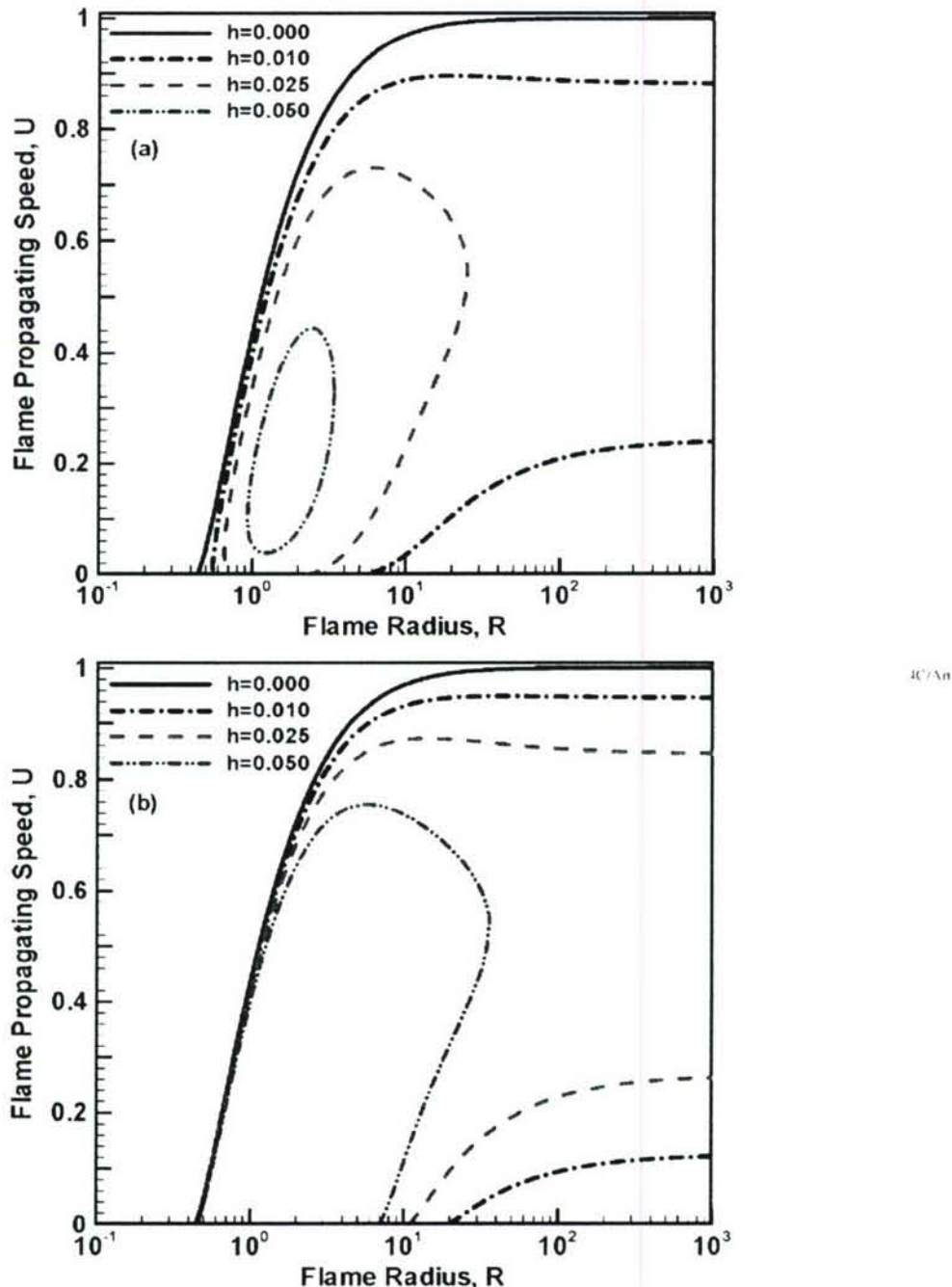


Figure 4. Flame propagating speed as a function of flame radius for  $Le = 0.8$  with different values of radiation heat loss constants: (a), with heat losses in both the burned and unburned zones; (b), with heat loss only in the burned zone.

the flammability limit of the planar flame. In addition, stationary flame balls start to appear at small radiation heat losses. These results are consistent with the experimental observation [1, 12–15]. At  $Le = 1.2$ , figure 5(a) shows that neither flame ball nor sub-limit SEF or ISEF exist. At large radiation heat loss or low fuel concentration, a flame does not exist because of the

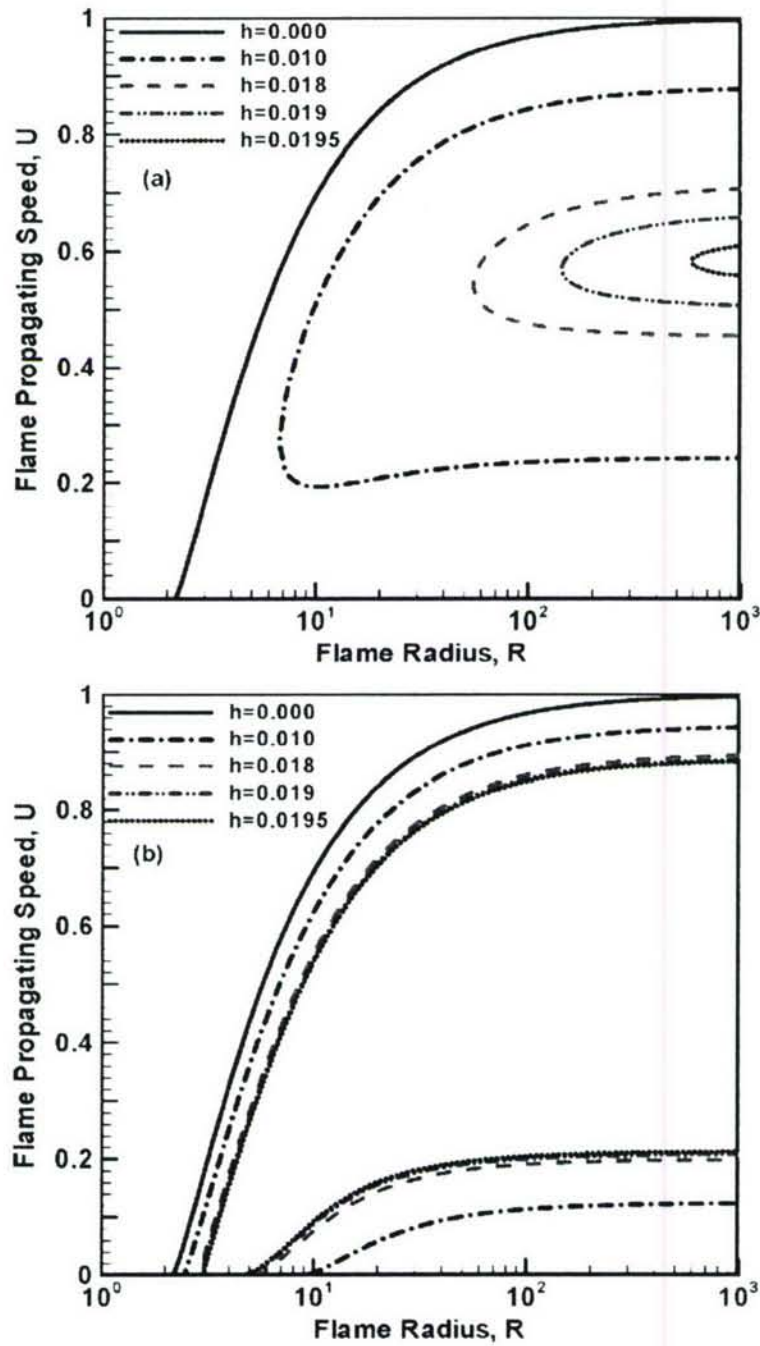


Figure 5. Flame propagating speed as a function of flame radius for  $Le = 1.2$  with different values of radiation heat loss constants; (a), with heat losses in both the burned and unburned zones; (b), with heat loss only in the burned zone.

combined effect of radiation heat loss in the unburned gas and of the flame stretch. Obviously, the predictions without inclusion of radiation heat loss in the unburned zone [figures 4(b), 5(b)] do not correctly predict this phenomenon. For example, figure 5(b) shows that flame balls exist at all fuel concentrations. This is contrary to experimental observation.

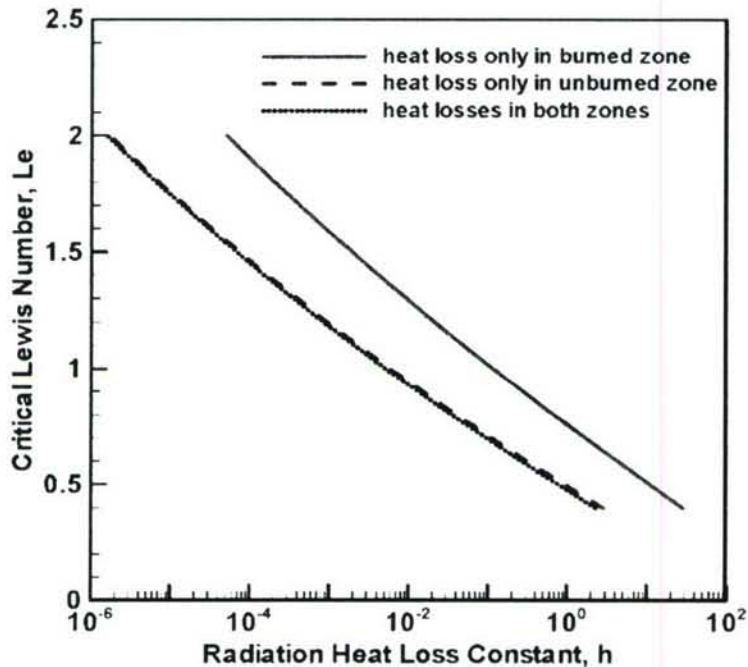


Figure 6. The dependence of critical Lewis number above which no solution exists for stationary flame ball for a given heat loss constant.

The effects of radiation heat loss on the critical Lewis number below which a quasi-steady state flame ball solution exists are shown in figure 6 for different radiation models. It is seen that for a large radiation heat loss constant, stationary flame balls exist only for small Lewis number, which is consistent with the experimental results in microgravity [1, 12–15]. The importance of radiation heat loss in the unburned zone can also be observed. It is seen that the effect of radiation heat loss on the critical Lewis number for flame ball is dominated by the heat loss in the unburned zone. This conclusion is different from the previous studies in which the radiation heat loss in the unburned region was often ignored. This is because the flame ball size is very small and the diffusion zone is very broad at zero and small flame speed. As a result, the radiation heat loss in the burned zone plays a negligible role in affecting the critical Lewis number.

### 3.5 Effect of ignition energy on flame initiation

We now consider the case in which an external energy flux is deposited in the centre of quiescent mixture and to examine how the ignition energy affects the flame diagram and the transition trajectory.

In the quasi-steady model, the ignition energy  $Q$  is modelled as a boundary condition (related discussions are presented at the end of this section), that is

$$r^2 \partial T / \partial r|_{r=0} = -Q \text{ with } \epsilon \rightarrow 0 \quad (25)$$

The fuel mass fraction distribution is the same as that obtained in section 3.1 and the temperature distribution in the burned gas region ( $0 \leq r \leq R$ ) is given by

$$T(r) = T_0(r) + Q \cdot T_Q(r) \quad (26)$$

where  $T_0(r)$  is the solution in the case of  $Q = 0$  [equations (12) and (13)] and  $T_Q(r)$  is the temperature increase caused by the external ignition power

$$T_Q(r) = \begin{cases} \int_r^R \frac{e^{-U/\tau}}{\tau^2} d\tau & \text{if } h_1 = 0 \\ e^{-0.5(U+k_1)r} \left[ C_1 \cdot G\left(-k_1 r, \frac{U}{k_1}, -\frac{U}{k_1}\right) + C_2 \cdot F\left(k_1 r, \frac{U}{k_1}, -\frac{U}{k_1}\right) \right] & \text{if } h_1 \neq 0 \end{cases} \quad (27)$$

with

$$C_1 = \left[ \varepsilon^2 \frac{U+k_1}{2} G(-k_1 r, U/k_1) + \varepsilon^2 k_1 G(-k_1 r, 1+U/k_1 - U/k_1) \right]^{-1}$$

and

$$C_2 = -C_1 \cdot G(-k_1 R, U/k_1 - U/k_1) / F(k_1 R, U/k_1 - U/k_1).$$

By using the jump relations given by equation (6), the flame speed equation can be obtained as

$$\Omega \cdot T_f + \Omega_Q \cdot Q = \frac{1}{Le} R^{-2} e^{-U Le R} / \int_R^\infty \tau^{-2} e^{-U L e \tau} d\tau = \exp \left[ \frac{Z}{2} \frac{T_f - 1}{\sigma + (1-\sigma) T_f} \right] \quad (28a)$$

where  $\Omega$  is given by equation (14b) and

$$\Omega_Q = \begin{cases} -R^{-2} e^{-U R} & \text{if } h_1 = 0 \\ k_1 e^{-0.5(U+k_1)R} \left[ -C_1 \cdot G\left(-k_1 R, 1+\frac{U}{k_1}, -\frac{U}{k_1}\right) + C_2 \cdot F\left(k_1 R, 1+\frac{U}{k_1}, -\frac{U}{k_1}\right) \right] & \text{if } h_1 \neq 0 \end{cases} \quad (28b)$$

The effect of ignition power and Lewis number on flame transition can be studied by solving equation (28) numerically. Figures 7 to 9 show the flame speed as a function of flame radius with different values of ignition power, radiation heat loss constant, and Lewis number. Figure 7(a) shows the results for  $Le = 1.0$  and  $h = 0$ . The solid line  $ab$  shows the result of zero ignition energy ( $Q = 0$ ) which is the same as that in figure 3(a). In this case, the outwardly propagating spherical flame only exists beyond a finite flame radius  $R_b = 1.0$ . When an external energy is deposited, it is seen that the flame transition trajectory is changed. At a low ignition energy of  $Q = 0.05$ , owing to the increase of flame temperature, the travelling flame branch  $ab$  is extended to branch  $ac$  and the critical flame initiation radius is reduced to  $R_i = 0.72$ . At the same time, a new branch (ignition kernel)  $de$  is formed at small radius and quenches as it grows. Therefore, flame initiation is not successful. However, by increasing the ignition power to  $Q = 0.092$ , a new ignition kernel branch  $fg$  starts to merge with the travelling flame branch  $ag$ , indicating that an outwardly propagating spherical flame can be successfully initiated via the flame transition curve  $fga$ . Therefore, we can define the critical ignition power ( $Q_C = 0.092$ ) above which the flame kernel branch always merges with the travelling flame branch.

Figure 7(b) shows the results of non-adiabatic flame evolution diagram for  $Le = 1.0$  and  $h = 0.01$ . Unlike the adiabatic case, no flame ball solution exists and the outwardly propagating spherical flame only exists at a much larger flame radius with a finite flame speed due to the effects of radiation heat loss. When ignition energy is deposited, the new flame kernel branch starts to merge with the travelling flame branch at  $Q = 0.107$  and forms three new flame branches, a fast flame transition branch  $dja$  and a slow branch isolated  $ic$  and an ISEF branch  $egh$ . As the ignition power increases, the ISEF branch degenerates and the fast transition branch becomes more monotonic, indicating a successful flame transition from ignition kernel to a

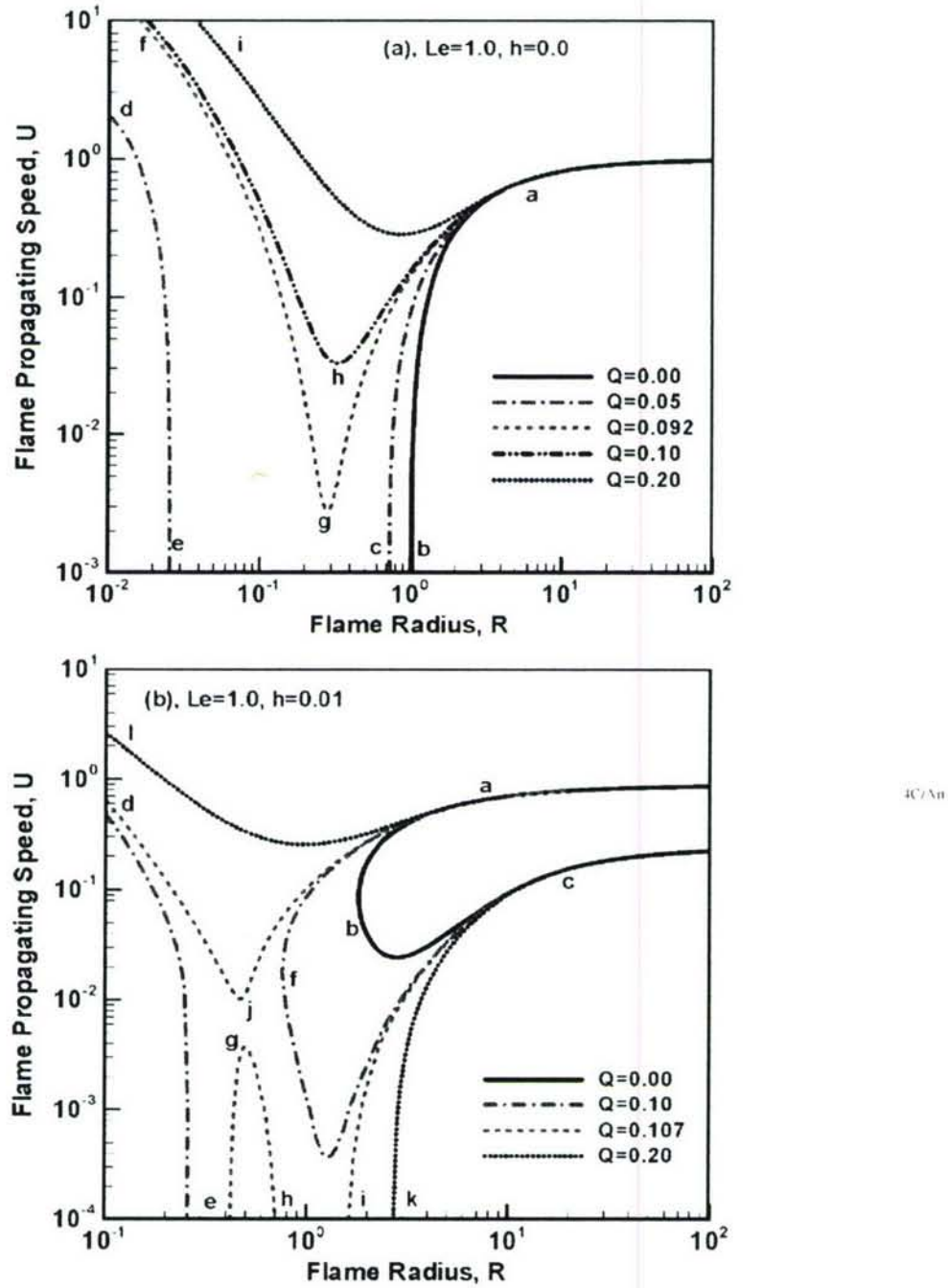


Figure 7. Flame propagating speed as a function of flame radius with different values of ignition power for  $Le = 1.0$ : (a),  $h = 0.0$ ; (b),  $h = 0.01$ .

travelling flame. Note that the radiation heat loss not only changes the flame bifurcation but also significantly increases the critical ignition radius (from  $R_f = 0.3$  to 0.6) and the critical ignition energy (from  $Q = 0.092$  to 0.107). Therefore, the adiabatic model does not adequately describe the flame initiation trajectory. This conclusion is different from that of a previous study [22].

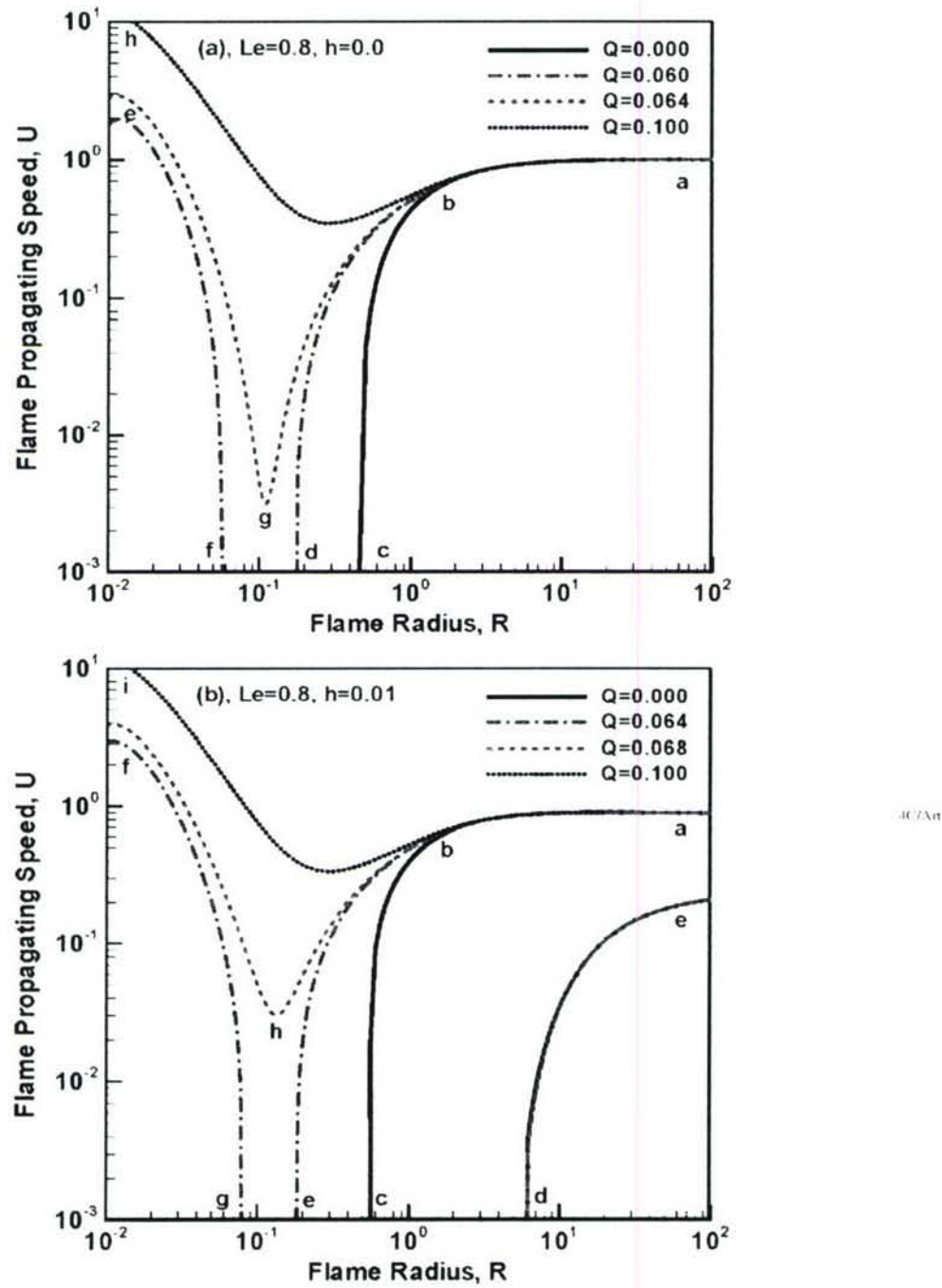


Figure 8. Flame propagating speed as a function of flame radius with different values of ignition power for  $Le = 0.8$ : (a),  $h = 0.0$ ; (b),  $h = 0.01$ .

The adiabatic and non-adiabatic flame trajectory with external ignition energy for  $Le = 0.8$  and 1.2 are shown in figures 8 and 9. For the case of small Lewis number (figure 8), owing to the Lewis number effect, the critical ignition radius becomes much smaller and the critical ignition power decreases. Moreover, the radiation effect becomes weaker with the decrease of

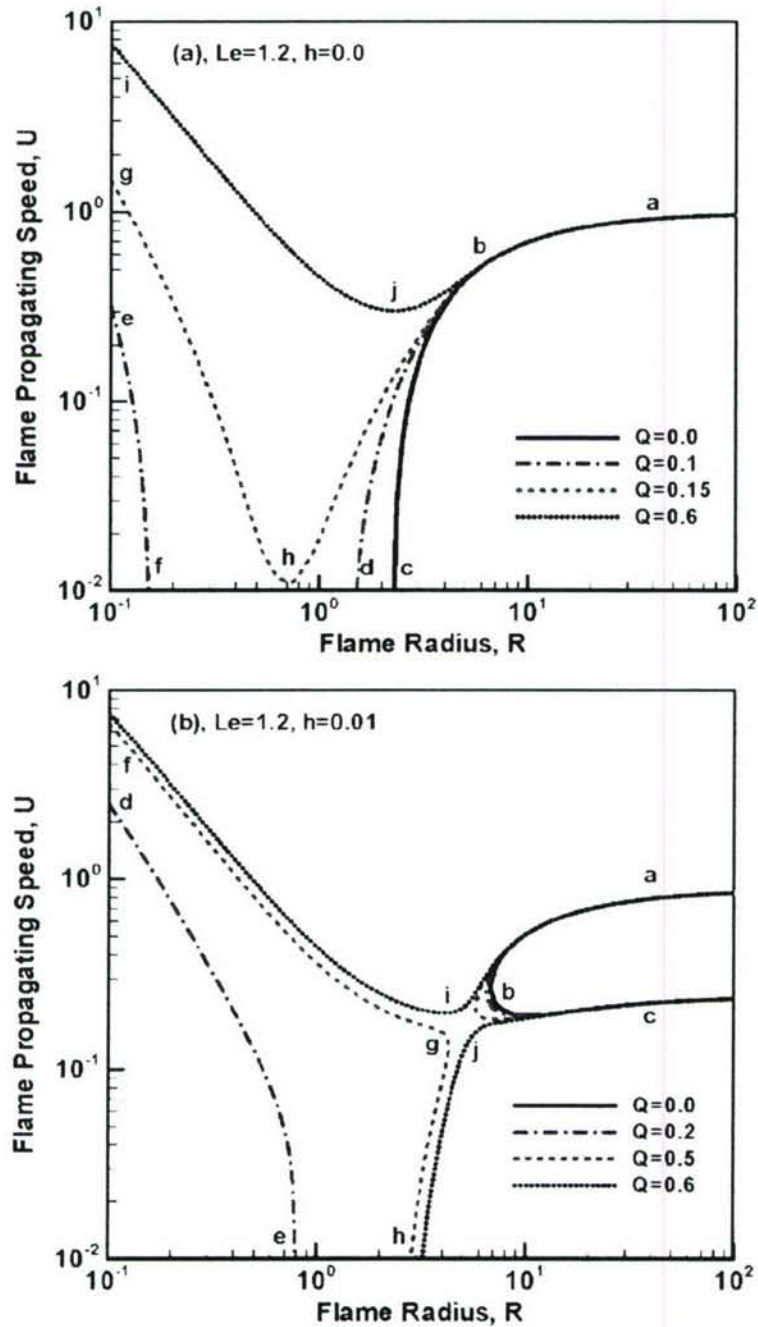


Figure 9. Flame propagating speed as a function of flame radius with different values of ignition power for  $Le = 1.2$ : (a),  $h = 0.0$ ; (b),  $h = 0.01$ .

Lewis number. However, at a large Lewis number (figure 9), both the critical ignition radius and the critical ignition power significantly increase. In particular, the adiabatic model [figure 9(a)] not only does not predict a correct flame bifurcation but also fails to predict the size of critical ignition kernel. This conclusion has a significant implication for the gasoline spark ignition process, particularly with  $\text{CO}_2$  recirculation.

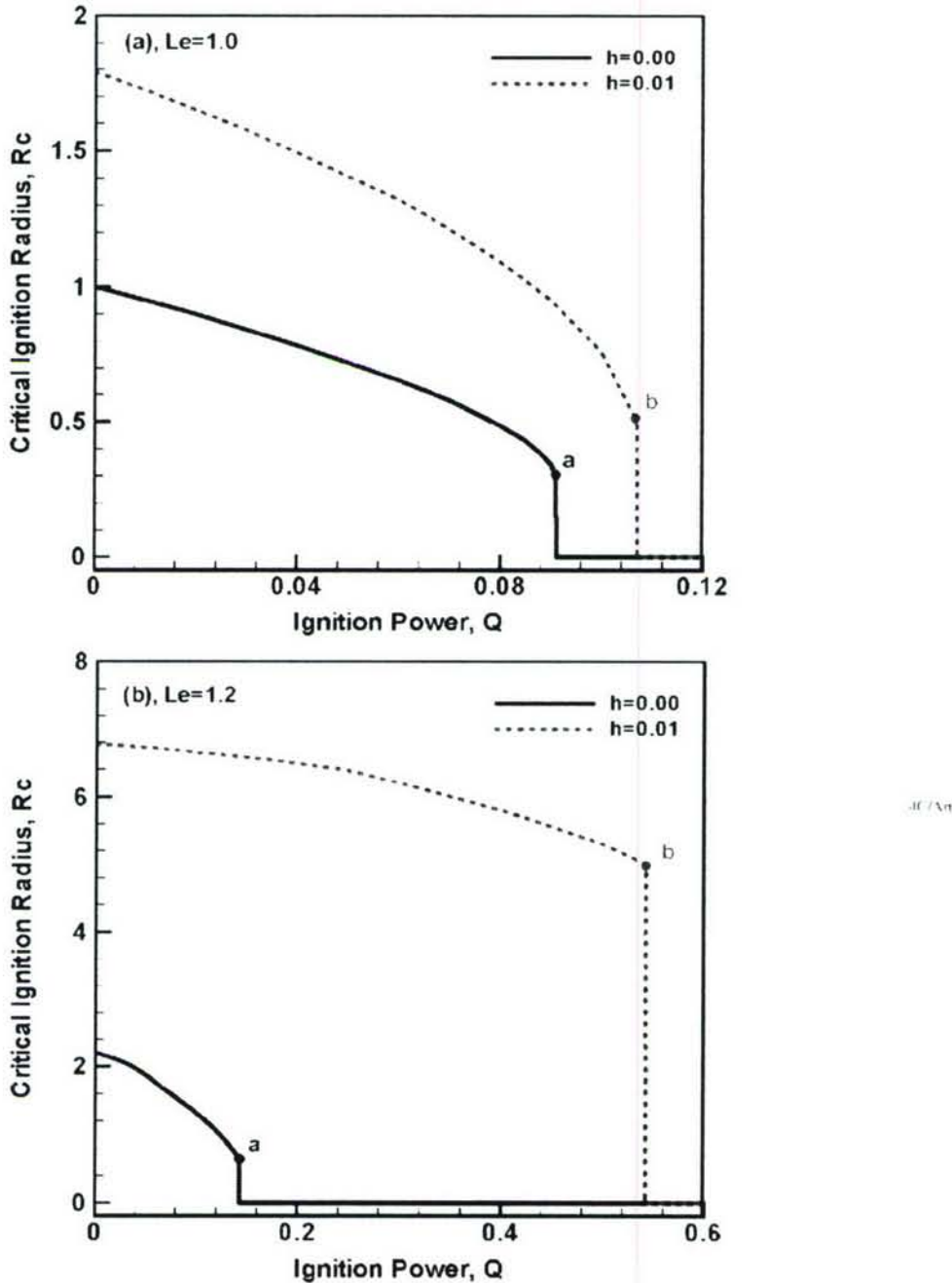


Figure 10. Critical ignition radius with respect to ignition power for adiabatic and non-adiabatic cases: (a),  $Le = 1.0$ ; (b),  $Le = 1.2$ .

Figure 10 shows the comparison of the critical ignition radius for adiabatic and non-adiabatic flames at  $Le = 1.0$  and  $1.2$ , respectively. For  $Le = 1.0$ , it is seen that for both cases, the critical ignition radius decreases with the increase of ignition power. However, the critical ignition radius for radiating flames is much greater than that of adiabatic flames. When the ignition power is larger than the critical ignition power ( $Q_a$  and  $Q_b$ ), the critical ignition radius goes

to zero, which means that outwardly propagating spherical flame can be successfully initiated from the centre. For  $Le = 1.2$ , the increase of the critical ignition radius owing to radiation heat loss becomes more profound. In addition, the ratio of critical ignition power between the radiative and adiabatic cases also becomes much larger.

The critical ignition power as a function of Lewis number for adiabatic and non-adiabatic cases is shown in figure 11(a). It is seen that when Lewis number is smaller than 0.8, the critical ignition power for adiabatic and non-adiabatic cases is nearly the same. However, as the Lewis number increases the dependence becomes significantly different. For the adiabatic mixture, the logarithm of critical ignition power only increases linearly with the increase of Lewis number. However, for the radiative mixture, the dependence of the critical ignition energy can be divided into three different regimes: a linear region at small Lewis numbers ( $Le < 1$ ); a nonlinear region at intermediate Lewis numbers ( $1 < Le < 1.6$ ); and a linear region at high Lewis numbers ( $Le > 1.6$ ). The appearance of the nonlinear region is owing to the coupling of the radiation heat loss from the unburned region and the Lewis number effect [figure 11(b)]. Therefore, the radiation heat loss from unburned gas region significantly affects the ignition energy. The present results have a strong relevance in ignition enhancement in internal combustion engines involving natural gas and large hydrocarbon fuels ( $Le > 1$ ).

Note that ignition is an essentially transient process. Depending on the relative magnitude of characteristic times of external heating, chemical reaction, travelling acoustic wave and heat conduction, there are fast-nondiffusive-ignition [25] and thermal-diffusive-ignition [26]. In the current study, the constant density assumption is used and the acoustic effect is neglected because its timescale is far shorter than the thermal diffusion timescale. Therefore, only the thermal-diffusive-ignition is investigated here. It is reasonable because in the practical device the initial flame kernel size is much smaller than the volume of combustion chamber so that the pressure increase can be neglected. Unlike the work of Vázquez-Espí and Liñán [26], in which the unsteady-diffusion-reaction equations similar to equation (1) were solved numerically and radiation heat loss was not considered, here we present a general theory [equation (28)] based on the quasi-steady assumption in which radiation heat loss is included. The shortcoming of current analysis is that the ignition energy deposition is modelled as a boundary condition [equation (25)]; while in practice it should be resolved in time and space. The employment of such a steady state energy deposition is for the purpose to seek analytical solution. However, this simplification does not prevent the model from producing qualitatively correct results. It will be shown in the next section that the results from the current theoretical analysis based on the quasi-steady assumption agree well with those from fully transient numerical simulations.

#### 4. Numerical modelling of the unsteady effects

In order to confirm the validity of the quasi-steady state assumption used in the previous analysis, we performed numerical simulations of the time-dependent flame initiation problem. The non-dimensional form of equations (1a) and (1b) under constant density assumption is solved numerically by means of an implicit finite volume method. To numerically resolve the moving flame front, a ten-level adaptive grinding algorithm has been developed [27]. The mesh addition and removal are based on the first and second order gradients of the temperature and reaction rate distributions. Uniform grids of 0.00125–0.01 (length normalized by flame thickness) are used in the reaction zone and kept moving with the flame front. The following finite reaction rate is used in the numerical simulation

$$\omega = \frac{1}{2Le} \cdot Y \cdot Z^2 \cdot \exp \left[ \frac{Z(T-1)}{\sigma + (1-\sigma)T} \right] \quad (29)$$

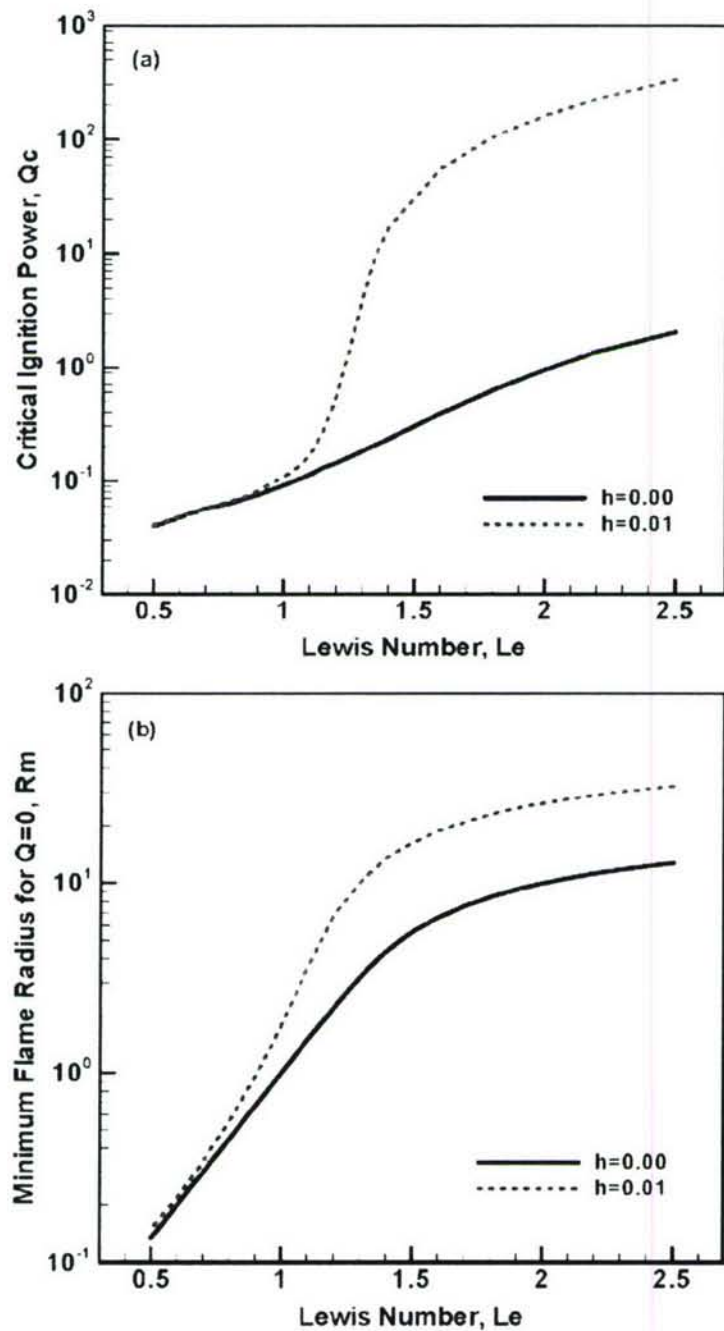


Figure 11. (a) Critical ignition power with respect to Lewis number for adiabatic and non-adiabatic cases; (b) smallest flame radius with respect to Lewis number for adiabatic and non-adiabatic cases without ignition power.

The boundary conditions are the same as those given by equations (7a) and (7c). With an initial uniform temperature and fuel mass fraction distribution of  $T(r) = 1 - Y(r) = 0$ , the unsteady flame initiation problem is resolved.

To justify the validity of the quasi-steady state assumption used in theoretical analysis, flame speeds at different flame radii predicted from theoretical analysis are compared with

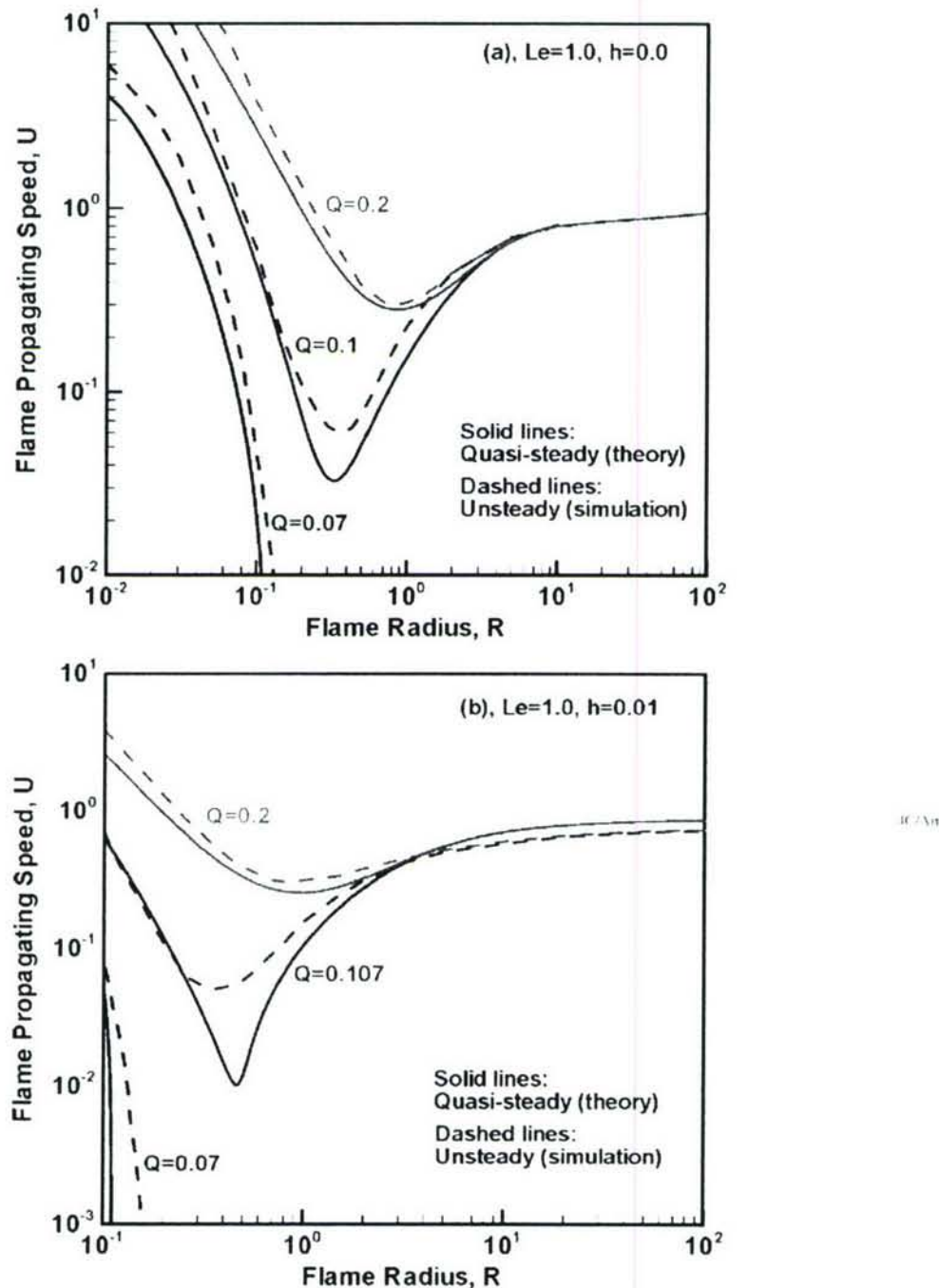


Figure 12. Comparison of flame propagating speeds predicted by numerical simulation and theoretical analysis for  $Le = 1.0$ : (a),  $h = 0.0$ ; (b),  $h = 0.01$ .

those from numerical simulations, in which the flame propagating speed is calculated from the flame front history, i.e.  $U = dR/dt$ , where the flame front is defined as where the maximum heat release appears. Figure 12 shows the results for  $Le = 1$  without and with radiation heat loss. It is seen that the results from theory agree reasonably well with those from the unsteady

simulations. As with most other studies on flame dynamics, the unstable branches predicted by theoretical analysis as labelled by  $egh$  and  $kc$  in figures 7(b) could not be recovered from numerical simulations. Comparisons for other Lewis numbers without and with radiation heat loss are also made. The qualitatively agreement is obtained.

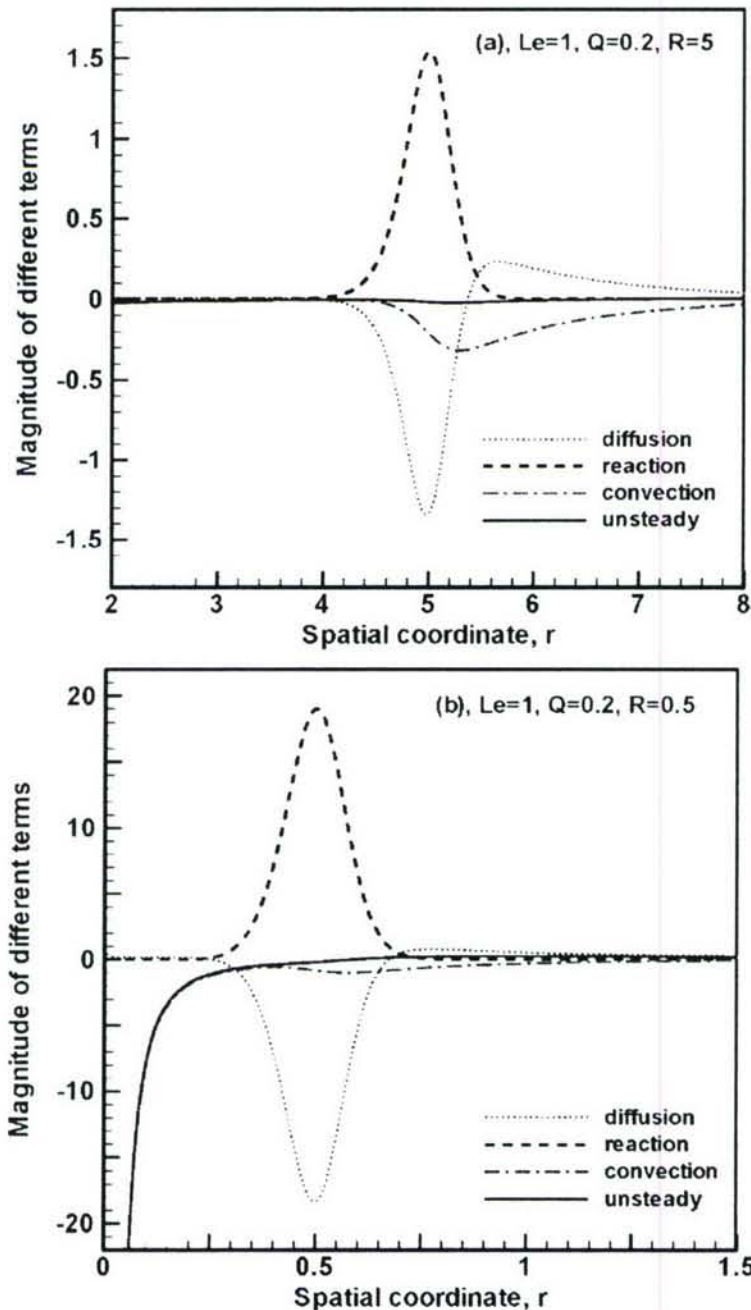


Figure 13. The unsteady term ( $\partial T / \partial t$ ), convection term ( $U \partial T / \partial r$ ), diffusion term ( $(q^2 T / r^2 \partial r) / h^2 \partial r$ ), and reaction term ( $\omega$ ) in equations (3a) predicted from numerical simulation for flames at different flame radii with  $Le = 1.0$  and  $Q = 0.2$ : (a),  $R = 5.0$ ; (b),  $R = 0.5$ .

In order to evaluate quantitatively the magnitude of the unsteady term, the numerical results from unsteady simulation were transformed into the flame front attaching coordinate (in which theoretical analysis was carried out). The magnitudes of unsteady term ( $\partial T / \partial t$ ), convection term ( $U \partial T / \partial r$ ), diffusion term ( $\partial(\partial T / r^2 \partial r) / r^2$ ) and reaction term ( $\omega$ ) in equations (3a) and (3b) are evaluated and compared in the transformed coordinate. The importance of the unsteady effects is shown by comparing the unsteady term with other terms. Figure 13 shows the distributions of the unsteady, convection, diffusion, and reaction terms in energy equation (3a) for flames at different flame radii with  $Le = 1.0$  and  $Q = 0.2$ . When the flame radius is large,  $R = 5.0$  in figure 13(a), the unsteady term is one order smaller than all other terms, therefore it is negligible. For cases of larger flame radii, the unsteady term becomes much smaller. Therefore it is reasonable to employ the quasi-steady state assumption. When the flame radius is small,  $R = 0.5$  in figure 13(b), the diffusion and reaction terms will dominate, while the unsteady and convection terms are relatively small near the flame front. However, near the centre where energy deposition exists, the unsteady term is very large and is balanced by the convection term. This is because the energy deposition in the centre (modelled as a boundary condition) is moving away from the flame front in the flame front attaching coordinate.

Furthermore, to investigate the effect of the timescale of energy deposition on the flame trajectory, we compared the flame-front trajectories obtained from time-dependent numerical computations with different duration time ( $ts$ ) at a given energy flux ( $Q$ ). In numerical simulation, the energy flux  $Q$  at the boundary [equation (7a)] is set to zero when the time is greater than the duration time ( $ts$ ). Figure 14 shows the results for  $Le = 1.0$ ,  $h = 0.01$  and  $Q = 0.2$ . It is seen that the flame initiation fails when the duration is too small. However, when  $ts \geq 6.5$  the flame-front trajectory (which is the same as that of  $ts = 6.5$ ) is not affected by the change of the timescale of energy deposition. Therefore in this case, the duration must be

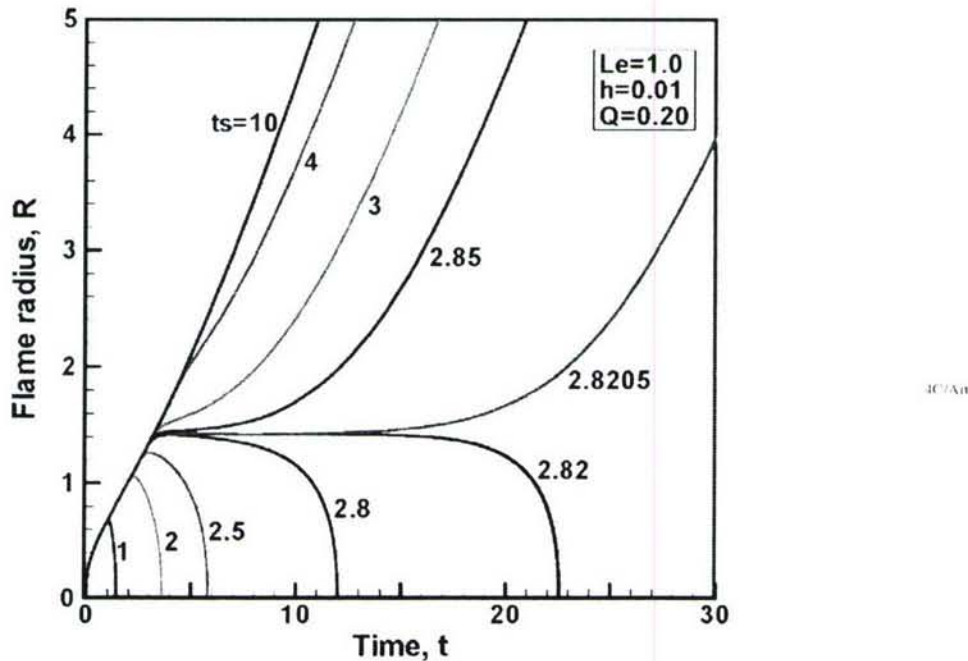


Figure 14. Flame-front trajectories obtained from numerical computations with different duration time ( $ts$ ) at a given energy flux ( $Q = 0.2$ ) for  $Le = 1.0$  and  $h = 0.01$ .

large than 6.5 (time normalized by flame thickness divided by planar flame speed) to make the quasi-steady model consistent. Similar results were also presented in He [22].

## 5. Conclusions

An analytical solution to describe the flame regimes and transitions between the flame kernel, the flame ball, the self-extinguishing flame, the outwardly propagating spherical flame and the propagating planar flame is obtained. The present study extends the previous results by bridging the theories of non-adiabatic stationary flame balls and travelling flames and allowing rigorous consideration of radiation heat losses in both the burned and unburned zones. The results show that the effects of radiation heat loss play a very important role on flame regimes, transition, and critical ignition radius and power and therefore it should not be neglected.

It is shown that radiation heat losses from the unburned and burned zones play different roles in affecting flame propagating speed. With the increase of flame radius, the radiation heat loss from the burned zone increases, while the radiation heat loss from the unburned zone decreases. As a result, there is a peak radiation loss at an intermediate flame radius, which dramatically affects the flame regimes and critical flame initiation parameters. It is also found that the radiation heat loss from the unburned zone results in a new flame regime: the isolated self-extinguishing flame with two radiation extinction limits respectively at small and large flame radius. In addition, it is shown that the critical Lewis number for the stationary flame ball is dominated by the heat loss from the unburned gas.

The results also show that radiation heat loss significantly affects the transition history of flame initiation with external energy deposition. The critical radius of successful flame initiation for radiative flames is much larger than that of adiabatic flames. Furthermore, this difference increases dramatically with the increase of the mixture Lewis number. It is shown that, owing to the coupling of radiation heat loss and the Lewis number effect, the dependence of the minimum ignition energy on Lewis number has three different regimes. At intermediate Lewis numbers, the results show that the minimum ignition energy increases exponentially with the increase of the Lewis number. The prediction agrees qualitative well with the unsteady numerical simulations. These results could have a significant impact on technological developments for ignition control of internal combustion engines.

## Acknowledgement

This work was partially supported by the NASA Microgravity Research Grant (NNC04GA59G) and the Air Force Research Grant (F49620-04-1-0038).

## References

- [1] Romney, P.D., 1988, On the mechanics of flame propagation limits and extinguishment processes at microgravity, *Proceedings of the Combustion Institute*, **22**, 1615–1623.
- [2] Ju, Y., Manita, K. and Niijima, T., 2001, Combustion limits, *Applied Mechanical Review*, **54**, 257–277.
- [3] He, L. and Law, C.K., 1999, On the dynamics of transition from propagating flame to stationary flame ball, *AIAA 99-0325*.
- [4] Spalding, D.B., 1957, A theory of inflammability limits and flame-quenching, *Proceedings of the Royal Society of London, Series A*, **240**, 82–100.
- [5] Buckmaster, J., 1976, The quenching of deflagration waves, *Combustion and Flame*, **26**, 151–162.
- [6] Ju, Y., Guo, H., Manita, K. and Liu, F., 1997, On the extinction limit and flammability limit of non-adiabatic stretched methane-air premixed flame, *Journal of Fluid Mechanics*, **342**, 315–334.

- [17] Maruta, K., Yoshida, M., Guo, H., Ju, Y. and Niitoka, T., 1998. Extinction of low-stretched diffusion flame in microgravity. *Combustion and Flame*, **112**, 181–187.
- [18] Ju, Y., Guo, H., Liu, F. and Maruta, K., 1999. Effects of the Lewis number and radiative heat loss on the bifurcation and extinction of  $\text{CH}_4/\text{O}_2\text{-N}_2\text{-He}$  flames. *Journal of Fluid Mechanics*, **379**, 165–190.
- [19] Zel'dovich, Ya. B., Barenblatt, G.I., Librovich, V.B. and Makhviladze, G.M., 1985. *The Mathematical Theory of Combustion and Explosions* (New York, Consultants Bureau). Q4
- [20] Deshais, B. and Joulin, G., 1984. On the initiation of a spherical flame kernel. *Combustion Science Technology*, **37**, 99–116.
- [21] He, L. and Clavin, P., 1993. Premixed hydrogen-oxygen flames. Part II: Quasi-isobaric ignition near the flammability limits. *Combustion and Flame*, **93**, 408–420.
- [22] Ronney, P.D. and Wachman, H.Y., 1985. Effect of gravity on laminar premixed gas combustion I: Flammability limits and burning velocities. *Combustion and Flame*, **62**, 107–119.
- [23] Ronney, P.D., 1985. Effect of gravity on laminar premixed gas combustion II: Ignition and extinction phenomena. *Combustion and Flame*, **62**, 121–133.
- [24] Ronney, P.D., 1990. Near-limit flame structures at low Lewis number. *Combustion and Flame*, **82**, 1–14.
- [25] Abbud-Madrid, A. and Ronney, P.D., 1990. Effects of radiative and diffusive transport processes on premixed flames near flammability limits. *Proceedings of the Combustion Institute*, **23**, 423–431.
- [26] Buckmaster, J., Joulin, G. and Ronney, P., 1990. The structure and stability of non-adiabatic flame balls. *Combustion and Flame*, **79**, 381–392.
- [27] Buckmaster, J., Joulin, G. and Ronney, P., 1991. The structure and stability of non-adiabatic flame balls: II. Effects of far field losses. *Combustion and Flame*, **84**, 411–422.
- [28] Wu, M.S., Ronney, P.D., Colantonio, R. and VanZandt, D., 1999. Detailed numerical simulation of flame ball structure and dynamics. *Combustion and Flame*, **116**, 387–397.
- [29] Bechtold, J.K., Cui, C. and Matalon, M., 2005. The role of radiative losses in self-extinguishing and self-wrinking flames. *Proceedings of the Combustion Institute*, **30**, 177–184.
- [30] Tse, S.D., He, L. and Law, C.K., 2000. A computational study of the transition from localized ignition to flame ball in lean hydrogen/air flames. *Proceedings of the Combustion Institute*, **28**, 1917–1924.
- [31] Yuan, J., Tse, S.D. and Law, C.K., 2002. Dynamics of flame-ball formation from localized ignition: effects of elevated pressure and temperature. *Proceedings of the Combustion Institute*, **29**, 2501–2507.
- [32] He, L., 2000. Critical conditions for spherical flame initiation in mixtures with high Lewis numbers. *Combustion Theory Modelling*, **4**, 159–172.
- [33] Joulin, G. and Clavin, P., 1979. Linear stability analysis of non-adiabatic flames: diffusional-thermal model. *Combustion and Flame*, **35**, 139–153.
- [34] Frankel, M.L. and Sivashinsky, G.I., 1984. On quenching of curved flames. *Combustion Science and Technology*, **40**, 257–268.
- [35] Vazquez-Espí, C. and Linán, A., 2001. Fast, non-diffusive ignition of a gaseous reacting mixture subject to a point energy source. *Combustion Theory Modelling*, **5**, 485–498.
- [36] Vazquez-Espí, C. and Linán, A., 2002. Thermal-diffusive ignition and flame initiation by a local energy source. *Combustion Theory Modelling*, **6**, 297–315.
- [37] Chen, Z., Qin, X., Xu, B., Ju, Y. and Liu, F., 2006. Studies of radiation absorption on flame speed and flammability limit of  $\text{CO}_2$  diluted methane flames at elevated pressures. *Proceedings of the Combustion Institute*, **31**. In press. Q5

## Queries

- Q1. Au: Both authors have been marked as the main corresponding.
- Q2. Au: There is no ref. 29 included in ref. list.
- Q3. Au: Page range and vol. no. needed?
- Q4. Au: Initial available for first author.
- Q5. Au: Further publication details available.

# Characteristics of the Gliding Arc and its Application in Combustion Enhancement

Alexander Fridman, Alexander Gutsol and Shailesh Gangoli

Drexel Plasma Institute, Mechanical Engineering and Mechanics Department,  
Drexel University, Philadelphia, PA, 19104

Yiguang Ju and Timothy Ombrello

Department of Mechanical and Aerospace Engineering,  
Princeton University, Princeton, NJ, 08544

A novel magnetically stabilized gliding arc reactor coupled with a counterflow burner was developed to study non-thermal plasma enhancement of ignition and extinction phenomena. The results showed that the new coupled plasma-flame system provides a well defined platform for understanding of the basic mechanism of the plasma-flame interaction. It was shown that with a plasma discharge in the air stream, up to a 220 percent increase in the extinction strain rate was possible at low power inputs for air and methane diluted with nitrogen. Measurements of temperature profiles via planar Rayleigh scattering thermometry and OH number density profiles via planar laser induced fluorescence (calibrated with absorption) were taken to quantify various effects. Detailed numerical simulations at elevated air temperatures and radical addition were performed for comparison with experimentally obtained results. Results of the extinction experiments initially suggested that the enhancement effect was predominantly thermal for our particular setup of experiments. However, in ignition experiments specifically for hydrogen, temperature measurements conducted for hydrogen-air mixtures suggested that the extent of enhancement effect could not be accounted for without the contribution of active species. Further comparison with numerical simulations also provides an insight into the participation of species other than radicals in the enhancement effect.

## Nomenclature

$a$	= strain rate of the counterflow flame
$B$	= magnetic field
$Cd$	= drag coefficient
$D$	= specific diameter of the magnetic gliding arc device
$d_{meas}$	= measured diameter of the arc
$d_{corr}$	= corrected diameter of the arc
$d$	= approximate diameter of the arc
$E$	= electric field
$E_n$	= excitation state energy
$f$	= arc rotation frequency
$F_a$	= ampere force per unit arc length
$F_d$	= drag force
$G_0, G_I, G_{ref}$	= identified peaks from an OH spectrum
$I_{nmref}, I_{nm}$	= reference and calculated intensity
$I$	= plasma current
$i, j$	= indices representing the two nozzles streams
$j$	= plasma current density
$L$	= distance between counterflow nozzles

$Q$	= volumetric flow rate
$t$	= exposure time period of high speed camera
$u$	= gas velocity
$v_d$	= drift velocity
$Z(T_{rep}, Z(T)$	= partition functions
$\rho$	= gas density

## I. Introduction

With the ever increasing want and need for practical high speed air breathing propulsion devices comes the major issue of designing a supersonic combustion system. Depending upon the Mach number, the residence times through the combustor of a scramjet may be on the order of the reaction time. This is not as much of an issue for fuels such as hydrogen because of its rapid ignition and reaction time, but does become a significant issue for hydrocarbon fuels because of their longer ignition delay times. Specifically, the two most critical problems in scramjet development arise in the form of ignition and flame stabilization in the supersonic combustor.

Over the course of the last few decades, much research has been focused on supersonic combustion development and has brought our understanding, closer to a tangible and reliable system. Many solutions have been realized in this regard, ranging from passive cavity flame holders<sup>1-5</sup> to energy addition via precombustors<sup>6-8</sup> and plasma<sup>9-17</sup>, to combat the aforementioned problems in supersonic flow systems. Cavities or ramped cavities provide a subsonic region for flame stabilization as well as enhanced mixing, but do not add any energy to the system, setting an upper limit on the extent of enhancement. By adding energy to the flow via a pre-combustor, especially in conjunction with a cavity, the flame becomes more stable with increased flammability limits. Here, the elevated temperatures and radical pools produced during the combustion have proven to be an effective means of decreasing the ignition time and increasing the flame stabilization. Unfortunately, this method is constrained by the requirement of an additional combustion chamber, but more importantly, by the flammability limits of the fuel-air mixture in the pre-combustor, especially for hydrocarbon fuels. In this regard, plasma based ignition is a promising technology because it is not constrained as much by the flammability limits of a mixture, unlike that of a pre-combustor or cavity flame holding design. To address this issue, plasma has been put forth in many configurations ranging from plasma torches<sup>9,10</sup> to high voltage nanosecond discharges.<sup>11,12</sup>

In order to determine the best kind of plasma system to be applied for ignition and combustion applications, we need to classify the various possibilities of electrically generated plasma discharge configurations into types that maybe effective for the enhancement process. Plasmas are broadly classified into two categories namely, thermal (or equilibrium) and non-thermal (or non-equilibrium). Thermal plasmas include arc discharges, plasma torches, and radio frequency inductively coupled plasmas (RF-ICPs). The step-wise processes of ionization and dissociation take place via large amounts of energy or heat addition. Because of this heat addition, the gas temperatures are very high (5,000 K – 50,000 K), with electron temperatures of the same order and energy input in all degrees of freedom. Also, it is unnecessary to have such a high increase in gas temperature from the point of view of ignition. This results in poor chemical reaction selectivity of the ignition process. In addition, there would be either large power requirements or localized activation such as with a plasma jet (e.g., only penetrating into a small portion of a transverse supersonic flow). Furthermore, in order to scale up a thermal plasma discharge, much higher specific power inputs are required.

Non-equilibrium plasmas have been traditionally generated in low pressures such as direct-current glow, corona, radio frequency, microwave, and nanosecond high-voltage discharges. Unlike thermal plasmas they have high chemical selectivity and are capable of homogeneous activation. The primary means of dissociation and ionization is direct electron impact from high energy (speed) electrons accelerated by a large electric field. However, homogeneous activation leads to power requirements that can become extremely high, sometimes in excess of several MJ/m<sup>3</sup>. Also, the gas temperatures typically achieved are either that of the room or too low from an ignition assistance point of view.

Therefore, an ideal plasma discharge should have intermediate temperatures between that of thermal and

non-thermal plasma. The temperatures should be high enough for the ignition of a mixture, and should have activation benefits of a homogeneous discharge, providing high levels of chemical reaction selectivity, have high electron temperatures, and high plasma densities with low power requirements.<sup>16</sup> The discharge that aptly suits the above description is the Gliding Arc (GA). The GA is a unique non-thermal plasma that has relatively high plasma density, power and operating pressure in comparison with other non-equilibrium discharges; high electron temperature ( $> 1$  eV), relatively low gas temperatures ( $< 3000$  K) and good chemical selectivity in comparison with thermal discharges. High temperature electrons are more efficient in producing ions, radicals, excited and dissociated molecules than those in equilibrium plasma ( $< 1$  eV) and the gas temperatures are still high enough to accelerate the interaction between neutral species. Also, the GA is known for its simplicity of design and applicability.

After establishing the GA as the best candidate for the parameters sought for our system, the next step is to understand under what conditions and to what extent there will be thermal and non-thermal effects. It is very clear and has been shown many times over that radical addition will shorten the ignition time. But what is not yet clear is to what extent the radicals can enhance a system, specifically from flame stabilization and burning rate perspective. This question of "non-thermal enhancement" has long been debated.<sup>9, 10</sup> Furthermore, is it possible to enhance a flame using plasma in a way that can not be explained by traditional combustion chemistry? In order to even begin to answer these questions, a system has to be developed to provide an ideal, or at a minimum, a simplified platform to study the plasma-flame interaction. This can be a daunting task because of the complexity of the interaction between the plasma discharge, flow field and flame.

The GA plasma discharge, which has been chosen as the basis of our work, has its roots in a traditional flat gliding arc system, as can be seen in Fig. 1. The arc is initiated at the shortest gap between the two electrodes, after which it elongates by transverse gas flow. Within a short time (microseconds), the arc current reaches its maximum value while the voltage drops to almost zero. As the gas flow pushes the arc, its voltage increases and current starts to decrease. The elongating arc demands more power to sustain itself, until it reaches the maximum that the power supply can provide. However, due to continuous gas flow, the length of the arc continues to grow, but the power supplied by the source is insufficient to balance the energy losses to the surrounding gas. If the power supply is capable of providing sufficiently high voltage, the arc changes its ionization mechanism to a non-thermal one, i.e., step-wise to direct. Due to instability, the arc cools down and finally extinguishes, marking the end of one cycle. The next cycle of arc evolution begins as voltage in the gap reaches its breakdown value and initiates at the shortest gap once again. The transition is attributed to a continuous increase in the electric field until extinction causing electrons to gain energy during transition, coupled with convective cooling of the gas in the plasma arc. Figure 2 shows the increase in electric field after the point of transition. From the perspective of using plasma for an ignition enhancement study, the traditional flat GA's pose a problem because of the requirement of high flow rates of transverse gas to obtain more-or-less uniformity of the discharge and also the inability to stabilize the non-thermal portion of the discharge.

The goal of this research was to develop an ideal and simplified GA plasma discharge and to integrate it with a counterflow burner (known for its ease of study) to secure a more fundamental understanding of the interaction between species generated by non-equilibrium plasma and diffusion flames. This was accomplished by first designing a magnetically stabilized non-equilibrium gliding arc plasma (MGA) discharge system. The design, development and diagnostics of this system are discussed further in this publication. This MGA system was then integrated with a counterflow burner, providing a simple platform to study the plasma flame interaction. A detailed analysis of the MGA and the flame was performed. This included optical spectroscopy of the MGA and experimental studies of the extinction behavior, laser diagnostics for flame temperatures via planar Rayleigh scattering and OH number densities via OH planar laser induced fluorescence (PLIF) for counterflow diffusion flames. These results were then compared to numerical computations using detailed chemistry to validate the measurements and clarify the roles of thermal and non-thermal effects in non-equilibrium plasma assisted combustion.

## **II. Design and Development of Magnetic Gliding Arc (MGA)**

### ***II. 1. Principle***

As discussed earlier, one of the key problems in the employment of traditional GAs for purposes of combustion studies is that the non-equilibrium portion of the discharge extinguishes rapidly after transition. However, recently it was found that during the gliding arc cycle, the arc can be stabilized well past the transition from the thermal equilibrium to the non-equilibrium regime before extinction.<sup>17</sup> This was an extremely important result as it opened up the possibility of stabilization of a strongly non-equilibrium gliding arc discharge. One of the technical solutions to achieve this was to drive and elongate the arc using a force other than transverse gas flow.

We used the concept of Lorentz force, wherein a moving charge in a magnetic field is subjected to a force. The direction of motion of the charge due to this force is determined by the well-known right-hand-rule; if you orient your right hand palm open, such that the fingers determine the direction of magnetic field and the thumb points towards the direction of motion of the charge, then the palm faces the direction of force experienced. In DC discharges like the MGA, there is no switching of polarity between electrodes. The directions of motion (between electrodes) of negatively and positively charged species are opposite. However, they experience a force in the same direction due to their charge (transversely). This inherently facilitates the motion of the arc as a single unit. We extend this onto the concept of Ampere force wherein the applied magnetic field was normal to the length of the current carrying ‘plasma arc conductor’, causing it to move. The plasma arc can be stabilized near extinction in the non-equilibrium regime for an indefinite amount of time

### ***II. 2. Construction and Magnetic Field Strength***

The MGA apparatus, as seen in Fig. 3, is comprised of stainless steel inner and outer electrodes, which serve as the cathode (high voltage) and anode (grounded) respectively. A wire is fixed to the cathode that is kept separated from the outer anode by approximately 2 mm at the smallest gap (point (1) in Fig. 4). The spiral wire gets progressively closer to the cathode (inner electrode) to where it is attached, which is at the largest gap between the two electrodes. In addition, there is a magnetic field in the discharge region produced by an external donut shaped permanent ceramic magnet as seen in Fig. 3 (Adams Magnetic Inc.). The direction of the magnetic field determines the direction of the rotation of the arc (in this case counterclockwise to follow the wire when looking down upon the system as in Fig. 4). The magnetic field strength as well as the plasma current determines the frequency of rotation discussed later in this work.

Simulations were performed using finite element based software, Ansoft Maxwell SV to estimate the magnetic field strength in the zone where the plasma rotates. The 2D simulation results presented in Fig. 5 show that the magnetic flux lines are parallel to the axis of the reactor (on the inside). Hence, when the arc is initiated along the radial direction, the electric and magnetic fields are normal to each other at all times. Figure 6 displays contours of magnetic field  $B$  in Tesla, in the vicinity of the reactor. Figure 7 shows a plot of variation of the magnetic field as a function of the distance between the electrodes at the plane where the arc stabilizes. Hence the average magnetic field in the discharge zone can be approximated to be 0.12 Tesla. This is a reasonable estimate for the magnetic field typically produced by ceramic magnets.

### ***II. 3. Rotating Plasma Disk and Uniformity***

When a high enough voltage is applied to the plasma device, there is an initial breakdown of the gas at the shortest gap between electrodes and quasi-thermal arc plasma is established. The arc then rotates in the magnetic field and elongates as the distance between the spiraled wire and the outer electrode increases (as seen in Fig. 4 from point (1) to (2) to (3)). The increased length of the arc results in transition to a non-equilibrium plasma leading to more rapid cooling and intermediate temperatures (2000 K – 3000 K) as well as an increase in electric field and average electron temperatures ( $> 1\text{eV}$ ). Once the arc reaches the cylindrical inner electrode (point (4) in Fig. 4), there is a stable rotating intermediate temperature arc in the gas flow. A top view of this plasma disk can be seen in Fig. 8. The plasma arc rotation frequency ranges from approximately 20Hz to 50Hz (during range of operation of current 30mA to 90mA) and only decreases by a few percent when the flow rate is increased (Fig. 9). The increased rotation frequency comes from the higher current input (and hence, higher power addition), forcing the arc to rotate faster in the fixed

magnetic field. When the arc reaches the largest gap, it remains at a fixed axial position with a constant length as it rotates. This is because the arc is no longer convecting downstream. The GA sustains itself during this period of continuous rotation between electrodes. This is because it moves repeatedly through a media that was previously ionized. It therefore requires less power input to remain at that position (stabilize) as opposed to quenching and reinitiating at the smallest electrode gap, as it does in the flat geometric configuration. Since the frequency of rotation of the arc is fast when compared to the gas velocity, there is quasi-uniform activation of the flow.

To emphasize this point, a simple model was proposed to estimate the flow rate,  $Q$ , of gas that could be quasi-uniformly activated by the gliding arc. The system was designed such that a distance of 10 mm was maintained at the largest gap where the plasma disk was located and a magnetic field,  $B$ , of 0.12 Tesla (estimated value from simulations). The low current, high voltage gliding arc operation would have an electric field strength,  $E$ , for the case of the gliding arc propagation through non-ionized air of about 0.1 kV/mm. This would lead to a gliding arc voltage drop of 1 kV for the given length of the gap. We make an assumption that the arc is "not transparent" to the surrounding air i.e. it experiences a drag force as it rotates. Hence, the plasma arc behaves like a current carrying cylinder (wire) which experiences two sets of forces namely, Ampere Force per unit length  $F_a = IB$  (assuming the current and magnetic field are normal at all times) and Drag Force per unit length,  $F_d = C_d \rho u^2 d$ . Here,  $C_d$  is the Coefficient of Drag,  $\rho$ , the density of air ( $\sim 1.29 \text{ kg/m}^3$ ),  $u$ , the velocity of propagation of the arc and  $d$ , the approximate diameter of the arc. Under steady state or equilibrium conditions we can approximate:  $F_a = F_d$ . The limits for the drag coefficient for a very wide range of Reynolds numbers (from  $10^2$  to  $10^5$ ) are  $1.3 < C_d < 1$ .<sup>18</sup>

Let us consider a specific case of 40 mA of operation. We use the above parameters in the force balance equation proposed earlier. The arc that is stabilized is approximately 0.385 mm in diameter ( $d$ , measured by a high speed camera for current of 40 mA), moves relative to the gas flow at a velocity of approximately 2.73m/s. Using the mean diameter of the reactor to compute the circumference covered during one rotation we can estimate the average rotation frequency of the arc  $\sim u / (\pi D)$ , where,  $D$  is the diameter ( $\sim 3.5\text{cm}$ ) of the reactor. The corresponding average rotation frequency value  $\sim 2.73/(\pi * 0.035) \sim 25 \text{ Hz}$ . This value matches up reasonably well with experimental value reported in Fig. 9 (40W corresponds to 40mA in figure). This means that at 40 mA current, the arc will appear at the same location 24 times in a second. Hence, the flow will be treated for sure if it passes the diameter of the arc within ( $\sim 1/25\text{sec}$ ) 0.04sec. So, the velocity of air flow that will be treated uniformly by the discharge is approximately  $d/\tau$ , which upon calculation gives us 0.96cm/s. This corresponds to a flow rate  $Q$  of  $11\text{cm}^3/\text{s}$  or  $550\text{sccm}$ .

#### **II. 4. Power Supply**

The electrical circuit typically used for gliding arc discharges<sup>16</sup> is as shown in the Fig. 10. As discussed earlier the quasi-thermal regime exists (due to restriction of current by external resistance) as long as the power supply is capable of providing energy enough to compensate for loses to the surrounding during arc elongation. The transition to non-thermal regime happens at a critical point, when the power drop in plasma is equivalent to that dropped on the external resistance. In order words, this happens when the plasma resistance nearly equals the external resistance.<sup>17</sup>

A power supply was custom made (Quinta Ltd.) to efficiently supply the needs of the gliding arc system stabilized by the magnetic field. It was designed to produce a magnetically stabilized arc with the capability of restricting current while maintaining smooth current regulation. This was accomplished by minimizing the active energy losses with the use of a reactive capacitive resistance that imitates the resistive voltage at all times. To minimize the output electric capacity and to provide the voltage-current characteristic of the power supply (which is close to the resistive voltage-current characteristics), changing the frequency of the high voltage converter allowed variation of the virtual resistance. After the output rectifier, there was unidirectional voltage and current with a very high frequency of the residual pulsation. The plasma arc behavior was then the same as that for the plasma arc at a constant current and voltage because of the limited time response of the gliding arc. This ensures that it operated more or less in the non-thermal regime. Also, during operation the current can be reduced manually (causing corresponding increase in voltage), to lower values than that were possible before it extinguishes and restarts again (i.e. instability sets in).

### III. Integration of Counterflow Flame Burner

A counterflow flame system was utilized because it provides four key benefits. These benefits include minimal buoyancy effects because of forced convection, simplified flame geometry, optical access for laser diagnostics and finally, the ability to define a flow velocity gradient (strain rate or inverse of residence time) along the centerline near the stagnation plane of the two opposed jets. This “global strain rate” can be defined as<sup>19-23</sup>

$$a_i = \left( \frac{2v_i}{L} \right) \left[ 1 + \left( \frac{v_j}{v_i} \right) \sqrt{\frac{\rho_j}{\rho_i}} \right]$$

Hence, it provides an ideal platform to integrate the MGA with a counterflow flame burner for combustion studies.

A schematic of the system is shown in Fig. 11. It consisted of two converging nozzles of 15 mm in diameter, separated by 13 mm. The upper nozzle was water cooled. The gas treated by the MGA was air and exited from the lower nozzle, while nitrogen-diluted methane flowed through the upper nozzle. To isolate the flame from the ambient air and disturbances, a nitrogen co-flow was used, emanating from a 0.75 mm annular slit around the circumference of each nozzle exit. The velocity of the curtain was maintained at or below the exit speed of the nozzle to minimize diffusion into the stream. The flame was established on the upstream air side of the stagnation plane. The use of this system allowed for examination of the strain rates at extinction.

A DryCal dry piston flow meter (1% error) was used to calibrate sonic nozzles that were employed to control the flow rates of individual gases. The methane and nitrogen were mixed in a hollow mixing cylinder (for minimal back pressure). A bypass system was used to ensure that the mixture input to the flame was held constant while the velocity was increased through the nozzles, and hence strain increased. The methane/nitrogen mixture, as well as the air, was teed off before the respective nozzles. The flow rate was increased or decreased through the nozzles by closing or opening the valves of the bypasses respectively. By measuring the flow through the bypass using the DryCal flow meter, the nozzle exit velocities were calculated.

To find the extinction limits, the flame was first established with the bypass fully open, and hence the lowest strained flame. Then each bypass was slowly closed, while maintaining the stagnation plane at a fixed position. During this process the flame moved closer to the stagnation plane between the two nozzles, therefore decreasing the residence mixing time as well as increasing the strain rate until flame extinction. Pictures with and without plasma power addition of the nitrogen diluted methane-air counterflow flames can be seen in Fig. 12. The one-dimensional structure of the flame can be noted here. In all cases the flame was very steady and had minimal curvature, providing an excellent platform to perform experimental measurements via laser diagnostics. These results were computationally reproducible. There was also a noticeable difference in luminosity between the flame with, a), and without, b), plasma activation of the air stream. The flame with plasma activation of the air had a larger luminous zone with a distinct white and orange coloring as compared to the typical bright blue of the non-activated flame. This indicated that there was an effect of the MGA on the diffusion flame.

### IV. Description of Diagnostic Systems

#### IV. 1. Plasma Diagnostic System

For optical emission spectroscopy from the air plasma, an Acton Research SpectraPro 500i scanning monochromator was used. The entrance slit to the monochromator was placed a few inches away from the discharge, facing the discharge. Spatially averaged emission spectra of the discharge were taken in a range of 200 nm – 450 nm. A Roper Scientific model 7430CCD camera was mounted onto the exit slit to

digitally acquire the spectra at a resolution of approximately 0.6 nm resolutions, with typical acquisition times for the CCD images being 1 sec – 5 sec. When the discharge was not in operation, a background noise spectrum was obtained. This was then subtracted from experimental data in order to improve the accuracy of the results. A low pressure mercury lamp was used to determine the slit (apparatus) function and calibrate the spectrometer.

For estimations of the current density, an imaging system was used and consisted of a Nikon D70 SLR camera, with a Sony make CCD type sensor. The sensor of size, 23.7mm x 15.5mm (Nikon DX), was used to capture images at a resolution of 3008 x 2000 pixels (~ 6 mega pixels). The shutter speeds available ranged from 30 seconds to 1/8000 seconds, which could be used to capture instantaneous arc images. These images were used to determine the approximate widths of the channels at various zones in the plasma discharge.

#### **IV. 2. Rayleigh Scattering and OH PLIF for Flame**

To obtain a detailed view of the structure of the MGA activated counterflow diffusion flames, measurements of the temperature profiles and OH distributions were performed via planar Rayleigh scattering and OH PLIF respectively. A schematic of the systems used can be seen in Fig. 13. A frequency-doubled, injection-seeded Nd:YAG laser (Quanta-Ray GCR-4) with an output of approximately 450 mJ per pulse was used. For OH measurements, the OH was excited via a Lumonics HD-300 dye laser pumped with the Nd:YAG laser previously described (Fig. 13). The scattering was imaged with a Princeton Instruments PIMAX intensified CCD camera (one with a photocathode optimized for the visible spectrum for Rayleigh scattering and one for the UV spectrum for OH fluorescence). For Rayleigh scattering, a Nikon 105 mm, f/2.8 macro lens was used while for OH PLIF, a Nikon UV Nikkor 105 mm f/4.5 lens was used along with UG-11 and WG-295 Schott glass filters to isolate fluorescence from the A-X(0,0) and A-X(1,1) bands and block background scattering. Both cameras employed a 512 by 512 pixel array that was binned to improve the framing rate.

To calibrate the Rayleigh scattering signal, images of the scattering intensity were taken of clean, particle-free air (at a known temperature) that was directed through the lower nozzle. To calibrate the intensity seen from the OH PLIF to an absolute number density of OH, measurements were first taken of a known system with the equivalent experimental arrangement. A detailed description of the planar Rayleigh scattering and OH PLIF system operation and calibration has been described in Ombrello et. al.<sup>24</sup>

## **V. Results and Discussion**

### **V. 1. Plasma Characterization**

The flat GA has been well studied over the years for its transition from the thermal to non-thermal regime. However, the MGA is a relatively new discharge which needs to be studied in order to characterize its non-equilibrium nature. Optical diagnostic techniques were employed in order to obtain average rotational and vibrational temperatures in the MGA with emission spectra obtained from OH and N<sub>2</sub> species from the discharge were used.

#### **V. 1. A. OH (A<sup>2</sup>Σ, v=0 → X<sup>2</sup>Π, v'=0) Spectrum for Rotational Temperature**

A spatially averaged optical spectrum was obtained from the MGA plasma disk operating at approximately 32 mA, 37 Watt at normal pressure in air.<sup>25</sup> The experimental spectrum, as seen in Fig. 14, had three major lines, G<sub>0</sub>, G<sub>1</sub>, and G<sub>REF</sub> that were of the most importance in the temperature range from 1000K – 4000K. This is because the reference peak, G<sub>REF</sub> is the strongest group of unresolved lines and G<sub>0</sub> and G<sub>1</sub> are highly sensitive to temperature variation in this range. For temperatures above 4000K their sensitivity is relatively low.<sup>26</sup> Hence, the ratios of these peaks are best considered for diagnostic analysis. A theoretical spectrum was then generated by using the technique specified in Izarra<sup>26</sup> and Pellerin et al.<sup>27</sup> by collecting data pertaining to the OH spectrum as studied by Dieke & Crosswhite<sup>28</sup> in the paper of Izarra<sup>26</sup>, wherein weak transitions were neglected and a set of delta functions corresponding to the strong transitions were generated from the relation below,

$$I_{nm} = I_{nm_{ref}} \frac{Z(T_{ref})}{Z(T)} e^{\frac{-E_n * (T_{ref} - T)}{(T * T_{ref})}}$$

Where,  $I_{nm}$  is the intensity of the OH transitions (nm) and occurs at a specific wavelength,  $E_n$  is the energy of the initial state and  $T_{ref}$  is the temperature at which the reference intensities  $I_{nm_{ref}}$  were obtained. The parameters were taken from the fundamental data found in Izarra.<sup>26</sup> There, the ratio of the partition functions,  $Z(T_{ref})/Z(T)$ , was assumed to be unity. By using different values of temperature,  $T$ , the corresponding normalized intensities were computed. Delta functions corresponding to each transition were then convolved with an apparatus function (i.e. impulse response of the optical device) obtained by employing sharp lines emitted by a low pressure mercury lamp. Figure 14 shows a theoretical plot for temperatures in 500K increments for the range of 1000K – 6000K and their comparison with those measured in experiments. The best fit of the ratios of  $G_0$  and  $G_1$  to  $G_{REF}$  yielded a rotational temperature of  $2350K \pm 150K$ , as shown in Fig. 15. The rotational temperature results obtained from the theoretical analysis above were compared with Spectrum Analyzer<sup>29</sup> software to identify peaks and compute rotational and vibrational temperatures. The results obtained from Spectrum Analyzer are more refined when larger numbers of correctly identified lines are used. The results obtained (Fig. 16) agreed with our calculations giving an average OH rotational temperature of  $\sim 2360K \pm 400K$ .

#### **V. I. B. The N<sub>2</sub> Spectrum for Rotational and Vibrational Temperature**

A spatially averaged N<sub>2</sub> spectrum was obtained from the MGA plasma disk operating at approximately 37 Watts at normal pressure in air. Using the SpecAir<sup>30</sup> code, the experimental and theoretical plots were compared and using best fit analysis, the rotational temperature of 3000K was obtained using the N<sub>2</sub> (electronic transition, C<sup>3</sup>Π<sub>u</sub>–B<sup>3</sup>Π<sub>g</sub>) line at wavelength 337.1 nm. This result was in agreement with investigations reported earlier pertaining to gliding arcs.<sup>31, 32</sup> The vibrational temperature computed using the Spectrum Analyzer<sup>29</sup> (Fig. 17) was found to be  $\sim 3500K \pm 600K$ . Correspondingly, Fig. 18 shows the fit of theoretical and experimental plots, with the best fit obtained for a vibrational temperature (C<sup>3</sup>Π<sub>u</sub>–B<sup>3</sup>Π<sub>g</sub>, vibrational transition, 0-0) of  $\sim 4000K$  using the SpecAir<sup>30</sup> code.

The discrepancy between spatially averaged temperatures measured using different species (i.e. OH and N<sub>2</sub> in our case) can be explained particularly by the fact that measurements were conducted without spatial resolution and that maximum radiation of different radicals could come from different parts of the discharge with different temperatures. For example, the study of the gliding arc in air using optical methods<sup>33</sup> molecular spectra of OH and N<sub>2</sub><sup>+</sup> band heads at 306.3nm and 391.4nm were used respectively. They proposed the plasma column to be divided into two regions, one being the core in which the intensity of N<sub>2</sub><sup>+</sup> lines are observed and the other, the outer “flame” in which the radiation from OH is typical of the surrounding excited molecular region.

A spatially resolved spectrum was also obtained to determine N<sub>2</sub> rotational temperature in the cathode spot (CS) region (shown in Fig. 19) for 40mA, conditions and was found to be  $\sim 1610K$ . A spatially resolved OH spectrum could not be obtained for the present experimental setup because the microscope used restricted our measurements to  $\sim 360nm$  and above. However, it is within the scope of our future work with the use of UV lenses.

#### **V. I. C. Electric Field in MGA plasma arc**

The snapshots in Fig. 19 show the gliding arc structure at different operating conditions (a) 44 mA (b) 140 mA and (c) 220 mA. For characterization of the plasma, we split the plasma into two zones namely – (1) Cathode Spot (CS) or Negative Glow (NG), and (2) Plasma Channel or Positive Column (PC). It was possible to notice that the CS width increased with current, thus keeping the current density nearly constant (covered in section V.I.E in this paper). This is typical for non-thermal atmospheric pressure glow discharge wherein the normal current density, remains constant.<sup>34, 35</sup> However, it is important to resolve the electric field in these zones as it was expected to have a significant voltage drop in the CS.

The typical value for voltage drops in the CS of glow discharges operating in air with iron electrodes  $\sim 260V$ .<sup>35</sup> Using visual quantification from high speed camera arc images, the approximate thickness of the cathode layer in our case (a) is about 0.03cm. Hence the electric field  $E \sim 8000$  V/cm and the reduced electric field  $E/n \sim 175$  Td (1 Td  $\sim 10^{-17}$  V.cm<sup>2</sup>) using spatially resolved CS temperature  $T \sim 1600K$ . Of course, the electric field in the negative glow region is expected to change drastically in space. However, the above calculation has been conducted for estimation purposes.

It follows that the voltage drop in the PC  $\sim (1170$  V  $- 260$  V)  $\sim 910$  V. Again, imaging analysis yielded a length of the PC to be approximately 1 cm. Hence, the electric field  $E \sim 910$  V/cm and reduced electric field  $E/n \sim 25$  Td  $- 35$  Td, using spatially averaged  $T \sim 2200$  K  $- 3000$ K.

The electric field can be used as a parameter for comparison of our discharge with non-thermal glow discharges where the reduced electric field values typically are in the range  $\sim 3$  V/cm/Torr  $- 30$  V/cm/Torr<sup>35</sup>. Using the calculated effective pressure parameters as discussed above, we estimate reduced electric field values of for our conditions  $\sim 9$  V/cm/Torr  $- 12$  V/cm/Torr in the plasma column of the discharge, which is within the range of non-thermal discharges. Also, earlier investigations<sup>45</sup> for conventional GA reveal that it is possible to have a non-thermal regime at reduced electric fields as low as 2.4 V/cm/Torr.

#### **V. I. D. Average Electron Energy Estimations**

Using the parameters of the system, such as the geometry and assuming that the electric field is uniform through the PC, the reduced electric field range obtained was for the CS and the PC regions (computed earlier, above). A Boltzmann equation solver, BOLSIG<sup>36</sup> was employed to calculate the average electron energy versus the reduced electric field for air i.e. 80% N<sub>2</sub> and 20% O<sub>2</sub>. The results obtained gave  $\sim 3.5$  eV for the CS region and  $\sim 1$  eV  $- 1.2$  eV for the PC region at atmospheric pressure air conditions. These high electron temperature estimates relative to the rotational gas temperature (energies  $\sim 0.13$  eV  $- 0.25$  eV) suggest the two-temperature (non-equilibrium) nature of the MGA.

#### **V. I. E. Current Density Estimations**

From Fig. 19 it can be noted that there was a change in the width of the plasma column with an increase in current/power on the arc. Considering the arc to have a cylindrical structure, we assume that this width corresponded to the diameter of the gliding arc. By using these diameters and quantifying them based on the length per pixel from known dimensions, we obtain approximate cross-sectional areas of the arc column. In section II.4, the frequency of arc rotation with current was presented. Using these results and the diameters/widths of the arc obtained by visual inspection and quantification at 1/8000 sec exposure time, we needed to incorporate a diametrical correction based on the frequency of arc rotation. These were approximated by the relation,

$$d = d_{meas} - \pi D f t$$

Where,  $d$  was the corrected diameter of the arc,  $d_{meas}$ , the measured diameter of the arc,  $D$ , the diametrical position in the device at which the measurement was taken,  $f$ , the frequency of arc rotation and  $t$ , the exposure time. As mentioned earlier, for non-thermal characterization of plasma, we consider the arc to be divided into CS zone and PC (rest of the arc zone). Fig. 20 shows plasma current density (A/cm<sup>2</sup>) results obtained by dividing the value of current with the cross-sectional area, calculated by assumptions as mentioned above. In low pressure non-thermal plasmas for air at room temperature and iron electrodes, typically current density is  $\sim 300$   $\mu$ A/cm<sup>2</sup>/Torr<sup>2</sup>.<sup>34,35</sup>

In low pressure non-thermal plasma, the ratio of electric field  $E$  to the pressure of operation  $p$ , i.e.  $E/p$  or ratio of electric field to the gas number density  $n$ , i.e.  $E/n$ , governs various plasma parameters. It is also sometimes known as the reduced electric field (REF). This scaling is applicable only if the gas temperature is ambient, which is in case of low pressure non-thermal plasmas. However, in the case of atmospheric non-thermal plasmas, the gas temperature mostly is higher than that of the room, in which case, scaling needs to be incorporated. The REF parameter is scaled based on effective pressure,  $P_{EFF} = P_{ATM} * (T_{ROOM}/T_{ACTUAL})$ . Where,  $P_{EFF}$  – effective pressure,  $P_{ATM}$  – atmospheric pressure,  $T_{ROOM}$  – room temperature and  $T_{ACTUAL}$  – is the gas temperature of plasma under consideration. The scaling is favorably formulated so as to preserve its initial values at room temperature.

Using this result for our conditions, i.e.,  $T \sim 1600$  K (from spatially resolved diagnostic results for CS zone) and scaling the pressure using number density, the effective pressure  $P_{EFF} \sim 760$  Torr \* (300 K / 1600 K) ~ 141.6 Torr and operating at 40 mA, we get a current density ~ 6 A/cm<sup>2</sup>, which is reasonably close to our experimentally estimated value in the CS zone ~ 5.8 A/cm<sup>2</sup>. Also, from spatially averaged rotational temperature values  $T \sim 2200$  K – 3000 K, the current density estimate in the PC zone was ~ 8.6 A/cm<sup>2</sup>. As the current was increased the temperature was expected to increase as well, which decreased the  $P_{EFF}$  value thereby decreasing the expected current density from literature estimations. This was observed in the CS data. However, in PC data an increase in current density was observed, which possibly could be compared to the property of contraction of non-thermal glow discharge with increase in current.

#### **V. 1. F. Electron Density Estimations**

The electron density in the PC could approximately be estimated from current density,  $j$  and electron drift velocity,  $v_d$ , from the relation:  $j/(e.v_d)$ . From our estimations above, current density in the PC for  $I = 40$  mA is ~ 8.6 A/cm<sup>2</sup>. Using  $T = 2200$  K - 3000K, we applied a corresponding  $E/n \sim 25$  Td - 35 Td into BOLSIG<sup>36</sup> to compute the electron drift velocity ~  $(4 - 5) \cdot 10^6$  cm/s, thereby the electron density ~  $(1.3 - 1) \times 10^{13}$  /cm<sup>3</sup> respectively, this gave an ionization degree ~  $(4 - 3.7) \times 10^{-6}$ . These results are reasonably consistent with earlier estimations in gliding arcs.<sup>31, 32</sup>

#### **V. 2. Diagnostics and Measurements of Interaction between Plasma Species and Diffusion Flame.**

Experimental measurements of the extinction limits, planar Rayleigh scattering for temperature profiles, OH PLIF for absolute OH number density, and numerical computations with radical addition were performed to quantify the combustion characteristics. Numerical computations were performed using a modified version of PREMIX code<sup>37</sup> for both potential and plug flow boundary conditions and using the detailed chemical mechanism of GRI-3.0.<sup>38</sup> Temperatures were measured just downstream of the exit of the nozzles via Rayleigh scattering thermometry and were used as inputs into the numerical computation. This was repeated for each of the various flow, concentration, and plasma power conditions.

#### **V. 2. A. Extinction Measurements**

The extinction limits for the counterflow flames were observed with and without plasma power addition. The strain rates for both situations were increased, causing the flame to move towards the stagnation plane, continuously increasing the heat loss and decreasing the residence time for reaction completion, eventually leading to extinction. The measured values for the strain rates at extinction can be seen in Fig. 21 for three different combinations of nitrogen diluted methane-air counterflow diffusion flames for various levels of plasma power. The extinction limits with no plasma power addition agree well with values reported by both Puri and Seshadri<sup>19</sup> and Bundy et al.<sup>23</sup> It was observed that using only 78 Watts of plasma power input, there was a ~ 220% increase in the extinction strain rate. This power input was less than six percent of the flame power, defined as the maximum power that could be obtained from the given amount of fuel in the mixture. These results showed that there was a significant extinction limit enhancement by using the MGA activation of the air. However, the reasons for this effect were not apparent.

In the quest to obtain an explanation for the enhancement, the results for the extinction strain rates were then compared to that of the numerical computation. The results shown in Fig. 22 described the maximum velocities (proportional to strain rates) achieved before extinction of the flame. Since the input to the computation was only elevated temperatures (obtained from the Rayleigh scattering, to be described in the next section V.2.B) to ‘mimic’ the plasma, and both the experiment and computation extinction results were in good agreement, this gave an indication that the effect of the non-equilibrium plasma on the flame was predominately thermal, within the scope of current measurements.

#### **V. 2. B. Rayleigh Scattering Intensity Ratio and Temperature Profiles**

To obtain a detailed look at the structure of the flame enhancement, quantitative measurements of the temperature distribution was found and compared with numerical simulations. Planar Rayleigh scattering thermometry was performed on the counterflow flame for various strain rates to accomplish this. The laser sheet was passed through the diameter of the disk shaped counterflow flame between the nozzles of the burner. Two sample images can be seen in Fig. 23 where a) is with no plasma power addition and b) is with

approximately 33 Watts of plasma power addition. The background has been subtracted and the air-reference divided into each image. The intensity observed was a function of scattering cross sections and number density distributions between the nozzles. The flame was located in the darkest region of these images (transition from dark to light depicts descending values of temperature and increased scattering). The nitrogen diluted methane mixture is entering the field of view from the top of the images and the air (MGA side) from the bottom of the images. The one-dimensional flame structure along the flow direction was observed even with the use of the MGA. This result greatly simplified the coupling between the flow field and the plasma-flame interaction. By comparison of the two images it was possible to differentiate them based on the extents of darkness, indicative of less scattering and higher temperatures. It can be observed that the region below the flame in b) (plasma on) is darker than a) (plasma off) below the flame. In each case, an averaged temperature from a ten pixel-wide "stripe" was taken from each image. These measured temperatures at the boundaries (just downstream of the nozzles) were then used as boundary conditions in the numerical computation.

The intensity observed by the ICCD camera was a function of both the scattering cross section, because of the distribution of different species, and number density change between the two nozzles. By simply referencing those intensities to the intensity of air at room temperature, ratios were found. These measurements were then compared to that of numerical computation and the results can be seen in Fig. 24 for both the plasma power off (to justify the use of the code for our application) and on. It can be seen that there was reasonably good agreement between the experiment and computation (the oscillations observed can be attributed to the absorptive filters used to "clip" the sheet to reduce scattering off the burner surfaces). Once again, the agreements between the experimental and computational results suggest that the enhancement via the MGA was predominately thermal, within the scope of current measurements.

Since the temperatures, and hence the concentrations of species change between the nozzles due to the presence of the flame, the scattering cross sections and number densities also change. However, number densities can be estimated from temperature, but the scattering cross sections cannot. The scattering cross sections needed to be known at each point along the profile as a reference to derive the temperature. Therefore the species concentrations associated with specific temperatures and axial positions from the numerical computation were used to convert scattering signal to temperature. Using refractory data from Gardiner et. al.,<sup>39</sup> the variation in scattering cross sections gave accurate temperature profiles from the Rayleigh scattering. The temperature profiles found from the Rayleigh scattering were then compared to the results of the numerical computation at the same input temperatures and flow conditions in order to further validate the use of the numerical computation for our specific application. Figure 25 shows the temperature profile comparisons between the experimental results via Rayleigh scattering and the numerical computation using the GRI-3.0 mechanism. The profiles, once again, are in good agreement. This further showed that the effect of the MGA on the flame was predominately thermal, within the scope of current measurements.

#### **V. 2. C. OH PLIF Measurements**

To investigate further and confirm that the enhancement of the flame via the MGA was dominated by thermal effects, OH PLIF measurements were performed. The OH number density was measured for different plasma powers and strain rates and referenced to a Hencken burner flame, as described in a previous work by Ombrello et al.,<sup>24</sup> to find the absolute OH number density. Figure 26 shows the results from the OH PLIF measurements when compared to the computation with and without plasma power addition. The plots show reasonably good agreement (within the uncertainty range of the measurement  $\pm 15\%$ ) between the experiment and the computation, therefore once again showing that the effect of the MGA on the flame was predominately thermal.

#### **V. 2. D. Radical Addition**

Since the enhancement of the strain rates at extinction via the MGA were observed to be predominately thermal, it would be reasonable to calculate the lifetime of the radicals produced by the plasma discharge in the air stream to see if they reach the flame. For this, since the plasma is only activating dry air, it can be assumed that the radicals produced in the flame will only consist of oxygen and nitrogen. As an example the effect of oxygen atom addition at the air side boundary on the flame structure will be shown (once again mimicking the plasma) because the nitrogen atom addition plays a similar role. Oxygen atom

concentrations from 0.01 percent to 1 percent were added at the air (plasma) side boundary. The temperature was fixed at 400 K at this boundary to ensure that low temperature chemistry did not come into play. Also, the velocities at the boundaries were similar to those used in the experiment for a flame that is highly strained and near extinction, where radical addition may be important. A plot of the temperature profiles and oxygen atom concentration distributions between the nozzles can be seen in Fig. 27. It is shown that there was no significant effect until almost 1 percent oxygen atom addition. The MGA plasma disk is located almost 4 cm upstream of this boundary, which is the production site for oxygen atoms. However, since we do not observe any ‘non-thermal’ enhancement in our results thus far, it can be construed that these radicals recombine well before they reach the flame, producing only elevated air temperatures. The radical induced non-thermal effects on the burning rate of diffusion flames are very limited at low air temperatures because the radical lifetime is too short to affect the chain branching reaction path. Figure 28 shows computational simulations of oxygen atom radical lifetimes as a function of temperatures and pressures of operation.

#### *V. 3. 1. Measurements of Ignition Points for H<sub>2</sub>-Air Flame*

In order to observe non-thermal contributions from active species, especially radicals and ions, the previous results suggested that it was necessary for us to go to elevated temperatures or reduced pressures. The first step was to simply consider elevated temperatures. For this, ignition experiments were performed using a pre-heater and the MGA on the upstream air side of the counterflow burner. This system would allow for increased radical lifetimes, suppressing their rapid rate of recombination. By simply adding a pre-heater to the current counterflow system upstream of the MGA plasma disk, the apparatus could be transformed into an ignition system that was able to provide elevated temperatures. The combination of the gliding arc, elevated temperatures and the precondition of no flame, prior to ignition, would allow for an ideal platform to observe the effect of ignition enhancement. Our experimental data using MGA activation of the air stream, starting with the simplest fuel, hydrogen, could on a preliminary basis be compared to that of published data on counterflow hydrogen diffusion flame ignition via heated air. Thus, any differences seen between the heated air ignition and the heated air plus gliding arc activation ignition would be non-thermal.

To accomplish this, a silicon carbide heater was placed upstream of the gliding arc plasma discharge device, effectively raising the air temperature to allow for ignition of hydrogen. The MGA was turned on and the heater power raised and hence the air temperature until the hydrogen diffusion flame ignited. The temperature of the hot air stream was measured with a 0.005 inch diameter type r thermocouple axially located at the exit of the air nozzle of the counterflow burner. The temperature readings from the thermocouple were corrected for radiation. The results of the ignition temperatures using the pre-heater and MGA can be seen in Fig. 29 compared to published data using only a pre-heater.<sup>40</sup> The ignition temperatures obtained are significantly lower than that of just heated air. These preliminary results suggested that there is more than just a thermal effect. This opens up the possibility of the effect of radicals and excited species. The mechanism of this enhancement needs to be investigated further, but at a minimum, these results offer up the observation of non-thermal effects using an ideal system for the plasma flame interaction.

#### *V. 3. 2. Auto-Ignition Enhancement of H<sub>2</sub>-Air mixtures*

To understand the above result better, kinetic computations for ignition of H<sub>2</sub>-air stoichiometric mixtures were conducted using three different mechanisms, namely, Balakrishnan, Matveev and Vlachos available and simulated in Chemical Workbench<sup>44</sup>. The ignition time delays for preheated H<sub>2</sub>-air mixtures at 900 K were found to be ~ 115 msec, 80 msec and 3 msec respectively, for the three mechanisms mentioned above. Atomic oxygen radicals (that are expected to be generated from dry air, as discussed earlier) were then added to the incoming charge to observe the radical enhancement effect, if any. When a reduction in delay time was observed for a particular amount of addition of O radicals, the preheat temperature was reduced such that the ignition occurred after the same time delay as it did without radical addition. Hence, it was possible to arrive at a radical concentration that was required to cause the same enhancement effect with the preheat temperature of 800 K. Fig. 30 shows that about 0.1 % – 2 % by volume atomic oxygen addition is required to cause 100 K reduction in required preheat. Such high concentration of radicals is not reasonable even inside non-thermal plasma and definitely not at some length outside, after treatment through the plasma.

#### V. 4. Non-Thermal Plasma Ignition and Combustion Enhancement Mechanism

Over the years, researchers have been debating over the possible mechanism of non-thermal enhancement of ignition using plasma. For a long time, the radicals produced by plasma were touted to be the contributors to ignition enhancement. From our discussion of radical addition simulations in section V.3.2 it is clear that it is not possible to achieve a significant enhancement effect, as we did in our results presented in section V.3.1, unless we have relatively high concentrations of radicals ( $\sim 0.1\% - 2\%$  or more). However, such high concentrations of radicals are not realistic in non-thermal plasma; leave alone the possibility of achieving such concentrations  $\sim 4\text{ cm}$  from the MGA plasma disk, after treatment. Typical time scales before the active species can reach the stagnation zone can be approximated as  $\sim 0.2\text{ sec} - 0.06\text{ sec}$ .<sup>41</sup> This was without considering increased mixing as it passes through the nozzle. This result qualitatively (maybe not quantitatively) proves the intervention of sources other than radicals that contribute to the reduced ignition delay process.

Plasma is a source of active species, meaning, it is not only a source of free radicals, but also charged and excited species. The numerical computation used to predict enhancement, only accounts for addition of radicals or increase in temperature. However, it does not take into consideration the effect of other active species. Ion-molecular reactions are fast processes that typically do not have an activation energy barrier to overcome in order to initiate a reaction. Hence, they can play a pivotal role in the enhancement process, when ignition is to be achieved in direct contact with plasma. However, in our specific experimental setup, the charged species, just like radicals, are expected to recombine well before they reach the stagnation zone. Some electronically and/or vibrationally excited species on the other hand can survive for longer durations of time. However, the time scales at which these processes take place depend upon gas flow rates and reactor geometry. Given below are estimates of typical lifetimes of some metastable species<sup>35</sup>,

Species	Excitation Level	Lifetime (sec)
N <sub>2</sub>	A <sup>3Σ<sup>+</sup> u</sup>	13
N <sub>2</sub>	E <sup>3Σ<sup>+</sup> g</sup>	300
O <sub>2</sub>	a <sup>1Δ<sub>g</sub></sup>	3000
O <sub>2</sub>	b <sup>1Δ<sub>g</sub><sup>+</sup></sup>	7

Table V.1: Typical lifetimes of metastable species<sup>35</sup>

To further bolster this notion of participation of excited species in ignition enhancement, recently Anikin et al.<sup>42</sup> have claimed that initial stages of hydrocarbon oxidation are determined by their dissociation in collisions with excited oxygen atoms O (<sup>1D</sup>) stage. Kosarev et al.<sup>43</sup> have also demonstrated the reduction in ignition delay by injection of O (<sup>1D</sup>) into H<sub>2</sub>-O<sub>2</sub>-N<sub>2</sub>O-Ar gas mixtures, wherein it was hypothesized that chain continuation reactions such as O (<sup>1D</sup>) + H<sub>2</sub> → H + OH, K<sub>r</sub> =  $2.9 \times 10^{-10}\text{ cm}^3/\text{s}$  and O (<sup>1D</sup>) + H<sub>2</sub>O → 2OH, K<sub>r</sub> =  $3.5 \times 10^{-10}\text{ cm}^3/\text{s}$  played a major role in enhancement whereas, O (<sup>1D</sup>) + N<sub>2</sub>O → N<sub>2</sub> + O<sub>2</sub>, K<sub>r</sub> =  $10^{-10}\text{ cm}^3/\text{s}$  and O (<sup>1D</sup>) + N<sub>2</sub>O → 2NO, K<sub>r</sub> =  $10^{-10}\text{ cm}^3/\text{s}$  played the role of quenching the excited species. In our system, it is expected to have contributions to enhancement from other excited particles as well, for example, O<sub>2</sub> (a<sup>1Δ<sub>g</sub></sup>), which is present in abundance due to the low energy of excitation 0.98 eV and long lifetimes ( $\sim 3000\text{ sec}$ , (Table V.1)). Most researchers have not studied its effect as it is difficult to quantify it experimentally. However, theoretical estimations can be made in order to address kinetics of excited species.<sup>35</sup> Hence, there is a need to develop a plasma-combustion mechanism that takes into account not only radical and thermal addition effects, but also the interaction between charged, charged-neutral, excited-neutral and excited-excited species.

#### VI. Conclusions

A new type of stabilized gliding arc system, the MGA, was successfully integrated with a counterflow diffusion flame burner to provide an ideal and simplified platform to study the plasma/flame interaction. The well defined system allowed for detailed experimental and computational studies of the characteristics of the MGA and its effect on the extinction and ignition of counterflow diffusion flames. The results yielded a classification of the MGA as having both thermal and non-thermal properties, proving that it was aptly suited for our system. The MGA was seen to significantly enhance the strain rates at extinction, but the detailed analysis of the flame via planar Rayleigh scattering and OH PLIF, and their comparison to

computations using just elevated air temperatures to mimic the plasma showed that the effect was predominately thermal. These results emphasized the importance of elevated temperatures to extend the radical lifetimes sufficiently enough to reach the flame. The ignition experiments showed that there is a possibly non-thermal enhancement, but the exact reasons still remain open for interpretation. Possible explanations have come in the form of active species that cannot be explained by traditional combustion radical chemistry. This offers up the suggestion of a new direction to follow in terms of the quest for the mechanisms of plasma/flame interactions other active species in plasma such as ions and excited species.

### VII. Acknowledgments

This work was graciously supported by the Air Force Office of Scientific Research under contract number F49620-04-1-0038. Also, we would like to thank Dr. Campbell Carter of the Air Force Research Laboratory for all his diagnostics help and the National Science Foundation under grant CTS-0418403 for the laser diagnostic equipment support.

### VII. References

- <sup>1</sup>Gruber, M. R., Baurle, R. A., Mathur, T., and Hsu, K.-Y., "Fundamental Studies of Cavity-Based Flameholder Concepts for Supersonic Combustors," *Journal of Propulsion and Power*, Vol. 17, No. 1, January-February 2001, pp. 146-153.
- <sup>2</sup>Gruber, M. R., Donbar, J. M., Carter, C. D., and Hsu, K.-Y., "Mixing and Combustion Studies Using Cavity-Based Flameholders in Supersonic Flow," *Journal of Propulsion and Power*, Vol. 20, No. 5, September-October 2004, pp. 769-778.
- <sup>3</sup>Yu, K. H., Wilson, K. J., and Schadow, K. C., "Effect of Flame-Holding Cavities on Supersonic Combustion Performance," 35th AIAA/ASME/SAE/ASEE Joint Propulsion Conference, AIAA-99-2638, Los Angeles, CA, June 20-24, 1999.
- <sup>4</sup>Yu, G., Li, J. G., Chang, X. Y., Chen, L. H., and Sung, C. J., "Fuel Injection and Flame Stabilization in Liquid-Kerosene-Fueled Supersonic Combustor," *Journal of Propulsion and Power*, Vol. 19, No. 5, September-October 2003, pp. 885-893.
- <sup>5</sup>Yu, G., Li, J. G., Zhang, X. Y., Chen, L. H., Han, B., and Sung, C. J., "Experimental Investigation on Flameholding Mechanism and Combustion Performance in Hydrogen-Fueled Supersonic Combustors," *Combustion Science and Technology*, Vol. 174, No. 3, March 2002, pp. 1-27.
- <sup>6</sup>Guerra, R., Waidmann, W., and Laible, C., "An Experimental Investigation of the Combustion of a Hydrogen Jet Injected Parallel in a Supersonic Air Stream," AIAA 3rd International Aerospace Planes Conference, AIAA-91-5102, Orlando, FL, December, 1991.
- <sup>7</sup>Ju, Y. and Niioka, T., "Ignition Simulation of Methane/Hydrogen Mixtures in a Supersonic Mixing Layer," *Combustion and Flame*, Vol. 102, No. 4, September 1995, pp. 462-470.
- <sup>8</sup>Tabejamaat, S., Ju, Y., and Niioka, T., "Numerical Simulation of Secondary Combustion of Hydrogen Injected from Preburner into Supersonic Airflow," *AIAA Journal*, Vol. 35, No. 9, September 1997, pp. 1441-1447.
- <sup>9</sup>Takita, K., "Ignition and Flame-holding by Oxygen, Nitrogen and Argon Plasma Torches in Supersonic Airflow," *Combustion and Flame*, Vol. 128, No. 3, February 2002, pp. 301-313.
- <sup>10</sup>Takita, K., Moriwaki, A., Kitagawa, T., and Masuya, G., "Ignition of H<sub>2</sub> and CH<sub>4</sub> in High Temperature Airflow by Plasma Torch," *Combustion and Flame*, Vol. 132, No. 4, March 2003, pp. 679-689.
- <sup>11</sup>Bozhenkov, S.M., Starikovskiaia, S.M., and Starikovskii, A. Yu., "Nanosecond Gas Discharge Ignition of H<sub>2</sub>- and CH<sub>4</sub> Containing Mixtures," *Combustion and Flame*, Vol. 133, No. 1-2, April 2003, pp. 133-146.
- <sup>12</sup>Starikovskiaia, S. M., Kukaev, E. N., Kuksin, A. Y., Nudnova, M. M., and Starikovskii, A. Y., "Analysis of the Spatial Uniformity of the Combustion of Gaseous Mixture Initiated by Nanosecond Discharge," *Combustion and Flame*, Vol. 139, No. 3, November 2004, pp. 177-187.
- <sup>13</sup>Chintala, N., Meyer, R., Hicks, A., Bystricky, B., Rich, J.W., Lempert, W.R., Adamovich, I.V., "Non-Thermal Ignition of Premixed Hydrocarbon-Air and CO-Air Flows by Non-Equilibrium RF Plasma," 42nd AIAA Aerospace Sciences Meeting and Exhibit, AIAA Paper 2004-0835, January 5-8, 2004.
- <sup>14</sup>Sullivan, D., Zaidi, S. H., Macheret, S. O., Ju, Y., and Miles, R. B., "Microwave Techniques for the Combustion Enhancement of Laminar Flames," 40th AIAA/ASME/SAE/ASEE Joint Propulsion Conference and Exhibit, AIAA-2004-3713, Fort Lauderdale, FL, July 11-14, 2004.

- <sup>15</sup>Zaidi, S., Macheret, S., Vasilyak, L., Miles, R., Ju, Y., "Increased Speed of Premixed Laminar Flames in a Microwave Resonator," 35th AIAA Plasmadynamics and Lasers Conference, AIAA-2004-2721, Fort Lauderdale, FL, June 28-July 1, 2004.
- <sup>16</sup>Kalra, C., Gutsol, A., and Fridman, A., "Gliding Arc Discharges as a Source of Intermediate Plasma for Methane Partial Oxidation," IEEE Transactions on Plasma Science, Vol. 33, No. 1, February 2005.
- <sup>17</sup>Kuznetsova, I.V., Kalashnikov, A.F., Gutsol, A.F., Fridman, A.A., and Kennedy, L.A., "Effect of 'Overshooting' in the Transitional Regimes of the Low-Current Gliding Arc Discharge," Journal of Applied Physics, Vol. 92, No. 8, 15 October 2002, pp. 4231-4237.
- <sup>18</sup>White, F., Viscous Fluid Flow, McGraw-Hill Book Company, New York, 1974, pp. 207.
- <sup>19</sup>Puri, I.K. and Seshadri, K., "Extinction of Diffusion Flames Burning Diluted Methane and Diluted Propane in Diluted Air," Combustion and Flame, Vol. 65, No. 2, August 1986, pp. 137-150.
- <sup>20</sup>Maruta, K., Yoshida, M., Guo, H., Ju, Y., and Niioka, T., "Extinction of Low-Stretched Diffusion Flame in Microgravity," Combustion and Flame, Vol. 112, No. 1-2, January 1998, pp. 181-187.
- <sup>21</sup>Seiser, R., Seshadri, K., Piskernik, E., and Linan, A., "Ignition in the Viscous Layer Between Counterflowing Streams: Asymptotic Theory with Comparison to Experiments," Combustion and Flame, Vol. 122, No. 3, August 2000, pp. 339-349.
- <sup>22</sup>Humer, S., Seiser, R., and Seshadri, K., "Non-Premixed and Premixed Extinction and Autoignition of C<sub>2</sub>H<sub>4</sub>, C<sub>2</sub>H<sub>6</sub>, C<sub>3</sub>H<sub>6</sub>, C<sub>3</sub>H<sub>8</sub>," Proceedings of the Combustion Institute, Vol. 29, 2002, pp. 1597-1604.
- <sup>23</sup>Bundy, M., Hammins, A., and Lee, K.Y., "Suppression Limits of Low Strain Rate Non-Premixed Methane Flames," Combustion and Flame, Vol. 133, No. 3, May 2003, pp. 299-310.
- <sup>24</sup>Ombrello, T., Qin, X., Ju, Y., Gutsol, A., Fridman, A., Carter, C., AIAA Journal 2006, vol.44 no.1 (142-150)
- <sup>25</sup>Gangoli S., Gutsol A., Fridman A., "Rotating Non-Equilibrium Gliding Arc (MGA) Plasma Disc for Enhancement in Ignition and Combustion of Hydrocarbon Fuels", 17<sup>th</sup> International Symposium of Plasma Chemistry, August 7- 12, 2005, Toronto, Canada.
- <sup>26</sup>Charles de, I., "UV OH Spectrum Used as a Molecular Pyrometer," Journal of Physics D:Applied Physics, Vol. 33, 2000, pp. 1697-1704.
- <sup>27</sup>Pellerin, S., Cormier, J.M., Richard, F., Musiol, K., Chapelle, J., "A Spectroscopic Diagnostics Technique Using UV OH Band Spectrum," Journal of Physics D: Applied Physics, Vol 29, 1996, pp. 726-739.
- <sup>28</sup>Dieke, G.H., Crosswhite, H.M., "The Ultraviolet Bands of OH, Fundamental Data," Journal of Quantum Spectroscopic Radiation Transfer, Vol. 2, 1961, pp. 97-199.
- <sup>29</sup>Spectrum Analyzer Software, <http://www.physics.muni.cz/~zdenek/span/>
- <sup>30</sup>Laux, C.O., Spence, T.G., Kruger, C.H., Zare, R.N., "Optical Diagnostics of Atmospheric Pressure Air Plasmas," Plasma Sources Science and Technology, Vol. 12, May 2003, pp. 125-138.
- <sup>31</sup>Ozlem, M.Y., Saveliev A.V., Porshnev, P.I., Fridman, A., Kennedy, L.A., Non-Equilibrium Effects in Gilding Arc discharge", 2nd International Symposium on Heat & Mass Transfer (1999).
- <sup>32</sup>Fridman, A., Nester, S., Kennedy, L. A., Saveliev, A., Yardimci, O. M., "Gliding Arc Gas Discharge", Progress in Energy and Combustion Science, 25 (1999) 211-231.
- <sup>33</sup>Richard, F., Cormier, J., Pellerin, S., Chapelle, J., "Physical study of a gliding arc discharge", Journal of Applied Physics, 79, 2245-2250 (1996)
- <sup>34</sup>Staack, D., Farouk, B., Gutsol, A., Fridman, A., "Characterization of a DC Atmospheric Pressure Normal Glow Discharge", Plasma Sources Science and Technology, Vol. 14, 2005, pp. 700-711.
- <sup>35</sup>Fridman, A., Kennedy, L.A., "Plasma Physics and Engineering", Taylor & Francis Books
- <sup>36</sup>Kinema Research & Software, BOLSIG, Boltzmann Equation Solver, [www.kinema.com](http://www.kinema.com)
- <sup>37</sup>Ju, Y., Guo, H., Maruta, K., and Liu, F., "On the Extinction Limit and Flammability Limit of Non-Adiabatic Stretched Methane-Air Premixed Flames," Journal of Fluid Mechanics, Vol. 342, 1997, pp. 315-334.
- <sup>38</sup>Bowman et al., GRI-Mech Homepage, Gas Research Institute, Chicago, 1994, URL: [http://www.me.berkeley.edu/gri\\_mech/](http://www.me.berkeley.edu/gri_mech/).
- <sup>39</sup>Gardiner, W.C., Jr., Hidaka, Y., and Tanzawa, T., "Refractivity of Combustion Gases," Combustion and Flame, Vol. 40, 1981, pp. 213-219.
- <sup>40</sup>Fotache, C. G., Kreutz, T. G., Zhu, D. L., Law, C. K., "An Experimental Study of Ignition in Nonpremixed Counterflowing Hydrogen versus Heated Air," Combustion Science and Technology, Vol. 109, 1995, pp.373-393.
- <sup>41</sup>Ombrello, T., Qin, X., Ju, Y., Gangoli, S., Gutsol, A., Fridman, A., AIAA-2006-1214, 44th AIAA Aerospace Sciences Meeting and Exhibit, Reno, Nevada, Jan. 9-12, 2006

- <sup>42</sup>Anikin, N.B., Starikovskaia, S.M., Starikovskii, A. Yu., 43<sup>rd</sup> AIAA Aerospace Sciences Meeting and Exhibit, 10-13 January 2005, Reno, Nevada.
- <sup>43</sup>Kosarev, I.N., Kukaev, E.N., Starikovskaia, S.M., Starikovskii, A., Yu. "Comparison of the Efficiency of Nanosecond Gas Discharge and Laser Flash-Photolysis in Initiation of Combustion", 17<sup>th</sup> International Symposium on Plasma Chemistry, Toronto, Canada, August 7-12, 2005: Full-Paper CD, ISPC\_sstar.pdf
- <sup>44</sup>Chemical Workbench Software, Kinetic Technologies – KINTECH, Version 3.3, [www.kintech.ru](http://www.kintech.ru)
- <sup>45</sup>Yardimci, O.M., Saveliev, A.V., Porshnev, P.I., Fridman, A.A., and Kennedy, L.A., Annals of the New York Academy of Sciences 891:304-308 (1999).

***List of Figures:***

- Figure 1:** Traditional Flat Gliding Arc; the arrow points in the direction of air flow
- Figure 2:** Increase in the electric field in plasma after transition point in GAs
- Figure 3: Photographs of the Magnetic Gliding Arc Device in front, top and isometric views.**
- Figure 4: Gliding arc plasma system.** a) top view of system, b) side view of central electrode. Numbers indicate the path of the gliding arc from initiation (1) to arc rotation/elongation (2) & (3) and finally arc stabilization (4).
- Figure 5:** Magnetic flux lines predicted in 2D simulation by Ansoft Maxwell SV. It can be observed that the flux lines run parallel to the axis of the reactor (dashed line).
- Figure 6:** Contours of magnetic field distribution in Tesla in the vicinity of the MGA reactor
- Figure 7:** Magnetic field variation along the radial distance between inner (cathode) and outer (grounded) electrodes at the plane of rotation of the plasma disc.
- Figure 8:** Top view of MGA plasma disc
- Figure 9:** Frequency of arc rotation for two air flow rates.
- Figure 10:** Typical electrical circuit used for DC gliding arc.
- Figure 11:** Counterflow burner with integrated plasma system.  
1. cathode, 2. anode, 3. diffuser, 4. gliding arc initiation wire, 5. insulator, 6. plasma disk, 7. magnets, 8. converging nozzle with N<sub>2</sub> curtain, 9. flat diffusion flame, 10. water cooled converging nozzle with N<sub>2</sub> curtain.
- Figure 12:** Photographs of methane-air counterflow diffusion flames at a strain rate of 298.5s<sup>-1</sup>.
- Figure 13:** Planar Rayleigh scattering and OH PLIF set-up.  
1. injection seeded Nd:YAG laser, 2. frequency doubler, 3. beam dump, 4. half-wave plate, 5. diode energy meter, 6. lens, 7. power meter, 8. lens, 9. clipper, 10. flame, 11. beam dump, 12. ICCD camera, 13. dye laser with frequency doubler, 14. Pellin-Broca prism.
- Figure 14:** The OH Spectrum obtained both experimentally (at ~ 80 Watt) and theoretically for different temperatures varying from 1000-6000K
- Figure 15:** The ratios of G<sub>0</sub>/G<sub>REF</sub> and G<sub>1</sub>/G<sub>REF</sub> peaks as a function of OH rotational temperature in the MGA. The comparison of the above theoretically generated plot with experimental result, yields a temperature of 2350 ± 150K
- Figure 16:** Spectrum Analyzer OH Rotational Temperature
- Figure 17:** Spectrum Analyzer N<sub>2</sub> Vibrational Temperature
- Figure 18:** SpecAir Code results for N<sub>2</sub> spectrum
- Figure 19:** Photographs taken by high speed camera captures a single magnetically driven arc in motion. The two main regions of the discharge namely, cathode spot (CS) and positive column (PC) can be clearly seen.
- Figure 20:** Photographs taken by high speed camera captures a single magnetically driven arc in motion. The two main regions of the discharge namely, cathode spot (CS) and positive column (PC) can be clearly seen.
- Figure 21:** Effects of plasma power addition on the strain rates at extinction for different levels of nitrogen dilution.
- Figure 22:** Comparison of nozzle exit velocities at extinction
- Figure 23:** Rayleigh scattering images at a strain rate of 98.6s<sup>-1</sup> a) No plasma power addition, b) 33 Watts of plasma power addition.
- Figure 24:** Comparison of Rayleigh scattering intensity ratio profiles with 0 Watts, 33 Watts and 60 Watts of plasma power addition at a strain rates of 87.1s<sup>-1</sup>, 98.6s<sup>-1</sup> and 298.5s<sup>-1</sup> respectively.

**Figure 25:** Comparison of temperature profiles with 0 Watts, 33 Watts and 60 Watts of plasma power addition at a strain rates of  $87.1\text{s}^{-1}$ ,  $98.6\text{s}^{-1}$  and  $298.5\text{s}^{-1}$  respectively.

**Figure 26:** Comparison of OH number density distributions with 0 Watts, 48 Watts and 78 Watts of plasma power addition at a strain rate of  $83.3\text{s}^{-1}$ ,  $127.7\text{s}^{-1}$  and  $183.0\text{s}^{-1}$  respectively.

**Figure 27:** Computed temperature and Oxygen atom distributions between the nozzles of the counterflow system with Oxygen atom addition.

**Figure 28:** Oxygen radical lifetimes in air, for typical residence times in the MGA counterflow burner system. It is seen that increasing the temperature or reducing the pressure can help survive the radicals until they reach the flame.

**Figure 29:** Comparison of ignition temperatures of counterflow hydrogen diffusion flames using pre-heater versus pre-heater and gliding arc activation of the air stream.

**Figure 30:** Comparison of preheat temperature required to achieve same ignition delay for various % additions of oxygen radicals using 3 mechanisms of H<sub>2</sub>-Air namely – Balakrishnan, Matveev and Vlachos.

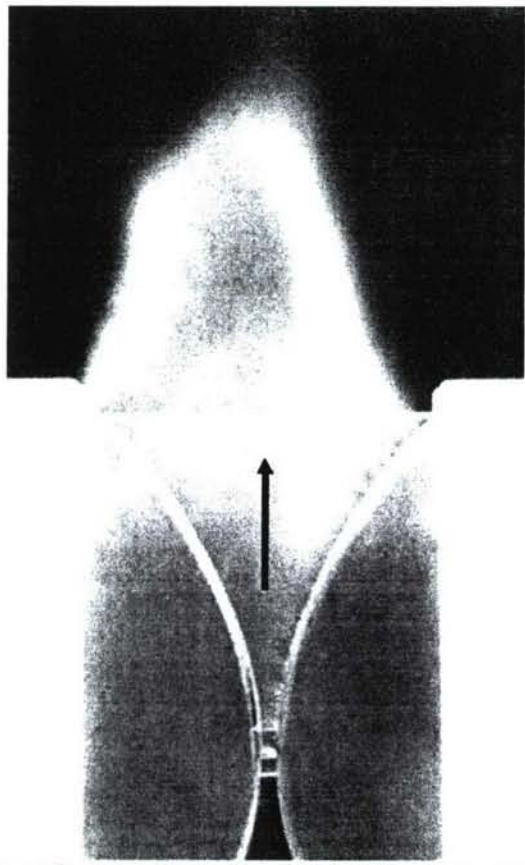


**Fig. 1 Traditional flat gliding arc (arrow points in the direction of air flow)**

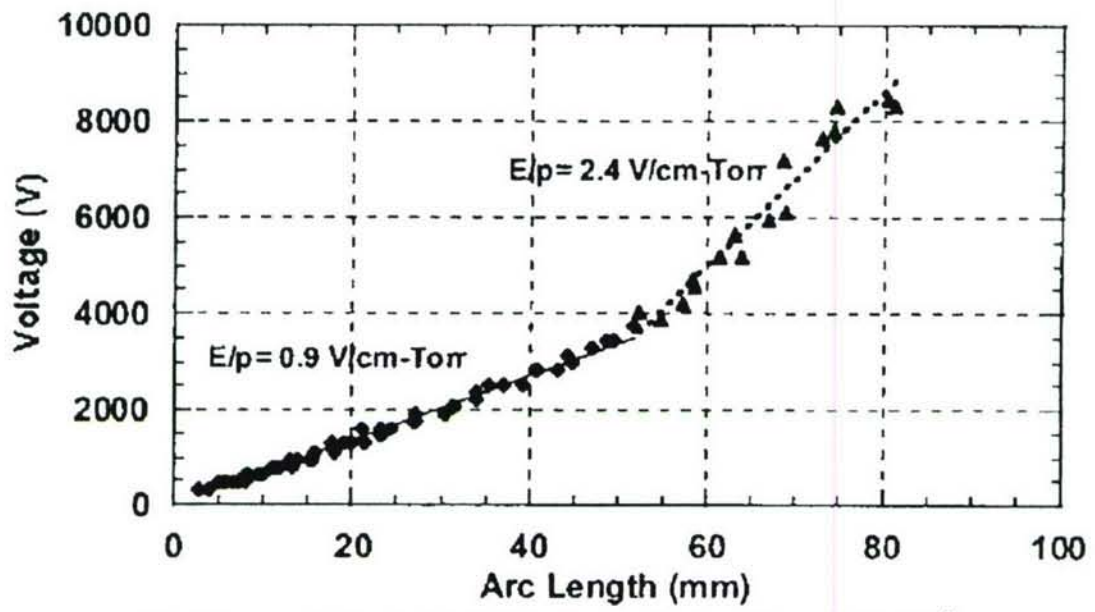


Fig. 2 Increase in the electric field in plasma after transition point in GA<sup>45</sup>

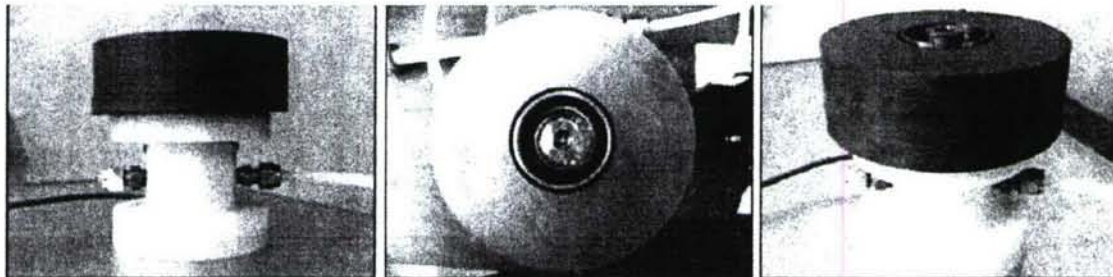
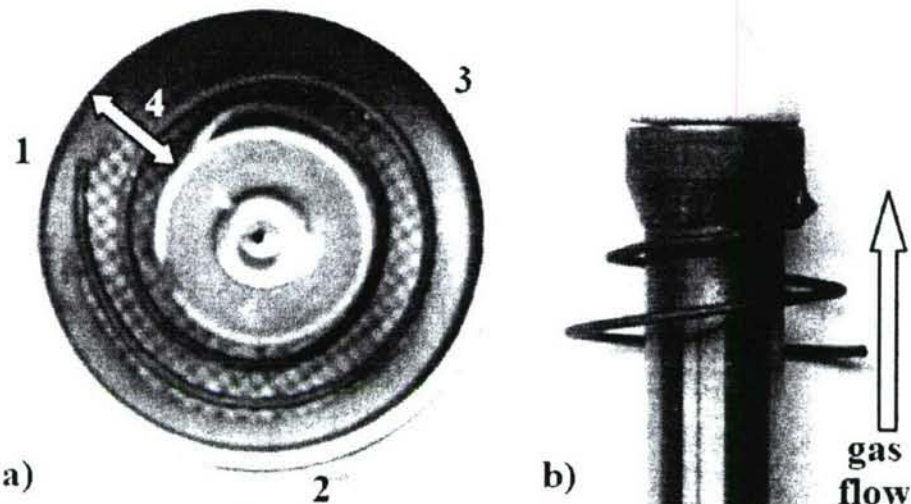
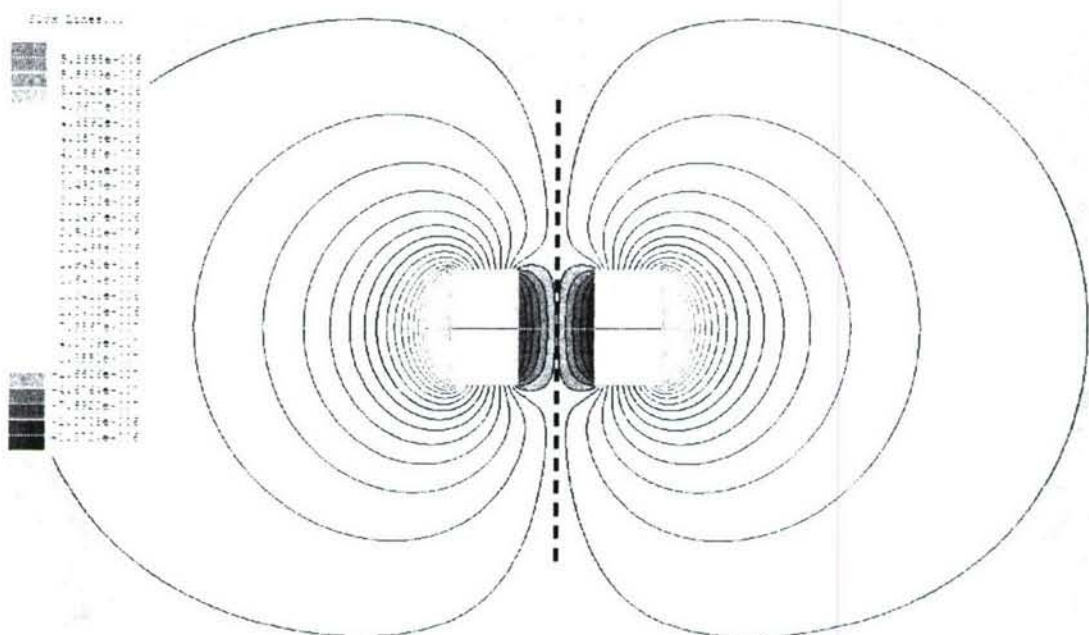


Fig. 3 Photographs of the Magnetic Gliding Arc device in front, top and isometric views.



**Fig. 4 Gliding arc plasma system.** a) top view of system, b) side view of central electrode. Numbers indicate the path of the gliding arc from initiation (1) to arc rotation/elongation (2) & (3) and finally arc stabilization (4).



**Fig. 5 Magnetic flux lines predicted in 2-D simulation by Ansoft Maxwell SV.** It can be observed that the flux lines run parallel to the axis of the reactor (dashed line).

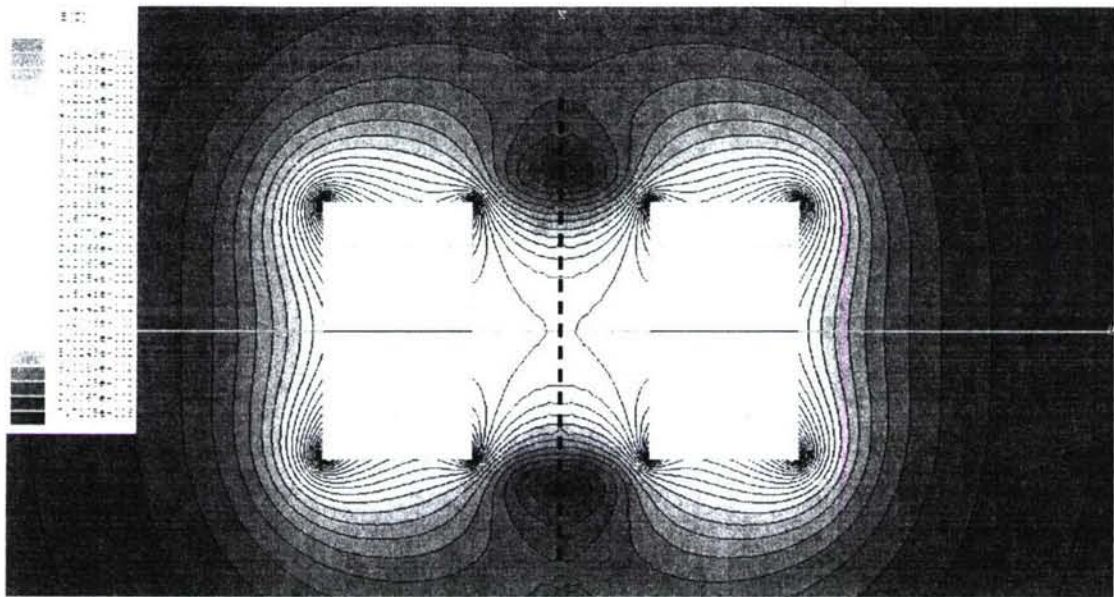


**Fig. 6 Contours of magnetic field distribution in Teslas in the vicinity of the MGA device.**

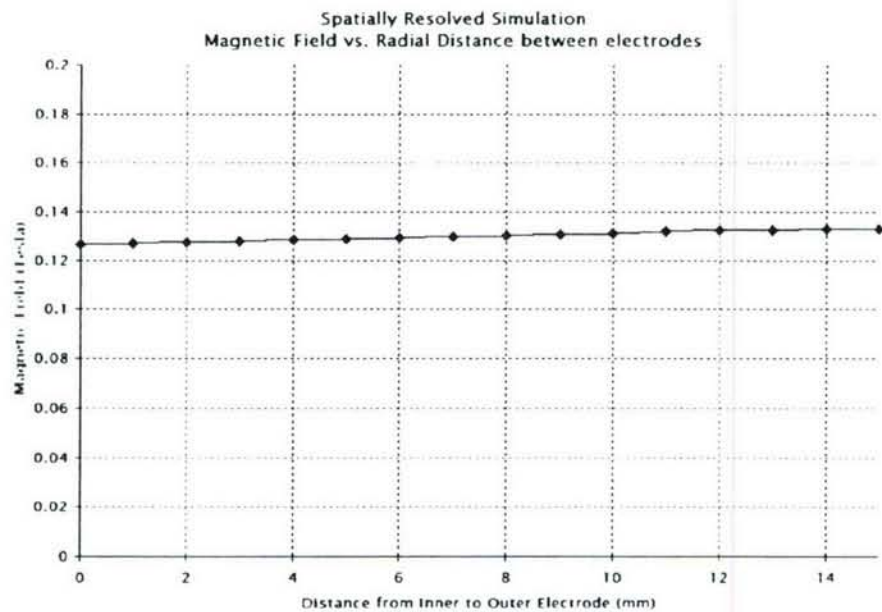


**Fig. 7 Magnetic field variation along the radial distance between the inner (cathode) and outer (grounded) electrodes at the plane of rotation of the MGA plasma disk.**

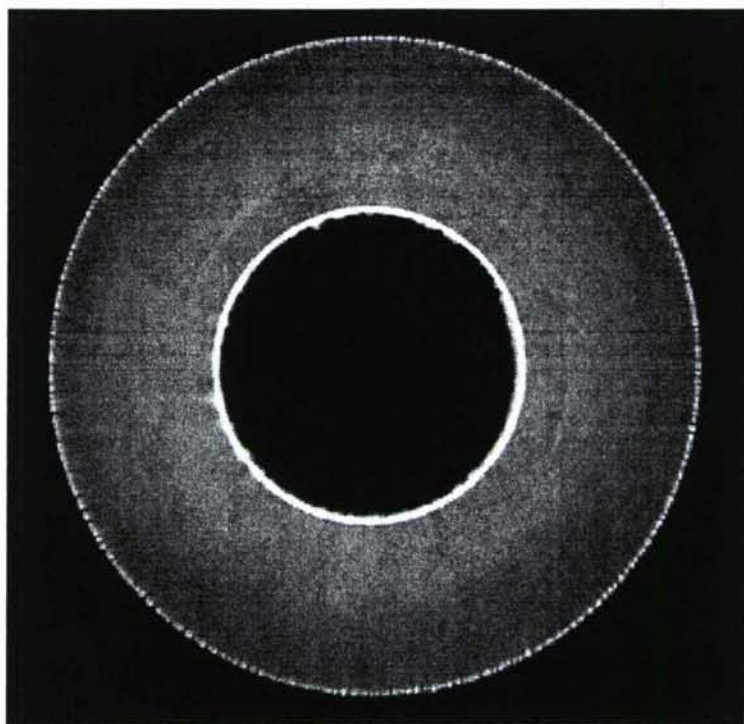


Fig. 8 Top view of MGA plasma disk.

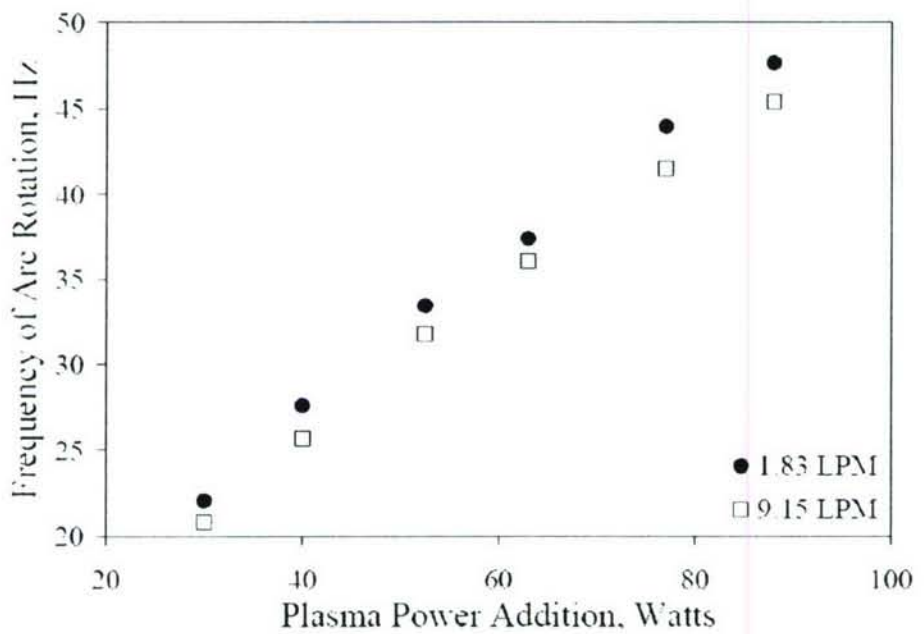


Fig. 9 Frequency of arc rotation for two air flow rates.

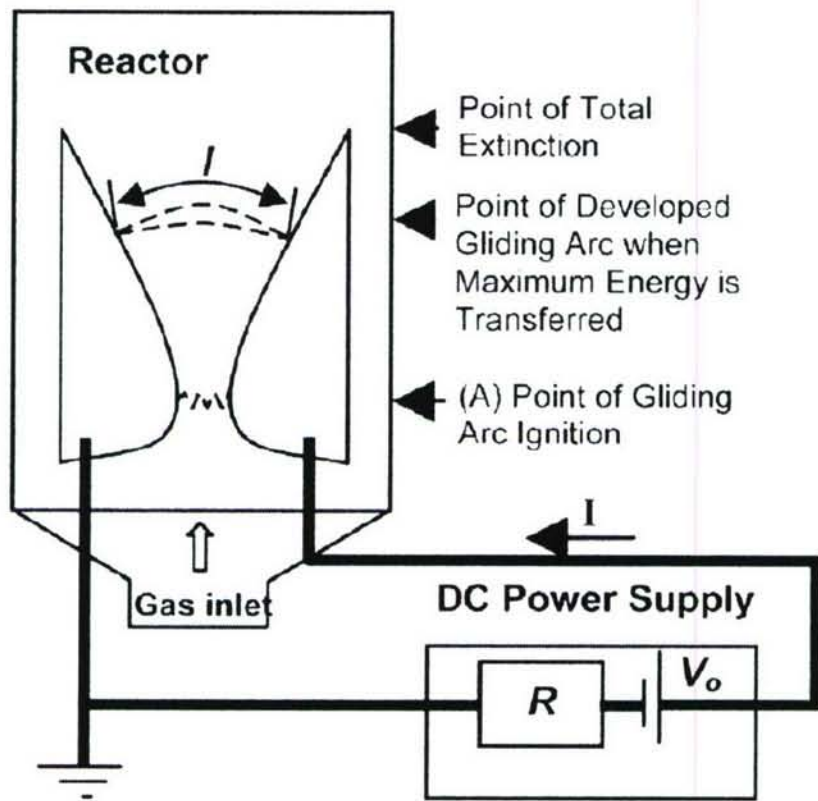
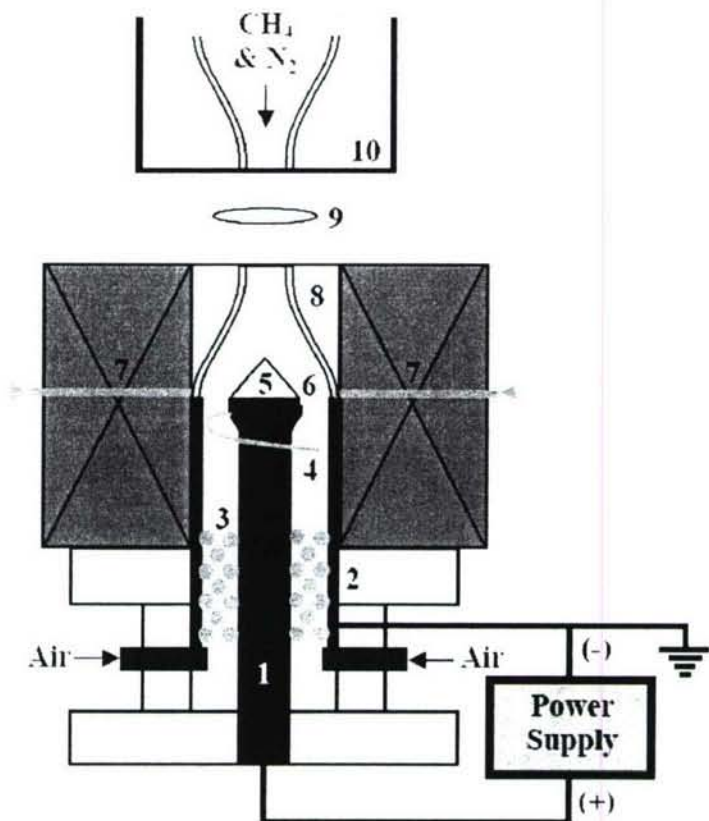
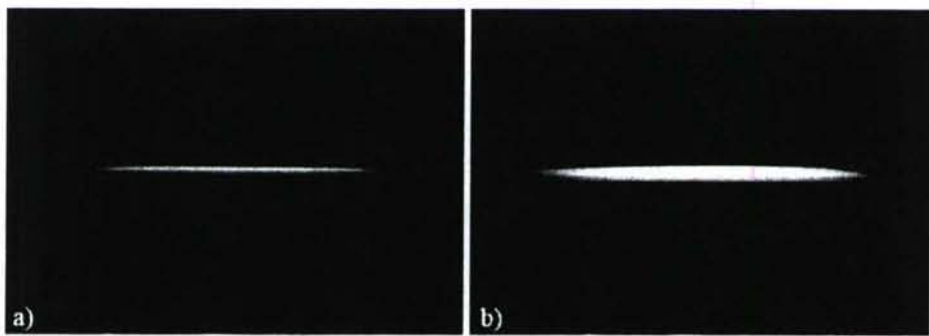


Fig. 10 Schematic of a typical DC gliding arc circuit setup<sup>16</sup>



**Fig. 11 Counterflow burner with integrated plasma system** 1. cathode, 2. anode, 3. diffuser, 4. gliding arc initiation wire, 5. insulator, 6. plasma disk, 7. magnets, 8. converging nozzle with  $N_2$  curtain, 9. flat diffusion flame, 10. water cooled converging nozzle with  $N_2$  curtain.



**Fig. 12 Photographs of methane-air counterflow diffusion flames at a strain rate of  $298.5\text{ s}^{-1}$ .** a) No plasma power addition, b) 60 Watts of plasma power addition.

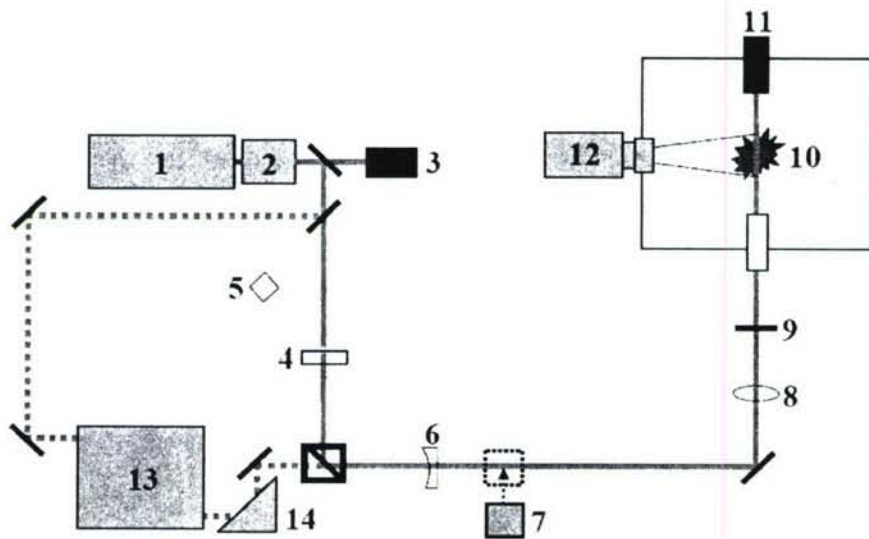


**Fig. 13 Planar Rayleigh scattering and OH PLIF set-up.** 1. injection seeded Nd:YAG laser, 2. frequency doubler, 3. beam dump, 4. half-wave plate, 5. diode energy meter, 6. lens, 7. power meter, 8. lens, 9. clipper, 10. flame, 11. beam dump, 12. ICCD camera, 13. dye laser with frequency doubler, 14. Pellin-Broca prism.

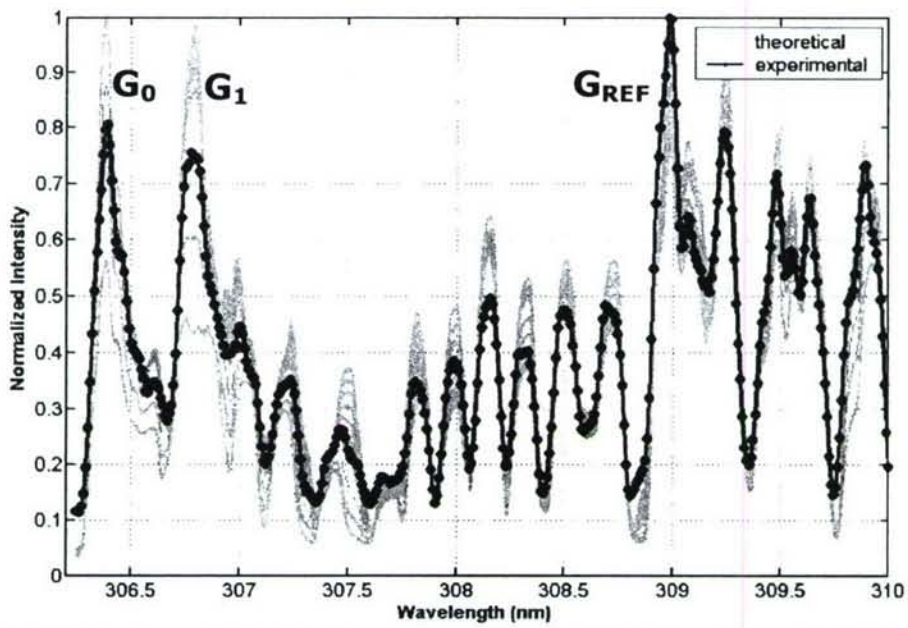


**Fig. 14** The OH Spectrum obtained both experimentally (at ~ 80 Watt) and theoretically for different temperatures varying from 1000 K – 6000 K.

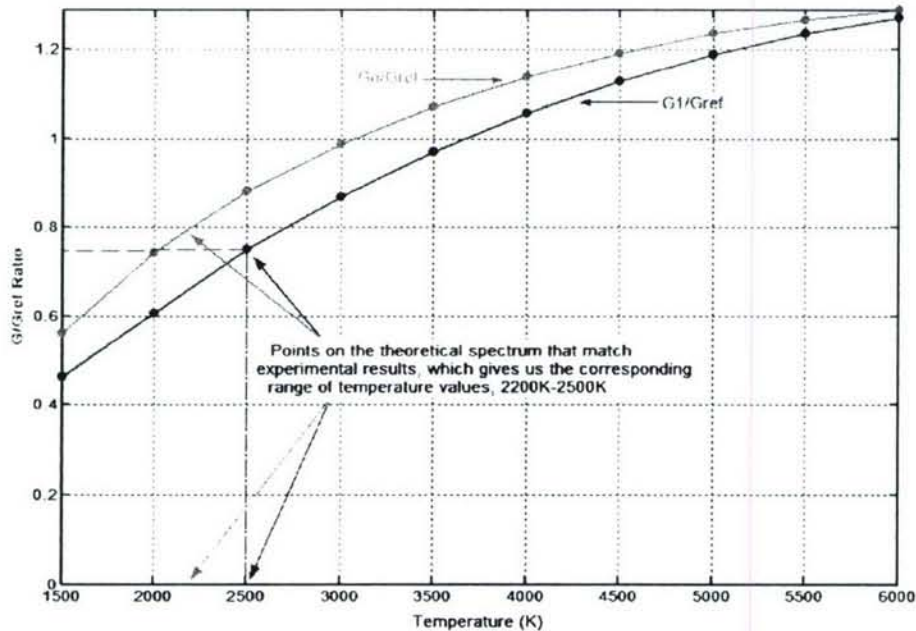


**Fig. 15** The ratios of  $G_0/G_{\text{REF}}$  and  $G_1/G_{\text{REF}}$  peaks as a function of OH rotational temperature in the MGA. The comparison of the above theoretically generated plot with experimental result, yields a temperature of  $2350 \pm 150$ K

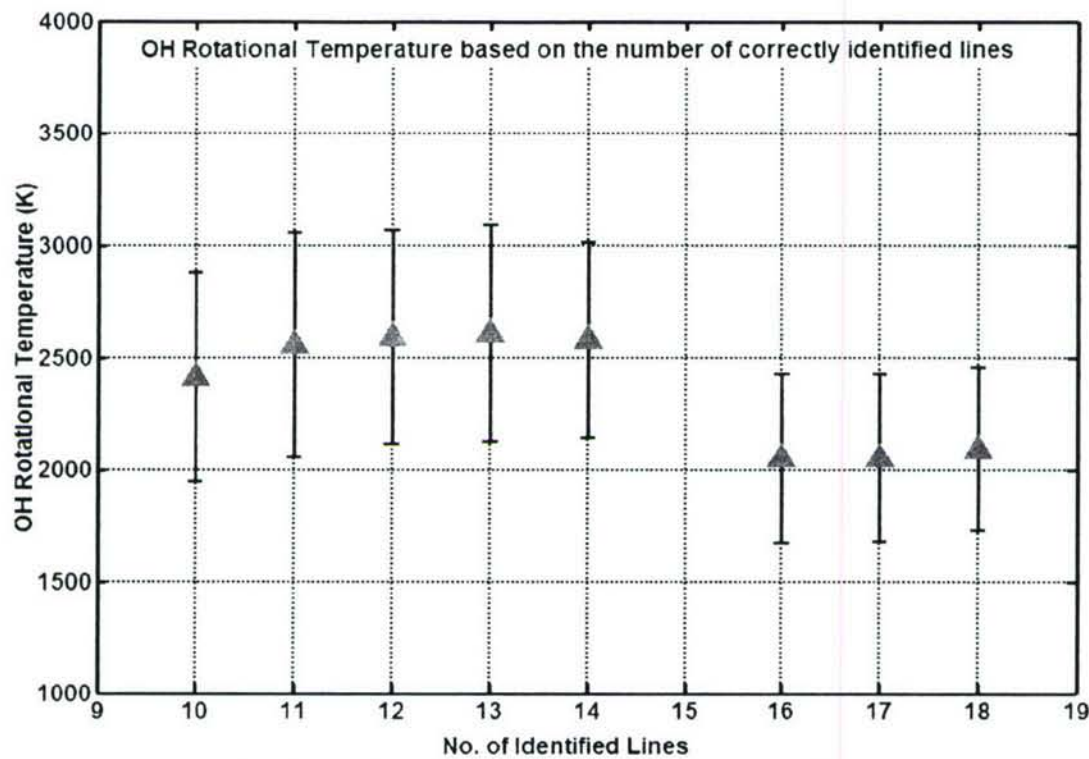


Fig. 16 Spectrum Analyzer OH Rotational Temperature.

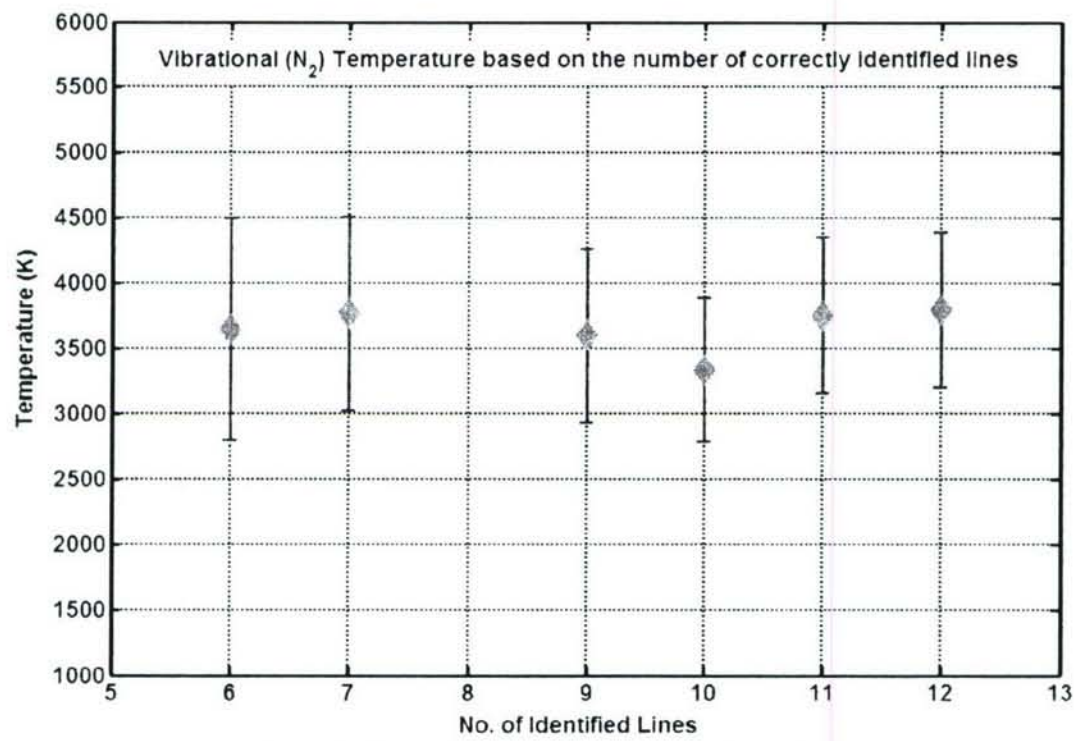


Fig. 17 Spectrum Analyzer  $N_2$  Vibrational Temperature.

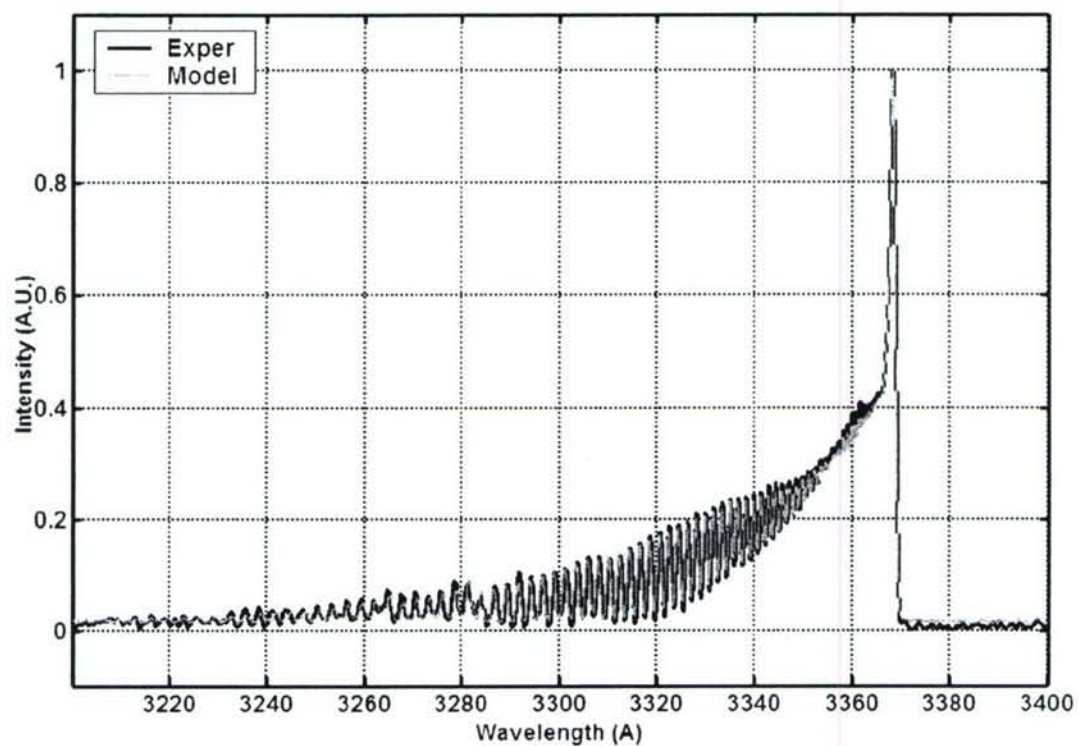


Fig. 18: SpecAir Code results for N<sub>2</sub> spectrum

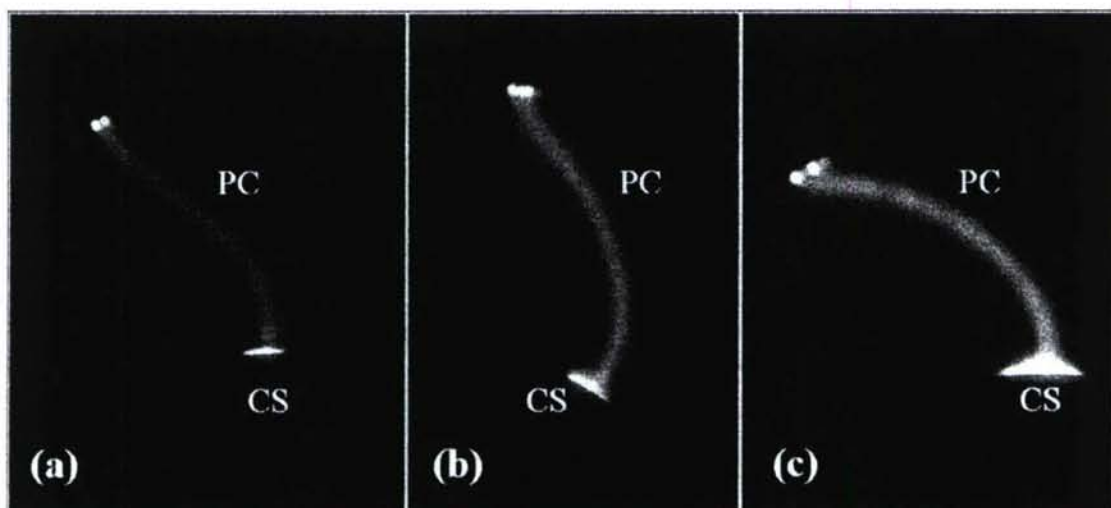


Fig. 19 Photographs taken by high speed camera capturing a single magnetically driven arc in motion. The two main regions of the discharge, namely the CS and PC can be clearly seen.

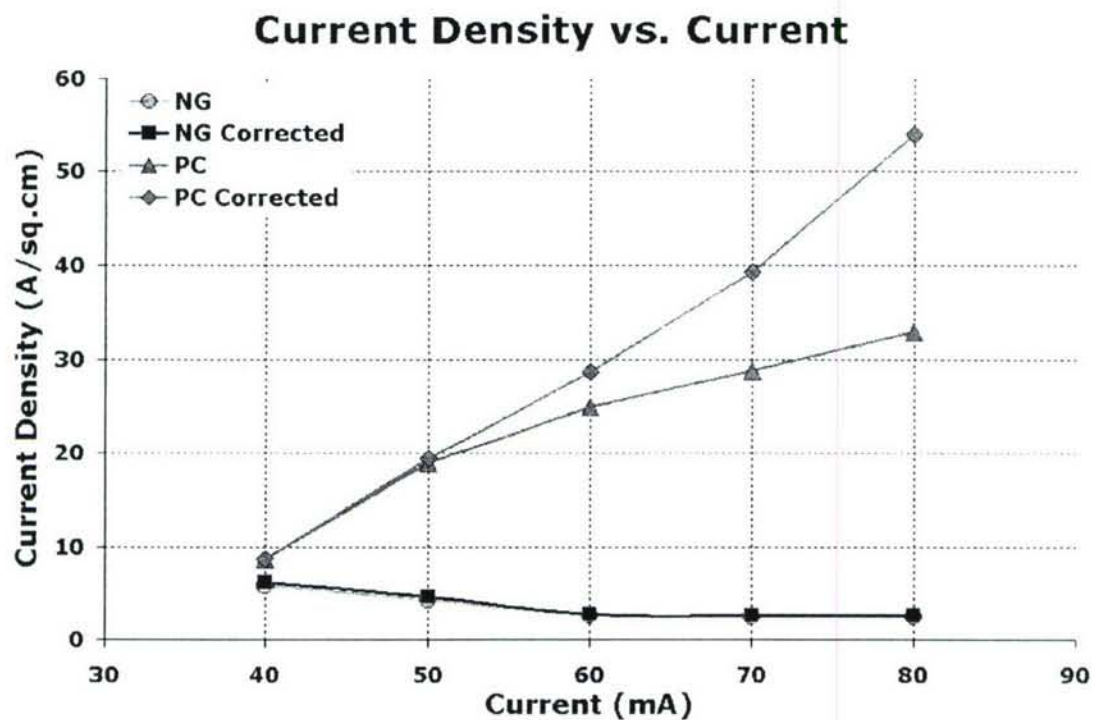


Fig. 20: Estimated MGA plasma current density in the CS and PC.

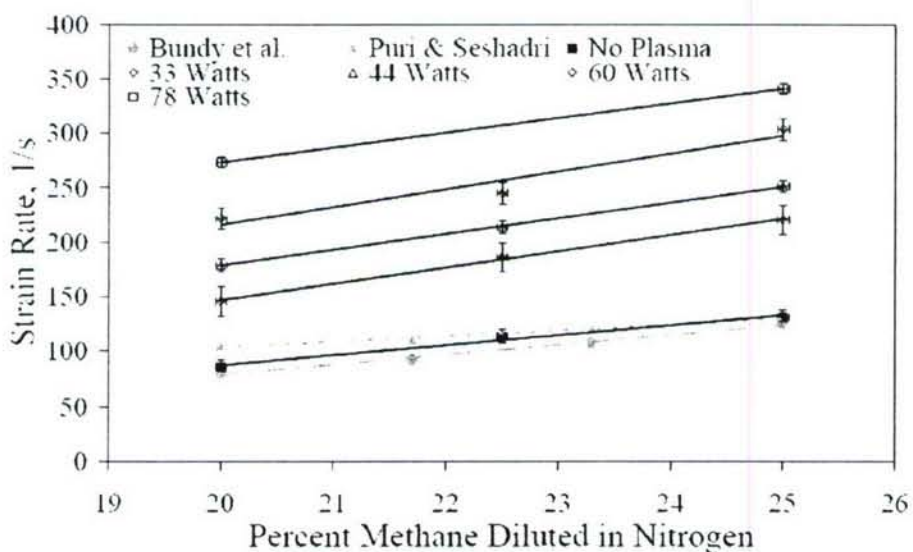
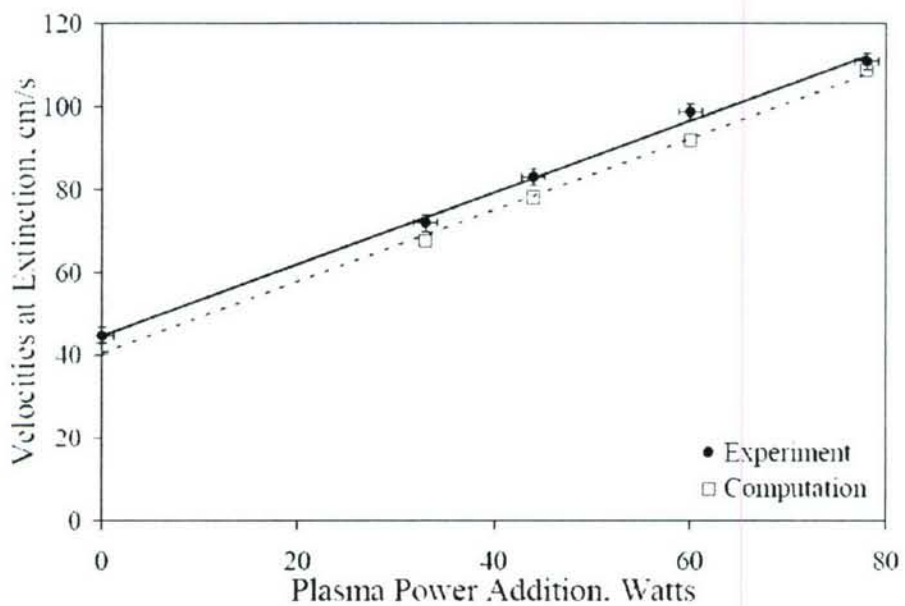
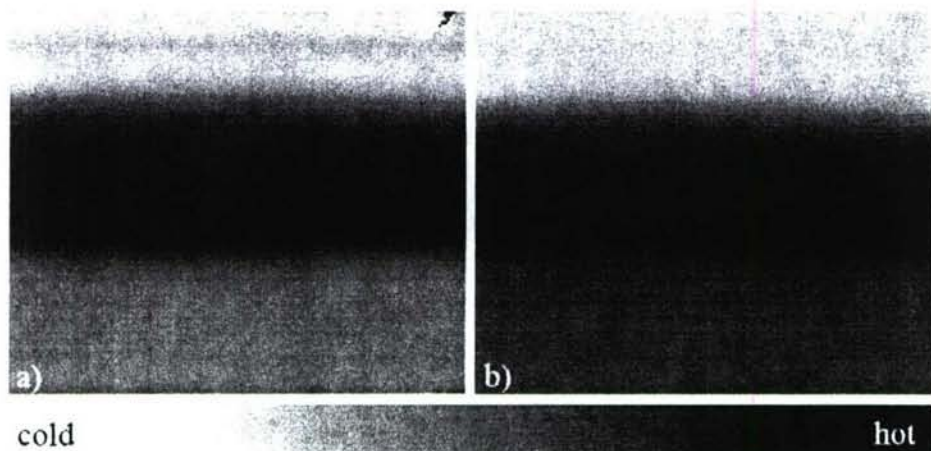


Fig. 21 Effects of plasma power addition on the strain rates at extinction for different levels of nitrogen dilution.



**Fig. 22 Comparison of nozzle exit velocities at extinction.**



**Fig. 23 Rayleigh scattering images at a strain rate of  $98.6 \text{ s}^{-1}$  a) No plasma power addition, b) 33 Watts of plasma power addition.**

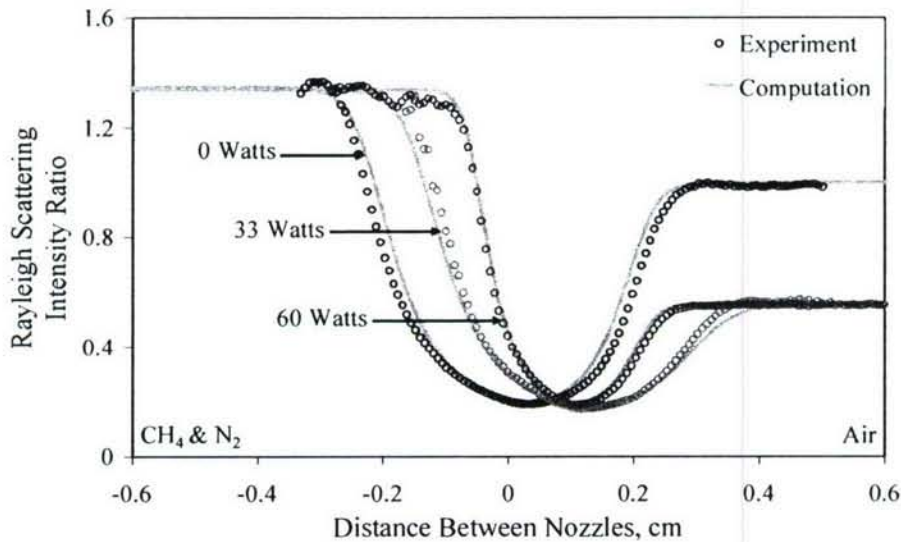


**Fig. 24 Comparison of Rayleigh scattering intensity ratio profiles with 0 Watts, 33 Watts and 60 Watts of plasma power addition at strain rates of  $87.1\text{ s}^{-1}$ ,  $98.6\text{ s}^{-1}$  and  $298.5\text{ s}^{-1}$  respectively.**

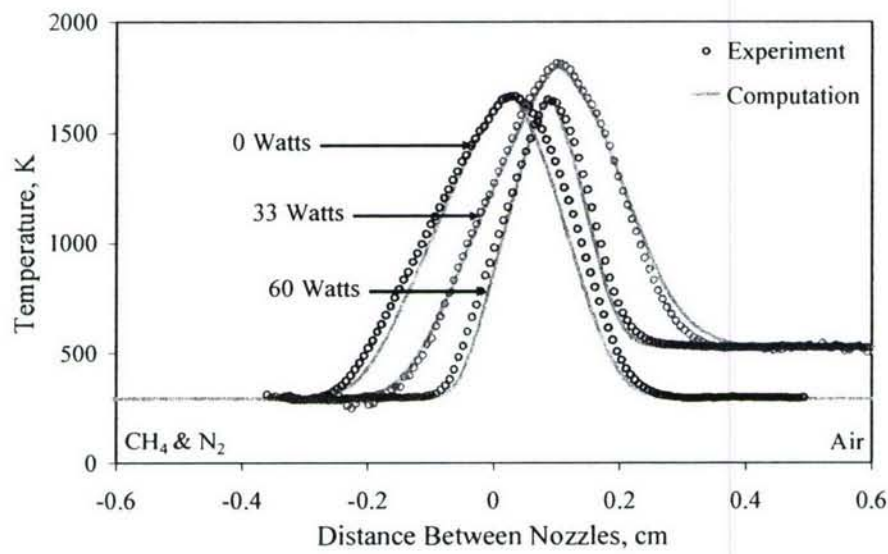


**Fig. 25 Comparison of temperature profiles with 0 Watts, 33 Watts and 60 Watts of plasma power addition at strain rates of  $87.1\text{ s}^{-1}$ ,  $98.6\text{ s}^{-1}$  and  $298.5\text{ s}^{-1}$  respectively.**

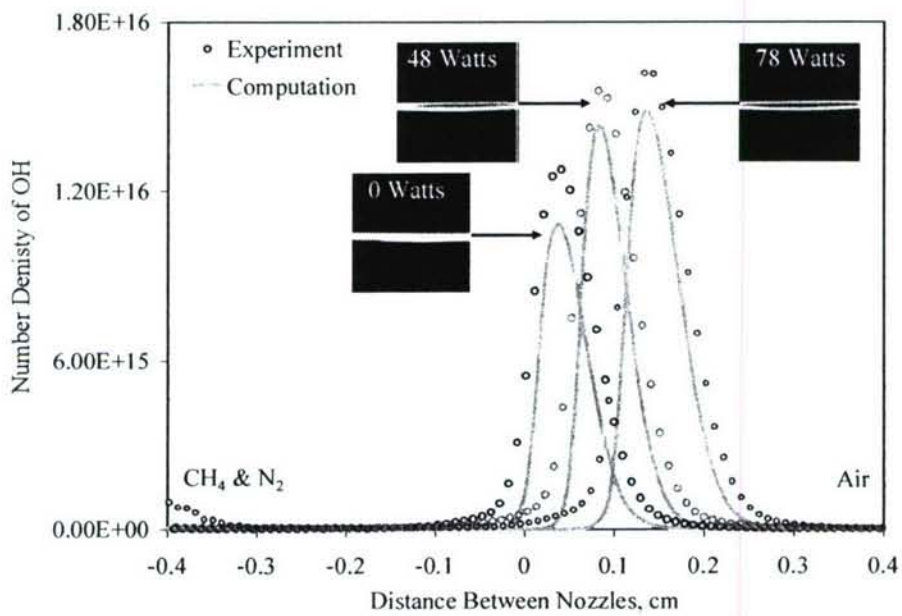


**Fig. 26 Comparison of OH number density distributions with 0 Watts, 48 Watts and 78 Watts of plasma power addition at strain rates of  $83.3\text{ s}^{-1}$ ,  $127.7\text{ s}^{-1}$  and  $183.0\text{ s}^{-1}$  respectively.**

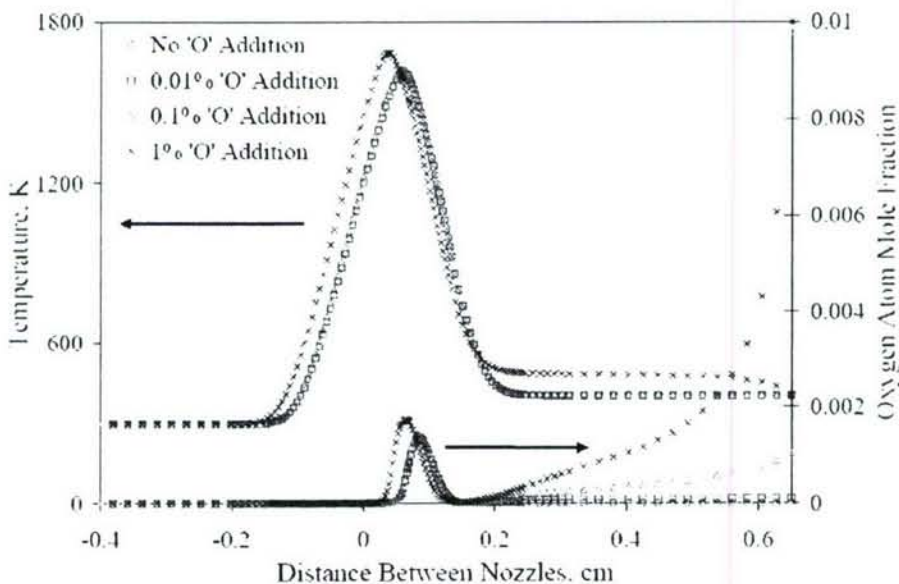


**Fig. 27 Computed temperature and Oxygen atom distributions between the nozzles of the counterflow system with Oxygen atom addition.**

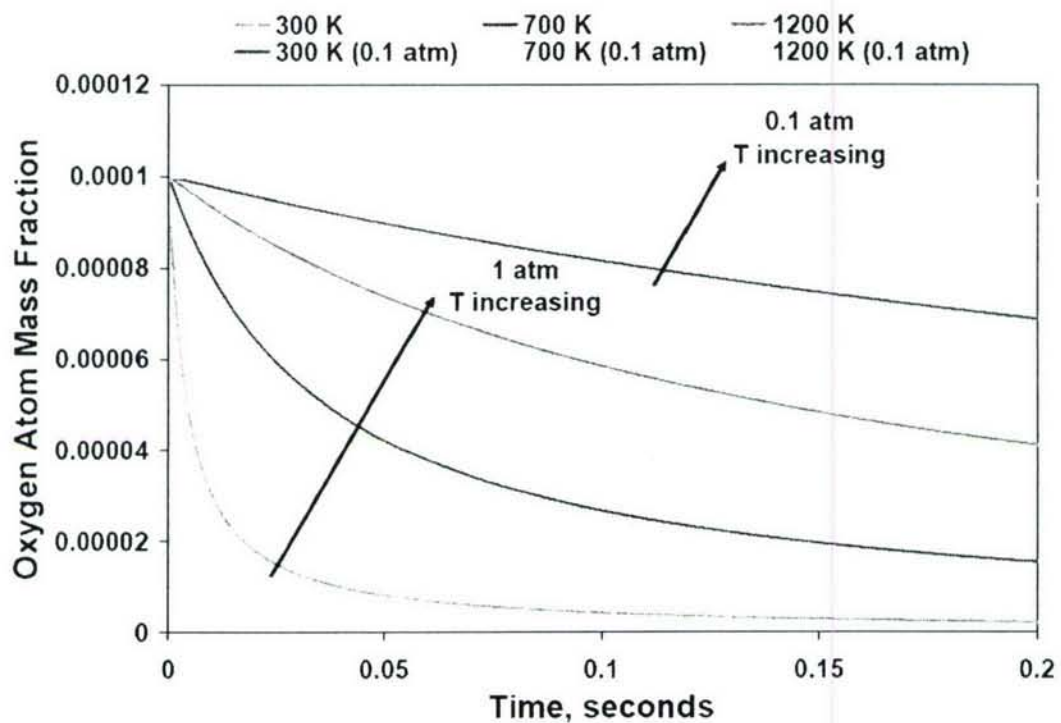


**Fig. 28** Oxygen radical lifetimes in air, for typical residence times in the MGA counterflow burner system. It is seen that increasing the temperature or reducing the pressure can help survive the radicals until they reach the flame.

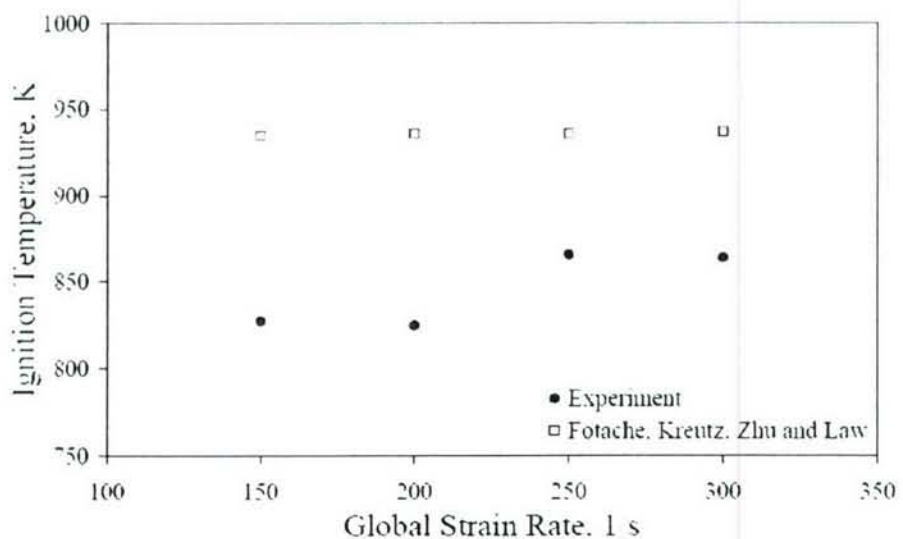


**Fig. 29** Comparison of ignition temperatures of counterflow hydrogen diffusion flames using pre-heater versus pre-heater and gliding arc activation of the air stream.

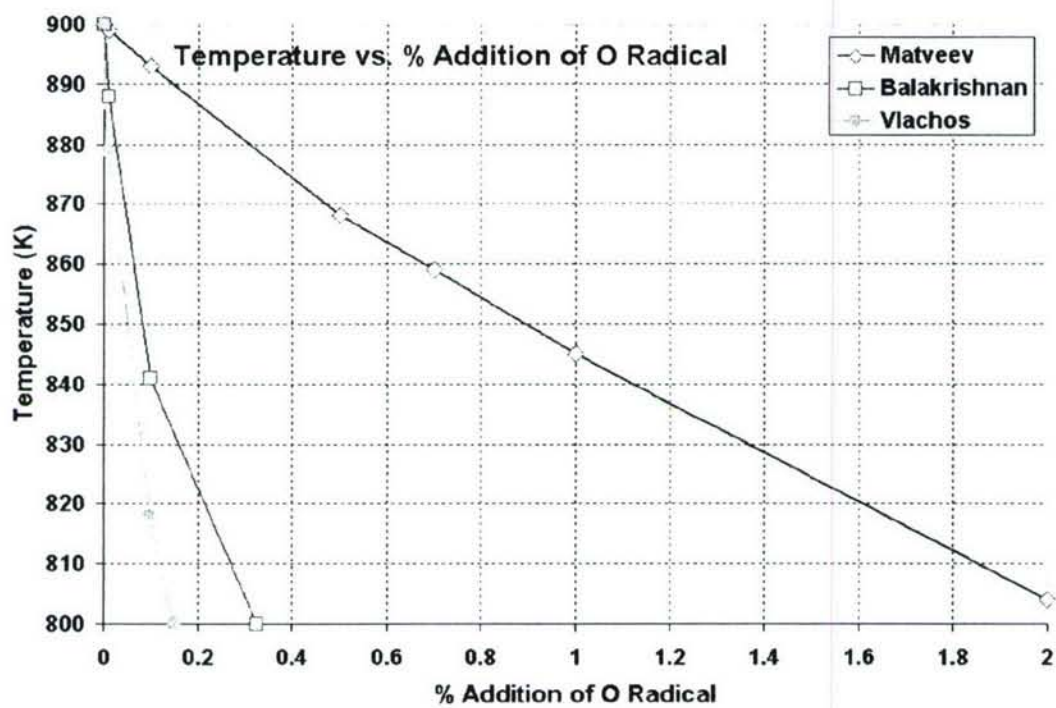


**Fig. 30 Comparison of preheat temperature required to achieve same ignition delay for various percent volume additions of oxygen radicals using three mechanisms for H<sub>2</sub>-air, namely – Balakrishnan, Matveev and Vlachos.**



Available online at [www.sciencedirect.com](http://www.sciencedirect.com)



Proceedings of the Combustion Institute 31 (2007) 2489–2496

Proceedings  
of the  
Combustion  
Institute

[www.elsevier.com/locate/proci](http://www.elsevier.com/locate/proci)

## Ignition enhancement by addition of NO and NO<sub>2</sub> from a N<sub>2</sub>/O<sub>2</sub> plasma torch in a supersonic flow

Kenichi Takita <sup>a,\*</sup>, Naoyuki Abe <sup>a</sup>, Goro Masuya <sup>a</sup>, Yiguang Ju <sup>b</sup>

<sup>a</sup> Department of Aeronautics and Space Engineering, Tohoku University, Aoba 6-6-01, Aramaki, Sendai 980-8579, Japan

<sup>b</sup> Department of Mechanical and Aerospace Engineering, Princeton University, Princeton, NJ 08544, USA

### Abstract

The effects of NO and NO<sub>2</sub> produced by using a plasma jet (PJ) of a N<sub>2</sub>/O<sub>2</sub> mixture on ignition of hydrogen, methane, and ethylene in a supersonic airflow were experimentally and numerically investigated. Numerical analysis of ignition delay time showed that the addition of a small amount of NO or NO<sub>2</sub> drastically reduced ignition delay times of hydrogen and hydrocarbon fuels at a relatively low initial temperature. In particular, NO and NO<sub>2</sub> were more effective than O radicals for ignition of a CH<sub>4</sub>/air mixture at 1200 K or lower. These ignition enhancement effects were examined by including the low temperature chemistry. Ignition tests by a N<sub>2</sub>/O<sub>2</sub> PJ in a supersonic flow ( $M = 1.7$ ) for using hydrogen, methane, and ethylene injected downstream of the PJ were conducted. The results showed that the ignitability of the N<sub>2</sub>/O<sub>2</sub> PJ is affected by the composition of the feedstock and that pure O<sub>2</sub> is not the optimum condition for downstream fuel injection. This result of ignition tests with downstream fuel injection demonstrated a significant difference in ignition characteristics of the PJ from the ignition tests with upstream fuel injection.

© 2006 The Combustion Institute. Published by Elsevier Inc. All rights reserved.

**Keywords:** Supersonic combustion; Scramjet; Plasma torch; Ignition; Radical

### 1. Introduction

A plasma jet (PJ) torch that can supply radicals to a combustor is suitable for use as the igniter of a scramjet engine [1], where only a short residence time of a fuel is allowed for mixing, ignition and completion of the combustion. Therefore, extensive research of ignition by the PJ in a supersonic flow has been experimentally and numerically conducted for both hydrogen [2–5] and hydrocarbon fuels [6,7]. In previous studies, however, isolation of the ignition

enhancement effect of radicals from that of high temperature in the PJ was difficult because radicals are able to exist only in the limited high temperature region of the PJ plume and their life time is very short due to the rapid radical quenching by recombination reactions [8]. This tendency has been clearly shown in past experimental findings [9]. Ignition by the PJ was easily achieved, even for a CH<sub>4</sub> fuel that has the longest ignition delay among hydrocarbons in the case of fuel injection upstream of the PJ, where the PJ played the role of flame holder. On the other hand, in the case of fuel injection downstream of the PJ, where temperature and radical concentration quickly decayed, ignition was rarely achieved even for H<sub>2</sub> fuel, unless a very large input PJ power is delivered.

\* Corresponding author. Fax: +81 22 795 7009.

E-mail address: [\(K. Takita\).](mailto:takita@cc.mech.tohoku.ac.jp)

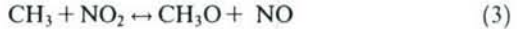
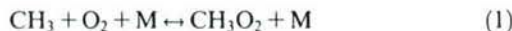
### Nomenclature

$C$	mole fraction	$P_{IN}$	electric power input
$ER$	equivalence ratio	$T_0$	initial temperature
$p_0$	system pressure or initial pressure	$T_i$	inlet temperature
$p_w$	wall pressure	$X_i$	position of fuel injector
$p_{t0}$	total pressure of main flow		

Although the radical quenching was very quick, a long yellow-blue plume of the PJ was observed in a supersonic flow in experiments [6,7,9]. This yellow-blue plume [6,7] was considered to consist of  $\text{NO}_x$  emissions produced by the contact of the high temperature PJ with the main airflow or of them included in a  $\text{N}_2/\text{O}_2$  PJ such as an air PJ. The effect of the  $\text{NO}_x$  included in the PJ has rarely been seriously considered in the past research, because it is much smaller than that of active radicals such as O, H and OH. However, it is well known that  $\text{NO}_x$  (NO and  $\text{NO}_2$ ) can accelerate ignition processes of hydrogen [10] and hydrocarbons [11,12] under particular temperature and pressure conditions. The results [11,12] showed that low temperature chemistry involving NO,  $\text{NO}_2$ ,  $\text{HO}_2$ ,  $\text{CH}_3\text{O}$ , and  $\text{CH}_3\text{O}_2$  plays a significant role in accelerating the chain-branching reaction of hydrocarbon fuels. A thermal PJ has a significant  $\text{NO}_x$  production, and once the  $\text{NO}_x$  are formed in plasma, they are very stable in the plume. Therefore, if NO and  $\text{NO}_2$  are supplied to a combustible mixture from the PJ of the  $\text{N}_2/\text{O}_2$  mixture with a suitable mixing ratio for ignition enhancement, such a PJ may be more effective than the existing one. The focus on relatively stable species such as NO,  $\text{NO}_2$ , and  $\text{HO}_2$  in the PJ leads to new combustion technology besides that of the scramjet engine. In the present study, the effects of NO and  $\text{NO}_2$  on ignition delay were numerically calculated, and then those effects were evaluated by ignition tests using the  $\text{N}_2/\text{O}_2$  PJ with different mixing ratios.

### 2. Numerical method and kinetic models

In numerical simulations, the ignition delay was calculated by using the SENKIN code in the CHEMKIN package [13]. The following low temperature chemistry [11,12,14] was added to GRI mech. Ver.3.0 [15]. The importance of them was carefully demonstrated by Tan et al. [11] and Amano et al. [12], based on their experimental results.



### 3. Experimental setup

#### 3.1. Wind tunnel and test section

The experiment was conducted using an intermittent suction type wind tunnel. Figure 1 shows a schematic of the test section. Atmospheric air was inhaled and accelerated to supersonic speed through a two-dimensional contoured nozzle. The test section had a 30 mm square uniform cross section and was 335 mm long. The Mach number and the characteristic length for unity Reynolds number of the main flow were 1.7 and  $8.9 \times 10^6 \text{ m}^{-1}$ , respectively. The Cartesian coordinate,  $X$ , was defined as the distance from the center of the torch nozzle. Success of ignition by the PJ was evaluated based on the wall pressure measured by a strain-gauge-type pressure transducer.

#### 3.2. Plasma torch

The same plasma torch as that used in a series of previous studies [3,8,9] was employed. The detailed structure has been reported in the cited papers. The cathode was made of hafnium to attain high durability when oxygen was used as the feedstock. The anode and the nozzle were made of  $\text{O}_2$ -free copper. The diameter of

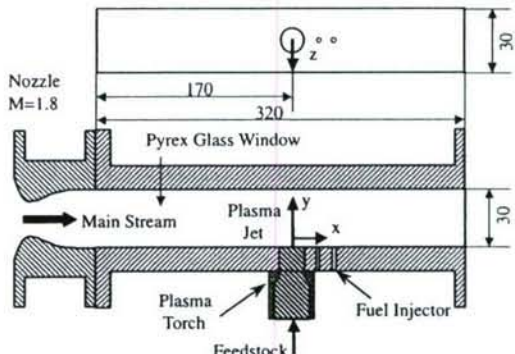


Fig. 1. Schematic of test section in experiment.

the nozzle throat was 1.5 mm. N<sub>2</sub>, O<sub>2</sub> and a N<sub>2</sub>/O<sub>2</sub> mixture were used as feedstock gases and their mole flow rates were set at 1.1 × 10<sup>-2</sup> mol/s.

### 3.3. Fuel injector

The fuel was injected perpendicularly into the main stream at its speed of sound from an orifice located at  $X_i = 24$  mm or 32 mm on the centerline of the bottom wall. The diameter of the orifice was 1.0 mm. Three kinds of fuels (H<sub>2</sub>, CH<sub>4</sub> and C<sub>2</sub>H<sub>4</sub>) at room temperature were tested. The bulk equivalence ratio and the dynamic pressure ratio of the fuel jet and the main flow were set at 0.062 and 2.0, respectively, for all fuels. The ratio of the amount of heat release via complete combustion of the fuels is 1.2, 1.1, and 1.0 for H<sub>2</sub>, C<sub>2</sub>H<sub>4</sub>, and CH<sub>4</sub>, respectively.

## 4. Results and discussion

### 4.1. Mole fractions of NO and NO<sub>2</sub> in N<sub>2</sub>/O<sub>2</sub> PJ

The relation between the mole fractions of NO and NO<sub>2</sub> in the PJ and the compositions of the N<sub>2</sub>/O<sub>2</sub> feedstock was investigated by using the PSR (perfectly stirred reactor) code in the CHEMKIN package [13]. The composition of the exhaust plasma was estimated as products of the high temperature N<sub>2</sub>/O<sub>2</sub> mixture after a specific residence time in a reactor. Figure 2a shows the mole fractions of NO<sub>2</sub> for different inlet temperatures ( $T_i$ ). The inlet temperature corresponds to the electric power input ( $P_{IN}$ ) to the torch and it can be estimated from the feedstock flow rates in the experiment. The residence time and the system pressure of the reactor were 0.1 s and 0.1 MPa, respectively. Changes in mole fractions of products were very small after such a long residence time, and therefore the results shown in Fig. 2 are considered to be close to the equilibrium conditions. Actually, the PJ does not necessarily reach the equilibrium condition. In such a case, mole fractions of NO and NO<sub>2</sub> are smaller than those at equilibrium.

An increase in  $T_i$ , namely, an increase in  $P_{IN}$ , resulted in an increase in the mole fraction of NO<sub>2</sub> in Fig. 2. A peak appeared around N<sub>2</sub> = 35% in the N<sub>2</sub>/O<sub>2</sub> mixture. This percentage agreed with the atomic ratio of N in a NO<sub>2</sub> molecule. The mole fraction of NO<sub>2</sub> at N<sub>2</sub> = 35% was about twice that of air (N<sub>2</sub> = 79%) feedstock. Figure 2b shows mole fractions of NO and NO<sub>2</sub> for different system pressures. The amount of NO produced by reactions of the N<sub>2</sub>/O<sub>2</sub> mixture was much greater than that of NO<sub>2</sub>, and it did not strongly depend on the pressure and composition of the mixture. On the other hand, the mole fraction of NO<sub>2</sub> was proportional to the pressure.

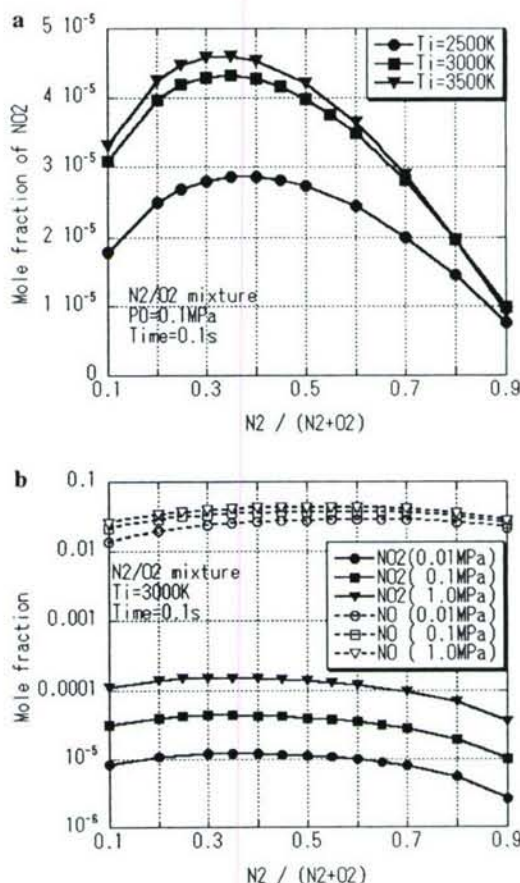
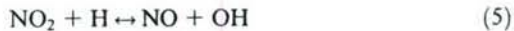


Fig. 2. Mole fractions of NO and NO<sub>2</sub> in near equilibrium state of high temperature N<sub>2</sub>/O<sub>2</sub> mixture. (a) Dependence on temperature of mixture. (b) Dependence on pressure of reactor.

### 4.2. Effect of the addition of NO and NO<sub>2</sub> on ignition delay

Figure 3 shows the effects of radical addition on ignition delays for three fuels, respectively. The ambient pressure, radical concentration in a mixture, and fuel equivalence ratio were 0.1 MPa, 0.1%, and 1.0, respectively, for all fuels.

In the case of H<sub>2</sub> fuel, the effect of NO strongly appeared at low initial temperature, though the effect of O radicals was much greater than that. The effect of the addition of NO<sub>2</sub> was very small in comparison to those of NO and O radicals. The catalytic effect of NO on ignition of H<sub>2</sub> is mainly via the following reactions [10]:



In contrast to the H<sub>2</sub> fuel, the effects of the addition of NO and NO<sub>2</sub> on ignition delay of CH<sub>4</sub>/air

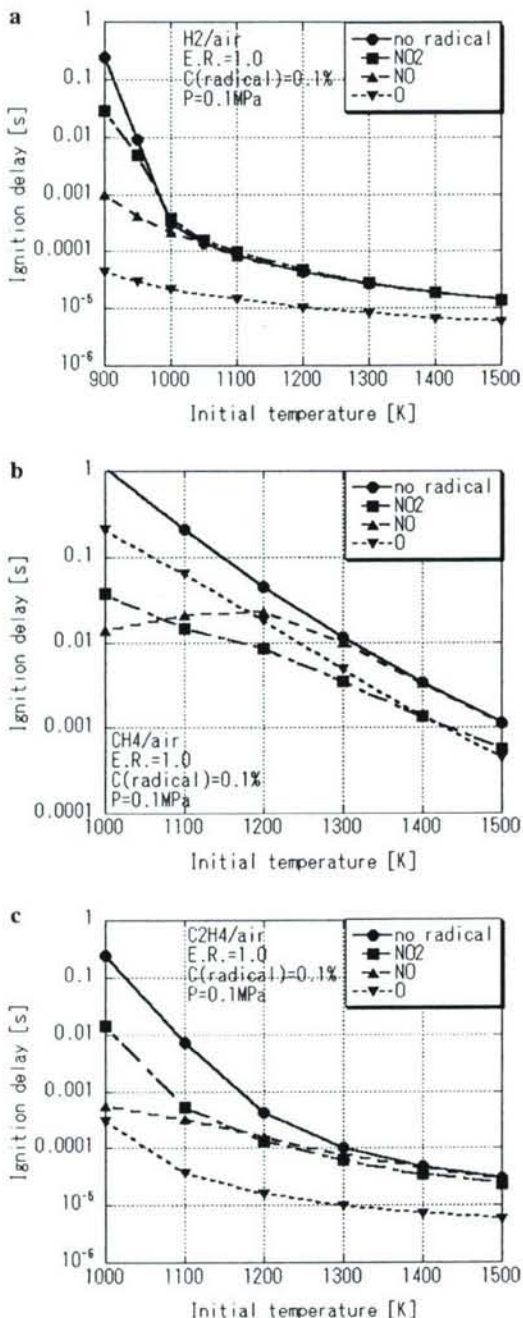


Fig. 3. Reduction of ignition delay time by addition of radicals ( $P_0 = 0.1 \text{ MPa}$ ). (a) H<sub>2</sub>/air mixture. (b) CH<sub>4</sub>/air mixture. (c) C<sub>2</sub>H<sub>4</sub>/air mixture.

mixture were greater than that of O radicals at an initial temperature lower than 1400 K. In particular, NO<sub>2</sub> was the most effective in the middle temperature range between 1100 and 1400 K. Note that such effect of NO<sub>2</sub> was not obtained when low temperature chemistry was not included. In

the case of C<sub>2</sub>H<sub>4</sub> fuel, similar to the CH<sub>4</sub> case, the addition of NO and NO<sub>2</sub> drastically reduced ignition delay at a low initial temperatures. However, the addition of O radicals was much more effective than those of NO and NO<sub>2</sub>. This tendency was different from the case of CH<sub>4</sub>, but it was the same as in the case of H<sub>2</sub>. The ignition delay of the C<sub>2</sub>H<sub>4</sub>/air mixture with the addition of O radicals was comparable to that of the H<sub>2</sub>/air mixture. These different tendencies of results for CH<sub>4</sub> and C<sub>2</sub>H<sub>4</sub> can be explained by considering the oxidation process of CH<sub>4</sub>. The oxidation of CH<sub>3</sub> to CH<sub>3</sub>O is very slow and dominates the ignition process of CH<sub>4</sub>, and therefore the acceleration of the oxidation via reaction (1)–(3) results in considerable decrease of the ignition delay time of CH<sub>4</sub>.

The static pressure of the main flow in the experiment was on the order of 0.01 MPa. Change in the ignition delay by the addition of radicals at  $P = 0.01 \text{ MPa}$  was investigated. Figure 4 shows the ignition delays of three fuels at  $P = 0.01 \text{ MPa}$  with and without radicals. Basically, the ignition delay increases with the decrease in pressure for the three fuels. Figure 4a shows the results of the H<sub>2</sub>/air mixture. The effect of the addition of NO was very small at  $P = 0.01 \text{ MPa}$ . Han et al. [10] suggested that the effect of NO on ignition of the H<sub>2</sub>/air mixture strongly appeared when the pressure was greater than the critical pressure of the mixture at the second explosion limit. The temperature region where the addition of NO was effective shifted to a temperature region lower than that at  $P = 0.1 \text{ MPa}$ . On the other hand, the addition of O radicals reduced the ignition delay of the H<sub>2</sub>/air mixture, even at  $P = 0.01 \text{ MPa}$  because the chain-branching reaction by O radicals did not strongly depend on pressure.

Figure 4b shows the ignition delay of the CH<sub>4</sub>/air mixture at  $P = 0.01 \text{ MPa}$ . It is seen that the effect of the addition of NO on the ignition delay of the CH<sub>4</sub>/air mixture also depended on pressure because the main path (reaction (1)) for acceleration reactions is a tri-molecular reaction. On the other hand, the main path of the NO<sub>2</sub> effect (reaction (3)) is a bimolecular reaction, and therefore it is less pressure dependent. Figure 4b shows that, even at  $P = 0.01 \text{ MPa}$ , NO<sub>2</sub> addition promotes ignition as good as the addition of O radicals. However, with the decrease in pressure the ignition delay of the CH<sub>4</sub>/air mixture without radical addition considerably increased. Therefore, at low pressure, a very high temperature region is needed to achieve ignition of the CH<sub>4</sub> fuel in a supersonic flow, even when a large number of radicals are supplied by the PJ. As for the C<sub>2</sub>H<sub>4</sub> fuel, at  $P = 0.01 \text{ MPa}$ , the addition of O radicals was much more effective in reducing the ignition delay than the addition of NO or NO<sub>2</sub> radicals at high temperatures. Nevertheless, as temperature decreases, the ignition enhancement via NO<sub>x</sub> addition becomes more significant.

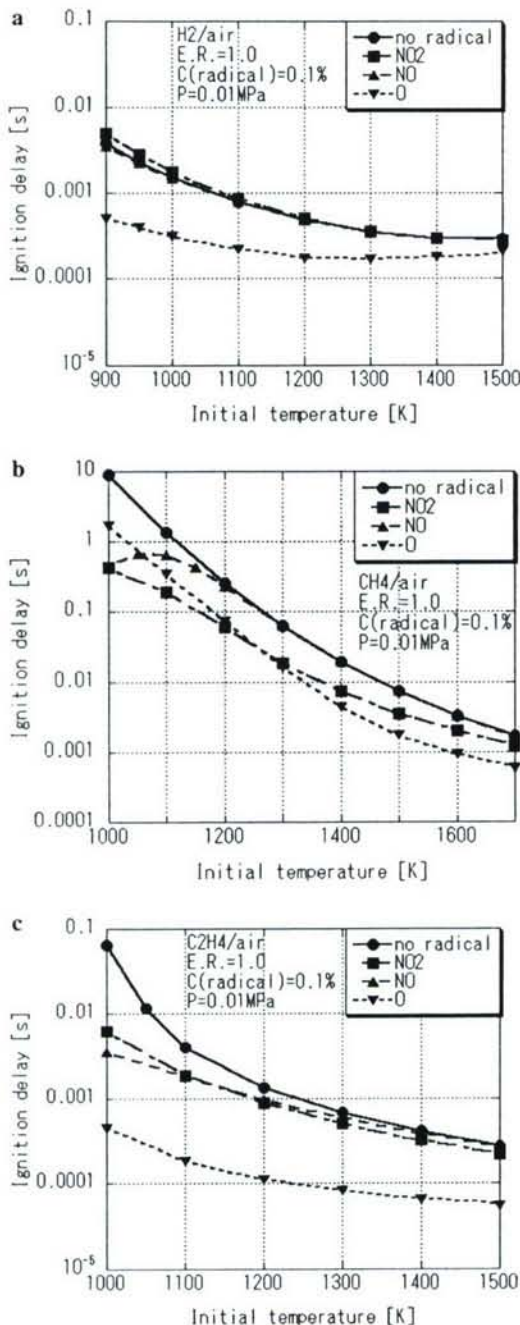


Fig. 4. Reduction of ignition delay time by addition of radicals ( $P_0 = 0.01 \text{ MPa}$ ). (a) H<sub>2</sub>/air mixture. (b) CH<sub>4</sub>/air mixture. (c) C<sub>2</sub>H<sub>4</sub>/air mixture.

#### 4.3. Ignition tests with N<sub>2</sub>/O<sub>2</sub> PJ torches

Ignition tests of the N<sub>2</sub>/O<sub>2</sub> PJ were conducted for three fuels, which were injected downstream of the PJ at  $X_i = 24 \text{ mm}$ . Figure 5 plots averaged

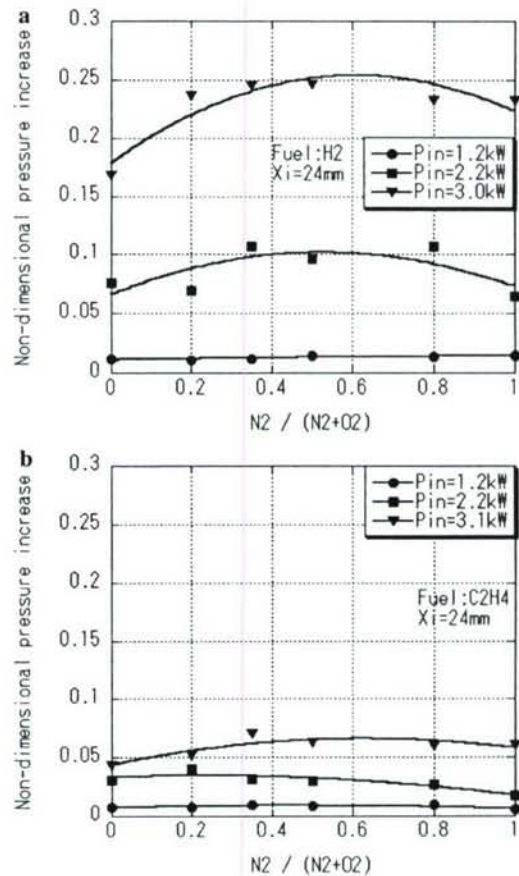


Fig. 5. Effect of mixing ratio of N<sub>2</sub>/O<sub>2</sub> feedstock on wall pressure increase due to combustion of fuel injected at  $X_i = 24 \text{ mm}$  in experiment. (a) H<sub>2</sub>/air mixture. (b) C<sub>2</sub>H<sub>4</sub>/air mixture.

non-dimensional wall pressure increases ( $P_w/P_{t0}$ ) due to combustion of the fuel (H<sub>2</sub> and C<sub>2</sub>H<sub>4</sub>) for different mixing ratios of the feedstock.

An increase in wall pressure was not obtained for the CH<sub>4</sub>/air mixture in any conditions due to the long ignition delay time of the CH<sub>4</sub>/air mixture. Ignition and combustion did not occur within the test section, even when many radicals were supplied by increasing the PJ power. As shown in Figs. 3 and 4, the temperature of the PJ plume was probably too low to ignite the CH<sub>4</sub> at the site of fuel injection.

Figure 5 shows that the wall pressures for H<sub>2</sub> and C<sub>2</sub>H<sub>4</sub> fuels injections increased considerably with the increase of the PJ power,  $P_{IN}$ . This result indicates that the amount of combustion is in proportion to the electric power input. Figure 5 also shows that increase of wall pressure depended on the composition of the feedstock gas, although it was small. At large PJ power inputs, it can be seen that the feedstock of the N<sub>2</sub>/O<sub>2</sub> mixture had a better performance than that

of mono-component feedstock of either pure N<sub>2</sub> or pure O<sub>2</sub>. Since O radical has a much shorter lifetime than NO<sub>x</sub> at intermediate temperatures, the ignition dependence on feedstock composition may be caused by the combined enhancement effect of NO<sub>x</sub> and O radical additions on ignition (Figs. 3 and 4).

In addition, this result was obviously different from the results in past experiments[6,9], in which the fuel was injected upstream of the PJ so that the O radical lifetime was not relevant. The authors have previously shown that the O<sub>2</sub> PJ is much superior to the N<sub>2</sub> PJ for hydrocarbon fuels in the case of upstream fuel injection [9]. Shuzenji et al. [6] have also demonstrated that the O<sub>2</sub> PJ is much more effective for ignition of CH<sub>4</sub> than the N<sub>2</sub> PJ and the air PJ for the upstream fuel injection. The difference in the order of effectiveness of the feedstock between the upstream and downstream fuel injections suggested that the process from ignition to development of a combustion region is different between the two cases and that lifetime of active radicals also play an important role. In the case of the upstream fuel injection, local ignition occurs right at the collision point of PJ and fuel flow, and after the local ignition, a large flame region is established even for the CH<sub>4</sub> fuel. Shuzenji et al.[16] estimated temperatures of core regions of the N<sub>2</sub> and O<sub>2</sub> PJs by spectroscopic measurement of atomic emission lines emitted from the PJs. They reported that temperatures of the core regions were about 8000–10,000 K at  $P_{IN} = 1$  kW. Such a high temperature and existence of rich radicals were sufficient for instantaneous ignition of even the CH<sub>4</sub>/air mixture. Characteristics of flame spread around the local ignition point become important for the upstream fuel injection.

On the other hand, results of the downstream fuel injection reflected solely an auto-ignition process affected by the radicals and temperature evolutions after the upstream plasma. In this case, the temperature profile is dominantly depended on the PJ power and the effect of feedstock composition is negligible. However, at a given PJ input power, the feedstock composition may have a significant effect on the radical profiles because different radicals have different residence time at a given temperature field in a supersonic flow. Although O radical has a better ignition enhancement effect for H<sub>2</sub> and C<sub>2</sub>H<sub>4</sub>, it has much shorter lifetime than that of NO<sub>x</sub>. Therefore, pure oxygen PJ is not a good choice in this case. In other words, the downstream injection approach provides an excellent platform to examine separately the thermal and non-thermal ignition enhancement effects. The sensitivity of thermal and non-thermal effects can be investigated by varying the PJ plasma power, the feedstock composition, and the flow residence time between the PJ and the site of downstream fuel injection.

Although the impact was not very profound, the dependence of wall pressure rise on feedstock composition shown in Fig. 5 has indicated that there existed a non-thermal effect via NO and NO<sub>2</sub> additions. To further confirm which effect plays a dominant role, ignition tests were conducted for fuel injected at  $X_i = 32$  mm, that is, the site of the fuel injector being moved downstream by 8 mm. Figure 6 shows wall pressure increases due to combustion. The amount of combustion considerably decreased with an increase in the distance between the PJ torch and the fuel injector of only 8 mm. This result suggests that at low temperatures, the thermal effect (the temperature increase) was dominant for ignition behavior. If the NO and NO<sub>2</sub> effects were remarkable, they must have been insensitive to the distance, because NO and NO<sub>2</sub> were stable and thus their concentrations were almost constant in the plume. This conclusion agrees with the results from the non-equilibrium plasma assisted combustion enhancement in a counterflow flame [17].

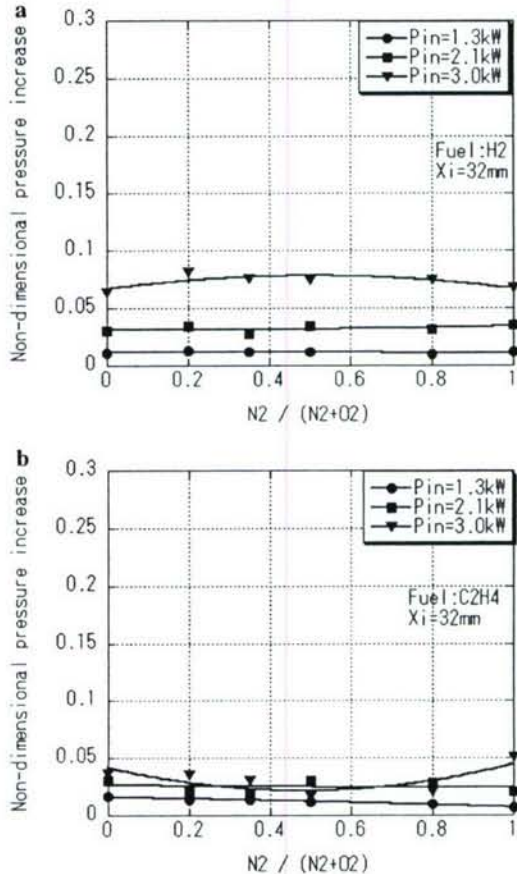


Fig. 6. Effect of mixing ratio of N<sub>2</sub>/O<sub>2</sub> feedstock on wall pressure increase due to combustion of fuel injected at  $X_i = 32$  mm in experiment. (a) H<sub>2</sub>/air mixture. (b) C<sub>2</sub>H<sub>4</sub>/air mixture.

The low static pressure of the tested cases was probably one cause of weak enhancement effect of NO and NO<sub>2</sub> in ignition. However, the actual scramjet engine conditions or experimental conditions of the sub-scale model scramjet engine test [18] include a region of static pressure that is much higher than that in this study. As such, the effects of NO and NO<sub>2</sub> can be expected to be stronger under such high static pressure. Strong dependence of the effect of NO<sub>2</sub> on pressure and temperature of the flowfield has been reported. For example, Pinald et al. [19] demonstrated that the addition of NO<sub>2</sub> caused no change in the DDT process because the NO<sub>2</sub> was not effective in promoting ignition at very high temperatures, a characteristic of detonation.

#### 4.4. Effect of addition of HO<sub>2</sub>

Similar to NO<sub>x</sub>, the HO<sub>2</sub> species are also stable at low temperatures and accelerate the NO catalytic effects on ignition of H<sub>2</sub> through reaction step (reaction 4). Moreover, the existence of HO<sub>2</sub> also accelerates oxidation of CH<sub>3</sub> radicals through the following reaction:



Therefore, the coexistence of HO<sub>2</sub> with NO and NO<sub>2</sub> may result in considerable acceleration of the ignition process for both H<sub>2</sub> and hydrocarbons. The ability of the PJ which employs a N<sub>2</sub>/O<sub>2</sub>/H<sub>2</sub> mixture is worth testing because, in addition to NO and NO<sub>2</sub>, the HO<sub>2</sub> are also formed in the PJ and through the reaction of H + O<sub>2</sub> + M = HO<sub>2</sub> + M in air. Figure 7 shows the effect of addition of HO<sub>2</sub> radicals to NO<sub>2</sub> radicals on reducing the ignition delay time of the CH<sub>4</sub>/air mixture. It was demonstrated in Fig. 7 that the addition of a small amount of HO<sub>2</sub> to NO<sub>2</sub> strongly enhanced the catalytic effect of

NO<sub>2</sub> at a low initial temperature. For example, the addition of 0.001% HO<sub>2</sub> to 0.099% NO<sub>2</sub> in volume reduced the ignition delay time by 64% of that for the CH<sub>4</sub>/air mixture with 0.1% NO<sub>2</sub> at T<sub>0</sub> = 1200 K.

## 5. Conclusions

- (1) The addition of NO and NO<sub>2</sub> significantly reduced ignition delay times of H<sub>2</sub> and hydrocarbon fuels at low initial temperature. For CH<sub>4</sub>/air mixtures, the ignition enhancement is even better than that of O radical due to the low temperature chemistry.
- (2) A downstream fuel injection approach was presented and tested. The results showed that this approach provides a new opportunity to separate the thermal and non-thermal effects of plasma jet on ignition enhancement in a supersonic flow.
- (3) The results showed that for downstream fuel injection, the feedstock composition affected the ignition and the pure O<sub>2</sub> PJ is not the optimum condition. This result is obviously different from the case of upstream fuel injection. This difference indicates that non-thermal effect plays a role in affecting ignition enhancement and that the radical lifetime is also an important parameter for choosing the optimum feedstock.
- (4) With the increase of pressure, the effect of ignition enhancement via NO<sub>x</sub> addition increases. This implies that the non-thermal ignition enhancement via NO<sub>x</sub> as addition may play greater role at actual scramjet engine conditions.

## Acknowledgments

This study was supported by the Sumitomo Foundation and the JFE 21st Century Foundation. The authors are grateful to Jun Ikeda, Sotaro Wada and Ryuta Ohashi for their help. Y. Ju appreciates the grant support from AFSOR.

## References

- [1] I. Kimura, H. Aoki, M. Kato, *Combust. Flame* 42 (1981) 297–305.
- [2] K. Takita, T. Uemoto, T. Sato, Y. Ju, G. Masuya, K. Ohwaki, *J. Prop. Power* 16 (2) (2000) 227–233.
- [3] K. Takita, *Combust. Flame* 128 (3) (2002) 301–313.
- [4] R. Minato, T. Niio, AIAA Paper 2003-6908 (2003).
- [5] K. Kobayashi, S. Tomioka, T. Mitani, *J. Prop. Power* 20 (2) (2004) 294–301.

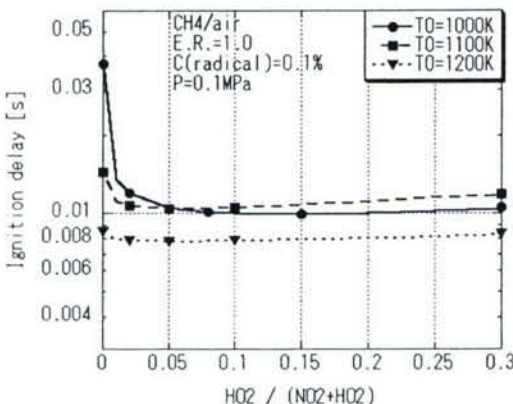


Fig. 7. Effect of coexistence of HO<sub>2</sub> with NO<sub>2</sub> on reduction of ignition delay time of CH<sub>4</sub>/air mixture (P<sub>0</sub> = 0.1 MPa).

- [6] K. Shuzenji, T. Tachibana, *Proc. Combust. Inst.* 29 (2002) 875–881.
- [7] S.D. Gallimore, L.S. Jacobsen, W.F. O'Brien, J.A. Schetz, *J. Prop. Power* 19 (2) (2003) 170–181.
- [8] K. Takita, A. Moriwaki, T. Kitagawa, G. Masuya, *Combust. Flame* 132 (3) (2003) 679–689.
- [9] T. Kitagawa, A. Moriwaki, K. Murakami, K. Takita, G. Masuya, *J. Prop. Power* 19 (5) (2003) 853–858.
- [10] B. Han, C.J. Sung, M. Nishioka, *Combust. Sci. Technol.* 176 (2004) 305–330.
- [11] Y. Tan, C.G. Fotache, C.K. Law, *Combust. Flame* 119 (1999) 346–355.
- [12] T. Amano, F.L. Dryer, *Proc. Combust. Inst.* 27 (1998) 397–404.
- [13] A.E. Lutz, R.J. Kee, J.A. Miller, SAND87-8248, Sandia National Laboratories, 1987.
- [14] J.H. Bromley, F.J. Barnes, S. Muris, X. You, B.S. Haynes, *Combust. Sci. Technol.* 115 (1996) 259–296.
- [15] G.P. Smith, D.M. Golden, M. Franklach, et al. GRI-Mech 3.0 (1999), available at [http://www.me.berkeley.edu/gri\\_mech/](http://www.me.berkeley.edu/gri_mech/).
- [16] K. Shuzenji, T. Tachibana, *J. Prop. Power* 21 (5) (2005) 908–913.
- [17] T. Ombrello, X. Qin, Y. Ju, A. Gutsol, A. Fridman, C. Carter, *AIAA J.* 119 (2006) 142–150.
- [18] T. Mitani, T. Hiraiwa, S. Sato, S. Tomioka, T. Kanda, K. Tani, *J. Prop. Power* 13 (1997) 635–641.
- [19] P.F. Pinard, A.J. Higgins, J.H.S. Lee, *Combust. Flame* 136 (1) (2004) 146–154.

### Comment

*Demitry Yarantsev, Russian Academy of Sciences, Russia.* Is the flow still supersonic in the region downstream of the injection? Because the diameter of the wind tunnel is just 30 mm, heat release due to the combustion may cause thermal choking of the flow.

*Reply.* If complete combustion of the fuel injected occurs, the flow reaches the thermal choking

condition and a shock train propagates upstream of the PJ. In such a case, the flow becomes subsonic. However, combustion efficiencies for cases of fuel injection downstream of the PJ described in this paper were low, and thermal choking did not occur. Therefore, the flow was still supersonic in most tests.